UNIVERSITAT POLITÈCNICA DE CATALUNYA
BARCELONATECH
Department of Signal Theory
and Communications

Transmission Impairments Mitigation in Next-Generation Coherent Optical Access Networks

Author

Jeison Alejandro Tabares Giraldo

Advisor

Josep Prat Gomà

A thesis submitted in fulfillment for the degree of Doctor of Philosophy

At the
Optical Communications Group
Department of Signal theory and Communications
Universitat Politècnica de Catalunya

July 2021

Abstract

Worldwide, the coherent technologies have revolutionized the optical communication systems, significantly increasing the capacity of the fiber channel owing to transmission of advanced modulation formats and effective mitigation of propagation impairments. However, the actual commercial solutions for long-haul core/backbone networks are still complex and costly, and therefore hardly feasible for deployment in optical access networks. In particular, the main limitations arise from the customer premises equipment whose cost, footprint and power consumption may be kept down. Thus, the optimal solutions for next generation coherent optical access are required to achieve high performance but at lower complexity and cost, since in the access scenario the cost-effectiveness takes more relevance over achieving the best system performance.

The research described in this thesis primarily aims at the development of the customer equipment –namely the coherent transceiver– for a passive optical access network that implements the novel wavelength-to-the-user concept by serving hundreds of users (e.g., 256 users) with dedicated wavelengths allocated in ultra-narrow optical grid. The proposed access network features complexity-reduced coherent technologies by leveraging photonic integration, commercial low-cost lasers and optics, and consumer electronics. To this end, the thesis investigates on the main transmission impairments that affect signal integrity from source to destination in the access network, and proposes novel and enhanced mitigation strategies by either low-complexity digital signal processing or analog hardware design.

The covered topics spread over both the optical transmitter and the coherent receiver subsystems. Simplified optical modulation is addressed by direct phase modulation of semiconductor lasers profiting from the laser chirp. Digital pre-equalization of non-ideal frequency response from electronic/photonic devices –such as lasers, amplifiers and data converters– is investigated, focusing on the tolerance to quantization noise from digital-to-analog converters with limited resolution. Hardware-efficient strategies for optical carrier recovery based on differential phase detection are explored in two scenarios: homodyne receivers aided by digital signal processing, or fully analog heterodyne receivers. Finally, to deal with the critical polarization matching in coherent systems, simplified architectures for polarization-independent coherent receivers using low-cost optics and simpler receiver front-end are investigated.

Table of Contents

Chapter 1

Introduction

1.1 Optical Access Networks

The global telecommunication infrastructure needs to continuously evolve facing the upcoming bandwidth-hungry multimedia services including ultra-high definition video, electronic commerce, Internet of Things (IoT) and business connectivity among others. In this regard, the optical communication networks have demonstrated that they can satisfy the requirements for broadband data services in a cost-effective manner, leveraging the vast bandwidth (BW) of the optical fibers and devices. The optical fiber exhibits the desired characteristics in a transmission medium: large BW, low attenuation, and immunity to electromagnetic interference. Moreover, the capital and operational expenditures (CAPEX and OPEX) for optical fiber deployment are lower than that of the traditional copper lines. For these reasons, optical fibers are now the preferred media to effectively transmit high speed data through long, medium, or even short distances.

Depending on the topology and the transmission link distance, optical networks are hierarchically classified as: core/backbone, metropolitan, and access. The access network is the last segment that reaches the final subscribers. Nowadays, access networks are becoming optical everywhere, substituting the legacy copper lines all the way from the central office (CO) up to the final user premise. These technologies are collectively known as fiber-to-the-x (FTTx), where x denotes the final optical fiber destination, i.e., home/building, business or radio antenna. Worldwide, the FTTx technologies experience an exponential growth driven by the Internet market demands and mobile connectivity. According to the number of residential fiber subscribers forecast, in 2022 most of the population will be reached by fiber-to-the-home (FTTH), at least in urban areas [Eff17].

The passive optical network (PON) is a type of access network intended for FTTx distribution that only employs passive elements –such as wavelength selective devices and power splitters– for the optical transport through the optical distribution network (ODN); thus, the overall PON only requires power at the transceiver (TRX) sides yielding high cost-savings in both implementation and maintenance. Since no active devices are placed within the ODN, the link power budget, i.e., the total power that can be assigned for a transmission path from the optical line terminal (OLT) to the optical network unit (ONU) by considering power splitting and insertion losses, should be carefully dimensioned to ensure that the receiver (RX) reaches the minimum optical signal power to operate error-free after forward error correction (FEC). Therefore, the RX sensitivity becomes a critical factor to be addressed in next generation PONs.

Currently deployed PON systems, or being under development as for next generation PON, are based on ITU/FSAN and IEEE international standards. Fig. 1.1 shows three different point-to-multipoint (P2MP) architectures for optical access networks. By considering the downstream

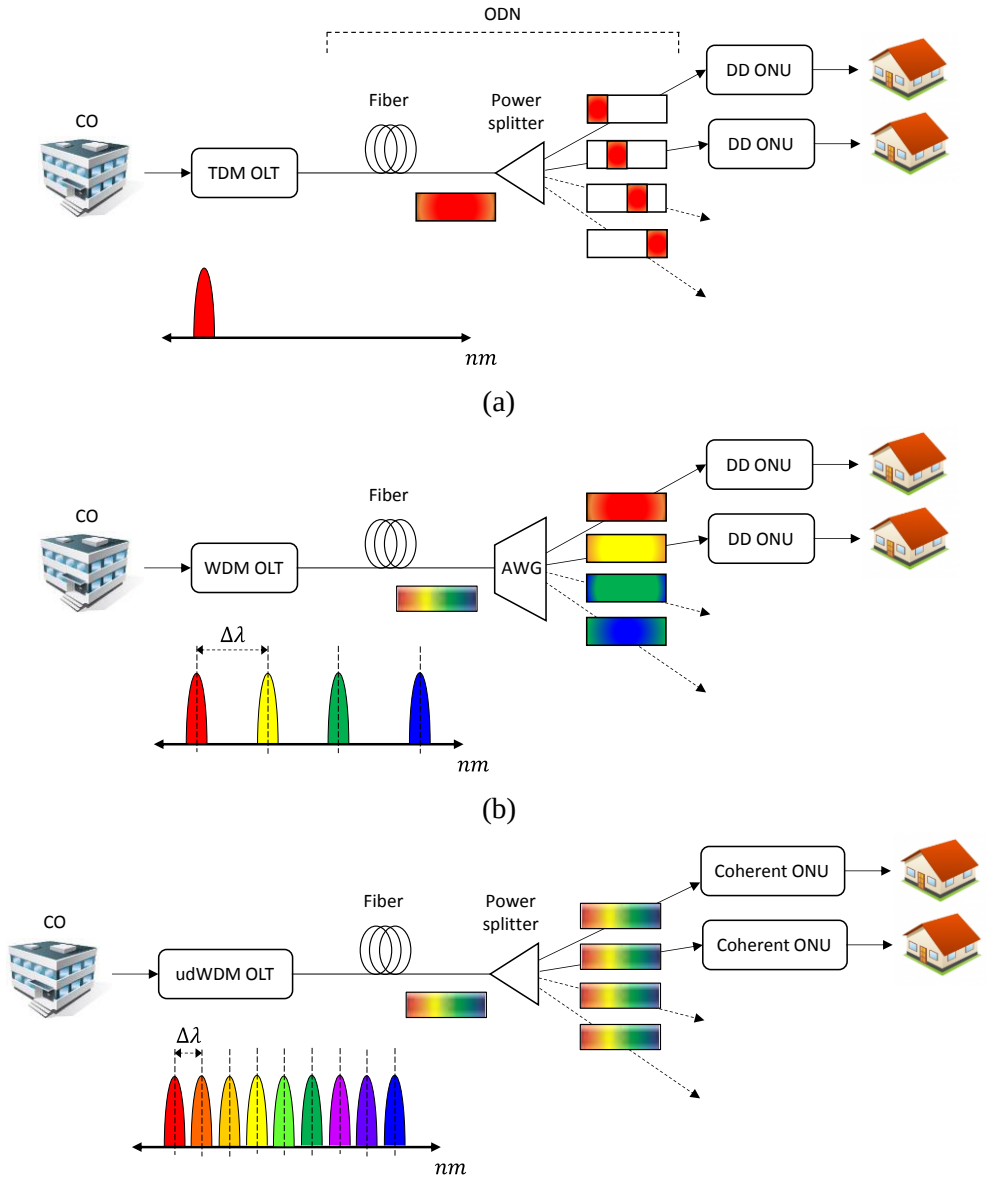

Figure 1.1. Network configuration for PON systems: (a) TDM-PON, (b) WDM-PON and (c) udWDM-PON.

(DS) direction, in the time division multiplexing PON (TDM-PON) in Fig. 1.1(a), all the users share the same wavelength (λ) and data transfer is achieved in the time domain by the assignment of time slots for each ONU. In this configuration, the aggregate PON capacity does not increase when new users are added since all users are served by the same λ. The user equipment implements direct detection (DD) RXs that are advantageous in terms of simplicity, but they are required to operate at the very high aggregate bit rate in both the opto-electronic components and in a relevant part of the media access control (MAC) layer, while the final user only benefits from a small fraction of it. For example, the XG-PON recommendation for current 10G optical access networks rely on intensity modulation and DD (IM-DD) TRXs at 10 Gb/s and lower, shared by TDM among 32/64 users [ITU17]; in these systems, the guaranteed effective BW per user is about 150/300 Mb/s while the ONU operates at the full 10 Gb/s. Taking into account that in fast

electronics (e.g., in CMOS) the power consumption scales with the clock (CLK) speed, there is a huge power and BW inefficiency in such a pure TDM distribution.

A step forward from TDM-PON consist of exploiting the optical frequency domain. The wavelength division multiplexing PON (WDM-PON) in Fig. 1.1(b) employs different λs for data transport that are distributed through the ODN by λ-selective optical components –such as arrayed waveguide grating (AWG)– behaving as optical channel selector. Now, each DD ONU detects a dedicated single λ already separated from the others by the AWG and operating only at the user BW, relaxing the hardware (HW) requirements and power consumption of the ONUs. However, the λ-selective characteristic of the ODN is the main drawback in this architecture because of the incompatibility with currently deployed TDM-PON ODN, and also because of the extra challenges and constraints for ONU provisioning and reconfiguration since each ONU needs to be matched in λ to that the assigned port of the AWG.

In the case of PON users requiring lower data rates, the WDM is also compatible with TDM by sharing some λs among several ONUs. Precisely, the latest ITU-T standard NG-PON2 [ITU19] exploits the WDM by stacking 4/8 XG-PON λs increasing the aggregate PON capacity up to 80 Gb/s. To keep up with increased BW demand and support future mobile traffic, next generation PONs target over 100 Gb/s aggregate capacity [Hou19] while ensuring coexistence with legacy access systems. However, scaling the actual time-and-wavelength division multiplexing (TWDM) technologies to higher data rates in a cost-effective way might not be compatible with low-cost commercial photonic and electronic devices, mandatory for affordable PON implementation. Specifically, increasing the bit rate per single λ constitutes a high cost and power consuming solution due to the large required BW of the HW devices such as lasers/modulators, photodiodes (PDs), and amplifiers. Moreover, transmission impairments like chromatic dispersion (CD) become more apparent on large BW signals, eventually requiring digital signal processing (DSP) techniques for their mitigation, with necessary data converters that are expensive and power-hungry if the required BW and sampling rate are high.

As a rule of thumb, the novel solutions for next generation PON must be: (I) affordable in cost by the final users, (II) fully compatible with legacy access systems based on power splitting at the outside plant, and (III) flexible in terms of user BW and channel allocation, with reconfigurable TRXs enabling convergence of residential, business and mobile services. A key technology fulfilling these requirements is a new class of coherent TRX implementing the λ-to-the-user concept, where each ONU owns a dedicated λ in a cost-effective manner by multiplexing in ultra-dense WDM (udWDM), as depicted in Fig. 1.1(c). The channel selection is done by λ-tuning of the local oscillator (LO) laser at the coherent RX; it increases the available optical BW by allowing very narrow channel spacing to accommodate hundreds of λs on a single fiber, in contrast with the sparse optical grid of WDM-PON in Fig. 1.1(b). Consequently, λ-selective devices are not required at the ODN that can be implemented with power splitters, achieving colorless (no pre-selected λs) PON operation fully compatible with legacy access systems. The use of coherent detection further enhances the RX sensitivity with respect to DD. Such extra power budget allows to either increase the maximum reach of the PON, or to allocate more users by adding more power splitting.

The coherent udWDM-PON can also take profit of state-of-the-art DSP techniques to enhance the total PON capacity and spectral efficiency by transmitting advanced modulation formats. Coherent detection supported by DSP also permits effective compensation of transmission impairments and distortions that make impact on the signal from origin to destination, increasing the maximum reach and number of users served by the PON as well. This unique ability facilitates PON deployments using low-cost and BW limited optical/electronic components. Furthermore, DSP based PON may enable convergency of optical and wireless broadband access, meeting the stringent requirements of these scenarios like low latency, flexibility, and scalability. In recent literature, the use of DSP has gained interest and has been proposed for udWDM-PON [Lav13], [Tei20], mainly promoted by the efficient HW implementation of the DSP by using field-programmable gate array (FPGA). It has demonstrated big potential, in terms of capacity and performance for deployment of the future optical access networks [Kan12], [Chu11], [Pra12], [Fer16a], [Roh11], [Rei11], [Gon11], [Smo11], [Luo19]. Although more complex compared with the analog counterpart mostly due to the need of high speed data converters for mapping into the digital domain, the digital implementation enables impairments mitigation, fast reconfiguration and flexible modulation formats, valuable characteristic for the new concept of flexible optical networks with software-defined TRXs [Nap14a].

1.2 Motivation and Objectives

There is no doubt that optical coherent technologies can enhance the overall performance, power budget and total capacity of the PON. Nevertheless, the main challenge is that the expensive optical and electronic components of the commercial coherent TRXs for core/backbone networks are hardly affordable in access due to cost, that directly impacts on the final users. Although conceptually complex, the coherent TRXs for PON must be compatible with commercial low-cost consumer electronics and optical devices. Hence, the crucial idea that drives the deployment of next generation optical access networks is that the simplicity and robustness of implementation take more relevance over achieving the best system performance. This motivated the author's research presented in this thesis, which addresses the development of an optical access network underpinned by simplified coherent technology and supporting udWDM operation. It implies the dimensioning, design and realization of a coherent TRX to implement the λ-to-the-user concept in a cost-effective way by exploiting low-cost components and simple electronics, so that typical user terminals (ONUs) would be affordable to the end-users but still achieving superior performance with respect to the actual standards for PON.

In pursuing these goals, the research activities were organized around the specific objectives listed below:

- Identify the key network configuration and the optimal opto-electronic devices to implement an udWDM-PON with high cost-effectiveness.

- Obtain the coherent RX architectures that exhibit the best trade-off between performance and complexity for different PON scenarios.

- Identify and analyze the main transmission impairments that affect the optical signal quality in the udWDM-PON scenario, evaluating their impact on the network performance and the transceiver design.

- Propose novel and enhanced mitigation strategies for the main transmission impairments by either low-complexity DSP or analog HW design.

- Demonstrate the complete functionalities and capacity of the cost-effective udWDM-PON with coherent technologies, including prototype implementation of the novel class of coherent TRXs for access.

1.3 Research Scenario

Most of the research activities carried out during the thesis were developed within the framework of the FP7 STREP "Cost-effective Coherent Ultra-dense WDM-PON for Lambda-to-the-user Access" (COCONUT, GA318515, *http://www.ict-coconut.eu*) project, granted by the European Commission, as well as the "Flexible Wavelength distribution for PONs with Elastic Bandwidth Range" (FLIPER, TEC2015-70835) project, granted by the Spanish MINECO. The COCONUT PON, conceived as an evolution from the present access networks architectures, is intended to support up to 256 ONUs by using 256 λs (dedicated λ per user) in a tight optical grid as low as 6.25 GHz spaced, with flexible data rates from 1.25 to 10 Gb/s per user. The aggregate PON capacity raises up to 320 Gb/s for the case of residential users at 1.25Gb/s. The aforementioned specifications are in contrast with the actual deployments for Gigabit-capable optical access networks (e.g. XG-PON) that offer aggregate capacity of 10 Gb/s and lower, divided among 32/64 individual users by TDM. On the other hand, the FLIPER project extends the research conducted in COCONUT, but endowing the PON with scalability and flexibility by means of reconfigurable coherent TRXs able to efficiently manage the optical spectrum in an elastic manner.

Fig. 1.2 depicts the envisioned flexible udWDM-PON enabled by coherent technologies, and supporting different applications like residential, corporative, and mobile services over the same fiber infrastructure deployed for current PONs [Pra16]. The ODN is totally passive and filterless, with user terminals implementing thermally-tunable low-cost lasers with non-preselected λ. The coherent detection, with channel selection done by LO tuning, allows for ultra-narrow spaced WDM grid compared with conventional selectivity by optical filters. Moreover, owing to the superior sensitivity of coherent detection the udWDM-PON can achieve the targeted power budget $>$30 dB for next generation PON with $20-40$ km fiber reach [Hou19], without increasing the launched power or extra optical amplification thus lowering the total power consumption of the PON. The bit rate per λ retains compatible with consumer electronics BW, but still achieving superior aggregate PON capacity with high spectral efficiency.

With the aim of effective implementation of such udWDM-PON, this thesis carries out a comprehensive analysis about how the optical coherent technologies, that are mature in high-capacity and long-haul core networks, can be migrated for access applications or, in general, optical networks with high terminal density. To this end, the thesis elaborates on the mitigation

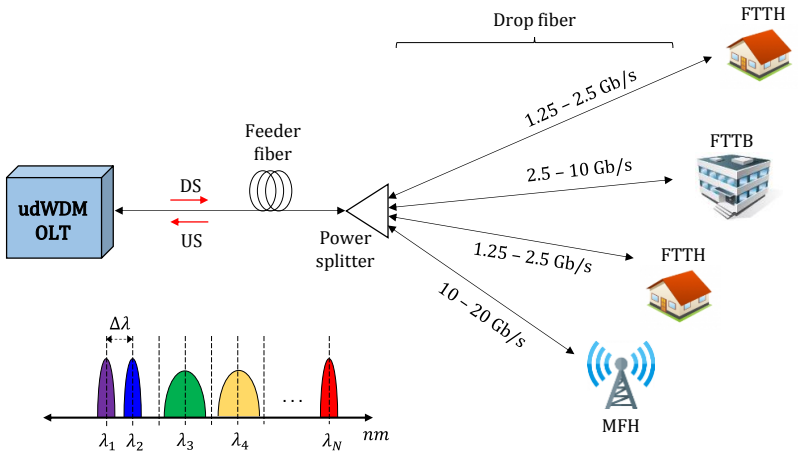

Figure 1.2. Flexible coherent udWDM-PON with dedicated λ per user supporting different types of services. DS: downstream, US: upstream, FTTH: fiber to the home, FTTB: fiber to the business, MFH: mobile front-haul.

strategies for the main transmission impairments that arise in the udWDM-PON scenario. The proposed solutions rely on either DSP aided techniques or novel analog HW design. It is worth mentioning that the capacity per λ of the udWDM-PON in this thesis is targeted to be 1.25 Gb/s for residential subscribers; however, the feasibility of higher data rates (e.g. 10 Gb/s) employing advanced modulation formats is also addressed and experimentally demonstrated.

1.4 Thesis Outline

The thesis is organized in 7 chapters, which are described as follows:

Chapter 2 provides the theoretical background and literature review on coherent systems, focusing on the key architectures for coherent RXs with phase and polarization diversity techniques. State-of-the-art techniques on direct laser modulation employing advanced modulation formats are pointed out as well.

Chapter 3 presents the coherent TRXs proposed for udWDM-PON with simplified architecture, inherited from conventional coherent technologies for long-haul networks. Novel strategies to reduce complexity and cost of the coherent TRX are analyzed, comprising both simplified DSP and analog HW design. The main transmission impairments in the udWDM-PON scenario are also identified, evaluating their impact on the PON performance and discussing the possible mitigation strategies.

Chapter 4, derived from the main conclusions in Chapter 3, discloses the dimensioning, implementation and experimental assessment of an udWDM access network with a novel class of cost-effective coherent technologies: the COCONUT PON. The results include the public demonstration of the complete PON functionalities in a field-trial at the city of Pisa, Italy, featuring real-time coherent ONU prototypes.

Chapter 5 addresses the carrier recovery strategies to deal with optical frequency and phase mismatch between the transmitter and LO lasers. HW-efficient differential field detection DSP

algorithms are explored to overcome the optical phase noise and the frequency mismatch from low-cost lasers. Alternatively, automatic frequency control systems for fully-analog heterodyne RXs are also covered.

Chapter 6 details research on simplified polarization-independent coherent RX architectures that substantially reduce the implementation complexity, cost, and power consumption, in two particular udWDM scenarios: intradyne detection with DSP and heterodyne detection with analog signal processing.

Chapter 7 applies a novel DSP algorithm at the coherent transmitter to compensate for the BW limitation and non-ideal frequency response of directly modulated lasers, digital-to-analog (DAC) converters, and the overall transmitter HW. The proposed algorithm is tolerant against the strong quantization noise from low-cost DACs with limited resolution. Experimental validation of the technique is carried out by utilizing direct amplitude-and-phase modulation of a photonic-integrated dual electro-absorption modulated laser up to 10 Gb/s.

Finally, in **Chapter 8** the main outcomes of this thesis are summarized and the conclusions drawn.

1.5 List of Publications

1.5.1 Patents

1. **J. Tabares** and J. Prat, "Polarization independent heterodyne receiver for differentially-encoded phase-modulated optical signals," ES2679403, May 3, 2019.

1.5.2 Publications in international, peer-reviewed Journals

1. G. Y. Chu, V. Polo, A. Lerín, **J. Tabares**, I. N. Cano and J. Prat, "1.25–3.125 Gb/s per user PON with RSOA as phase modulator for statistical wavelength ONU", *Opt. Commun.*, vol. 357, pp. 34-40, 2015.

2. **J. Tabares**, V. Polo, I. Cano, and J. Prat, "Automatic λ-control with offset compensation in DFB intradyne receiver for udWDM-PON," *IEEE Photon. Technol. Lett.*, vol. 27, no. 4, pp. 443–446, Feb. 15, 2015.

3. M. Presi, M. Artiglia, F. Bottoni, M. Rannello, I. Cano, **J. Tabares**, J. C. Velásquez, S. Ghasemi, V. Polo, G. Y. Chu, J. Prat, G. Azcarate, R. Pous, C. Vilà, H. Debregeas, G. Vall-llosera, A. Rafel, and E. Ciaramella, "Field-trial of a high budget, filterless, λ-to-the-user, UDWDM-PON enabled by an innovative class of low-cost coherent transceivers," *J. Lightw. Technol.*, vol. 35, no. 23, pp. 5250–5259, Dec. 2017.

4. J. C. Velásquez, **J. Tabares**, I. Cano, and J. Prat, "1.25–2.5 Gb/s simple Nyquist transmitters forcoherent UDWDM-PON with enhanced spectral efficiency," *Fiber Integr. Opt.*, vol. 37, no. 4, pp. 219–228, Apr. 2018.

5. **J. Tabares**, S. Ghasemi, V. Polo, and J. Prat, "Simplified carrier recovery for intradyne optical PSK receivers in udWDM-PON," *J. Lightw. Technol.*, vol. 36, no. 14, pp. 2941–2947, Jul. 2018.

6. S. Ghasemi, **J. Tabares**, V. Polo, and J. Prat, "LUT-free carrier recovery for intradyne optical DPSK receivers in udWDM-PON," *J. Lightw. Technol.*, vol. 37, no. 6, pp. 1608–1613, Mar. 2019.

7. J. C. Velásquez, **J. Tabares**, and J. Prat, "Differential 8-APSK monolithically integrated dual-EML transmitter for flexible coherent PONs," *Opt. Lett.*, vol. 44, no. 11, pp. 2760–2763, Jun. 2019.

8. **J. Tabares**, S. Ghasemi, J. C. Velásquez, and J. Prat, "Coherent ultra-dense WDM-PON enabled by complexity-reduced digital transceivers," *J. Lightw. Technol.*, vol. 38, no. 6, pp. 1305–1313, Mar. 2020.

9. J. Segarra, V. Sales, V. Polo, **J. Tabares**, and J. Prat, "Flexible coherent UDWDM-PON with dynamic user allocation based on limited-tunability lasers," *IEEE J. Opt. Commun. Netw.*, vol. 12, no. 9, pp. D27–D35, Sep. 2020.

1.5.3 Publications in scientific conferences

1. I. Cano, J. Prat, **J. Tabares**, J. C. Velásquez, S. Ghasemi, V. Polo, G. Y. Chu, M. Presi, E. Ciaramella, M. Rannello, F. Bottoni, M. Artiglia, G. Cossu, R. Pous, G. Azcarate, C. Vilà, H. Debregeas, G. Vall-llosera, and A. Rafel, "Field-trial of low-cost coherent UDWDM-PON with realtime processing, λ-monitoring and EPON coexistence," in *Proc. 42nd Eur. Conf. Opt. Commun. (ECOC)*, Dusseldorf, DE: VDE, 2016, Paper M.1.E5.

2. J. Prat, I. Cano, M. Presi, **J. Tabares**, M. Rannello, J. C. Velásquez, F. Bottoni, S. Ghasemi, V. Polo, G. Y. Chu, M. Artiglia, R. Pous, G. Azcarate, C. Vilà, H. Debregeas, and E. Ciaramella, "Ultra-dense WDM access network field trial," *2016 21st Eur. Conf. on Networks and Opt. Commun. (NOC)*, Lisbon, 2016, pp. 117-118.

3. M. Rannello, I. Cano, **J. Tabares**, J. C. Velásquez, S. Ghasemi, V. Polo, G. Y. Chu, J. Prat, R. Pous, G. Azcarate, C. Vilà, H. Debregeas, G. Vall-llosera, A. Rafel, M. Artiglia, F. Bottoni, M. Presi, and E. Ciaramella, "Field-trial of a λ-to-the-user high-budget PON using a novel class of low-cost coherent transceivers and compatible with EPON system operation," in *2017 19th Int. Conf. Transparent Opt. Networks (ICTON)*, Girona, 2017, pp. 1-4, Paper Th.B1.3.

4. J. C. Velásquez, **J. Tabares**, I. Cano, V. Polo, and J. Prat, "Coherent Nyquist UDWDM-PON with 2.5 Gb/s/user and 15 dB Differential Link-Loss", *2017 Int. Workshop on Fiber Opt. in Access Network (FOAN)*, Munich, Nov. 6 – 8, 2017.

5. **J. Tabares**, V. Polo, and J. Prat, "Polarization-independent heterodyne DPSK receiver based on 3x3 coupler for cost-effective udWDM PON," *in 2017 Proc. Opt. Fiber Commun. Conf. Expo (OFC)*, Los Angeles, Paper Th1K3.

6. S. Ghasemi, **J. Tabares**, V. Polo, and J. Prat, "Optimized differential detection-based optical carrier recovery for intradyne PSK receivers in udWDM-PON," *in 2018 Proc. Opt. Fiber Commun. Conf. Expo (OFC)*, San Diego, Paper M2B.7.

7. S. Ghasemi, **J. Tabares**, V. Polo, and J. Prat, "LUT-free carrier recovery for intradyne optical DPSK receivers in udWDM-PON," *in 2018 Proc. Eur. Conf. Opt. Commun. (ECOC)*, Rome, Paper Tu1B.4.

8. **J. Tabares**, A. Napoli, V. Polo, S. Calabrò, B. Sommerkorn-Krombholz, B. Spinnler, and J. Prat, "Digital pre-emphasis for 10 Gb/s with low-cost directly phase-modulated lasers for PONs," in *2018 Proc. Signal Process. Photon. Commun. (SPPCom)*, Zurich, Paper SpTh3G.2.

9. J. C. Velásquez, I. Cano, **J. Tabares**, V. Polo and J. Prat, "Direct Phase Modulation for UDWDM ONU with Beat Signals", in *2018 20th Int. Conf. Transparent Opt. Networks (ICTON)*, Bucharest, Jul. 1 – 5, 2018, Paper Th.B1.2.

10. **J. Tabares**, J. C. Velásquez, A. Napoli, and J. Prat, "Direct amplitude-phase modulated dual-EML 10 Gb/s optical transmitter," in *2019 Proc. 45th Eur. Conf. Opt. Commun. (ECOC)*, Dublin, Paper P59.

11. S. Ghasemi, **J. Tabares**, and J. Prat, "Symbol-rate digital signal processing for low-complexity polarization diversity intradyne optical PSK receivers," in *2019 Proc. 45th Eur. Conf. Opt. Commun. (ECOC)*, Dublin, Paper P67.

12. J. Prat, J. C. Velásquez, and **J. Tabares**, "Direct PSK-ASK Modulation for Coherent udWDM," in *2019 21st Int. Conf. Transparent Opt. Networks (ICTON)*, Angers, pp. 1-4, Paper Th.C1.2.

Chapter 2

State of the Art

2.1 Fundamentals of Coherent Systems

Coherent systems present many advantages with respect to the conventional DD systems mainly due to its high selectivity, enhanced sensitivity, and ability for linear detection of the electrical field. First, in the WDM environment with coherent detection, channel selection is done by λ-tuning of the LO combined with sharp electrical filtering after photodetection, much better discriminating the λ channels compared with optical filters whose selectivity is in the order of nanometers (hundreds of GHz). Second, the use of a LO further improves the sensitivity when compared with DD because of the boosting effect of the high LO power on the received optical carrier after mixing. Third, the DD is only sensitive to changes in the optical power thus only detects intensity modulation formats; instead, coherent detection linearly maps all the information carried by the received electrical field into a photocurrent, enabling transmission of advanced modulation formats and effective mitigation of transmission impairments with complex dynamics.

In terms of implementation, the main difference between DD and coherent detection is that the received signal is mixed with the LO in an optical hybrid or coupler, as depicted in Fig. 2.1. Afterwards the resulting combination is photodetected, then low-pass filtered for noise suppression.

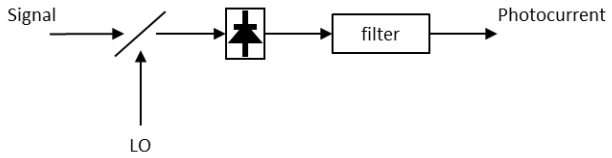

Figure 2.1. Ideal coherent receiver.

Depending on the use of an intermediate frequency (IF) stage, defined as the difference between the signal and LO optical frequencies, the coherent detection can be classified into homodyne, intradyne and heterodyne. Table 2.1 provides the electrical spectra after photodetection comparing the coherent detection schemes, as well as the main requirements for each. In homodyne systems, the received signal and the LO are matched in frequency and phase, then the data-carrying electrical field is directly downconverted into base-band at the photodetection stage. The intradyne detection differs from homodyne detection in that the LO is free running, i.e., not matched in phase with the received signal. Such a phase mismatch is alleviated by the use of optical phase diversity along with electrical signal processing, that will be treated in Section 2.1.2. In addition, the IF in intradyne systems is set to be lower than the data BW, and as close to zero as possible in many applications. Last, in heterodyne detection the received optical signal is downconverted into a high frequency electrical carrier with IF larger than the data BW. Due to

Table 2.1. Photodetected electrical spectra and main requirement for coherent detection schemes. B: data BW; IF: intermediate frequency.

System	Photodetected spectrum	IF	Requirements
Homodyne	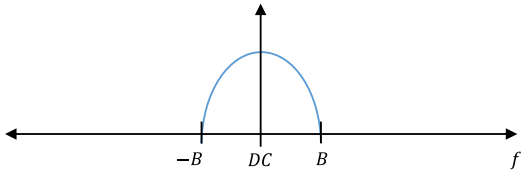	IF = 0	Frequency + phase locking. Baseband processing.
Intradyne	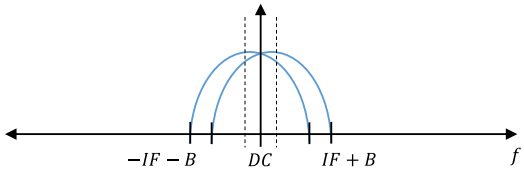	IF < B	Frequency locking + optical phase diversity. ~Baseband processing.
Heterodyne	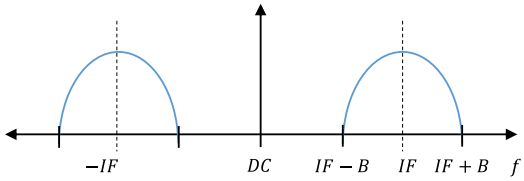	IF > B	Only frequency locking. Large receiver BW

the fast oscillations of the IF carrier, the absence of signal–LO phase matching has no effect on the photodetection and phase-looking is not required. As a particular feature, the intradyne detection can be considered either a "near-zero" IF heterodyne detection, or a homodyne detection without phase locking.

Each of the three coherent detection schemes exhibit some advantages and drawbacks that must be considered when dimensioning and designing the coherent PON. As a brief comparison, the homodyne RX requires only base-band signal processing thus featuring the highest spectral efficiency; however, the need of optical phase-and-frequency locking between TX and LO leads to problems with the phase and frequency noise of commercial low-cost lasers. On the other hand, the intradyne RX replaces the phase-locking loop (PLL) system by simpler feedforward electrical processing, at the cost of extra HW at the RX front-end for the optical phase diversity. Moreover, the use of free-running LO in intradyne detectors slightly spreads the photodetected spectrum with respect to pure homodyne detection (see Table 2.1), requiring extra BW for the residual IF yet neglictible in most of the applications. In the case of heterodyne RX, as no optical phase matching is needed for correct photodetection, the RX implementation is the simplest; nevertheless, the use of an IF carrier, usually larger than twice the data BW, imposes extra challenges as limited electronic functionalities and larger channel spacing between users, lowering the spectral efficiency. In all cases, frequency locking is required at the coherent RX to maintain the LO λ at the selected value, maximizing the detection quality but also avoiding interference from adjacent channels in the tight udWDM optical grid. Next sections provide a more detailed comparison among the coherent detection architectures, evaluating their performance, complexity and robustness against transmission impairments.

2.1.1 Coherent receiver analysis

The basic model for an ideal coherent receiver is shown in Fig. 2.2. The incoming optical signal $e_S(t)$ is ideally mixed with the continuous wave (CW) LO laser beam $e_{LO}(t)$ resulting in a beating electrical field $e_C(t)$ that is next mapped into the electrical domain by an ideal photodetector.

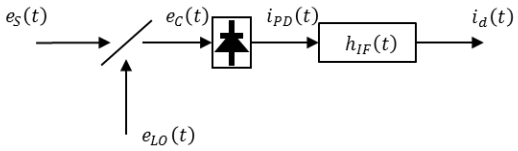

Figure 2.2. Ideal coherent receiver.

The electrical field for the received signal and the LO can be modelled respectively as

$$\begin{aligned} e_S(t) &= E_S(t)e^{j(\omega_S t+\phi_S(t))} \\ e_{LO}(t) &= E_{LO}e^{j(\omega_{LO}t+\phi_{LO}(t))} \end{aligned} \tag{2.1}$$

Where ω_S and ω_{LO} are the angular optical frequencies, $\phi_S(t)$ and $\phi_{LO}(t)$ the relative optical phase of each signal. $E_S(t)$ is the envelope of the received electrical field, that is a constant (E_{LO}) for the LO as it emits in CW. The optical signal after ideal coherent mixing becomes

$$e_C(t) = E_S(t)e^{j(\omega_S t+\phi_S(t))} + E_{LO}e^{j(\omega_{LO}t+\phi_{LO}(t))} \tag{2.2}$$

In the photoconversion process, the output current from a photodetector is proportional to the incident optical power. Therefore, without BW limitations it can be calculated as: $i_{PD}(t) = \Re|e_C(t)|^2$, with $\Re$ the responsivity of the photodiode, yielding

$$\begin{aligned} i_{PD}(t) = \Re\big[&E_S(t)E_S{}^*(t) + {E_{LO}}^2 + E_S(t)E_{LO}e^{j((\omega_S-\omega_{LO})t+\phi_S(t)-\phi_{LO}(t))} \\ &+ E_S{}^*(t)E_{LO}e^{-j((\omega_S-\omega_{LO})t+\phi_S(t)-\phi_{LO}(t))}\big] \end{aligned} \tag{2.3}$$

Here we define the intermediate frequency $\omega_{IF} = \omega_S - \omega_{LO}$ and the instantaneous phase difference $\Delta\phi(t) = \phi_S(t) - \phi_{LO}(t)$. The $(\cdot)^*$ denotes the complex conjugate. The photocurrent can be rewritten as

$$i_{PD}(t) = \Re\big[|E_S(t)|^2 + {E_{LO}}^2 + E_S(t)E_{LO}\big(e^{j(\omega_{IF}t+\Delta\phi(t))} + e^{-j(\omega_{IF}t+\Delta\phi(t))}\big)\big] \tag{2.4}$$

where $|E_S(t)|^2 = P_S(t)$ and ${E_{LO}}^2 = P_{LO}$ represent the signal and LO power respectively. Finally, the photocurrent assumes the form

$$i_{PD}(t) = \Re\big[P_S(t) + P_{LO} + 2\sqrt{P_S(t)P_{LO}}cos(\omega_{IF}t + \Delta\phi(t))\big] \tag{2.5}$$

which is the noiseless general expression for ideal coherent detection. It is composed by the DD terms $P_S(t)$ and P_{LO}, and the third coherent beating term. Afterwards, the signal $i_{PD}(t)$ is low-pass filtered by the convolution in time with the filter impulse response $h_{IF}(t)$ with equivalent BW B, that limits the noise and crosstalk components before the decision stage of the RX. For the upcoming analysis of the coherent detection performance, let us focus on the beating term by

neglecting the DD terms P_{LO} and $P_S(t)$ that are the constant LO power –the DC level of the photocurrent–, and the received signal power $P_S(t)$ being much lower than the coherent term. Moreover, both terms can be removed by balanced photodetection as explained in next section. Hence, the variable for data decision at the filter output can be expressed as:

$$i_d(t) = 2\Re\sqrt{P_S(t)P_{LO}}cos(\omega_{IF}t + \Delta\phi(t)) * h_{IF}(t) \tag{2.6}$$

To calculate the signal-to-noise ratio (SNR) and the detection performance, initially the considered noise sources are the shot noise produced in the photoconversion process due to the quantum nature of light, and the thermal noise generated at the electronic part of the RX, both being white Gaussian random process with variance σ^2. The SNR, defined as the ratio between the average signal power and the average noise power, can be calculated as

$$SNR = \frac{\langle {i_d}^2(t)\rangle}{\langle {\sigma_{sh}}^2\rangle + \langle {\sigma_{th}}^2\rangle} \tag{2.7}$$

where $\langle\cdot\rangle$ stands for averaging and ${\sigma_{sh}}^2$ and ${\sigma_{th}}^2$ represent the variance of the shot noise and thermal noise respectively, which are defined as [Kaz96]:

$${\sigma_{sh}}^2 = 2q\Re(P_S + P_{LO})B \tag{2.8}$$

$${\sigma_{th}}^2 = 4kTB/R_L \tag{2.9}$$

with q the electron charge, B the BW of the RX, k the Boltzmann constant, T the absolute temperature of the RX and R_L the load resistance. Let us first assume the case of homodyne detection for binary $0-180°$ phase modulation. In that case, in Eq. (2.6) the $\Delta\phi(t)$ is the information-bearing variable and the signal power $P_S(t)$ becomes a constant. For homodyne detection ($\omega_{IF} = 0$), the signal power ${i_d}^2(t)$ within the RX BW (B) yields

$${i_d}^2(t) = 4\Re^2 P_S P_{LO} cos^2\Delta\phi(t) \tag{2.10}$$

where the term $cos^2\Delta\phi(t) = 1$ for $0-180°$ phase modulation. Thus, by replacing Eq. (2.10) into Eq. (2.7) the SNR is calculated as

$$SNR = \frac{4\Re^2 P_S P_{LO}}{(2q\Re(P_S + P_{LO}) + 4kT/R_L)B} \tag{2.11}$$

Taking into account that $P_{LO} \gg P_S$, there exist a P_{LO} value that makes the left term in the denominator of Eq. (2.11) dominant, simplifying the SNR to:

$$SNR = \frac{2\Re P_S}{qB} \tag{2.12}$$

which is defined as the quantum-limit SNR. Here one can see one of the main advantages of coherent detection; by controlling the LO power the shot-noise SNR limit can be achieved even for electronic RXs whose performance is generally dominated by thermal noise.

For the case of heterodyne detection, the power of the signal in Eq. (2.6) becomes

$$i_d{}^2(t) = 2\Re^2 P_S P_{LO}\big(1 + cos(2\omega_{IF}t + 2\Delta\phi(t))\big) \tag{2.13}$$

The second term in Eq. (2.13) oscillates at twice the ω_{IF} and completely falls out of the RX BW, being suppressed by filtering. Thus, the SNR for heterodyne detection reads as

$$SNR = \frac{2\Re^2 P_S P_{LO}}{(2q\Re(P_S + P_{LO}) + 4kT/R_L)B} \tag{2.14}$$

Note that it only differs from the calculated homodyne SNR in Eq. (2.11) by a factor of two, that corresponds to 3dB SNR penalty for heterodyne detection against homodyne (or intradyne with neglictible IF).

In order to estimate the LO power that reaches the quantum-limit SNR in Eq. (2.11), the SNR in terms of the received and LO optical power are plotted in Fig. 2.3 for the case of homodyne detection with binary $0 - 180°$ phase modulation, assuming 1 GHz RX BW capable for gigabit data transmission.

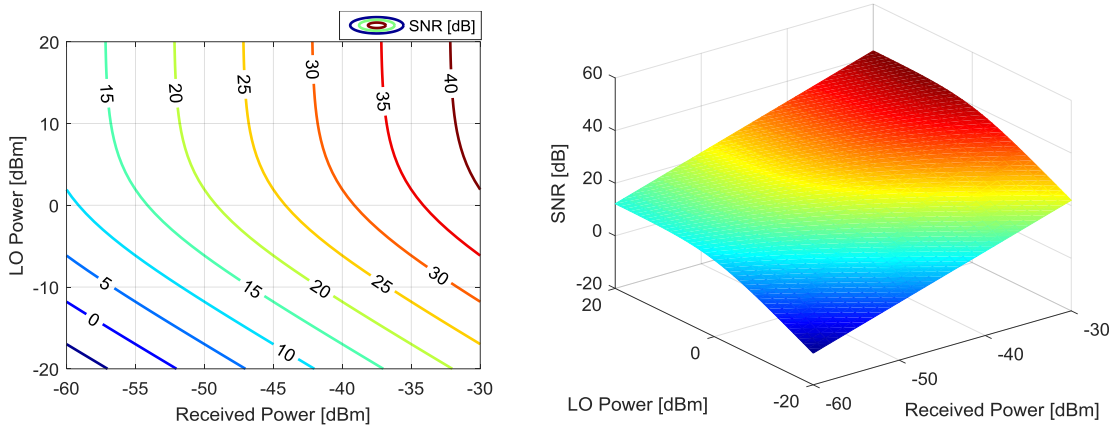

(a) (b)

Figure 2.3. SNR as a function of received and LO optical power for homodyne detection: (a) contour plot; (b) surface plot. Parameters: $\Re = 1\,{}^{A}/_{W}$, $B = 1\,GHz$, $R_L = 50\,\Omega$, $T = 300\,K$

As observed in both Fig. 2.3a and Fig. 2.3b, for a fixed LO power the SNR is linearly proportional to the received optical power. Conversely, for a constant received power the shot noise contribution in equation (2.11) becomes dominant for a LO power higher than ~0dBm, the limit for linear SNR–LO power variations. The quantum-limit SNR is achieved for LO power higher than ~15dBm; beyond this limit, the SNR is totally independent from the LO power and only depends on the signal power. Otherwise, if the LO power is not strong enough, the SNR is linearly reduced. The heterodyne detection performs similar, except for the 3dB penalty in the SNR values.

In summary, the foregoing analyses emphasize the three main advantages of coherent detection when compared with DD systems:

- *Enhanced sensitivity.* Due to the boosting effect of the LO laser after mixing, the coherent RX reaches the shot-noise SNR limit overcoming the thermal noise effect that generally dominates the electronic RXs.

- *Linear electrical-field detection*. Coherent detection is sensitive to the incident optical power but, more important, also sensitive to the frequency and phase differences between signal–LO after optical mixing, enabling full reconstruction of the complex transmitted electrical field.

- *High selectivity.* In a WDM scenario, the coherent RX is able to discriminate among the set of optical frequencies by tuning the LO λ, which in combination with sharp electrical filtering after photodetection allows for ultra-narrow channel spacing.

2.1.2 Key architectures in coherent receivers

The coherent RX needs to combine the received signal containing data, with the LO laser before photodetection. Such a mixing is realized by optical hybrids composed by directional couplers, or by simple bi-directional fused-fiber couplers, depending on the RX configuration. This section provides an overview of the key architectures to implement the three aforementioned coherent detection schemes, i.e., homodyne, intradyne and heterodyne. As mentioned in Section 2.1, intradyne detection with zero IF is similar to homodyne detection except for the LO that is free-running without PLL for the case of intradyne. Therefore, in the remainder of this thesis the terms homodyne and intradyne indistinctly refer to RXs that perform base-band detection, whereas heterodyne is used for RXs that perform IF detection.

2.1.2.1 90° hybrid phase-diversity homodyne

The first approach for homodyne coherent RX uses an optical 90° hybrid whose internal structure is shown Fig. 2.4. The upper and lower arms of the optical hybrid differ in that one is 90º phase shifted against the other, leading to the upper arm detects the in-phase (I) beat product while the lower arm detects the quadrature (Q) beat product, composing a phase-diversity homodyne architecture. The four PDs are connected in pairs for balanced photodetection.

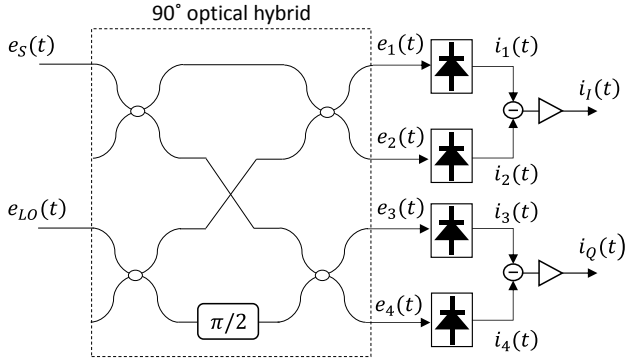

Figure 2.4. Structure of an optical 90º hybrid with balanced photodetection for phase-diversity coherent homodyne RX.

In practice, the optical 90° hybrid can be implemented in a waveguide platform by polarization beam-splitters (PBS) setting appropriately the state-of-polarization (SOP) of signal and LO, or by

passive couplers with correctly dimensioned coupling region [Kik16]. In this phase-diversity homodyne architecture, the I and Q components of the coherent beating have to be present to correctly track the random optical phase from transmitter (TX) and LO lasers without PLL.

The output of the optical 90° hybrid can be obtained through the following scatter matrix:

$$\begin{bmatrix} e_1(t) \\ e_2(t) \\ e_3(t) \\ e_4(t) \end{bmatrix} = \frac{1}{2}\begin{bmatrix} 1 & 1 \\ 1 & -1 \\ 1 & j \\ 1 & -j \end{bmatrix}\begin{bmatrix} e_S(t) \\ e_{LO}(t) \end{bmatrix} \tag{2.15}$$

The resulting photocurrents at each of the PD outputs is calculated by: $i_k(t) = \Re|e_k(t)|^2$, being $\Re$ the photodiode responsivity and $k \in \{1, 2, 3, 4\}$ the photocurrent index. Hence, the four photocurrents turn to be

$$\begin{bmatrix} i_1(t) \\ i_2(t) \\ i_3(t) \\ i_4(t) \end{bmatrix} = \frac{\Re}{4}\begin{bmatrix} P_S(t) + P_{LO} \\ P_S(t) + P_{LO} \\ P_S(t) + P_{LO} \\ P_S(t) + P_{LO} \end{bmatrix} + \frac{\Re}{2}\begin{bmatrix} \sqrt{P_S(t)P_{LO}}\, cos(\omega_{IF}t + \Delta\phi(t)) \\ -\sqrt{P_S(t)P_{LO}}\, cos(\omega_{IF}t + \Delta\phi(t)) \\ \sqrt{P_S(t)P_{LO}}\, sin(\omega_{IF}t + \Delta\phi(t)) \\ -\sqrt{P_S(t)P_{LO}}\, sin(\omega_{IF}t + \Delta\phi(t)) \end{bmatrix} \tag{2.16}$$

which are composed by the DD terms and the coherent beating terms. Here, ω_{IF} represents the residual frequency mismatch between signal–LO that may be kept as low as possible for homodyne detection (ideally $\omega_{IF} = 0$), and $\Delta\phi(t)$ contains the phase noise contribution from the lasers. Note that the coherent mixing in the 90° hybrid produces four photocurrents with relative $\pi/2$ phase difference between consecutive index currents; therefore, those photocurrents with relative π phase difference between them are later connected in pairs for balanced photodetection, as seen in Fig. 2.4. It cancels the DD terms that contains the relative intensity noise (RIN) from the lasers, and the strong LO power term P_{LO} that may cause amplifiers saturation. After balanced photodetection, the extracted I and Q components read as

$$i_I(t) = \Re\sqrt{P_S(t)P_{LO}}\, cos(\omega_{IF}t + \Delta\phi(t)) \tag{2.17}$$

$$i_Q(t) = \Re\sqrt{P_S(t)P_{LO}}\, sin(\omega_{IF}t + \Delta\phi(t)) \tag{2.18}$$

This phase-diversity homodyne RX is usually the reference for implementation in long-haul core networks with coherent detection. The main drawback for real deployments in access networks is the optical 90° hybrid that is still a complex and expensive device. Then, simplified architectures with less complex optical couplers are also explored for homodyne RX implementation.

2.1.2.2 3x3 coupler phase-diversity homodyne

A much simpler alternative for the optical 90° hybrid at the homodyne RX is the use of symmetric 3x3 fused-fiber couplers. The main advantage is that the critical $\pi/2$ phase shift between the 2 branches of the 90° hybrid is not required thus the fabrication complexity is significantly lower. To achieve the phase diversity characteristic, the relative phase difference at the 3x3 coupler outputs is adjusted by a proper control of the coupling region length of the three fibers. When

symmetric 33% power splitting is observed at the coupler outputs, 120° phase difference among outputs is naturally obtained.

The simplified architecture for phase-diversity homodyne detection implementing the 3x3 coupler is depicted in Fig. 2.5. This architecture also saves one PD, lowering the overall RX complexity and power consumption.

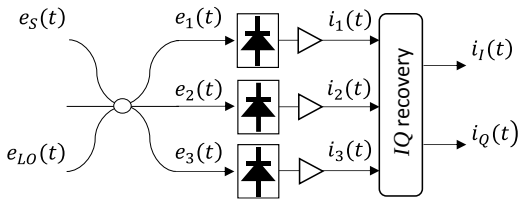

Figure 2.5. Simplified phase-diversity homodyne RX based on 3x3 fiber coupler.

The three electrical fields at the 3x3 coupler outputs are calculated by [Pie89]:

$$\begin{bmatrix} e_1(t) \\ e_2(t) \\ e_3(t) \end{bmatrix} = \frac{1}{3}\begin{bmatrix} a & b & b \\ b & a & b \\ b & b & a \end{bmatrix}\begin{bmatrix} e_S(t) \\ 0 \\ e_{LO}(t) \end{bmatrix} \tag{2.19}$$

where the scatter matrix coefficients a, b from the symmetric 3x3 coupler are respectively

$$a = e^{-j4\pi/9} + 2e^{j2\pi/9} \tag{2.20}$$

$$b = e^{-j4\pi/9} - e^{j2\pi/9} \tag{2.21}$$

After photodetection, the three photocurrents read as

$$\begin{bmatrix} i_1(t) \\ i_2(t) \\ i_3(t) \end{bmatrix} = \frac{\Re}{3}\begin{bmatrix} P_S(t) + P_{LO} \\ P_S(t) + P_{LO} \\ P_S(t) + P_{LO} \end{bmatrix} + \frac{2\Re}{3}\begin{bmatrix} \sqrt{P_S(t)P_{LO}}\, cos(\omega_{IF}t + \Delta\phi(t) + 2\pi/3) \\ \sqrt{P_S(t)P_{LO}}\, cos\big(\omega_{IF}t + \Delta\phi(t)\big) \\ \sqrt{P_S(t)P_{LO}}\, cos(\omega_{IF}t + \Delta\phi(t) - 2\pi/3) \end{bmatrix} \tag{2.22}$$

In contrast with the 90° hybrid RX, here single-ended photodetection is carried out and the three photocurrents have a relative $2\pi/3$ phase shift among them. To extract the orthogonal IQ signals, as well as to cancel the DD terms and common mode noise, the three photocurrents are linearly combined according to the following expressions [Nic89], [Xie12]:

$$i_I(t) = i_2(t) - \frac{1}{2}(i_3(t) + i_1(t)) \tag{2.23}$$

$$i_Q(t) = \frac{\sqrt{3}}{2}\,(i_3(t) - i_1(t)) \tag{2.24}$$

that can be realized by passive hardware for analog RX implementation, or into the digital domain after analog-to-digital (A/D) conversion for digital RXs. Finally, the IQ recovery yields

$$i_I(t) = \Re\sqrt{P_S(t)P_{LO}}\, cos(\omega_{IF}t + \Delta\phi(t)) \tag{2.25}$$

$$i_Q(t) = \Re\sqrt{P_S(t)P_{LO}}\, sin(\omega_{IF}t + \Delta\phi(t)) \tag{2.26}$$

This simpler architecture enables phase-diversity homodyne detection with only three PDs, employing conventional and low-cost 3x3 couplers, becoming an attractive alternative for coherent homodyne RXs for access networks deployments.

2.1.2.3 2x2 coupler heterodyne

In the coherent heterodyne RX the beating signal after photodetection is not directly downconverted to base-band ($\omega_{IF} = 0$) as in homodyne detection, but downconverted into an IF carrier with a frequency larger than the data BW, as pointed out in Table 2.1. Owing to the fast oscillations of such IF carrier, I- and Q- photodetection namely phase-diversity is not required. Therefore, optical mixing between signal and LO is made by common 2x2 optical couplers, followed by balanced photodetection with two PDs, as represented in Fig. 2.6.

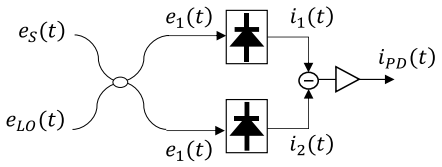

Figure 2.6. 2x2 coupler heterodyne RX architecture.

The two coherent beating components are obtained by the scatter matrix of a symmetric 3dB coupler, as follows:

$$\begin{bmatrix} e_1(t) \\ e_2(t) \end{bmatrix} = \frac{1}{\sqrt{2}} \begin{bmatrix} 1 & j \\ j & 1 \end{bmatrix} \begin{bmatrix} e_S(t) \\ e_{LO}(t) \end{bmatrix} \tag{2.27}$$

After photodetection, the two photocurrents are found to be:

$$\begin{bmatrix} i_1(t) \\ i_2(t) \end{bmatrix} = \frac{\Re}{2} \begin{bmatrix} P_S(t) + P_{LO} \\ P_S(t) + P_{LO} \end{bmatrix} + \Re \begin{bmatrix} \sqrt{P_S(t)P_{LO}}\, sin\big(\omega_{IF}t + \Delta\phi(t)\big) \\ -\sqrt{P_S(t)P_{LO}}\, sin\big(\omega_{IF}t + \Delta\phi(t)\big) \end{bmatrix} \tag{2.28}$$

which correspond to two similar signals but shifted 180° between them. After balancing the photocurrents, the heterodyne RX output becomes

$$i_{PD}(t) = 2\Re\sqrt{P_S(t)P_{LO}}\, sin\big(\omega_{IF}t + \Delta\phi(t)\big) \tag{2.29}$$

The frequency f_{IF} ($\omega_{IF} = 2\pi f_{IF}$) of the IF carrier in Eq. (2.29) is larger than the data BW, and usually set to two or three times. Depending on the modulation format, data can be demodulated by squaring the signal for envelope detection, or by delay-and-multiply for differential demodulation (see Section 2.3). In both cases, the demodulator performs as an RF down-converter by extracting the base-band data from the IF carrier without the need of extra processing.

The heterodyne RX is also attractive for access networks due to its simplicity, requiring only two PDs and a conventional 2x2 optical coupler. However, the simplicity comes at the cost of larger electronics BW and larger spacing with adjacent WDM channels compared with homodyne detection.

2.2 State-of-Polarization of Lightwaves

In coherent systems, the detection process is based on the non-linear mixing between the received signal and the LO that occurs within the photodiodes. This holds for any type of coherent RX: homodyne, intradyne or heterodyne. The full mixing is only possible if photons from the signal and LO reach the PDs with the same SOP; otherwise, the coherent mixing suffers a power loss due to destructive interference between waves. When signal and LO have orthogonal SOP there is no coherent mixing between both ligthwaves, as the worst case.

The SOP of lightwaves defines the geometry of the electrical field propagation through the waveguide or the transmission medium. Let us consider that the electrical field can be decomposed into two orthogonal components $e_{\mathbb{X}}$, $e_{\mathbb{Y}}$ which in turn are orthogonal to the propagation direction of the ligthwave, as depicted in Fig. 2.7(a). The complex field propagation geometry will depend on the interaction between the two oscillating waves $e_{\mathbb{X}}$, $e_{\mathbb{Y}}$ having different amplitudes −represented by the polarization splitting ratio δ − but also having a relative phase shift ψ between them, as shown in Fig. 2.7(b). As a result, one may have three fundamental SOP:

(I) Linear: when one of the components vanishes, or when $\psi = 0$ or π.
(II) Circular: when both components have the same amplitude and $\psi = \pm\pi/2$
(III) Elliptical: in the rest of cases

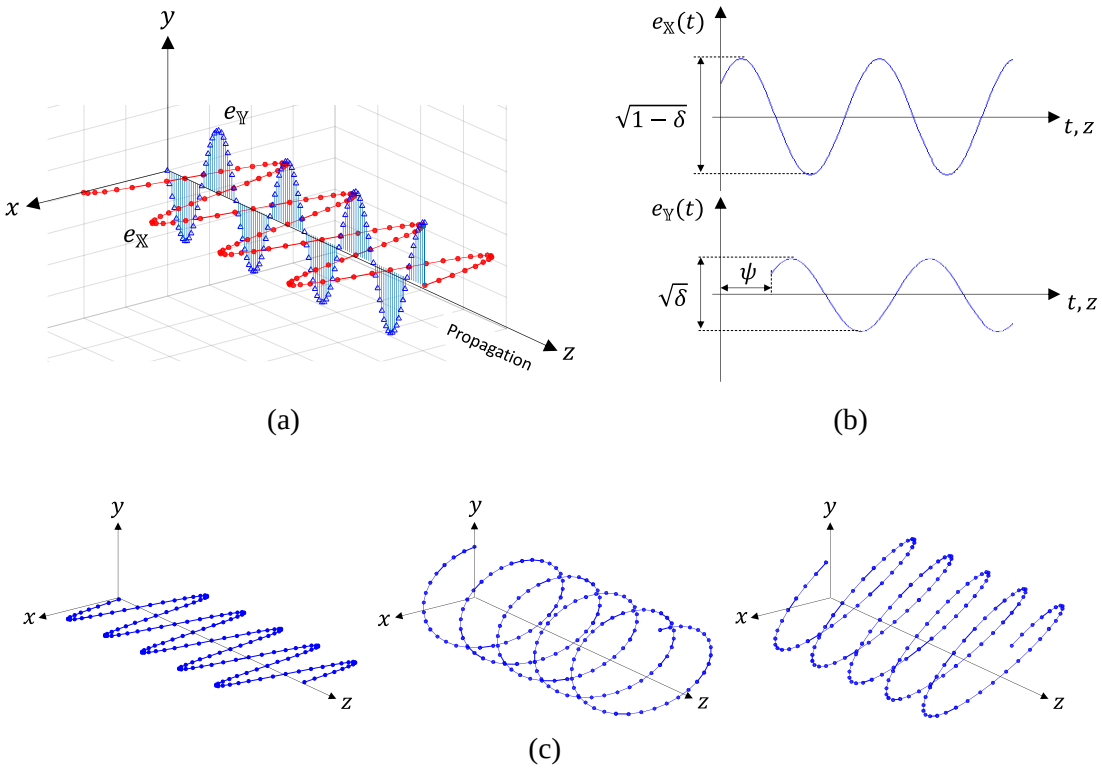

Figure 2.7. Orthogonal decomposition of ligthwaves: (a) complex electrical field propagation and (b) the individual orthogonal plane waves. (c) Three different polarization states (from left to rigth): linear, circular and elliptical.

Fig. 2.7(c) depicts the complex field propagation along the z-axis for the three different SOP. Note that these definitions hold for a complex electrical field that oscillates in a well-defined way, namely a polarized ligthwave; otherwise, if the field variations are totally uncorrelated the lightwave is said to be unpolarized. Mathematically, the arbitrary-polarized lightwave can be modelled by the Jones vector notation that describes the instantaneous electrical field as [Amn84]

$$\mathcal{J}_S(t) = \begin{bmatrix} e_{\mathbb{X}}(t) \\ e_{\mathbb{Y}}(t) \end{bmatrix} = \begin{bmatrix} \sqrt{1-\delta}\,\mathbb{X} \\ \sqrt{\delta} e^{j\psi}\,\mathbb{Y} \end{bmatrix} \left[E_S e^{j(\omega_S t + \phi_S(t))} \right] \tag{2.30}$$

with δ ranging between 0 and 1. The notation $\mathbb{X}$, $\mathbb{Y}$ stands for the horizontal and vertical SOP components, while the other terms follow the definition of the optical signal in Eq. (2.1). Alternatively, the Jones vector in Eq. (2.30) can also be written in polar coordinates by substituting $\delta = \sin^2 \varphi$. It reads as

$$\mathcal{J}_S(t) = \begin{bmatrix} e_{\mathbb{X}}(t) \\ e_{\mathbb{Y}}(t) \end{bmatrix} = \begin{bmatrix} \cos\varphi\,\mathbb{X} \\ \sin\varphi\, e^{j\psi}\,\mathbb{Y} \end{bmatrix} \left[E_S e^{j(\omega_S t + \phi_S(t))} \right] \tag{2.31}$$

where $\varphi \in \{0 \leq \varphi \leq \pi/2\}$ represents the azimuth and $\psi \in \{-\pi \leq \psi \leq \pi\}$ the ellipticity of the SOP in polar coordinates respectively. In the remainder of the thesis, the polar coordinates notation is adopted for convenience.

Next sections will treat the signal SOP representation in the Stokes space, useful for SOP characterization, and the coherent detection strategies to deal with random SOP changes when ligthwaves propagate through the fiber and optical devices.

2.2.1 Stokes space representation

The stokes space is a mathematical technique that allows representation of the optical signals dependent on the SOP coordinates φ, ψ, but totally independent on the instantaneous carrier phase $\omega_S t + \phi_S(t)$. Let us define the Stokes vector as

$$\boldsymbol{S} = \begin{bmatrix} S_1 \\ S_2 \\ S_3 \end{bmatrix} \tag{2.32}$$

The Stokes parameters S_k, for $k = 0, 1, 2, 3$, are calculated from the Jones vector in Eq. (2.31) as follows

$$\begin{aligned} S_0 &= |e_{\mathbb{X}}(t)|^2 + |e_{\mathbb{Y}}(t)|^2 \\ &= E_s^2 \end{aligned} \tag{2.33}$$

$$\begin{aligned} S_1 &= |e_{\mathbb{X}}(t)|^2 - |e_{\mathbb{Y}}(t)|^2 \\ &= E_s^2 \cos 2\varphi \end{aligned} \tag{2.34}$$

$$\begin{aligned} S_2 &= 2Re\{e_{\mathbb{X}}{}^*(t) e_{\mathbb{Y}}(t)\} \\ &= E_s^2 \sin 2\varphi \cos\psi \end{aligned} \tag{2.35}$$

$$S_3 = 2Im\{e_{\mathbb{X}}{}^*(t)e_{\mathbb{Y}}(t)\}$$
$$= E_s^2 \sin 2\varphi \sin\psi \tag{2.36}$$

As observed, the Stokes vector is immune to the optical carrier phase, being only sensitive to the power ratio and relative phase between the $\mathbb{X}$ and $\mathbb{Y}$ SOP components, denoted by φ, ψ. The S_0 relates to the optical signal power, and can also be calculated from the other parameters as ${S_0}^2 = {S_1}^2 + {S_2}^2 + {S_3}^2$. Finally, the Stokes vector can be rewritten as

$$\boldsymbol{S} = S_0 \begin{bmatrix} \cos 2\varphi \\ \sin 2\varphi \cos\psi \\ \sin 2\varphi \sin\psi \end{bmatrix} \tag{2.38}$$

which is equivalent to a 3-dimensional representation of the SOP in spherical coordinates on the so-called Poincaré sphere. Such a Poincaré sphere is usually normalized with respect to S_0, thus the S_1, S_2, S_3 are distributed on an unitary sphere. It allows graphic visualization of the different types of polarized light, as depicted in Fig. 2.8.

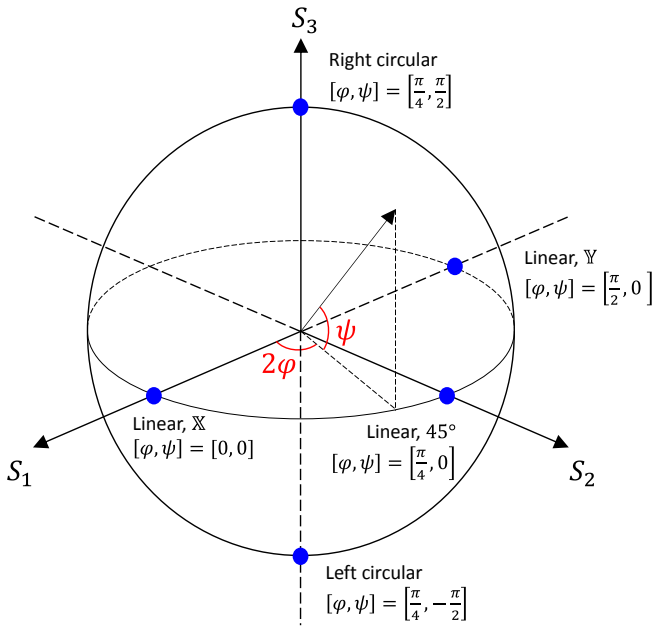

Figure 2.8. The Poincaré sphere: 3-dimensional representation of the Stokes vector for polarized light.

2.2.2 Polarization-diversity coherent receivers

When optical signals travel across the optical network, i.e., propagate through optical devices and fibers, the polarization matching becomes a serious problem because the SOP of the transmitted signals evolves in an unpredictable and uncontrollable way due to the birefringence of the materials for optics. Therefore, polarization tracking systems are needed at the coherent RX to continuously align the LO SOP to that of the received signal before the coherent beating.

Nevertheless, similar to the phase-diversity strategy analyzed in Section 2.1.2 to counteract the optical phase noise, the SOP tracking at the coherent RX can be avoided by polarization diversity.

This technique consists of splitting the received signal into two orthogonal $\mathbb{X}$ and $\mathbb{Y}$ polarization components, then processing them separately with two independent coherent RXs. After electrical signal processing, the combination of the two demodulated signals results in a baseband signal independent on the received signal SOP. Hereafter, for polarization-diversity coherent detection let us assume that the LO is linearly polarized at 45º ($\varphi = \pi/4, \psi = 0$) to ensure that, after polarization splitting, the signal–LO optical beating is carried out at the same LO power for both $\mathbb{X}$ and $\mathbb{Y}$ polarizations, maximizing the SNR at the input of the RX.

2.2.2.1 Phase-and-polarization-diversity 90º hybrid / 3x3 coupler homodyne

For homodyne detection, the phase-diversity RXs introduced in Sections 2.1.2.1 and 2.1.2.2 implementing 90° optical hybrid and 3x3 coupler respectively, are stacked in pairs to separately detect the $\mathbb{X}-$ and $\mathbb{Y}-$ polarization components. The resulting phase-and-polarization-diversity homodyne architectures are depicted in Fig. 2.9.

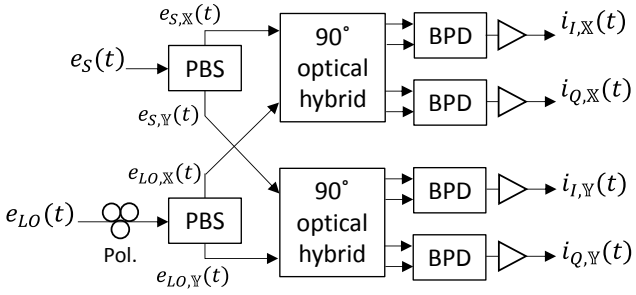

(a)

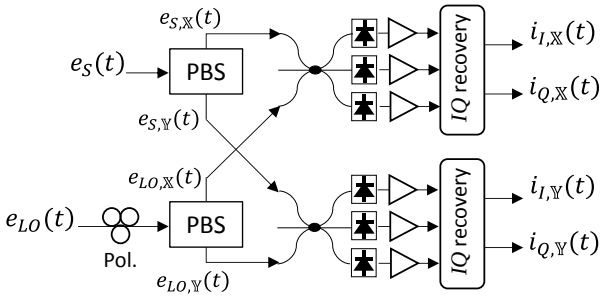

(b)

Figure 2.9. Phase-and-polarization-diversity coherent homodyne detection based on (a) 90° optical hybrids or (b) 3x3 couplers. BPD: balanced photodetection.

The working principle is similar in both schemes. First, the received signal $e_S(t)$ with random SOP passes through a PBS that separates the two orthogonal $\mathbb{X}$ and $\mathbb{Y}$ polarization components according to Eq. (2.31). The LO, set to have 45° linear SOP ($\varphi = \pi/4,\ \psi = 0$), also passes through a PBS yielding two equal lightwaves represented by its Jones vector as:

$$\mathcal{J}_{LO}(t) = \frac{1}{\sqrt{2}}\begin{bmatrix}\mathbb{X}\\ \mathbb{Y}\end{bmatrix}\left[E_{LO}e^{j(\omega_{LO}t+\phi_{LO}(t))}\right] \tag{2.39}$$

Note that the signal-LO coherent beating carried out here, separately for each SOP, only differs from the single polarization case in Sections 2.1.2.1 and 2.1.2.2 in that the signal and LO are scaled in amplitude, as well as in the relative phase shift ψ between the signal SOP components. Therefore, the four photocurrents at the output of the phase-and-polarization-diversity coherent RX are straightforwardly derived from the single polarization RX as:

$$i_{I,\mathbb{X}}(t) = \frac{\Re \cos\varphi}{\sqrt{2}}\sqrt{P_S(t)P_{LO}}\, cos(\omega_{IF}t + \Delta\phi(t)) \tag{2.40}$$

$$i_{Q,\mathbb{X}}(t) = \frac{\Re \cos\varphi}{\sqrt{2}}\sqrt{P_S(t)P_{LO}}\, sin(\omega_{IF}t + \Delta\phi(t)) \tag{2.41}$$

$$i_{I,\mathbb{Y}}(t) = \frac{\Re \sin\varphi}{\sqrt{2}}\sqrt{P_S(t)P_{LO}}\, cos(\omega_{IF}t + \Delta\phi(t) + \psi) \tag{2.42}$$

$$i_{Q,\mathbb{Y}}(t) = \frac{\Re \sin\varphi}{\sqrt{2}}\sqrt{P_S(t)P_{LO}}\, sin(\omega_{IF}t + \Delta\phi(t) + \psi) \tag{2.43}$$

It is worth mentioning that, in practice, the PBS in the LO path can be replaced by a 3 dB optical coupler with polarization maintaining fibers, at expenses of extra 3 dB LO power penalty since there is no coherent beating between the signal and the LO orthogonal SOP component at each of the two independent coherent RXs of the polarization-diversity architecture.

2.2.2.2 Polarization-diversity 2x2 coupler heterodyne

In heterodyne detection, phase-diversity is not needed due to fast variation of the instantaneous phase of the IF carrier after photodetection, as pointed out in Section 2.1.2.3. Nevertheless, for the case of polarization matching if the signal and LO lightwaves have orthogonal SOP no coherent beating is obtained at the PDs output. Hence, polarization-diversity by duplicating the heterodyne RX in Fig. 2.6 seems in principle hard to be avoided. The conventional polarization-diversity heterodyne RX becomes

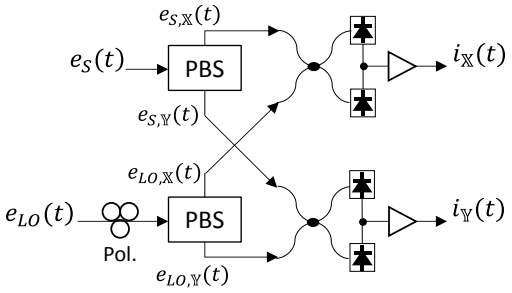

Figure 2.10. Polarization-diversity coherent heterodyne RX with balanced photodetection.

Similar to the homodyne detection in previous section, the LO is linearly polarized at 45° as in Eq. (2.39), and both signal and LO are splitted into orthogonal SOP components by a pair of PBS before coherent mixing. The two photocurrents, one per each SOP, are found to be

$$i_{\mathbb{X}}(t) = \sqrt{2}\Re \cos\varphi \sqrt{P_S(t)P_{LO}}\, \sin(\omega_{IF}t + \Delta\phi(t)) \tag{2.44}$$

$$i_{\mathbb{Y}}(t) = \sqrt{2}\Re \sin\varphi \sqrt{P_S(t)P_{LO}}\, \sin(\omega_{IF}t + \Delta\phi(t) + \psi) \tag{2.45}$$

Here, the variations of the received signal SOP, denoted by φ, ψ, are much slower than ω_{IF} in the order of several GHz.

Again, the PBS attached to the LO can be replaced by a 3 dB coupler with the extra 3 dB LO power penalty. Further simplifications on the RX architecture, as well as novel configurations for polarization-independent heterodyne RXs are analyzed in Chapter 6.

2.3 Modulation Formats

Optical communications uses light as a very high frequency optical carrier whose physical parameters as amplitude, phase, frequency or polarization can be modulated to transport information. These four degree-of-freedom, in the context of a single optical carrier operating in continuous mode (i.e., no burst mode or multiplexing in time), are fully exploited in coherent systems, significantly increasing the transmission rates and total network capacity when compared with DD systems that only employ intensity modulation formats.

This section analyses the basic digital modulation formats relying on amplitude and phase, also including the differential phase coding. Afterwards, advanced modulation formats derived from simultaneous amplitude-and-phase modulation in the complex plane are examined as well.

2.3.1 Binary phase shift keying

Phase shift keying (PSK) is a constant-envelope digital modulation format which carries data as variations in the instantaneous phase of the lightwave. The analytic form of a phase modulated optical signal is:

$$\begin{aligned} e_S(t) &= E_s e^{j(\omega_S t + \phi_S(t))} \\ &= E_s e^{j\omega_S t} e^{j\phi_S(t)} \end{aligned} \tag{2.46}$$

For the case of binary-PSK (BPSK), the binary data translate into an optical phase $\phi_S(t)$ that takes the values 0 or π when optical phase noise is not considered. Thus, the term $e^{j\phi_S(t)}$ can be replaced by a random variable $a(t)$ representing the phase information and assuming the values +1 and -1 for phase values 0 and π respectively, yielding

$$e_S(t) = a(t) E_s e^{j\omega_S t} \tag{2.47}$$

By replacing the notation introduced in Eq. (2.47) for BPSK into Eq. (2.6) and assuming: (I) the detection is homodyne ($\omega_{IF} = 0$), (II) the frequency components of the signal $a(t)$ are limited within the RX BW, the following variable for data decision is obtained at the homodyne RX output:

$$i_d(t) = 2\Re a(t)\sqrt{P_S P_{LO}} + n(t) \tag{2.48}$$

Here, $n(t)$ stands for the noise, modelled as additive white Gaussian noise (AWGN) with zero-mean and variance ${\sigma_n}^2$. In order to evaluate the error probability for BPSK from equation (2.48),

one must solve a problem of data decision in presence of AWGN over the random variable $i_d(t)$. Let us define the random process $\mathcal{X}$ with observations of $i_d(t)$ in Eq. (2.48). By considering that $a(t)$ assumes the values +1 and -1 with equal probability, the two BPSK symbols s_0 and s_1 are antipodal and the optimal decision threshold for the information-bearing random variable $\mathcal{X}$ –with Gaussian noise statistics– is found to be 0. Therefore, the error probability P_e is given by

$$P_e = P(s_0)P(\mathcal{X} > 0|s_0) + P(s_1)P(\mathcal{X} < 0|s_1) \tag{2.49}$$

with $P(s_0) = P(s_1) = 1/2$ the probability of the individual BPSK symbols, and $P(\mathcal{X} > 0|s_0)$, $P(\mathcal{X} < 0|s_1)$ the probability of wrongly detect a given symbol when the opposite symbol was transmitted. After solving for Eq. (2.49) [Pro02], the error probability for BPSK as a function of the SNR reads as

$$P_e = \frac{1}{2} erfc\left(\sqrt{SNR}\right) \tag{2.50}$$

where $erfc(\cdot)$ is the complementary error function. By going back to the quantum-limit SNR in Eq. (2.12) that is linearly proportional to the received signal power, one can calculate the needed received power for a given SNR at the symbol rate $R_b = 1/T$. Fig. 2.11 plots the error probability against both the SNR and the received power, to determine the sensitivity of the ideal homodyne BPSK RX.

From Fig. 2.11, the required SNR for an error probability of 10^{-3} is 6.8 dB, and raises up to 12.5 dB for error probability of 10^{-9}. In a 1 Gb/s data transmission, these SNR values translate into -65.1 and -59.4 dBm received optical power respectively. These values are defined as the quantum-limit sensitivity and represent the theoretical limit of the ideal BPSK coherent RX.

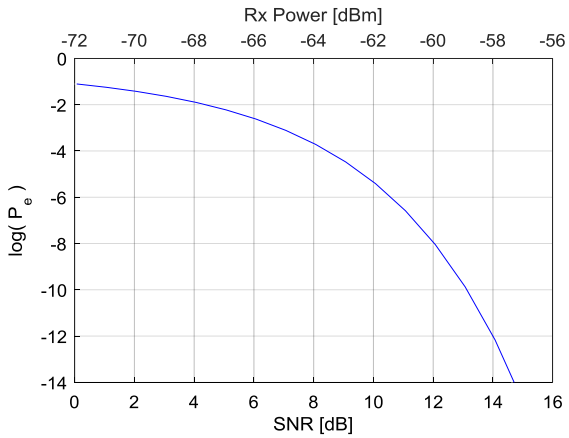

Figure 2.11. Error probability for BPSK as a function of SNR and received optical power. $R_b =$ 1 Gb/s for received power calculation.

2.3.2 Differential phase shift keying

In BPSK the information is recovered from the absolute phase of the optical carrier, thus requiring phase and frequency locking between the received signal and the LO for synchronous

demodulation. An alternative consist of recovering the transmitted information from the phase difference between two consecutive symbols. The binary modulation obtained from this encoding technique is called differential-PSK (DPSK), having the great advantage of relaxing the use of synchronization systems. To correctly decode the optical phase changes at the coherent RX, also avoiding error propagation, the binary data must be encoded at the TX side according to the structure depicted in Fig. 2.12(a), that implements the expression:

$$m[k] = \overline{d[k] \oplus m[k-1]} \tag{2.51}$$

At the RX side, the photodetected current $i_{PD}(t)$ after filtering is multiplied by a version of itself delayed by one symbol time T_b to extract the phase difference between two consecutive symbols, as shown in Fig. 2.12(b). Afterwards, the product is low-pass filtered by the base-band filter to get rid of the second order harmonic from the electrical mixing.

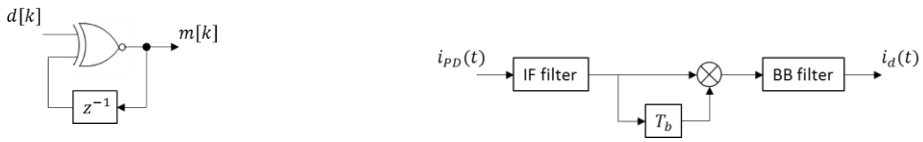

(a) (b)

Figure 2.12. DPSK system: (a) differential encoding at the TX; (b) differential detection at the RX. IF: intermediate frequency; BB: base-band.

From Eq. (2.48), the photocurrent at the input of the differential demodulator in Fig. 2.12(b), after being filtered by the IF filter matched to the BW of the information signal $a(t)$, reads as

$$i_{PD}(t) = 2\Re a(t)\sqrt{P_S(t)P_{LO}}\cos\big(\omega_{IF}t + \Delta\phi(t)\big) + n(t) \tag{2.52}$$

In this case, the carrier phase term $\omega_{IF}t + \Delta\phi(t)$ related to the optical frequency-and-phase mismatch between signal and LO is also included due to the absence of PLL synchronization. After the demodulation process, the performance of the DPSK modulation in presence of AWGN is calculated by computing the statistics of the decision variable $i_d(t)$. Nevertheless, analytical derivation of the error probability for DPSK is not a straightforward task –especially for higher order modulation– due to the statistics of the non-linear term $n(t)n(t-T_b)$ that appears in $i_d(t)$ after the delay and multiply operation.

By following the analytical derivation in [Pro02] with respect to Eq. (2.52), the error probability for DPSK with homodyne detection is found to be

$$P_e = \frac{1}{2}e^{-SNR} \tag{2.53}$$

It only exhibits a small SNR penalty compared with synchronous detection of BPSK, with less than ~1 dB penalty for error probabilities below 10^{-3}. Such behavior is plotted in Fig. 2.13. It is worth emphasizing that, for the case of heterodyne detection, the photocurrent in Eq. (2.52) is a

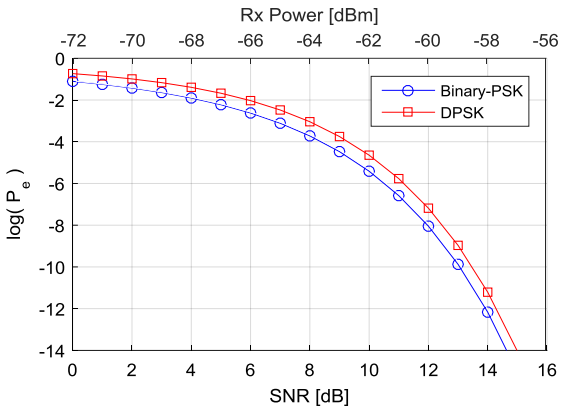

Figure 2.13. Error probability for homodyne detection of DPSK as a function of SNR and received optical power. $R_b = 1$ Gb/s for received power calculation.

high frequency carrier centered at ω_{IF}, that carries the base-band data $a(t)$. The delay-and-multiply operation of the differential demodulator realizes the frequency down-conversion by extracting the base-band data from the IF carrier. This is verified by making $i_d(t)$ explicit, after the base-band filtering and without considering the noise terms, yielding

$$i_d(t) = 2\Re^2 a(t)a(t-T_b)P_S P_{LO} cos(\omega_{IF} T_b) \tag{2.54}$$

where $a(t)a(t-T_b)$ are the differentially-demodulated symbols. In order to maximize the decision variable $i_d(t)$, the condition $\omega_{IF} T_b = 2n\pi$, with $n = 1, 2, 3, ...$, must be satisfied, being fulfilled when $f_{IF} = nR_b$. Hence, for optimal decision in heterodyne DPSK detection the IF should be set as an integer multiple of the symbol rate R_b. Although $f_{IF} = R_b$ is the lowest IF satisfying the optimal condition, in practice the IF is usually set to two or three times R_b to avoid low-frequency issues near DC.

As a final remark, the DPSK modulation format is very attractive for cost-effective implementation in access networks, as the phase-encoded information can be demodulated in asynchronous way without any PLL system.

2.3.3 Amplitude shift keying

The foregoing phase modulation formats transport information as the variations in the optical carrier phase, thus they have a constant envelope characteristic. Conversely, in amplitude shift keying (ASK) the binary data are carried on the amplitude of the optical carrier by switching it on and off, in the ideal case.

By following the same procedure than the BPSK modulation in Eq. (2.47), for ASK one can define an information-bearing random variable $a(t)$ taking the values 0 and 1 when the carrier amplitude is switched off and on respectively. Thus the ideal noiseless ASK-modulated optical signal becomes

$$e_S(t) = a(t)E_s e^{j\omega_S t} \tag{2.55}$$

If synchronous homodyne detection is assumed at the RX, with ideal phase matching with the LO, the decision variable for ASK in presence of AWGN is given by

$$i_d(t) = 2\Re a(t)\sqrt{P_S P_{LO}} + n(t) \tag{2.56}$$

which is exactly the same than the BPSK decision variable in Eq. (2.48), except for the random variable $a(t)$ that takes the values 1 and -1 for BPSK, and now 1 and 0 for ASK. The latter implies that, for a given noise variance, the two ASK symbols have half the Euclidean distance compared with the BPSK symbols, thus the SNR is halved. Accordingly, the error probability for ASK derived from Eq. (2.50) is

$$P_e = \frac{1}{2} erfc\left(\sqrt{\frac{SNR}{2}}\right) \tag{2.57}$$

In Fig. 2.14, the performance of ASK is compared with the phase-modulated formats, showing 3dB SNR penalty for synchronous ASK with respect to BPSK. Although practical implementations of ASK are, in general, simpler than the PSK systems, this thesis primarily focuses on the phase modulated formats as they exhibit better performance, and are assumed to be more robust against the intensity noise from lasers and the optical power fluctuations through the transmission path.

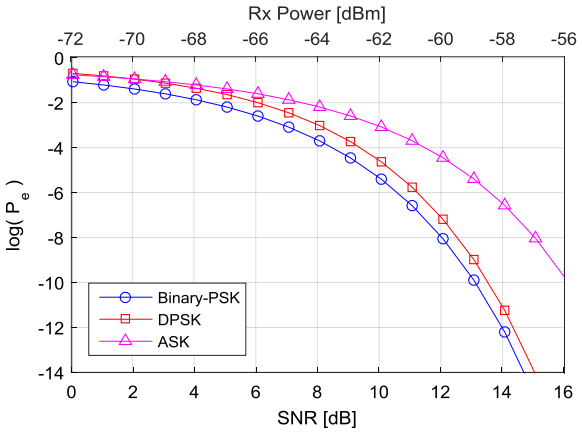

Figure 2.14. Error probability for ideal homodyne detection, as a function of SNR and received optical power. R_b = 1 Gb/s for received power calculation.

2.3.4 Complex quadrature amplitude modulation

To fully harness the capabilities of the coherent detection, and more specifically, the ability for full electrical field reconstruction at the RX, binary data are mapped into m-ary complex constellations by simultaneous amplitude and phase modulation of the complex electrical field. It composes the so-called quadrature amplitude modulation (QAM), where m represents the number of constellation points in the complex I–Q plane.

In the previous real-valued modulations, i.e., BPSK, DPSK, and ASK, the two-level electrical data directly drives the optical modulation either by directly modulated laser or by external modulator. Now, for m-QAM modulation, the bit-to-symbol mapping is required to translate each group of $log_2(m)$ bits into a constellation symbol, according to a predefined modulation alphabet. Rectangular m-QAM constellations are usually generated for convenient optical modulation employing external IQ modulators. Alternatively, m-QAM constellations in polar coordinates r, ϕ can also be generated by directly modulating intensity and phase respectively. It is advantageous, for instance, when cascading AM/PM external modulators, or when semiconductor lasers are directly phase-modulated by exploiting the laser chirp, as explained in Section 2.4.2. These kind of polar coordinates-like constellations are also known as amplitude-and-phase shift keying (APSK). Since this thesis primarily targets access networks applications with low-cost coherent technologies, here we focus on APSK modulation rather than rectangular QAM due to the possibility of simple and cheaper direct laser modulation.

For m-ary phase modulation only, namely m-PSK, the constellation symbols are $s_k = Re^{j\phi_k}$, with R the constant radius and ϕ_k the phase-encoded data defined by $\phi_k = \{2\pi n/m;\ n = 0,1,\dots,m-1\}$. The mean symbol power is given by $\bar{\Gamma} = R^2$. Table 2.1 depicts the constellation diagrams for m-PSK, with $m = \{1, 2, 3\}$ corresponding to BPSK, QPSK and 8-PSK respectively. As expected, the higher is the constellation order the smaller is the Euclidean distance d between symbols for the same average power $\bar{\Gamma}$, thus more difficult the symbol decision when the constellation is corrupted by noise.

Table 2.2. Constellation diagrams for m-ary PSK.

	BPSK	QPSK	8-PSK
Constellation	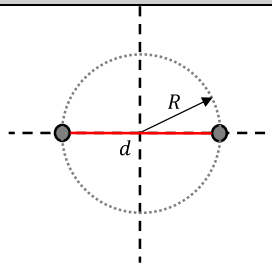	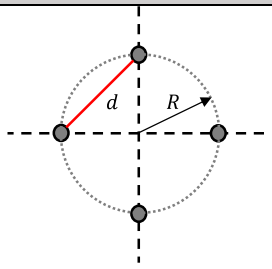	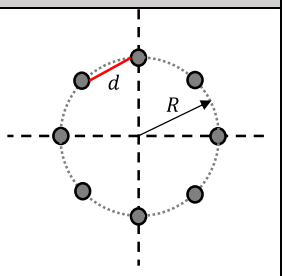
Euclidean distance	$d = 2R$	$d = \sqrt{2}R$ $\approx 1.41R$	$d = \left(2-\sqrt{2}\right)^{1/2}R$ $\approx 0.76R$

In the case of amplitude and phase modulation, consecutive symbols in the m-APSK constellation are set to have symmetric distance d among them to optimize the decision thresholds. For instance, Table 2.3 shows the constellation diagram for 8-APSK, in two different configurations. In conventional 8-APSK (Table 2.3, left), the outer ring is rotated 45° with respect to the inner ring. The symbols are defined by $s_k = r_k e^{j\phi_k}$, with $r_k = \{R_1, R_2\}$ the two radii, and $\phi_k = \{n\pi/4;\ n = 0,1,\dots,m-1\}$ the phase information similar to 8-PSK. The ratio between radii for symmetric d is found to be $R_2/R_1 = \left(1+\sqrt{3}\right)/\sqrt{2}$.

In the other configuration for 8-APSK in Table 2.3(right), referred as star 8-APSK, the constellation points are disposed with equal phase angles for both rings. The symbols are also defined by $s_k = r_k e^{j\phi_k}$, with $r_k = \{R_1, R_2\}$ the two radii, but the phase information is $\phi_k =$

$\{0, \pm\pi/2, \pi\}$, equivalent to QPSK. The ratio between radii for symmetric d becomes $R_2/R_1 = 1 + \sqrt{2}$.

Table 2.3. Constellation diagram for 8-APSK in two configurations.

	8-APSK	Star 8-APSK
Constellation	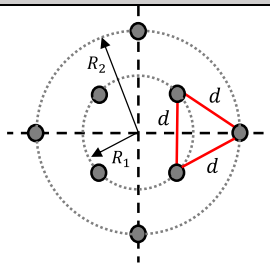	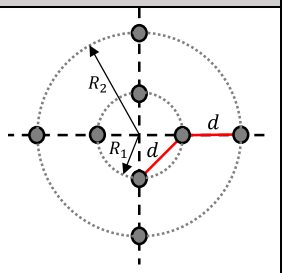
Euclidean distance	$d = \dfrac{2}{\left(3+\sqrt{3}\right)^{1/2}} R$ $\approx 0.92R$	$d = \left(2-\sqrt{2}\right)^{1/2} R$ $\approx 0.76R$

In both cases, the mean symbol power is given by $\bar{\Gamma} = (R_1^2 + R_2^2)/2$. By setting the same average power $\bar{\Gamma}$ for all the constellations in Table 2.2 and 2.3, the Star 8-APSK exhibits smaller Euclidean distance between points compared with the two rotated-rings 8-APSK constellation, thus the SNR requirement is higher for the same error probability. Here, R is the radius of the benchmark m-PSK constellation in Table 2.2.

In order to assess the performance of the complex QAM modulation, binary data were mapped into different m-(A)PSK constellations, spanning from BPSK up to 16-APSK, then corrupted by AWGN to set the SNR. The bit error ratio (BER) was computed by direct error counting over 10^7 bits. For comparison, rectangular 16-QAM was also considered. Results are plotted in Fig. 2.15. The constellation diagrams at BER = 10^3 are also shown in Fig. 2.16.

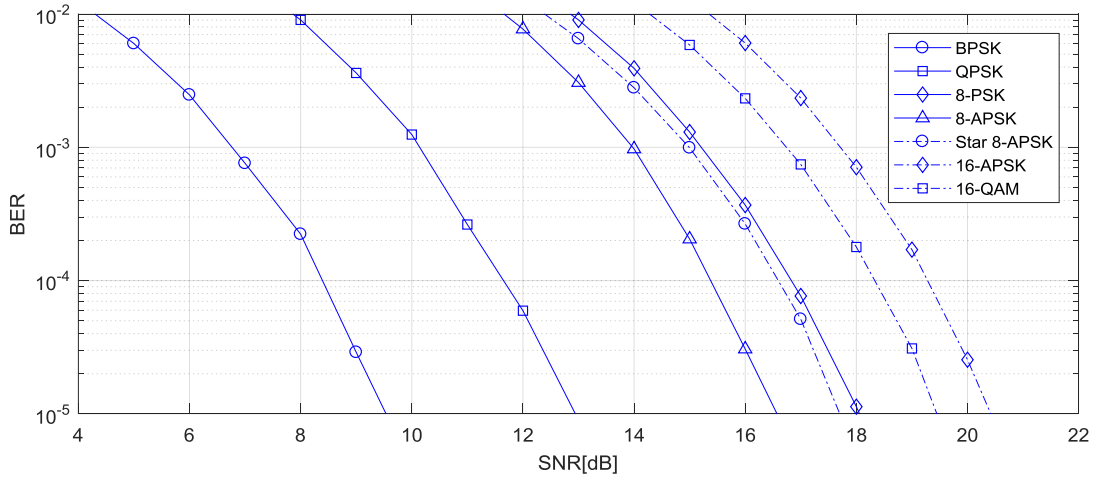

Figure 2.15. Error probability for m-(A)PSK as a function of the SNR, in presence of AWGN.

As expected, the different modulation formats perform according to their Euclidean distance d. BPSK and QPSK show the lowest SNR requirement respectively, as they have the largest d for

the same average symbol power. For the case of modulation formats with 3-bits/symbol (m = 8), 8-APSK shows 1.2 dB SNR improvement compared with 8-PSK and Star 8-APSK, for BER = 10^{-3}. Moreover, 8-PSK and Star 8-APSK constellations have similar d (See Table 2.2 and 2.3) thus perform almost the same. However, Star 8-APSK is expected to be more robust against the phase noise due to the underpinning QPSK phase modulation that has larger angle separation than 8-PSK. For m = 16, i.e. 4-bit/symbol, 16-APSK performs worse than 16-QAM, with ~1 dB SNR penalty for error probability of 10^{-3}. Nevertheless, it is worth noting that 16-APSK only has two different amplitudes or rings, in contrast with the three different symbol amplitudes of rectangular 16-QAM, as observed in Fig. 2.16(f) and 2.16(g) respectively. This feature translates into less

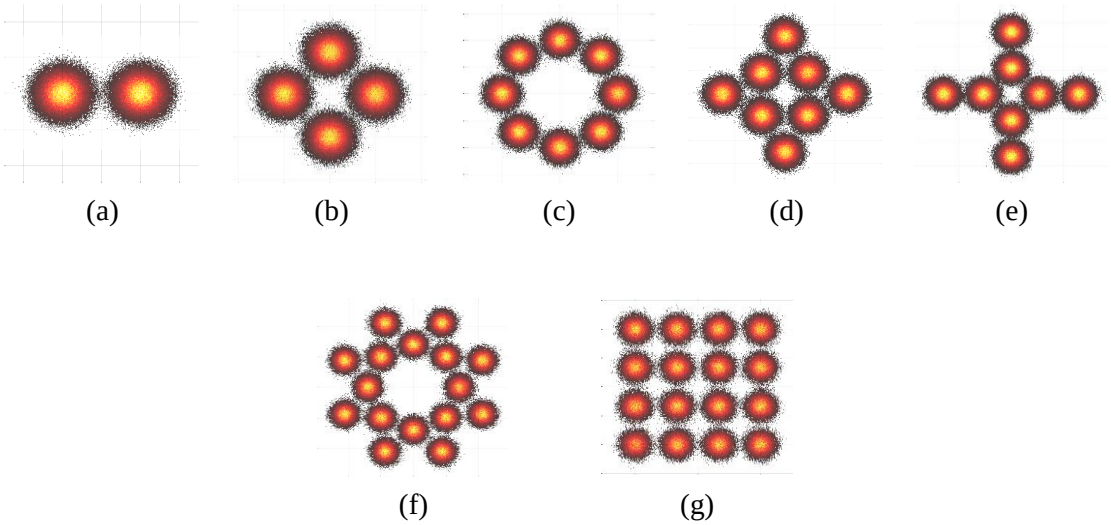

Figure 2.16. Constellation diagrams at error probability of 10^{-3} for (a) BPSK, (b) QPSK, (c) 8-PSK, (d) 8-APSK, (e) Star 8-APSK, (f) 16-APSK, (g) 16-QAM.

tolerance of 16-QAM against nonlinearities of amplifiers and/or modulators. In general, APSK is preferred over rectangular QAM, for the same constellation order m, when nonlinearities of the TX HW dominate [Häg13].

2.3.4.1 Differential detection of m-ary PSK

The differential PSK, introduced in Section 2.3.2 for binary signals, can also be applied to m-ary PSK constellations. In binary DPSK the encoding process at the TX is realized on the bits, as depicted in Fig. 2.12(a). Nonetheless, for m-ary PSK where the constellation symbols are composed by groups of $log_2(m)$ bits, the encoding process in the basis of bits becomes a very complex task as the constellation order increases.

A more practical solution consists of differentially encoding the m-PSK symbols $s[k]$ after bit-to-symbol mapping [Gin98], as represented in Fig. 2.17(a). At the RX, the differential demodulator shown in Fig. 2.17(b) is fed by the complex signal $c_d(t) = I(t) + jQ(t)$ arising from the phase-diversity coherent detection process. Here, $(\cdot)^*$ stands for the complex conjugate. Note that the TX encoding and the RX demodulation in Fig. 2.17 are complementary operations, by integrating and differentiating the phase between consecutive symbols respectively. In terms

of performance, differential m-PSK detection yields 3 dB SNR penalty with respect to synchronous m-PSK, for $m \geq 4$ [Pro02].

In the case of m-APSK, the differential detection can be easily implemented when the symbols have equal phase angles among rings, like in Star 8-APSK in Fig. 2.16(e). In such case, the phasors $s[k]$ and $c_d(t)$ entering the differential encoder and decoder respectively, must be normalized in amplitude to only operate on the symbol phase. Otherwise, if the m-APSK constellation has rotated rings, like in 8-APSK and 16-APSK in Fig 2.16(d) and 2.16(f) respectively, symbol-phase ambiguity occurs after the encoding process [Fis00].

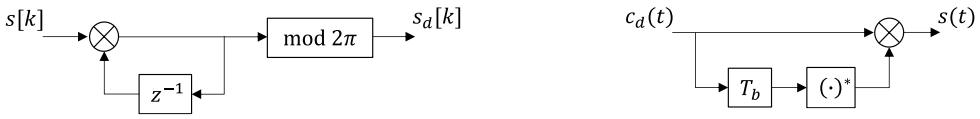

(a) (b)

Figure 2.17. Differential (a) encoding at the TX and (b) demodulation at the RX for m-ary PSK.

2.4 Direct Modulation of Semiconductor Lasers

Injection-current modulation of semiconductor lasers is a widespread technology in optical communication networks, with the benefit of less complexity, lower footprint and higher power efficiency when compared with external modulation. In particular, direct laser modulation dominates the PON and intra-data center interconnect (DCI) market segments, where simple and low-cost TRXs are mandatory. In these scenarios, intensity modulation (IM) formats are usually implemented by either binary or multilevel signaling (e.g., pulse-amplitude modulation (PAM)). Nevertheless, the modulation information could potentially be carried on the optical phase of the laser output field through modulation of the frequency chirp. It exploits the fact that when a semiconductor laser is under injection-current modulation ΔI, the emission optical frequency $\Delta \nu$ varies according to variations in the optical power ΔP, due to the chirp parameter of the laser. This behavior is represented in Fig. 2.18.

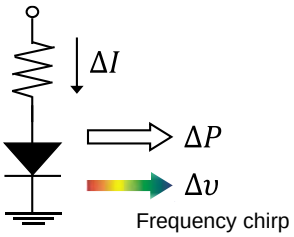

Figure 2.18. Direct laser modulation characteristics.

Such a frequency chirp –or dynamic change in the optical frequency– when the laser is under injection current modulation obeys two reasons. First, changes in the laser injection current produce variations in the density of excited carriers (electrons), which in turn induce changes in the semiconductor refractive index and, therefore, in the optical frequency. Secondly, temperature variations modify the relative permittivity of the semiconductor, also varying the semiconductor

refractive index. Since the temperature variations have large time constants, those thermal effects are only relevant for modulation frequencies lower than few MHz (e.g., < 10 MHz). Hence, for the upcoming analysis let us assume modulation frequencies larger than 10 MHz, so that only carrier density effects are considered.

In this section, the dynamics of the direct semiconductor laser modulation are briefly examined, giving special attention to the frequency chirp parameter. Moreover, simple strategies to generate direct optical phase modulation through the laser chirp are discussed.

2.4.1 Laser rate equations

The laser rate equations are a set of differential equations that describe the dynamic characteristics of the laser diode operation. From the general expression for the complex laser field output

$$e(t) = \sqrt{S(t)}e^{j\phi(t)} \tag{2.58}$$

let us define $S(t)$ as the photons density inside the optical cavity, related to the optical power, and being calculated as $S(t) = |e(t)|^2$. Using Eq. (2.58), the dynamics of both $S(t)$ and the instantaneous optical phase $\phi(t)$ are derived from

$$\frac{dS(t)}{dt} = e^*(t)\frac{de(t)}{dt} + e(t)\frac{de^*(t)}{dt} \tag{2.59}$$

$$\frac{d\phi(t)}{dt} = \frac{1}{S(t)}\mathrm{Im}\left\{e^*(t)\frac{de(t)}{dt}\right\} \tag{2.60}$$

If the electrical field $e(t)$ at the laser output is expressed in terms of the physical parameters of the semiconductor optical cavity, as in [Pet88] and [Bje96], the solutions of Eq. (2.59) and (2.60) yield the standard set of rate equations for single-mode laser emission, for the photon density $S(t)$, the carrier density $N(t)$, and the optical phase $\phi(t)$ respectively, as

$$\frac{dS(t)}{dt} = S(t)\left[R_{st} - \frac{1}{\tau_{ph}}\right] + R_{sp} \tag{2.61}$$

$$\frac{dN(t)}{dt} = \frac{I(t) - I_{th}}{eV} - \frac{R_{st}}{V}S(t) - R(N) \tag{2.62}$$

$$\frac{d\phi(t)}{dt} = \frac{1}{2}\alpha_H v_g \frac{\partial g}{\partial N}[N(t) - N_{th}] \tag{2.63}$$

In Eq. (2.61), R_{st} and R_{sp} are the effective stimulated/spontaneous emission coefficient respectively, related to the optical cavity gain and the confinement factor, and τ_{ph} is the photon lifetime. This rate equation for the photons density may be simply interpreted as follows: $S(t)R_{st}$ photons are generated per unit of time due to stimulated emission, and $S(t)/\tau_{ph}$ photons are lost per unit of time due to stimulated absorption subject to the photon lifetime. Also, R_{sp} photons are generated per unit of time due to spontaneous emission.

Eq. (2.62) describes the dynamics of the carrier density. Here, $I(t)$ is the injection current, I_{th} is the threshold current, e stands for the electron charge, V is the volume of the active region, and

$R(N)$ is the carrier recombination with respect to spontaneous emission. This rate equation is explained as follows: the carrier density generated by the continuous pumping of the injection current (first term of Eq. (2.62)) decays $R(N)$ per unit of time due to spontaneous recombination, and $(R_{st}/V)S(t)$ per unit of time due to stimulated recombination, i.e., the carrier consumption of the stimulated emission.

The last Eq. (2.63) is the rate equation for the optical phase. Note that the time derivative of the optical phase is proportional to the optical frequency variation –the laser chirp– , given that

$$\Delta v(t) = \frac{1}{2\pi}\frac{d\phi(t)}{dt} \tag{2.64}$$

Hence, it can be derived from Eq. (2.63) that the optical frequency varies proportional to the carrier density variations as a result of modulating the injection current. This explains the underlying mechanism for the laser FM modulation. In Eq. (2.63), v_g is the group velocity of the lightwave, N_{th} the carrier density at the threshold, $\partial g/\partial N$ is the slope of the stimulated emission gain, and α_H is the linewidth enhancement factor or Henry coefficient.

The pair of rate equations (2.61) and (2.62) mathematically model the three different interactions that occur between photons and electrons inside the lasing medium (i.e., the optical cavity), namely the spontaneous emission, the stimulated emission and the stimulated absorption. If the pumping rate, the spontaneous emission effects and the loss terms are neglected in Eqs. (2.61) and (2.62), one obtains

$$\frac{dS(t)}{dt} = R_{st}S(t) \tag{2.65}$$

$$\frac{dN(t)}{dt} = -\frac{R_{st}}{V}S(t) \tag{2.66}$$

Now, Eq. (2.65) is the stimulated emission contribution and Eq. (2.66) is the stimulated recombination contribution. They clearly show that an increase in the number of generated photons directly relates to a decrease in the number of carriers (excited electrons). These phenomena constitutes the operating principle of lasers: light amplification inside the semiconductor optical cavity by stimulated emission of photons, that is graphically summarized in Fig. 2.19.

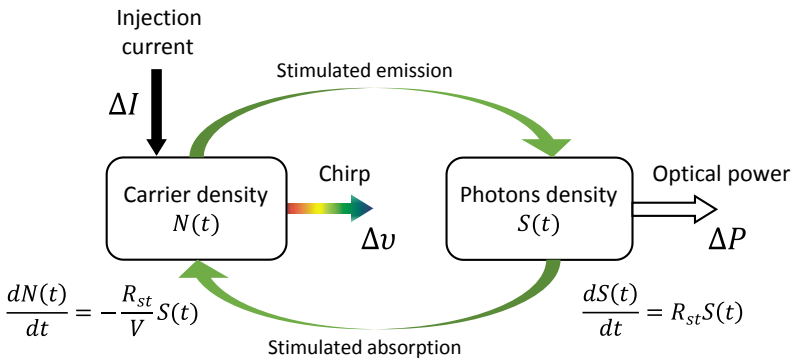

Figure 2.19. Laser principle: light amplification by stimulated emission of radiation

2.4.2 Direct phase modulation

The inherent frequency chirp of semiconductor lasers under direct current-modulation can be exploited for generation of phase-modulated optical signals, without the need of external modulators. This is particularly advantageous for coherent PON that may benefit from the high performance, capacity and robustness of advanced m-PSK modulation formats. In such case, the coherent TX is now conceptually more sophisticated than the employed in conventional IM-DD systems, yet simple and low-cost.

Using Eqs. (2.61) and (2.63), one can set up an expression that relates the photons density (i.e., the optical power ΔP) with the frequency chirp $\Delta\upsilon$, yielding [Hen82], [Tuc85]

$$\Delta\upsilon(t) = \frac{\alpha_H}{4\pi}\left(\kappa P(t) + \frac{1}{P(t)}\frac{dP(t)}{dt}\right) \tag{2.67}$$

where κ is the adiabatic chirp coefficient. The first term in Eq. (2.67) is the adiabatic chirp that is dominant at mid frequencies (from MHz up to several GHz [Pro11]), whereas the second term is the transient chirp that is more apparent for high frequencies with fast symbol transitions. It is worth mentioning that Eq. (2.67) lacks from the thermal chirp contribution since only carrier density effects are considered. Nevertheless, the optical frequency variations due to low-frequency thermal effects and their impact on the laser FM response for broadband modulation, are examined in Section 3.3.3.1. Also, the detailed technique for laser chirp measurement is presented in [Pro11] and [Sat05].

The best configuration to directly modulate the optical phase through the frequency chirp consist of setting the laser bias current to large values, while applying a small current swing for modulation. This produces variations of the optical power that are significantly lower than the mean emitted power. Under this small-signal condition and considering the modulation BWs for the proposed PON scenario, < 10 GBd with m-(A)PSK formats (see Fig 1.2), the adiabatic chirp term in Eq. (2.67) prevails; then $\Delta\upsilon(t) \propto \alpha_H \kappa P(t)$, and the semiconductor laser can be modelled as an optical FM modulator with residual IM. Accordingly, one can infer that lasers with large $\alpha_H\kappa$ value are optimal for direct chirp modulation to lower the modulation current swing thus the residual IM.

Next step is to translate the chirp FM modulation into phase modulation (PM). It is a matter of observing the relationship between frequency and phase given by Eq. (2.64), that can be rewritten as

$$\begin{aligned}\phi(t) &= 2\pi\int_0^t \Delta\upsilon(\tau)d\tau \\ &\propto 2\pi\int_0^t \alpha_H\kappa P(t)d\tau\end{aligned} \tag{2.68}$$

or expressed in the frequency domain as

$$\Delta\phi(\omega) = \frac{2\pi}{j\omega}\Delta\upsilon(\omega)$$

$$\Delta\phi(\omega) \propto \frac{2\pi}{j\omega}\alpha_H \kappa \Delta P(\omega) \tag{2.69}$$

with $\omega = 2\pi f$ the angular frequency. In pure PM modulation, the optical phase changes *linearly* with the modulating current. Hence, to obtain phase modulation through the frequency chirp modulation, the integral term $(1/j\omega)$ in Eqs. (2.68) and (2.69) needs to be canceled by introducing a derivative term $(j\omega)$, so that $\Delta\phi$ varies linearly with ΔP, or, equivalently, with ΔI in the small-signal regime. This frequency-phase relationship is illustrated in Fig. 2.20. When the high frequency carrier $c(t)$ is modulated in frequency by $x(t)$, as in Fig. 2.20(a), the phase of $c_{FM}(t)$ is proportional to the time-integral of $x(t)$. On the other hand, if the FM modulator is fed by the time derivative of $x(t)$, as in Fig. 2.20(b), one obtain a phase modulated carrier $c_{PM}(t)$ whose phase changes are driven by $x(t)$.

(a) (b)

Figure 2.20. Scheme for generating (a) FM modulation of the carrier $c(t)$, and (b) PM modulation of $c(t)$ by using a FM modulator.

In practice the symbol pulse-shaping required for direct phase modulation, performing the time derivative of the information symbols, can be implemented either in analog or digital domain. The simplest method consists of analog pulse-shaping preceding the laser modulation. The time derivative of the modulating current is approximated by a first-order resistor-capacitor (RC) filter with high-pass response, as depicted in Fig. 2.21(a). The cut-off frequency of the RC filter is set according to the data BW in order to suppress the low-frequency components of the data spectrum, keeping only the symbol transitions (Fig. 2.21(a) inset). As an example, for direct DPSK at 1.25 Gb/s, as in [Can14a], the capacitance is C = 1.2 pF with respect to R = 50 Ω.

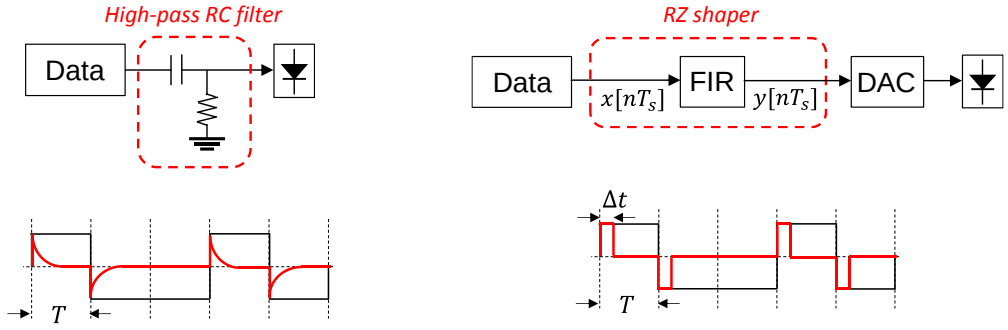

(a) (b)

Figure 2.21. Pulse shaping for direct laser phase modulation: (a) analog and (b) digital implementation. The insets show the modulating current after high-pass shaping for direct BPSK.

In the other approach in Fig. 2.21(b), the pulse shaping is realized in the digital domain by a finite impulse response (FIR) filter that implements the difference equation

$$y[nT_s] = x[nT_s] - x[(n-1)T_s] \tag{2.70}$$

with T_s the sampling time. The result is a return-to-zero (RZ) pulse shape with variable duty-cycle Δt that drives the direct phase modulation of the laser [Vel18b]. The desired phase shift $\Delta\phi(t)$ is set by controlling both the frequency deviation $\Delta v(t)$ (by the modulation current amplitude) and the duty-cycle of the modulating pulse, according to the expression $\Delta\phi(t) = 2\pi\Delta v(t)\Delta t$, that arises from Eq. (2.68) after solving the time-integral with respect to the waveform in Fig 2.21(b) inset. As an example, for a reference phase shift of π the product $\Delta v(t)\Delta t$ equals to 0.5. Note that the higher is the sampling rate, the lower is the duty-cycle of the RZ pulse; when 2 samples per symbol are used, the Nyquist limit, then Δt = 50%, as the lower bound.

Since the optical phase changes linearly with the current in the small-signal regime, as stated before, this pre-equalization technique for direct phase modulation straightforwardly upgrades to advanced m-PSK formats by modulating the laser with a multilevel signal according to the different phase levels [Can16a], [Can16b]. This is illustrated in Fig. 2.22 for direct QPSK, using digital pulse shaping.

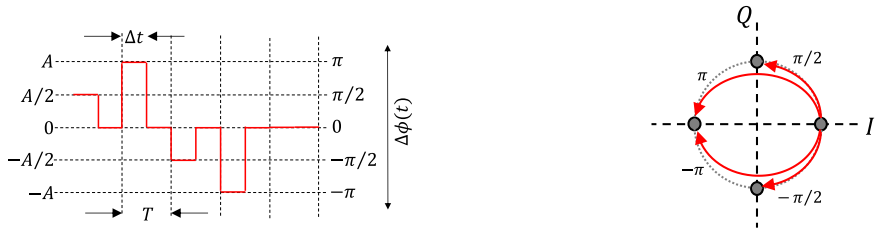

(a) (b)

Figure 2.21. (a) RZ waveform with 50% duty-cycle for direct QPSK, and (b) the resulting constellation.

As a final remark, the analog pulse shaping is very simple and cheap, without requiring DSP and DACs, thus optimal for fully analog implementation of the coherent TRX using binary modulation. Alternatively, the digital pulse shaping is preferred for DSP-based TRXs with advanced m-PSK formats, also allowing for flexibility and easy reconfiguration of the modulation format and the transmission rate without modifying the HW.

Chapter 3

Transmission Impairments in Coherent Access Networks

In the PON, the transmitted optical signals carrying information are affected by several sources of noise and distortions through the transmission path, including the TX and RX structures, that degrade the quality of the detection and, in some cases, complete hinder the information recovery. Therefore, is highly relevant to identify the main transmission impairments within the udWDM scenario, evaluate their impact on the PON performance, and set the maximum tolerance to each of those detrimental effects in order to avoid extreme system degradation. The insights obtained directly influence on the PON dimensioning, as well as on the coherent TRX design.

In order to identify the most relevant transmission impairments in the udWDM PON, let us refer back to the research scenario proposed in this thesis, and depicted in Fig. 1.2. It consists of a tree-based PON with udWDM distribution enabled by coherent technologies. The PON is colorless, then fully compatible with legacy access systems that potentially may share the same ODN. Each subscriber owns a dedicated λ, that is later multiplexed in ultra-narrow optical grid configuration. The optical grid is flexible in terms of channel allocation and data BWs, allowing for the convergence of residential, business and mobile services. The transmission rate per single λ retains down, lower than 10 GBd using advanced modulation formats, and generated by cost-effective direct laser modulation. This contrast with actual TDM PON systems that require high aggregate bit rate per single λ to be shared among individual users.

The optical fiber channel is recognized as the mayor source of effects that impair the transmitted signal in optical communication systems, especially for high-capacity core networks that transport large data rates through ultra-long fiber distances (thousands of km). The reason is the nonlinear characteristics of the fiber transmission, which are governed by the nonlinear Schrödinger equation (NLSE) [Agr10]. Nonetheless, some of those fiber impairments have no significant impact on the coherent udWDM-PON scenario, while others can be simply mitigated by proper dimensioning the PON parameters, such as data BW, fiber length, wavelength allocation, and optical power launched into the fiber, among others.

The first of them is chromatic dispersion (CD). The large majority of the fibers installed in metro/access network outside plants comply with ITU-T Recommendation G.652. The CD coefficient at 1550 nm is typically 17 ps/(nm×km), ranging from 16 to 18 ps/(nm×km) across the C-band [ITU16]. The CD causes inter-symbol interference (ISI) due to the time-spreading of the received symbols after fiber propagation. This impairment is more apparent for modulation BWs >10 GBd and fiber distances longer than 60 km [Agr10], thus of minimum impact on the proposed udWDM-PON with <10 GBd modulation BW and fiber spans shorter than 40 or 60 km [ITU19].

Rayleigh backscattering (RBS) is another impairment arising from the fiber channel and related to accumulated micro-reflections of light due to fluctuations on the fiber refractive index at molecular scale. The RBS interferes to lightwaves at the same λ that propagate in counter

directions over the same optical fiber, and can be avoided by using different λs for the US and DS links thus eliminating the spectral overlap. On the other hand, polarization mode dispersion (PMD) effects are not considered because the PMD coefficient of the standard G.652 single-mode fiber (SMF) link is very low ($< 0.1\ \mathrm{ps}/\sqrt{\mathrm{km}}$) [ITU16], and those PMD impairments are negligible even for 10 GBd signals over the typical fiber distances of the PON scenario.

Last, a set of nonlinear impairments arise from the optical power level injected into the fiber, namely the self-phase modulation (SPM), the cross-phase modulation (XPM) and the four-wave mixing (FWM). All of them are grouped into the Kerr nonlinear interactions that occur in a silica optical fiber [Agr10]. Owing to the superior sensitivity of the coherent detection intended for the udWDM-PON, the launched power per λ can be reduced below the threshold for the nonlinear Kerr impairments [Pra16], [Rei12], but still achieving the target loss budget $>$30 dB for a launched power of, e.g., 0 dBm per user or even lower. Moreover, the low-cost lasers employed as optical sources in the PON exhibit large laser linewidths and λ fluctuations around the nominal frequencies in the udWDM grid, that, in combination with the random polarization misalignments among the multiple WDM channels, can bring to further resilience to Kerr impairments because the optical signals interacting in the fiber media are highly uncorrelated.

Accordingly, the main conclusion is that the impairments originated from the optical fiber channel are not yet the limiting factor in the coherent udWDM access network, and the dominant impairments mostly originate from the photonic/electronic subsystems of the coherent TRX. Certainly, the CD and fiber nonlinearities are relevant when scaling the PON to higher transmission rates and fiber reach than the considered here, but this study is beyond the scope of this thesis and has been left for future research.

This chapter carries out a comprehensive analysis of the dominant transmission impairments in the udWDM-PON by means of numerical simulation, assessing their impact on the PON performance and their implication on the coherent TRX design. Some experimental results are also included to contrast with simulations. The key outcomes serve as a benchmark for implementation of a gigabit-capable udWDM access network.

3.1 Design of Coherent Transceivers for PON

The coherent TRXs are a mature technology in high-capacity core networks supporting large volumes of data traffic. They are also gaining interest for short-reach DCI to increase the total data rate within the same BW. Performance evaluation of coherent TRXs for 400G DCI systems reveals that the overall complexity and energy consumption is comparable to that the IM-DD counterpart that dominates the DCI market segment, but with superior power budget and spectral efficiency [Che19]. To efficiently transport large volumes of data, information is mapped into advanced modulation formats with dense QAM constellations that propagate through the electronics and optics of the coherent TRX, and through the transmission media, i.e., the optical fiber infrastructure.

Fig. 3.1 depicts a block diagram of the conventional coherent TRX for core networks, with all the HW components and the DSP subsystems [OIF15]. At the TX part, in Fig 3.1(a), the DSP

generates the I and Q signals for the complex QAM modulation to be transmitted on each polarization. Four DACs drive the optical modulation, carried out by a dual-polarization IQ (DP-IQ) modulator fed by a laser with narrow linewidth, e.g., external cavity laser (ECL). An optical amplifier (OA) at the TX output (erbium-doped fiber amplifier (EDFA) or semiconductor optical amplifier (SOA)) compensates for the optical losses of the Mach-Zehnder modulators (MZM) and the polarization beam splitter/combiner (PBS/PBC). The Rx side, in Fig. 3.1(b), implements the phase-and-polarization-diversity 90° hybrid optical front-end introduced in Section 2.2.2.1 (see Fig. 2.9(a)) for beating the incoming optical signal with the LO, producing a set of four electrical signals corresponding to the IQ components for each received SOP. After the analog-to-digital converters (ADCs), the DSP of the RX compensates for all the distortions and interferences from channel and components, and recovers the transmitted data.

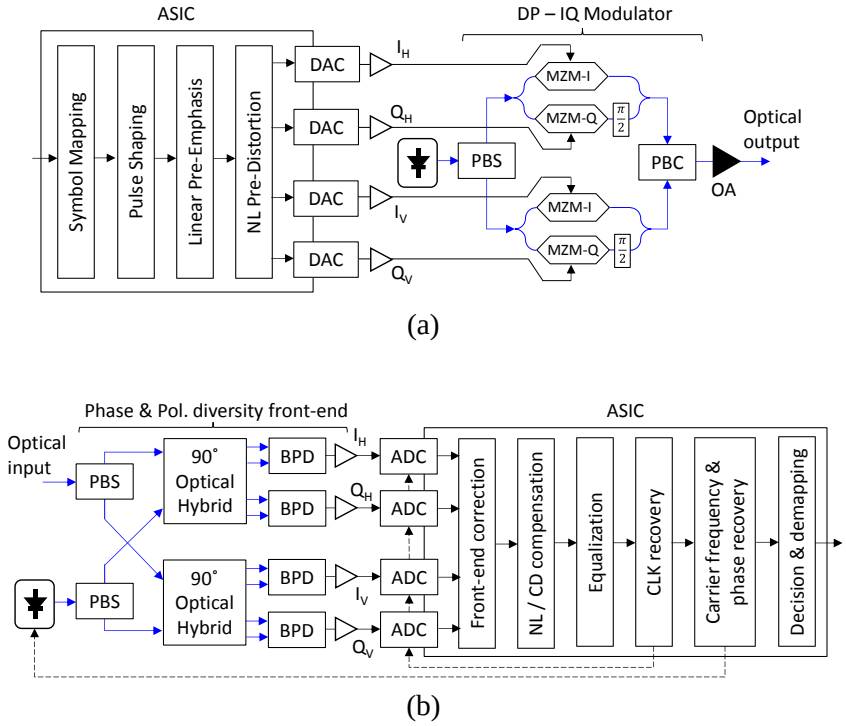

Figure 3.1. Conventional coherent TRX for optical core networks: (a) TX and (b) RX.

The DSP subsystems of the coherent TRX in Fig. 3.1 are briefly described in what follows, starting by the TX DSP. After bit-to-symbol mapping, the pulse-shaping determines the spectral characteristics and the electrical/optical BW of the signal. Usually, Nyquist filters with low roll-off parameter are employed. The linear pre-emphasis compensates all the linear distortion due to non-ideal frequency response and BW limitation of the subsequent TX HW, including MZMs, driver amplifiers and DACs. Along with linear distortions, the TX HW also exhibits non-linear responses that can be fully pre-compensated by the non-linear (NL) pre-distortion algorithm [Kha16]. In practice, the linear pre-emphasis and the NL pre-distortion can be merged in a single algorithm.

At the RX, the first DSP subsystem compensates for the optical front-end imbalance, comprising IQ skew from non-symmetrical path lengths and orthonormalization for imbalanced 90˚ hybrids. Next, CD and NL propagation effects are mitigated by estimating the digital coefficients that back-propagate the received signal through the dispersive fiber channel [Nap14b]. Afterwards,

the equalization algorithm compensates for the residual ISI due to band-limited RX HW, similar to the DPE at the TX, as well as for the time-variant dynamics such as changes in the SOP, or PMD. After mitigating the propagation impairments, the CLK recovery estimates and corrects the timing error between the TX and the RX, as they do not operate with synchronous CLK. At the carrier recovery (CR), the transmitted constellation is recovered by getting rid of the phase noise and frequency drifts from TX and LO lasers. Finally, decision and de-mapping are carried out to recover data going towards error correction and decoding.

In general, the commercial coherent TRXs are still complex and very expensive for deployment in optical access networks with high terminal density. Also, the DACs and ADCs are critical elements as their cost and power consumption increases if the required sample rate, resolution bits, and BW are high. To overcome these technological hurdles, efforts in research are being taken during the last years to develop coherent TRXs with simplified architectures, analog signal processing, and HW efficient DSP [Fer17], [Art15], [Shi19], [Erk16], [Mat19]. Yet, most of the proposed solutions still rely on external modulators, or extra BW at the RX that unfavorably scales with the bit rate. A recent alternative for coherent TRXs is the Kramers-Kronig RX [Mec16] that substantially reduces the RX front-end to a single PD per each SOP, but does not exhibit the high sensitivity and λ-selectivity of coherent systems. Also, the required BW twofold compared with coherent homodyne detection.

Accordingly, the adoption of coherent systems for PONs in a cost-effective way will depend on (I) reducing the footprint of the coherent TRX photonic elements; (II) lowering the requirements for ADCs and DACs in case they are needed, in terms of BW, resolution, and sample rate; (III) simplifying the signal processing complexity, thus reducing the energy consumption and overall cost of the electronic processor. This raises two different paradigms for the design of the coherent TRX depending on the final type of PON subscriber (see Fig. 1.2). On the one hand, premium users like enterprise (FTTB) and mobile services that demand the highest data rates, up to 10 - 20 Gb/s, can benefit from coherent homodyne RXs with real-time DSP to transmit advanced complex constellations with enhanced spectral efficiency. On the other hand, residential users (FTTH) that comprise the majority of the PON subscribers, are the market segment where the cost, complexity, and power consumption of the ONUs impact the most. For those FTTH users, heterodyne RXs fully analog without DACs/ADCs nor DSP, are the option that better suits the strict requirements. Next sections explore in detail both coherent ONU approaches.

3.1.1 3x3 homodyne transceiver

Fig. 3.2 presents the proposed realization of a homodyne TRX for udWDM-PON addressing the lower complexity requirement. First, for generation of advanced modulation formats the IQ modulators represent a severe limitation in terms of footprint, cost, and power budget. Instead, the TX in Fig. 3.2(a) implements a cost-effective complex optical modulator based on dual electro-absorption modulated laser (DEML). It generates m-(A)PSK constellations in polar coordinates r, ϕ, as explained in Section 2.3.4, by directly modulating the intensity with the electro-absorption modulator (EAM) and the phase with the distributed feedback (DFB) laser

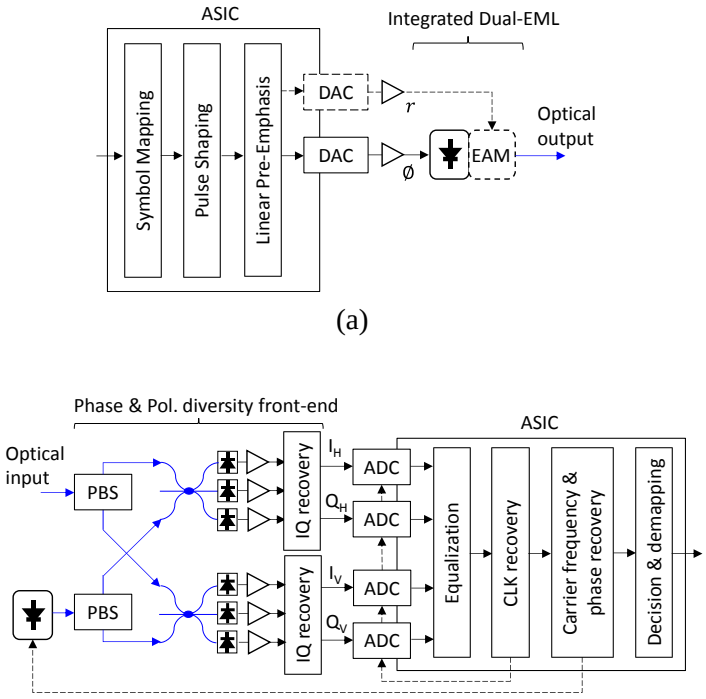

Figure 3.2. Coherent homodyne TRX for udWDM-PON with simplified architecture based on (a) DEML at the TX, and (b) 3x3 optical front-end at the RX.

chirp. Chapter 7 provides technical details for the DEML characterization and operation with m-APSK. Moreover, optical amplification is not necessary since no external power-losing devices are attached to the DEML output, lowering the power consumption of the coherent TX.

At the RX in Fig. 3.2(b), optical 90° hybrids are replaced by the much simpler 3x3 coupler front-end presented in Section 2.2.2.1. This allows for phase-and-polarization diversity with six single-ended PDs, two less than the eight PDs of the conventional balanced homodyne RX. The linear combination of the photocurrents for IQ recovery is carried out by passive HW. Note that although the IQ recovery may be implemented into the DSP of the RX, this simple analog pre-processing saves two ADC channels that are critical components of the RX.

The DSP part, the algorithms inherited from the coherent TRX for core networks in Fig. 3.1 can also be adapted and further simplified for the udWDM access scenario having different requirements and constraints. Specifically, some of the DSP algorithms for equalization and impairments mitigation play a secondary role in the access scenario with lower data rates, simpler modulation formats, and shorter fiber spans. For example, at the simplified TX the EAM integrated into the DEML has a nonlinear electro-optic response (see Fig. 7.10). Nevertheless, the EAM bias and the extinction ratio (ER) can be adjusted to operate in the linear region, and the nonlinear pre-distortion by DSP might be optional or discarded. Therefore, the key DSP subsystems for the TX are: symbol mapping for m-(A)PSK (Section 2.3.4), pulse shaping for both spectral compactness (Section 3.4.1.1) and direct phase modulation (Section 2.4.2), and linear pre-emphasis (Chapter 7).

Similarly, the DSP of the RX is further reduced by considering that the impairments from the optical fiber channel, like CD and PMD, have minor impact for the signal BWs and fiber spans

of the udWDM-PON scenario. Also, the front-end correction and orthonormalization for imbalanced optical hybrids are more critical for dense QAM constellations that are not feasible for PONs. Hence, the key DSP subsystems of the RX are: equalization for residual ISI, CLK recovery (Section 6.2.2), CR based on differential phase detection (Chapter 5), and constellation demapping.

The DSP of the coherent TRX can be implemented either in an application-specific integrated circuit (ASIC) or in a FPGA. Whereas, in general, the FPGA is more versatile in terms of reconfiguration and synthesis of the DSP algorithms, the ASIC is more suitable for mass production and lower cost, including embedded data converters. As a final remark, the DSP-based coherent TRX reconfigures easily, dynamically adjusting its parameters such as modulation format and data BW to adapt to the type of service and user. This is advantageous for network flexibility compared with analog systems that require HW changes.

3.1.2 2x2 heterodyne transceiver

The heterodyne TRX in Fig. 3.3, intended for residential services that require mass ONUs deployment, may benefit from the remarkable lower cost and simpler HW complexity offered by the fully analog implementation, without DACs or ADCs. The heterodyne detection has the drawback of extra BW requirement at the RX to process the broadband detected spectrum centered at IF. However, in the particular case of residential user at 1.25 – 2.5 Gb/s, this has very limited practical impact for state-of-art electronics.

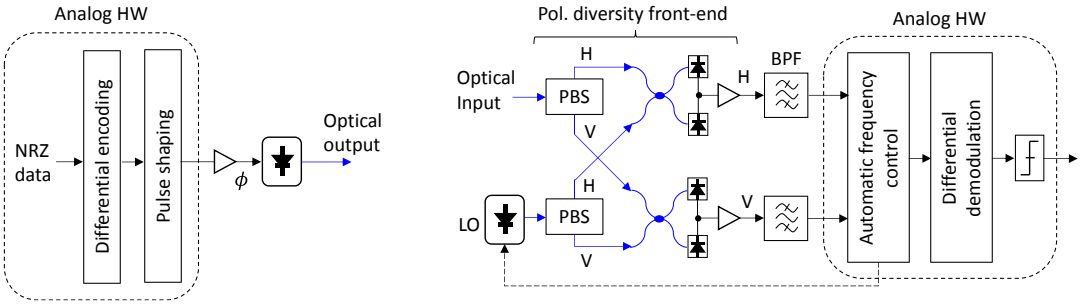

Figure 3.3. Coherent heterodyne TRX for udWDM-PON with fully analog transmission and detection of DPSK signals: (a) TX and (b) RX.

The TX in Fig 3.3(a) uses direct phase modulation of a DFB laser. Here, DPSK modulation is adopted to avoid the use of DSP for data processing at both the TX and RX side. The binary NRZ data are first differentially encoded, then followed by the high pass pre-equalization, similar to Fig. 2.21(a), to proper adapt the pulse shape of the modulating current for direct phase modulation.

The RX in Fig. 3.3(b) implements the polarization-diversity heterodyne front-end introduced in Section 2.2.2.2. All the electrical signal processing is carried out by analog HW. Band-pass filtering (BPF) centered at IF (~2 or 3 times R_b) and matched in BW to that of the transmitted signal is applied. The automatic frequency control (AFC) system owns an analog frequency discriminator (see Section 5.2) to drive the optical frequency tuning of the LO. The binary data

encoded in the DPSK signal are recovered by differential demodulation, then thresholded for data decision and bit recovery.

3.2 Coherent Receiver Sensitivity in the udWDM-PON

One of the great advantages of coherent detection is the high RX sensitivity, which eventually reaches the quantum-limit for strong LO power as analyzed in Section 2.1.1. Nonetheless, the final RX sensitivity in the PON is determined by the external sources of noise, interferences and distortions, as well as by the specific implementation of the coherent RX. In this section, the impact of the udWDM-PON scenario on the final coherent RX sensitivity, employing the RX architectures described in previous Section 3.1, is assessed by numerical simulation with Monte-Carlo method, using VPITransmissionMaker® and MATLAB®. For the sake of brevity, here and in the remainder of the chapter, the analysis and key conclusions are restricted to the FTTH use case, i.e., residential users with dedicated λ at 1.25 Gb/s with DPSK. Next chapters, though, cover the rest of scenarios including higher data rates with complex modulation formats.

The general simulation setup is represented in Fig. 3.4. The 1.25 Gb/s DPSK signal generated at the TX is sent through 25km of standard SMF. The ODN losses from power splitting are emulated by a variable optical attenuator (VOA) at the coherent RX input, that also adjust the received optical power for the target BER. The simulation results are mostly referred to BER = 10^{-3}, the FEC limit given in ITU-T Rec. 975.1. This FEC limit is assumed as the basis for sensitivity and penalty definition.

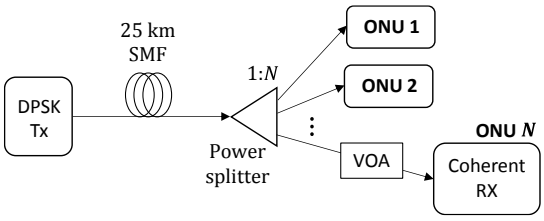

Figure 3.4. General setup for numerical simulation with DPSK at 1.25 Gb/s.

The direct DPSK TX in Fig. 3.5 emulates the direct phase modulation of a DFB. The CW optical carrier from the laser is modulated in phase by an ideal PM modulator, followed by an AM modulator driven by the high-pass equalized data needed for the direct phase modulation (see Section 2.4.2). It mimics the simultaneous intensity-chirp variations of the laser under injection current modulation. Data consist of pseudo-random binary sequences (PRBS) that are mapped into the electrical domain by a non-return-to-zero (NRZ) pulse shaper with $0.1T_b$ raise time. The mean emitted power is set to 0dBm. It is worth mentioning that for PRBS the differential encoding at the TX is not necessary because the differentially demodulated data are a time-delayed version of the transmitted PRBS.

At the RX side, the coherent front-end, i.e., the section of the RX that realizes the optical beating with the LO and the photodetection, is implemented by the two different architectures analyzed in Section 3.1 for PON: the 3x3 homodyne and the 2x2 heterodyne. Also, the conventional 90°

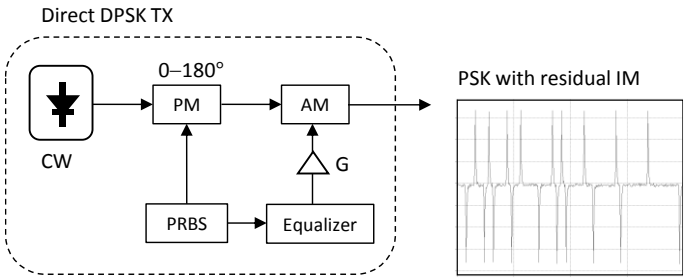

Figure 3.5. DPSK TX for simulation of the direct phase modulation. The inset shows the residual IM on the complex field envelope.

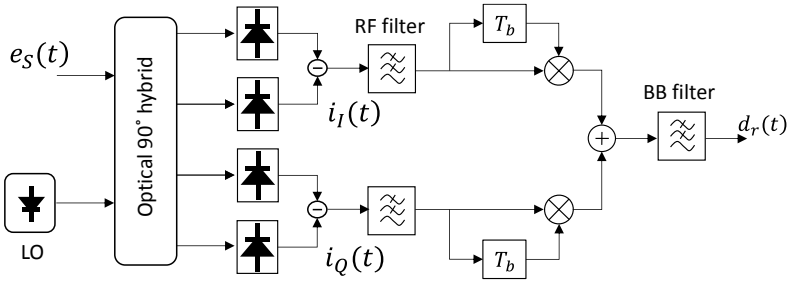

(a)

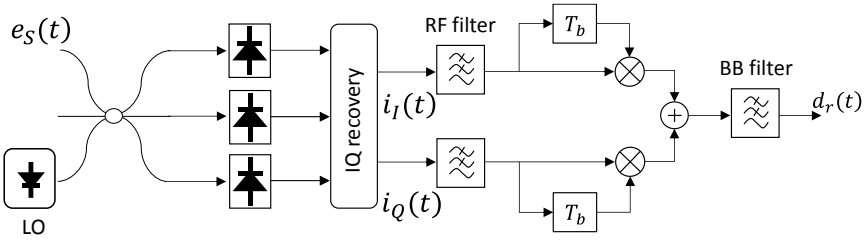

(b)

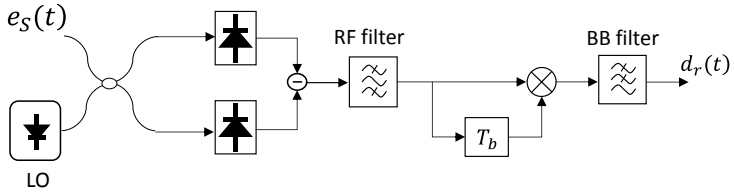

(c)

Figure 3.6. RX architecture for numerical simulation of the (a) 90º homodyne, (b) 3x3 homodyne, and (c) 2x2 heterodyne coherent DPSK RXs.

hybrid homodyne front-end is included as benchmark for performance evaluation. In the simulations, only one SOP is considered as the polarization matching is assumed to be addressed by polarization-diversity at the RX duplicating its architecture.

For the homodyne RXs, depicted in Fig. 3.6(a) and 3.6(b), the two photodetected currents corresponding to the I and Q components, are first low-pass filtered by the RF filter for out-band noise suppression. Next, the photocurrents are differentially demodulated each to extract the data

encoded in the phase of the optical carrier, then combined to overcome the phase mismatch due to the free-running LO, without PLL. Finally, the base-band (BB) signal is low-pass filtered for further noise suppression before the decision part of the RX. The RF and BB filters are 4^{th}-order Bessel filters because of their desirable linear-phase characteristics. In the heterodyne RX in Fig.3.6(c), the single photocurrent after balancing is first band-pass filtered by the RF filter, whose center frequency is set to the IF value. Then, the signal is differentially demodulated and low-pass filtered for noise suppression and rejection of second-order harmonics after the frequency down-conversion carried out by the differential demodulator. The LO is separated in λ from the Tx to obtain IF = $2R_b$.

The performance of each coherent RX is evaluated by computing the BER over the recovered data $d_r(t)$ by direct error counting. Table 3.1 summarizes the main simulation parameters; here, Δv represents the effective laser linewidth and RIN is the relative intensity noise.

Table 3.1. Summary of main parameters for Monte-Carlo simulation.

Device		**Parameter**	**Value**
General		Bit rate	1.25 Gb/s
		Sample rate	20 GSa/s
		Number of bits	2^{18}
		Modulation	DPSK
		Simulation method	Monte-Carlo
		Reference λ	1553 nm
TX	Laser	Output power	0 dBm
		RIN	-150 dB/Hz
		Δv	100 kHz
		Residual IM	1 dB
	Data generator	Data sequence	PRBS-7
	Pulse shaper	Format	NRZ
		Rise time	$0.1T_b$
ODN	Optical fiber	Type	SMF
		Length	25 km
		Attenuation	0.2 dB/km
		Dispersion	16 ps/(nm·km)
RX	LO	Output power	0 dBm
		RIN	-150 dB/Hz
		Δv	100 kHz
		IF	0 (homodyne) $2R_b$ (heterodyne)
		SOP	Adjusted to be matched
	Photodiode	Type	PIN
		Responsivity	1 A/W

First, the optimal cut-off frequency of the RF and BB filters for each RX is identified. Results are plotted in Fig. 3.7 in terms of the measured BER as a function of the filter BW normalized to the symbol time T_b.

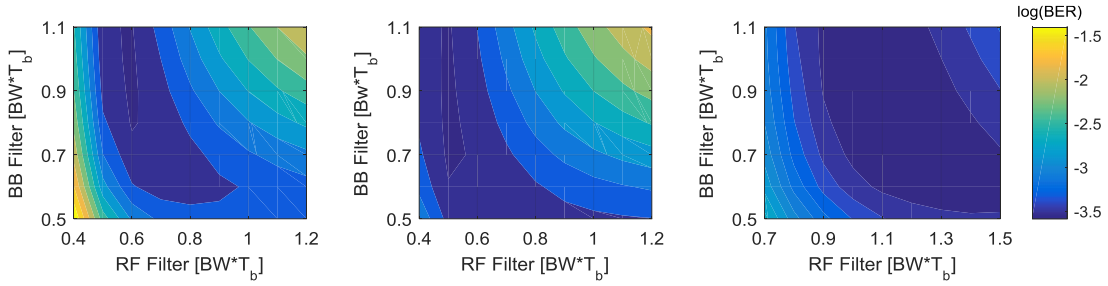

Figure 3.7. Filter BW optimization for the (a) 90º homodyne, (b) 3x3 homodyne and (c) 2x2 heterodyne coherent RXs.

For the 90° homodyne, plotted in Fig. 3.7(a), the optimal RF filter BW is found to be $0.6/T_b$, close to the conventional $0.75/T_b$ filtering, while the optimal BB filter BW ranges from $0.8/T_b$ to $1.1/T_b$. The 3x3 homodyne in Fig. 3.7(b) performs very similar to the previous one, with optimal RF filter BW = $0.55/T_b$, and BB filter BW ranging from $0.6/T_b$ to $1.1/T_b$. In the 2x2 heterodyne in Fig. 3.7(c), the optimal RF filter BW is about twice the homodyne RF filter BW, because of the two modulation side-lobes of the IF spectrum after heterodyning. The BB filtering behaves similar than that of homodyne RXs. For 1.25 Gb/s data rate, the optimal filter values are summarized in Table 3.2. These values are obtained from simulation with ideal frequency responses and absence of distortions; in practice, however, these values must be optimized in order not to incur on extra symbol distortion and ISI.

Table 3.2. Optimal 3dB filter BW for 1.25 Gb/s DPSK.

	Filter BW	
Receiver	**RF filter**	**BB filter**
90º homodyne	750 MHz	1.25 GHz
3x3 homodyne	700 MHz	1.25 GHz
2x2 heterodyne	1.5 GHz	1 GHz

After filter optimization, the RX sensitivity with DPSK at 1.25 Gb/s is evaluated. Results plotted in Fig. 3.8 indicate that, for a FEC limit of BER = 10^{-3}, the RX sensitivity reaches -58.5 dBm for both the 90° and the 3x3 homodyne architectures, that perform very similar. The 2x2 heterodyne RX exhibits 2.6 dB power penalty at FEC level when compared with the homodyne RXs, close to the expected 3 dB penalty from the heterodyne detection. These values are taken as a reference in next sections to evaluate de performance degradation due to transmission impairments.

3.2.1 Additive noise at the receiver

The high sensitivity achieved by the coherent RXs is ascribed to the boosting effect of the strong LO power. The limit sensitivity is determined by the amount noise generated at the optical-to-

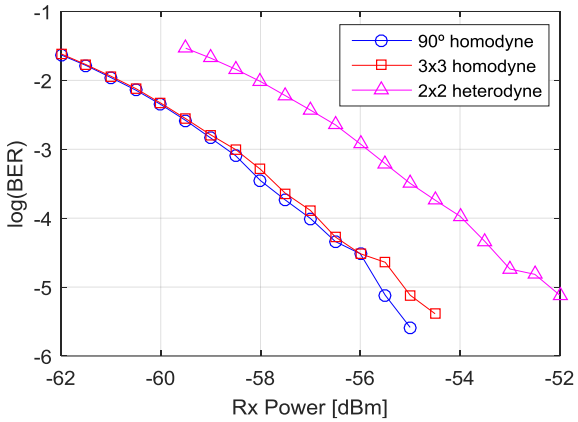

Figure 3.8. Coherent RXs sensitivity for 1.25 Gb/s DPSK, assessed by Monte-Carlo simulation.

electrical conversion in the photodetection stage. On the one hand, the shot noise originated by the quantum-nature of light, is linearly dependent on the incident optical power to the PDs after coherent beating, and it establishes the quantum-limit sensitivity as analyzed in Section 2.1.1. On the other hand, the most relevant thermal noise contribution is the noise generated by the transimpedance amplifiers (TIA) after photodetection [Zha12], employed to convert the photodetected current into voltage variations. The thermal noise, expressed in terms of the equivalent noise spectral density S_f in $\mathrm{pA}/\sqrt{\mathrm{Hz}}$, depends on the quality of the TIAs and the architecture of the coherent Rx, and specifically, in the number of photocurrent branches, as can be appreciated in Fig. 3.9 for the 90º homodyne, 3x3 homodyne and 2x2 heterodyne RX front-ends respectively.

To evaluate the impact of the thermal noise, isolating from other effects, let us first focus on the homodyne detection. Numerical simulation was done by using the coherent homodyne front-ends depicted in Figs. 3.9(a) and 3.9(b). The LO power was initially set to 0 dBm, in the region where

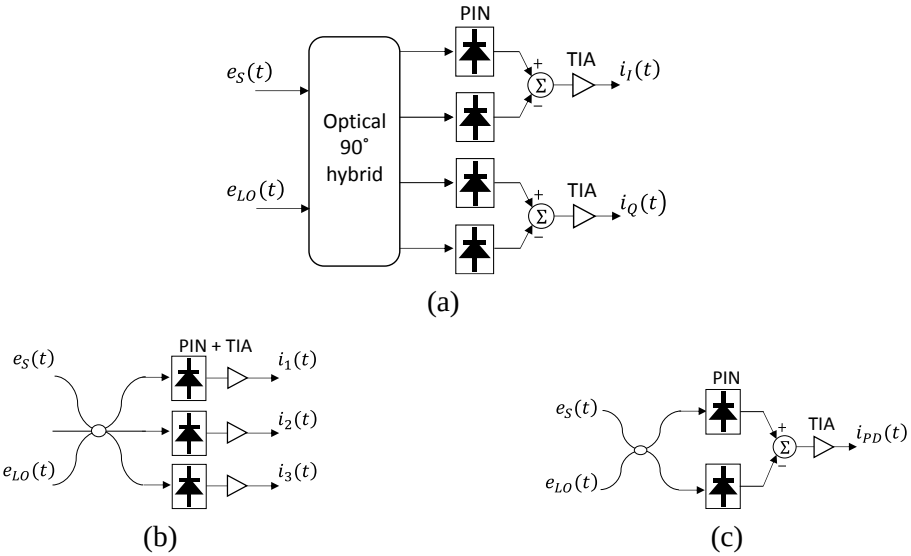

Figure 3.9. Coherent RX front-end for (a) 90º homodyne, (b) 3x3 homodyne and (c) 2x2 heterodyne.

the thermal noise still has influence on the SNR of the RX (see Fig. 2.3). The results are plotted in Fig. 3.10, in terms of the sensitivity penalty at BER = 10^{-3} as a function of the spectral noise density S_f. The 3x3 homodyne RX with three branches is slightly more sensitive to increments of the thermal noise factor than the 90° homodyne RX with two branches. For such constant LO power (0 dBm), the thermal noise factor increase that yields 1dB power penalty at BER = 10^{-3} is nearby 5 pA/$\sqrt{\text{Hz}}$ for both RXs. Note that the calculated penalty in Fig. 3.10 is relative to the case when the LO power is limited, but the thermal noise factor is 0 pA/$\sqrt{\text{Hz}}$, thus reaching the quantum-limit sensitivity in Fig. 3.8. Otherwise, as the thermal noise factor increases the power penalty increases as well. This dictates the RX sensitivity penalty when, in practice, the LO power is not strong enough due to HW constraints, with thermal noise factor spanning from 10 to 18 pA/$\sqrt{\text{Hz}}$ for commercial TIAs.

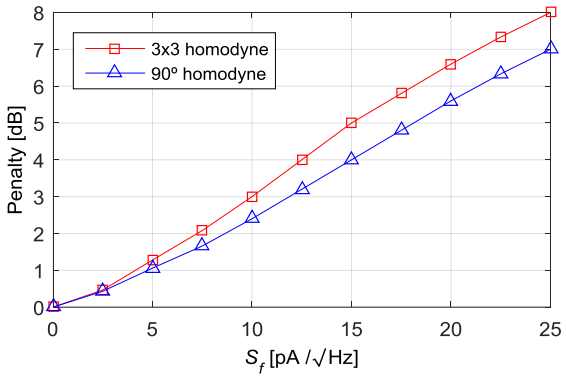

Figure 3.10. Sensitivity penalty at BER = 10^{-3} vs. thermal noise spectral density for homodyne RXs.

As stated in Section 2.1.1, for a given received optical power, with other parameters unchanged, the LO power can be adjusted to reach the quantum-limit sensitivity, limited only by the shot noise. Hence, a further simulation was carried out to establish the optimal LO power that minimizes the thermal noise effect, thus maximizing the SNR, for the coherent RXs in Fig. 3.9. The thermal noise spectral density was set to S_f = 12 pA/$\sqrt{\text{Hz}}$. Results are plotted in Fig. 3.11.

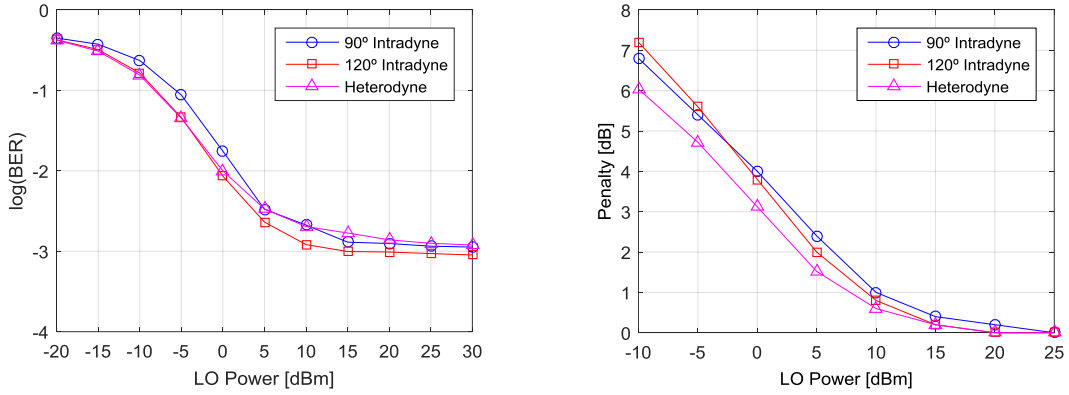

(a) (b)

Figure 3.11. (a) BER and (b) sensitivity penalty at BER = 10^{-3} against LO power, for thermal noise spectral density S_f = 12 pA/$\sqrt{\text{Hz}}$.

As observed in Fig. 3.11(a), the BER varies when sweeping the LO power, even if the received signal power keeps constant, as a consequence of the noise generated inside the coherent RX that dominates the ultimate RX sensitivity, reached for high LO power. In Fig. 3.11(b) the detriment of the BER is translated into sensitivity penalty at BER = 10^{-3}, showing that LO power >10 dBm ensures sensitivity penalty less than 1dB with respect to the quantum-limit sensitivity, for the three RX types. These results are in good agreement with theoretical values obtained from Fig. 2.3.

The LO power, however, must be carefully adjusted in practice according to the HW parameters. When the LO power increases, the undesired RIN from semiconductor lasers makes impact on the RX performance if the balancing of photocurrents is not ideal. The RIN relates to intensity fluctuations from spontaneous emission even if the bias current of the laser keeps constant. For ideal balanced detection, these power fluctuations are completely suppressed from the photodetected signal. In contrast, the RIN can be only partially suppressed when imperfect photocurrent balancing, and it becomes the dominant noise source at the RX for large LO power. The suppression ratio is determined by the common-mode rejection ratio (CMRR) of the balanced RX. For example, results in [Zha12] for a RIN value of −150 dB/Hz, the typical of DFBs, indicate that for CMRR > 25 dB the RIN has minimum impact and the system performance is close to that the ideal balanced RX in Fig. 3.11. Otherwise, for CMRR < 25 dB there is an optimum LO power between 8 and 12 dBm. These results very well match the simulations here.

3.3 Laser Phase and Frequency Error

Having in mind the strict requirements for PON in terms of complexity and cost, DFBs or vertical-cavity surface-emitting lasers (VCSELs) are the best solution as for optical sources in the udWDM scenario because of their low fabrication cost and mass production. Moreover, they allow for direct intensity/phase modulation, and thermal λ-tuning. Nevertheless, those benefits come at the cost of wide spectral linewidth and optical frequency drifts. This section evaluates the impact of the carrier phase fluctuations on phase modulated data, employing differential phase detection.

3.3.1 Impact of phase noise

Phase noise from a laser relates to its 3dB power spectrum bandwidth so-called laser linewidth $\Delta\upsilon$. It becomes a serious problem in coherent detection of phase modulated data, and eventually, the laser linewidth-symbol time product ($\Delta\upsilon T_b$) determines the feasibility and accuracy to recover the phase encoded symbols.

To analytically determine the impact of phase noise on the PSK signals, let us consider the case of BPSK with homodyne detection. Here, the phase noise is represented by the random variable ϕ and modeled as a Wiener-Lévy process [Kik12], i.e., a Gaussian process with zero-mean and variance

$$\sigma^2 = 2\pi\Delta\upsilon T_b \tag{3.1}$$

From Eq. (2.48), the decision variable at the RX for homodyne detection in presence of the phase error ϕ turns out to be

$$i_d(t) = 2\Re a(t)\sqrt{P_S P_{LO}}\cos\phi + n(t) \tag{3.2}$$

and the error probability in Eq. (2.50), assuming AWGN channel, becomes [Kaz96]

$$P_e{}' = \frac{1}{2} erfc\left(\sqrt{SNR}\cos\phi\right) \tag{3.3}$$

Now, the error probability is also dependent from the random process ϕ; therefore, the expression in Eq. (3.3) must be averaged over the statistics of ϕ, assumed to be Gaussian, yielding

$$P_e = \frac{1}{2\sqrt{2\pi}\sigma}\int_{-\infty}^{\infty} erfc\left(\sqrt{SNR}\cos\phi\right) e^{-\frac{\phi^2}{2\sigma^2}}\, d\phi \tag{3.4}$$

The integral in Eq. (3.4) was numerically evaluated by Gauss-Hermite quadrature rules [Ben02], and the results plotted Fig. 3.12 in terms of the error probability as a function of the SNR, for several phase-error standard deviation values. As observed, the fact of having a phase error different from zero leads to an error-floor, thus the error probability limit is a finite value independent from the SNR.

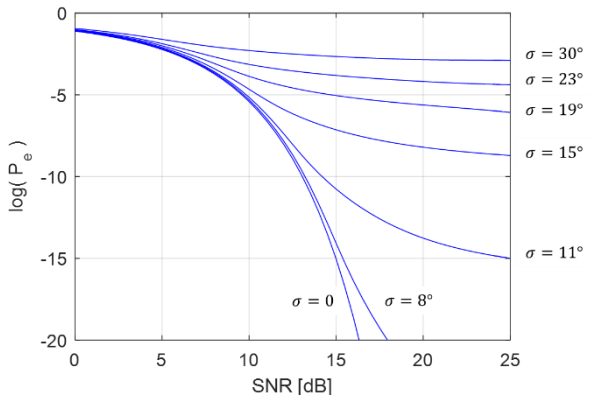

Figure 3.12. Error probability of homodyne BPSK for several phase-noise standard deviation values.

The phase-noise standard deviation (σ) values shown in Fig. 3.12 are useful to evaluate the limits of the BPSK modulation corrupted by phase noise. From Eq. (3.1) one can calculate the product $\Delta\upsilon T_b$, which denotes the maximum laser linewidth tolerance, for a given symbol rate and an error probability. Table 3.3 summarizes the σ values –and their corresponding $\Delta\upsilon T_b$ values– to produce 1 dB SNR penalty at several error probabilities. The equivalent error-floor is also computed for each case. For FEC limit ($P_e = 10^{-3}$), the phase noise tolerance at 1dB SNR penalty is found to be $\Delta\upsilon T_b = 0.018$, which means that, for 1.25 Gb/s bit rate, maximum 22.5 MHz total laser linewidth is tolerated. For m-ary PSK, with shorter distance between constellation symbols as m increases, the linewidth tolerance is correspondingly lower. Table 1 of [Pfa09] summarizes the maximum $\Delta\upsilon T_b$ for 1dB SNR penalty at BER = 10^{-3} with QAM constellations, indicating $\Delta\upsilon T_b = 4.1\times10^{-4}$ for QPSK as the best case.

Table 3.3. Standard deviation for 1dB SNR penalty at several BER values, and equivalent error-floor.

	1dB SNR Penalty Tolerance		
P_e	σ	$\Delta v T_b$	**Equivalent error-floor**
10^{-1}	30°	0.044	10^{-3}
10^{-3}	19°	0.018	10^{-6}
10^{-6}	15°	0.011	10^{-9}
10^{-9}	11°	0.006	10^{-16}

The phase noise effect can be observed in the detected constellation as a random rotation of the transmitted symbols. In asynchronous DPSK, such effect is mitigated at the RX by combination of phase-diversity detection and differential demodulation. For lower values of $\Delta v T_b$, the transmission rate is several orders of magnitude larger than the laser linewidth, and the extracted optical phase difference between two consecutive symbols only changes due to the modulation, getting rid of the phase noise contribution, and yielding a noiseless differentially-demodulated DPSK constellation. Otherwise, for higher values of $\Delta v T_b$ the phase noise contribution is not totally canceled by the differential demodulation, thus producing phase-widening of the DPSK symbols and power penalty at the detection. This behavior can be appreciated in Fig. 3.13, for high SNR.

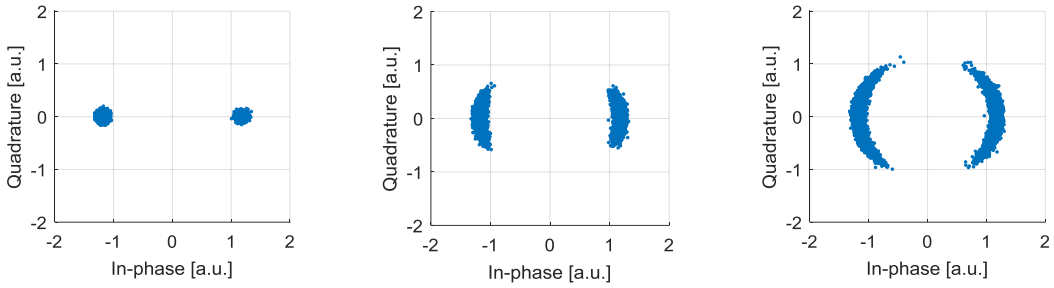

(a) (b) (c)

Figure 3.13. DPSK constellation after differential demodulation, for total laser linewidth of (a) 200 kHz, (b) 5 MHz and (c) 20 MHz.

To compute the BER degradation induced by the phase-noise in the udWDM-PON scenario, and the tolerable values, numerical simulation is carried out using the three coherent RXs in Fig. 3.6. Results are plotted in Fig. 3.14 in terms of the computed BER against the received optical power for several values of the total laser linewidth Δv, calculated as the TX + LO lasers linewidth. The three coherent RXs perform very similar, being the 2x2 heterodyne RX slightly more tolerant to the phase noise. At FEC limit of BER = 10^{-3}, the maximum tolerance for a sensitivity penalty less than 1dB is 20MHz total linewidth, representing a tolerance of 1.6% of the bit rate ($\Delta v T_b = 0.016$). This value well matches the theoretical prediction in Table 3.3, and is high enough to validate for the use of commercial DFBs, with linewidths in between 1 and 10 MHz.

Alternatives to the differential demodulation for optical phase recovery involve the use of DSP, like the well-known Viterbi & Viterbi feedforward phase estimation algorithm [Vit83]. In

addition, alternatives to simplify the phase-diversity architecture of the homodyne RX have also been proposed [Pra12].

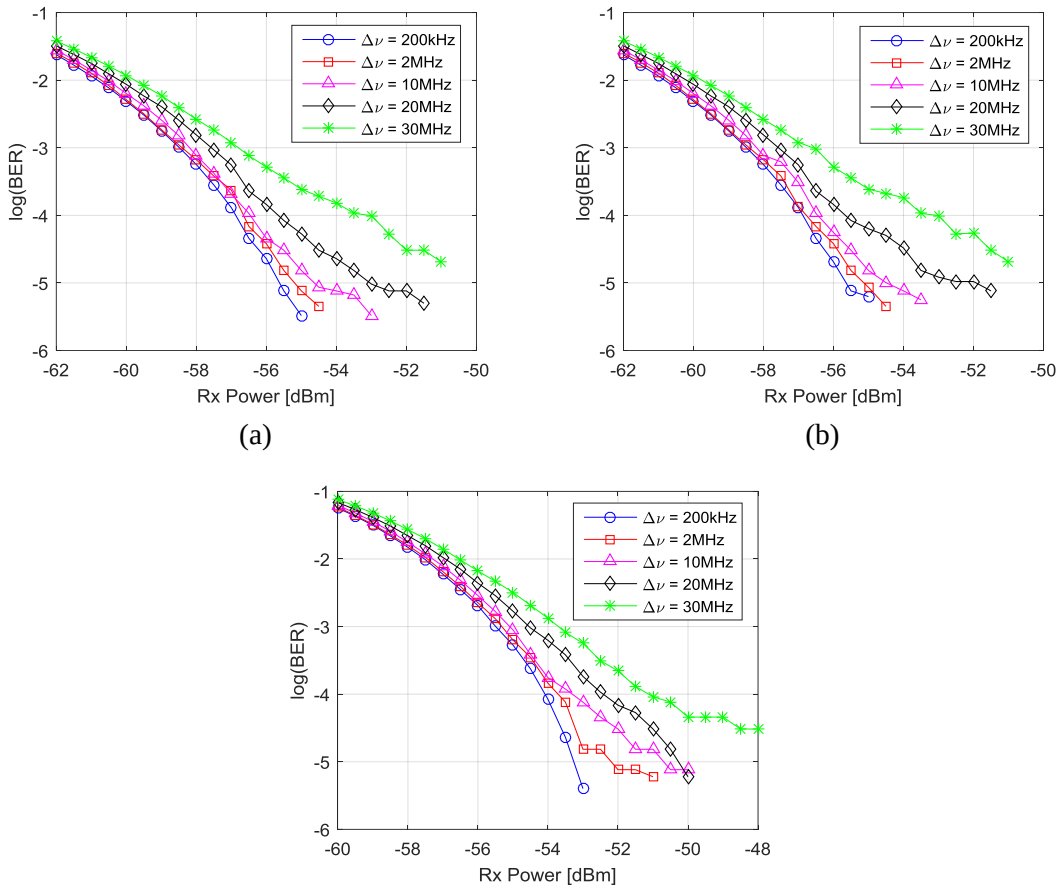

Figure 3.14. BER vs. received optical power at several total laser linewidths, for (a) the 90º homodyne, (b) the 3x3 homodyne and (c) the 2x2 heterodyne coherent RXs.

3.3.2 Impact of frequency detuning

The emitted lightwave from a laser is not only affected by random variations in the optical phase, as analyzed in previous section, but also by changes in the optical frequency ascribed to carrier density effects, temperature variations and laser aging. Regarding the latter, typical DFBs exhibit frequency accuracy of about ±2.5 GHz over lifetime [Tao07]. These frequency drifts cause strong impact on the performance of coherent detection, that features the beating of the received signal with the LO at a precise λ. Moreover, the optical frequency drifts become a major issue in udWDM-PON where hundreds of λs are closely allocated in a dense spectral distribution, as narrow as 6.25 GHz spacing, producing interference between adjacent channels. Accordingly, in homodyne RXs the IF –the frequency mismatch between the TX and LO lasers– must be as low as possible. For the heterodyne RX, when detecting DPSK the IF is properly set as an integer multiple of the transmission rate for optimal detection, as pointed out in Section 2.3.2. Any undesired frequency drift causes system performance degradation and must be corrected.

To understand the effect of frequency drifts on the coherently detected signal, let us refer back to the I and Q components of the homodyne RX in Eqs. (2.17) and (2.18) respectively, which in complex format I+jQ read as

$$r(t) = \Re\sqrt{P_S P_{LO}}\, e^{j(\omega_{IF} t + \phi_\Delta(t))} \tag{3.5}$$

Here, $\omega_{IF} = 2\pi f_{IF}$ is the frequency mismatch, and $\phi_\Delta(t)$ stands for the optical phase difference between TX and LO lasers, comprising both the modulated data and the phase-noise. To extract the phase encoded data, the signal $r(t)$ is differentially demodulated as indicated in Fig. 2.17(b) for complex signals, obtaining

$$s(t) = \Re^2 P_S P_{LO}\, e^{j(\omega_{IF} T_b + \phi_\Delta(t) - \phi_\Delta(t-T_b))} \tag{3.6}$$

For phase-noise values much lower than the symbol rate, the phase term $\phi_\Delta(t) - \phi_\Delta(t - T_b)$ contains the demodulated symbols without phase noise. Note that the presence of the IF produces a fixed incremental phase rotation of the PSK symbols, proportional to $\omega_{IF} T_b$, as represented in Fig. 3.15 for DPSK. The phase rotation of the detected DPSK constellation at 1.25 Gb/s in Fig. 3.15(c), for 200 MHz frequency detuning, corresponds to 57.6º.

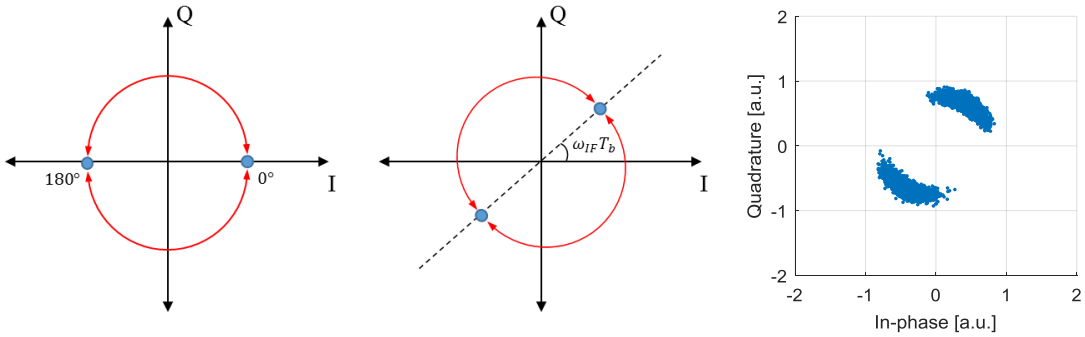

(a) (b) (c)

Figure 3.15. Phase rotation of the DPSK constellation after differential demodulation as a consequence of laser frequency detuning. (a) Ideal frequency matching; (b) DPSK with frequency detuning; (c) example of a detected DPSK constellation for 200 MHz frequency detuning and 10 MHz total linewidth.

Numerical simulation is carried out on the three coherent RXs to determine the tolerance to frequency detuning. For the homodyne RXs, the LO λ is separated from the TX λ yielding the frequency detuning denoted by f_{IF}. In the heterodyne RX, the LO λ is already separated from the TX λ by $f_{IF} = 2R_b$ (2.5 GHz), then Δf_{IF} denotes the frequency detuning with respect to f_{IF}. Results plotted in Fig. 3.16 indicate that, at BER = 10^{-3} FEC limit, maximum 75MHz frequency detuning is tolerated by the three RXs, for less than 1 dB sensitivity penalty. This represents 6% of the bit rate, imposing some design challenges and revealing the need of AFC systems when working with commercial DFBs. Chapter 5 addresses the design and implementation of AFC systems by either DSP-based frequency estimation, or frequency discrimination employing analog HW. Strategies for λ-control of the LO are also discussed.

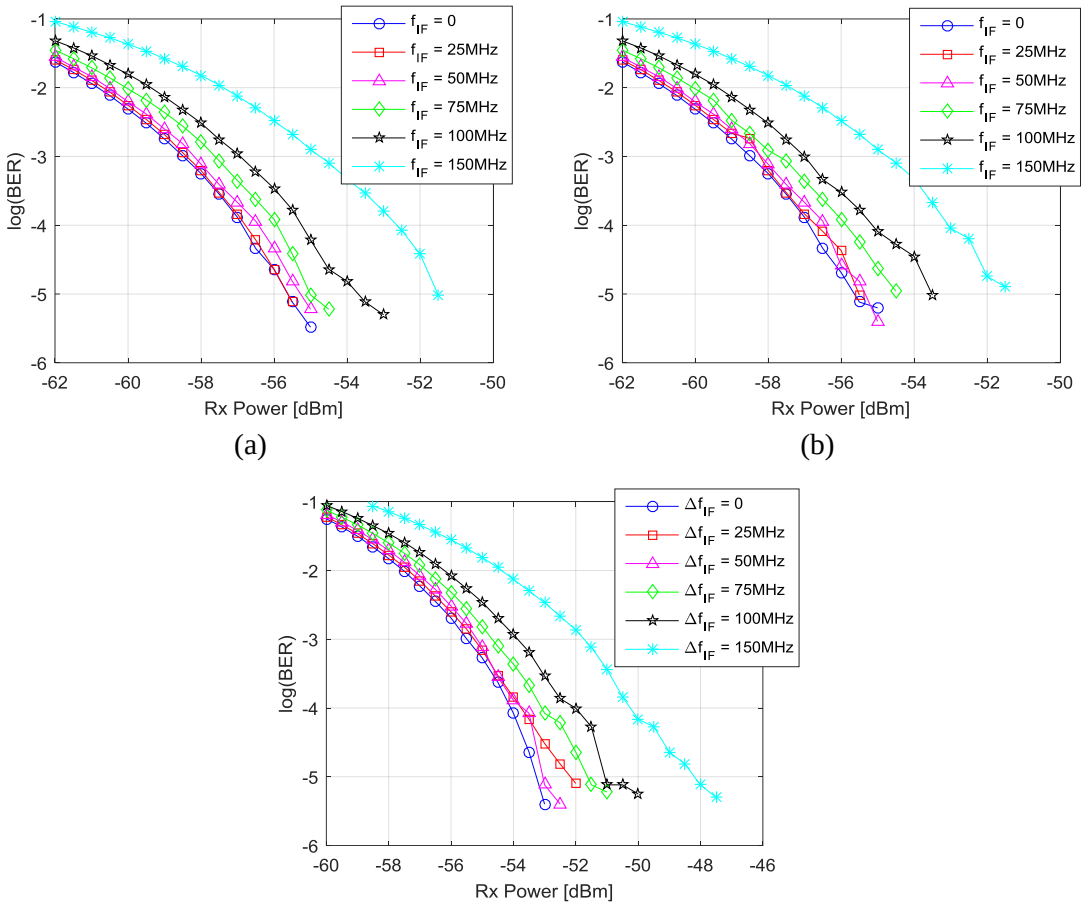

Figure 3.16. BER vs. received optical power for several TX-LO frequency detuning values; (a) 90º homodyne, (b) 3x3 homodyne, and (c) 2x2 heterodyne coherent RXs.

3.4 Inter- and Intra-Channel Crosstalk

Crosstalk is the general term given to the undesired effect caused by other signals on the transmitted signal. Multiple factors in the udWDM system introduce crosstalk, as the HW components (optical connectors, fiber nonlinearities, λ-multiplexers, etc.), or the network design (channel spacing, spectral management, λ-allocation, etc.). Two forms of crosstalk arise in the udWDM system: interchannel and intrachannel crosstalk. The first case, interchannel crosstalk, occurs when the λ-difference between the desired signal and the crosstalk signal is larger than the electrical BW of the coherent RX. Conversely, the intrachannel crosstalk occurs when both the crosstalk and the desired signal are at the same λ, or sufficiently close in a way that the λ-difference falls within the RX BW. This form of in-band crosstalk is also known as coherent crosstalk, and is usually more severe than the out-band interchannel crosstalk.

This section analyzes the inter- and intra-channel crosstalk in the udWDM-PON originated from adjacent channels in the closely spaced optical grid, as well as from optical reflections due to optical components with limited isolation. The crosstalk caused by the optical fiber through the nonlinear effects is not considered since the individual λs of the PON operate below the power threshold for the Kerr-like nonlinearities, as stated at the beginning of the chapter.

3.4.1 Crosstalk by adjacent udWDM channels

In the udWDM-PON, the management of the available optical BW is optimized by using very narrow channel spacing to accommodate many users on a single fiber. The high selectivity of the coherent RXs, by combination of LO λ-tuning and sharp electrical filtering, is the enabling technique to allocate the WDM users in ultra-dense grid configuration. This contrasts with conventional IM-DD systems for PON that employ optical filters and require much larger channel separation. For instance, NG-PON2 implements 50 or 100 GHz spacing between individual λs at 2.5–10 Gb/s.

A major concern, however, is that unwanted optical power from modulated side-lobes may cause interference to adjacent channels in such a closely spaced udWDM grid, producing BER degradation. This kind of interchannel crosstalk can be mitigated by electrical pulse-shaping at the TX to compact the modulated spectrum, thus reducing its BW and further suppressing the ISI. Two widespread pulse-shaping filters for communications are the Raised-cosine and the Gaussian filters, which are analyzed in what follows.

3.4.1.1 Raised cosine pulse-shaping

The raised cosine is a type of Nyquist filter that allows to adjust the excess filter BW beyond the Nyquist BW ($R_b/2$) through the roll-off parameter (β), that ranges between 0 and 1. The frequency response of the raised cosine filter is given by

$$N(f) = \begin{cases} 1, & |f| \le (1-\beta)\dfrac{R_b}{2} \\ \dfrac{1}{2}\left[1+\cos\left(\dfrac{\pi}{\beta R_b}[|f|-(1-\beta)R_b]\right)\right], & (1-\beta)\dfrac{R_b}{2} \le |f| \le (1+\beta)\dfrac{R_b}{2} \\ 0, & \text{elsewhere} \end{cases} \quad (3.7)$$

The lower is β the lower is the total filter BW and the higher the spectral compactness. The BW of the raised cosine filter as a function of β becomes: $\text{BW} = (1+\beta)\,R_b/2$. As β tends to cero, the magnitude of $N(f)$ in Eq. (3.7) approaches the rectangular function with a sharp cut-off frequency at $R_b/2$. This behavior is shown in Fig. 3.17.

In communication systems, it is found to be advantageous filtering the information signal, at both the TX and the RX side, using the same filter response. This technique is known as matched filtering, and optimizes the detection by totally cancelling the out-band noise and lowering the ISI at most. The method to achieve matched filtering with the raised cosine filter consist of taking the square root of the raised cosine frequency response $N(f)$ and using this new filter response $\sqrt{N(f)}$ in the TX and the RX. This is the so-called root raised cosine filter. When the TX and RX filters are cascaded, one gets a raised cosine filter transfer characteristic of the overall system.

Nonetheless, if the primary objective of the pulse shaping is to compact the modulated spectrum to avoid interference to adjacent channels, the raised cosine filtering can be applied at the TX side

only, thus lowering the complexity of the RX that implements standard low-pass filtering for noise suppression. This comes at the cost of a small power penalty at the detection due to the signal distortion and extra ISI induced by the unmatched TX–RX filtering.

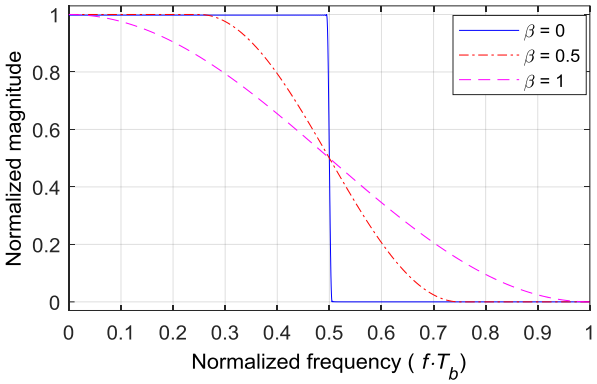

Figure 3.17. Magnitude spectra of the raised cosine filter $N(f)$ for several roll-off values

3.4.1.2 Gaussian pulse-shaping

The second method for pulse shaping consist of passing the NRZ binary data sequence through a filter whose impulse response is the Gaussian function. The result is that the sharp symbol transitions are smoothed into Gaussian dynamics, with a rise-time t_r dependent from the 3 dB BW of the filter, here represented by B. The rise time is defined as the elapsed time from 10% to 90% of the rising edge of symbols, and relates to the filter BW by: $B = 0.35/t_r$. The frequency response of the Gaussian filter is given by

$$G(f) = e^{-\left(\frac{\ln(2)}{2}\frac{f^2}{B^2}\right)} \tag{3.8}$$

The Gaussian pulse-shape is typically used in systems for radio, as in Gaussian-filtered minimum shift keying (GMSK) transmission, to suppress the high frequency components of the transmitted spectrum. The setup in Fig. 3.18(a) was used to evaluate the trade-off between spectral compactness and signal distortion introduced by the narrow filtering, thus giving the optimal filter BW.

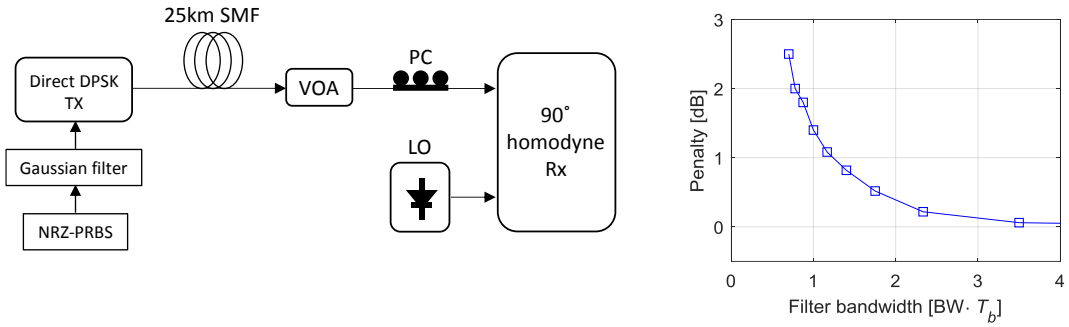

(a) (b)

Figure 3.18. (a) Simulation setup for DPSK TX with Gaussian pulse shaping before optical modulation; (b) sensitivity penalty at BER = 10^{-3} against the normalized Gaussian filter BW.

PRBS data sequences with NRZ pulse-shape passed through the Gaussian filter prior to the optical modulation. The generated Gaussian PSK signal was detected by the 90º homodyne RX, as reference. The input power was adjusted to obtain BER = 10^{-3} for the case of NRZ data without Gaussian filtering, then the power penalty due to the BW of the Gaussian filter was computed and plotted in Fig. 3.18(b). The results indicate that the sensitivity penalty raises to 1 dB for BW = $1.2/T_b$, which in terms of the rise time yields $t_r = 0.29T_b$.

3.4.1.3 Minimum channel spacing in udWDM-PON

To evaluate the benefit of electrical pulse-shaping at the TX on the mitigation of crosstalk by adjacent channels, numerical simulation was carried out using the setup depicted in Fig. 3.19(a) to determine the minimum channel separation in the udWDM grid. The setup consisted of two users, one of them at a fixed λ_1, and the other passing through by sweeping ±7.5 GHz with respect to λ_1, as illustrated in Fig. 3.19(b). The channel to be detected modulated PRBS-7, whereas the interference channel modulated PRBS-15 for uncorrelated data. The emission power was set to 0 dBm for both users, that were later combined in a 3 dB optical coupler, propagated through 25 km of SMF, and detected by a 90º homodyne Rx. The LO of the RX was tuned to detect λ_1, and the received optical power adjusted to obtain BER = 10^{-3} for the case of single channel.

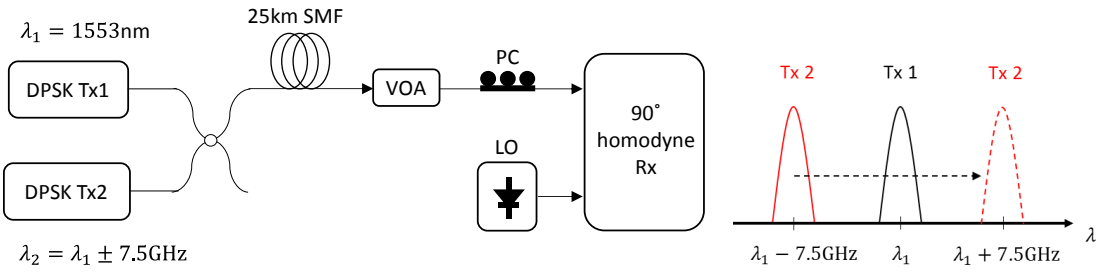

(a) (b)

Figure 3.19. (a) Simulation setup to evaluate the crosstalk by adjacent channel in the udWDM-PON; (b) Optical spectra for the λ-sweep of User 2 with respect to User 1.

At the TX, bits from PRBS sequences are mapped into the electrical domain by the pulse-shaping filter, and the resulting electrical signal drives the optical DPSK modulation at 1.25 Gb/s. Three pulse shapes were considered for the simulation: pure NRZ, Gaussian and raised cosine. The BW of the Gaussian filter was set to BW = $1.2/T_b$, corresponding to $t_r = 0.29T_b$, and derived from Fig. 3.18(b) for maximum 1 dB sensitivity penalty. For the raised cosine filter, the roll-off was first set to $\beta = 1$, then the BW = $1/T_b$. In both cases, the BW of the pulse-shaping filter was properly selected to reduce the secondary modulation lobes at most, without producing excessive BER degradation. To only translate the filter complexity to the TX side, the RX implements standard low-pass Bessel filtering for noise suppression. Table 3.4 summarizes the main pulse-shaping filter parameters, and depicts the electrical spectrum and the eye diagram of the electrical signal at the filter output.

Table 3.4. Electrical spectra and eye diagram for PRBS data at 1.25 Gb/s, for three different pulse-shaping filters implemented at the TX.

Pulse-shaping filter	**Electrical spectrum**	**Eye diagram**
NRZ $t_r = 0.1T_b$	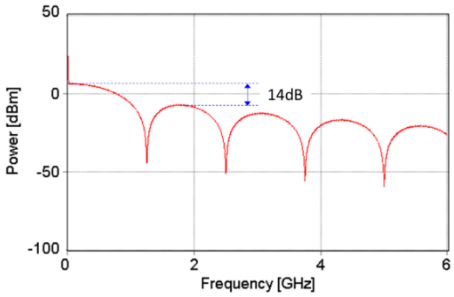	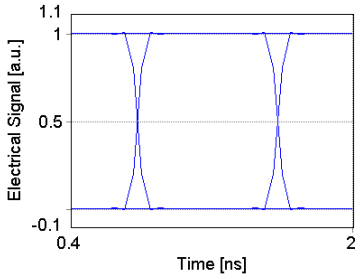
Gaussian BW = $1.2/T_b$ $t_r = 0.29T_b$	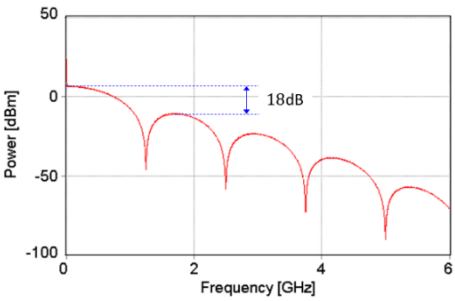	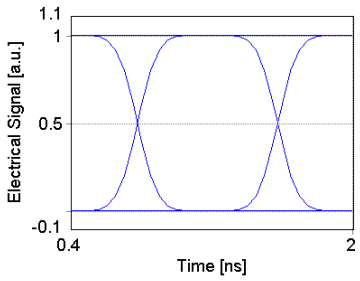
Raised cosine BW = $1/T_b$ $\beta = 1$	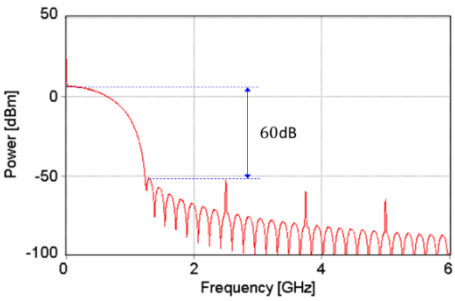	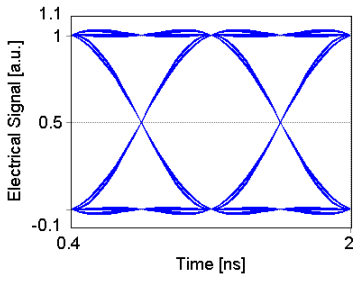

The main conclusions of Table 3.4 are as follows. In the case of NRZ data, with $t_r = 0.1T_b$, the sharp symbol transitions resulted in high-frequency harmonics of the spectrum, with significant power beyond the 1.25 GHz data BW, and 14 dB suppression of the main modulation lobe with respect to the secondary lobe. By applying Gaussian filtering the sharp symbol transitions are smoothed and more of the power is now close to the data BW, enhancing the secondary lobe suppression up to 18 dB, and reducing the power of the rest of harmonics. When raised cosine filtering is applied, the electrical pulses in the time domain adopt the sinc (cardinal sine) shape, and all the signal power is now within the data BW, with more than 60 dB suppression over the residual harmonics of the spectrum.

Next, optical DPSK modulation at 1.25 Gb/s takes place. After modulation, though, the same spectral distribution and secondary-lobe suppression obtained in the electrical domain in Table 3.4, are not expected to be achieved in the optical domain due to the non-linear characteristic of the phase modulation, which exhibits strong Bessel harmonic dynamics influencing on the modulated optical BW [Hay01]. Table 3.5 shows the obtained optical DPSK spectra for two users separated by 6.25 GHz. First, the optical DPSK modulation with NRZ data reveals 12 dB

suppression over the secondary lobes that potentially lead to interchannel crosstalk in the udWDM grid. Second, DPSK modulation by Gaussian-shaped signals increases by 1 dB the secondary lobe suppression, and the total spectral width per user is lowered. Last, the raised cosine filtering enhances the secondary-lobe suppression of the DPSK spectrum up to more than 19 dB, and the harmonics at higher frequencies have been completely suppressed.

Table 3.5. Optical spectra of two DPSK users at 1.25 Gb/s separated by 6.25GHz, for three different pulse-shaping filters implemented at the TX.

Pulse-shaping filter	**Two-channel optical spectra**
NRZ $t_r = 0.1T_b$	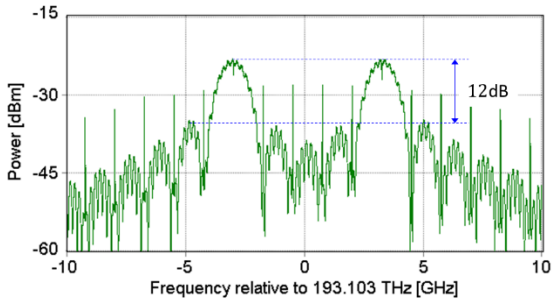
Gaussian BW = $1.2/T_b$ $t_r = 0.29T_b$	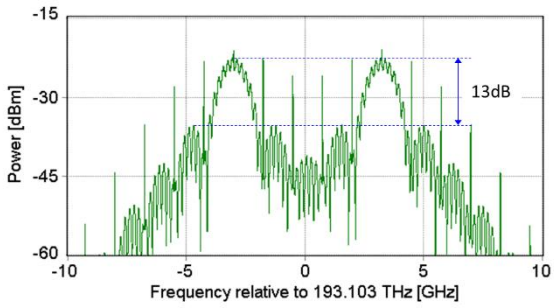
Raised cosine BW = $1/T_b$ $\beta = 1$	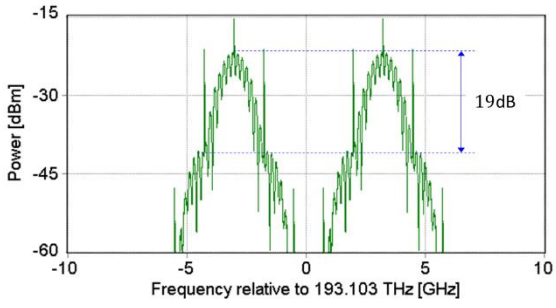

It is worth mentioning that reducing the roll-off parameter (β) of the raised cosine filter does not increase the secondary-lobe suppression nor lower the modulated optical BW achieved in Table 3.5, because of the non-linear phase modulation. Further details and experimental verification are provided in Section 3.4.1.5.

Next, the minimum channel spacing between udWDM users was evaluated by computing the sensitivity penalty at BER = 10^{-3} as a function of channel separation, for the three different pulse-shaping filters at the TX and homodyne detection at the RX. Results are presented in Fig. 3.20. Not surprisingly the raised cosine pulse-shape outperforms the NRZ and Gaussian filtering as the

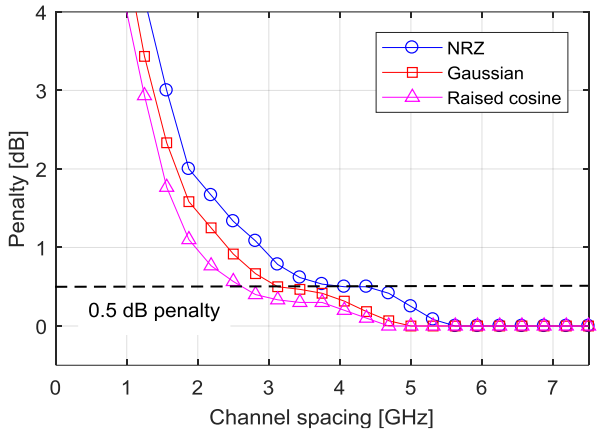

Figure 3.20. Sensitivity penalty at BER = 10^{-3} against channel separation between udWDM users at 1.25 Gb/s with homodyne detection.

channel spacing decreases, because of the lowest modulated optical BW and the highest secondary-lobe suppression achieved in Table 3.5. Notably, the minimum channel spacing for a sensitivity penalty of 0.5 dB only, is found to be 4 GHz, 3.1 GHz and 2.6 GHz for the NRZ, Gaussian and raised cosine pulse-shape respectively, validating for the implementation of the udWDM grid with ultra-narrow channel spacing.

Note that the power penalty in Fig 3.20 was computed from a single interfering channel; in practice, however, every single channel in the udWDM experiences crosstalk from two adjacent users at each side, as illustrated in Fig. 3.21 for three channels at the same power. P_I denotes the crosstalk power.

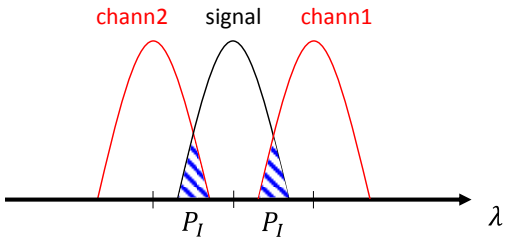

Figure 3.21. Crosstalk from two adjacent users in the udWDM-PON with narrow channel spacing.

In order to relate the power penalty found for a single interferer to that of two interfering users, let us define $\Delta P^{(1)}$, $\Delta P^{(2)}$ as the power penalty for one and two adjacent channels respectively, calculated as

$$\Delta P^{(k)}{}_{dB} = 10log_{10}(c_k) \tag{3.9}$$

for $k = 1, 2$. Here c_k represents the power scaling factor translating into the power penalty. In the absence of adjacent channels, $SNR = P_S/P_N$ is the basic definition SNR at the RX that dictates the BER of the system, with P_S and P_N the received signal power and the noise power respectively. On the other hand, the SNR at the RX in presence of crosstalk from one or two adjacent channels becomes

$$SNR^{(k)} = \frac{c_k P_S}{P_N + c_k(kP_I)} \tag{3.10}$$

The power penalty factor c_k scales the optical power reaching the RX thus affects P_S and P_I, but not P_N since in coherent detection the dominating noise source at the RX is the shot noise from the strong LO power, and P_N is independent from the received power, as examined in Section 2.1.1. For a given BER, one may find the power penalty factor c_2 for two interfering users that keeps constant the reference SNR, by equating the Eq. (3.10) for $k = 2$ to the single-channel $SNR = P_S/P_N$, yielding

$$c_2 = \frac{P_N}{P_N - 2P_I} \tag{3.11}$$

and expressed in dBs from Eq. (3.9) as

$$\Delta P^{(2)}{}_{dB} = 10log_{10}\left(\frac{P_N}{P_N - 2P_I}\right) \tag{3.12}$$

Similarly, the crosstalk power P_I can be expressed in terms of the power penalty factor c_1 for one adjacent user, by equating the Eq. (3.10) for $k = 1$ to the reference single-channel $SNR = P_S/P_N$, obtaining

$$P_I = \frac{P_N(c_1 - 1)}{c_1} \tag{3.13}$$

By replacing Eq. (3.13) into Eq (3.12), one gets

$$\Delta P^{(2)}{}_{dB} = P_{N\,dB} - 10log_{10}\left(P_N - \frac{2P_N(c_1 - 1)}{c_1}\right) \tag{3.14}$$

that yields

$$\Delta P^{(2)}{}_{dB} = \Delta P^{(1)}{}_{dB} - 10log_{10}\left(2 - 10^{\left(\Delta P^{(1)}{}_{dB}/10\right)}\right) \tag{3.15}$$

Eq. (3.15) is a useful expression to determine the power penalty from two adjacent channels emitting at the same power, using the power penalty calculated from only one adjacent channel, and independently from the SNR or the modulation format. Graphically, the relationship is depicted in Fig. 3.22. As observed, for single-interferer power penalties lower than 1dB, there is a linear relationship (slope = 2.14) with the penalty for two adjacent users. This means that the calculated channel spacing in Fig. 3.20 for 0.5 dB sensitivity penalty and a single interferer, translate into about 1 dB penalty when two users generate crosstalk at each side. Table 3.6 summarizes the minimum channel spacing found.

Taking as reference the 50/100 GHz spaced WDM grid defined in NG-PON2 [ITU19], the channelization of the proposed udWDM-PON is found to be as low as 6.25 GHz for residential users at 1.25 Gb/s. This value was selected as the lowest integer divisor of the standardized 50 GHz NG-PON2 grid that satisfies the required minimum channel spacing in Table 3.6. In the case

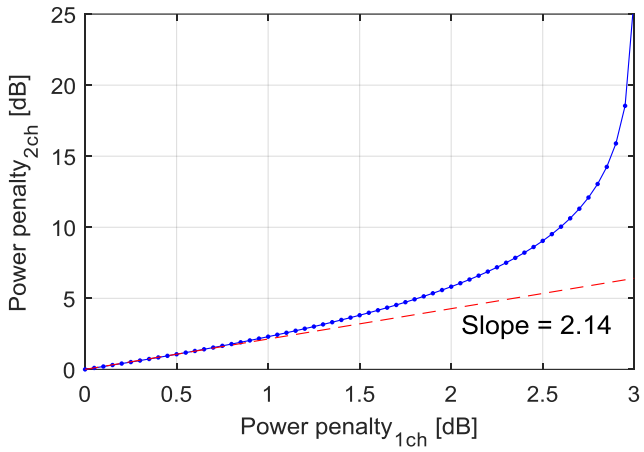

Figure 3.22. Relationship between the power penalty for two interfering users and the power penalty for a single interferer.

of heterodyne RXs, the defined channel spacing is twofold, i.e., 12.5 GHz, in order to allocate for the image frequency of the heterodyne detection located at 2×IF. The minimum 6.25 GHz channel spacing found for the udWDM-PON provides for full backward compatibility with legacy PON systems (G-PON, XG-PON, TWDM-PON) and allows to exploit narrow spectral windows where no other communication systems are allocated.

Table 3.6. Summary of pulse-shaping filters performance for DPSK at 1.25 Gb/s, with closely spaced udWDM channels and homodyne detection.

Pulse shaping	**Optical secondary lobe suppression**	**Minimum channel spacing for 1dB power penalty tolerance**
NRZ	12 dB	4 GHz
Gaussian	13 dB	3.1 GHz
Raised cosine	19 dB	2.6 GHz

3.4.1.4 Laser side-modes

Another highly relevant characteristic of semiconductor lasers based on optical cavities is that they generate light at several spurious λs around the central λ. Typical lasers for optical communication systems exhibit side-modes separated by ~150 GHz (1.2 nm) with respect to the central λ. Also, the power difference between the main and side modes of the laser is over 30 dB, denoted by the side-mode suppression ratio (SMSR) parameter. These side-modes are close enough to generate crosstalk on other users in the udWDM-PON, that implements up to 256 λs spaced by minimum 6.25GHz, for a total optical band covering 12.8nm. The optical spectrum in Fig. 3.23 illustrates the potential interference of the laser side-modes on the other PON users. The power difference between one channel and the overlapped spurious λ is represented by the signal-to-interference ratio (SIR).

To determine how variations in the SMSR of one of the channels affect the performance of other channel located at the same λ then the interfering side-mode, further simulation was carried out using the same setup and parameters in Fig. 3.19(a), but in this case, the two DPSK TXs emit at the same λ for total spectral overlap ($\lambda_1 = \lambda_2$), as the worst case. It is worth mentioning that the interfering λ_2 was also modulated because, in practice, the side-modes exhibit approximately the same spectral shape than the main laser mode [Pet88]. The output power of the transmitted channel λ_1 was set to 0dBm, whereas the interfering λ_2 power was variable to adjust the SIR.

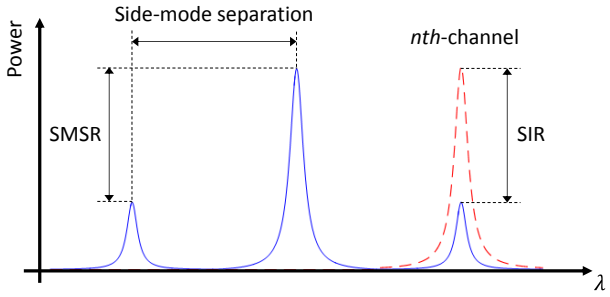

Figure 3.23. Optical spectrum of a single-mode laser with spurious side-modes generating crosstalk on adjacent udWDM channels.

First, the BER against the received optical power was computed for several SIR values, and plotted in Fig. 3.24(a). As the SIR decreases, the laser side-modes crosstalk causes BER degradation and produces error-floor on the channel located at the same λ than the spurious side mode. Fig. 3.24(b) depicts the sensitivity penalty at BER = 10^{-3} in terms of the SIR, revealing that the crosstalk power must be at least 18 dB lower than the transmitted power to avoid penalties larger than 1 dB. This value serves as reference to determine the required SMSR for the lasers in the udWDM-PON, to avoid severe interference on adjacent channels. Note that in the udWDM scenario, the side-modes crosstalk originates from not only one but two far channels located at the same λ-difference from the user λ, but in opposite sides. Hence, extra 3 dB tolerance should be added to the SMSR limit, as the worst case. Furthermore, all the udWDM channels do not emit at the same power, being allowed 15 dB maximum power difference between λs [ITU19] that should be considered as well.

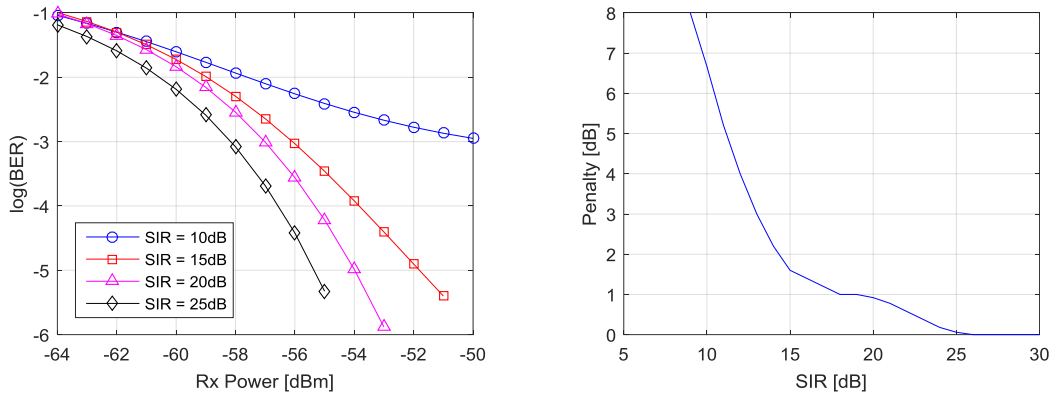

(a) (b)

Figure 3.24. (a) BER as a function of the received power for several SIR, and (b) sensitivity penalty at BER = 10^{-3} for the same test.

Accordingly, SMSR = 36 dB is considered an appropriate value to mitigate the crosstalk by laser side-modes, in the margin of the available technology for optics. Another interesting remark that can be derived from the simulations is that, during the activation process of new ONUs connecting to the PON, it is necessary to attenuate the output power of the TX during its λ transition, in at least 18 dB with respect to its nominal emission power, to avoid BER degradation on the already active channels in the PON.

3.4.1.5 Experimental assessment of channel spacing in udWDM-PON

The udWDM system was implemented to experimentally verify the pulse shaping effect on the mitigation of adjacent channel crosstalk, and the minimum channel separation in the udWDM-PON found by numerical simulation. The experimental setup is depicted in Fig. 3.25, and consisted of two identical TXs (TX1 and TX2) based on directly-modulated DFBs, with 4 MHz and 3 MHz linewidth respectively, and modulated by two uncorrelated PRBS sequences. The RZ-shapers perform the time-derivative of the NRZ data for direct phase modulation, as pointed out in Section 2.4.2, followed by the raised cosine filters for Nyquist spectral shaping. After 25 km of SMF, the signal was detected by the 3x3 homodyne RX introduced in Fig. 3.6(b), that implemented a 100 kHz linewidth ECL as LO, and emitting at 0 dBm. The LO λ was tuned to detect TX1. No matched filtering at the RX is considered to lower the overall ONU complexity.

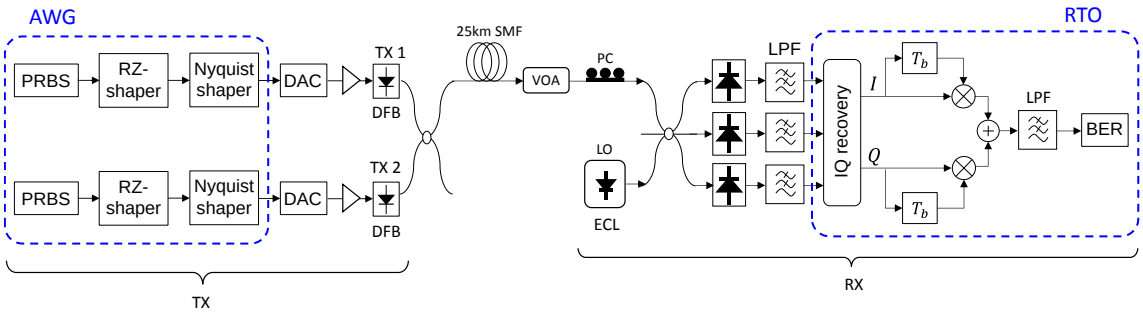

Figure 3.25. Experimental setup to evaluate the pulse-shaping impact on the minimum channel spacing between udWDM users. AWG: arbitrary waveform generator; RTO: real-time oscilloscope.

The eye diagram and time-domain waveforms of the direct-DPSK modulating current are plotted in Fig. 3.26, for 50% duty-cycle RZ signal with and without Nyquist filtering. It is worth noting that in direct phase modulation, data symbols with zero phase-shift apply no current swing to the laser during the symbol time T_b producing zero-crossing in the eye diagram of the laser driving current, as appreciated in Fig. 3.26(a).

An important outcome is that the Nyquist filtering eliminates the modulation side-lobes, but the filter roll-off has no impact on the width of the main modulation-lobe because of the non-linear PM modulation, as stated before. This phenomena can be appreciated in Fig. 3.27 that plots the experimental photodetected spectra for DPSK at 2.5 Gb/s, centered at 10 GHz, for two roll-off values of the Nyquist filter. Observe that the width of the main PM modulation-lobe remains

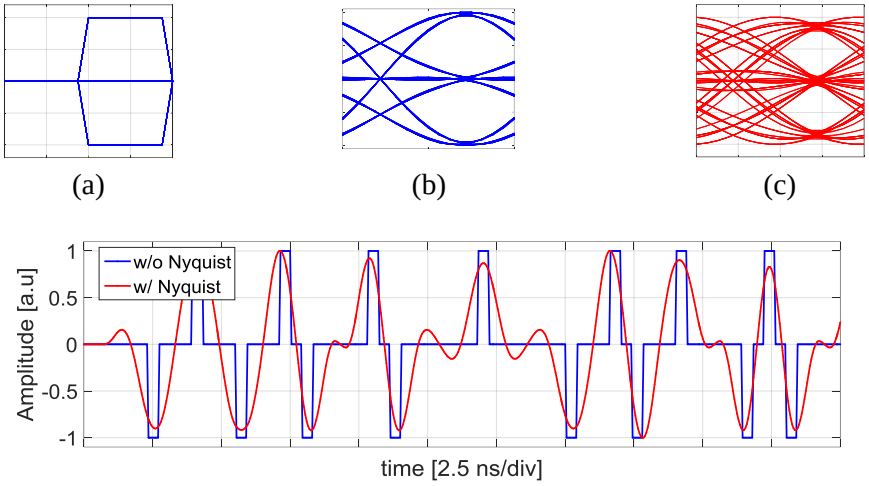

Figure 3.26. Eye diagram of the 50% duty-cycle RZ signal for direct DPSK modulation: (a) without Nyquist pulse-shaping, and with Nyquist shaping for (b) $\beta = 1$ and (c) $\beta = 0.25$; (d) time domain waveforms of (a) and (c).

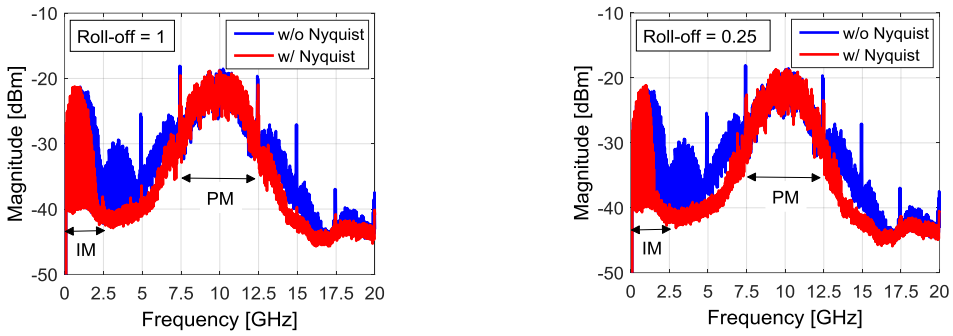

Figure 3.27. Photodetected spectra for DPSK at 2.5 Gb/s with Nyquist filtering, for (a) $\beta = 1$ and (b) $\beta = 0.25$.

unchanged, regardless the filter roll-off, while the width of the residual IM in the base-band is narrowed, because the IM is generated by a linear modulation. Accordingly, $\beta = 1$ was selected for the following tests as the effect of lower β is barely noticed.

First, the DFB laser were directly modulated at 1.25 and 2.5 Gb/s DPSK. The BER curves in Fig. 3.28(a) indicate that, without Nyquist shaping, the Rx sensitivities were -52 and -49.5 dBm respectively, measured at a FEC limit of BER = 10^{-3}. These values were approximately 3 and 5.5 dB better with respect to the case with Nyquist shaping, (-49 and -44 dBm for 1.25 and 2.5 Gb/s respectively). The sensitivity penalty can be ascribed to strong Nyquist filtering in combination with non-flat RF response of the electro-optical components that introduce distortion and extra ISI, thus reducing the eye-opening at the RX. This effect is clearly observed in Fig. 3.28(b) by comparing the received eye diagrams w/. and w/o. Nyquist shaping. The use of matched filtering at the RX with further equalization to flatten the channel response may lead to ISI reduction and improvement of the eye-opening.

Next, the minimum channel spacing between users was assessed for the highest R_b, i.e., 2.5 Gb/s. The received optical power was adjusted for BER = 3×10^{-4} when detecting TX1, and the TX2 λ

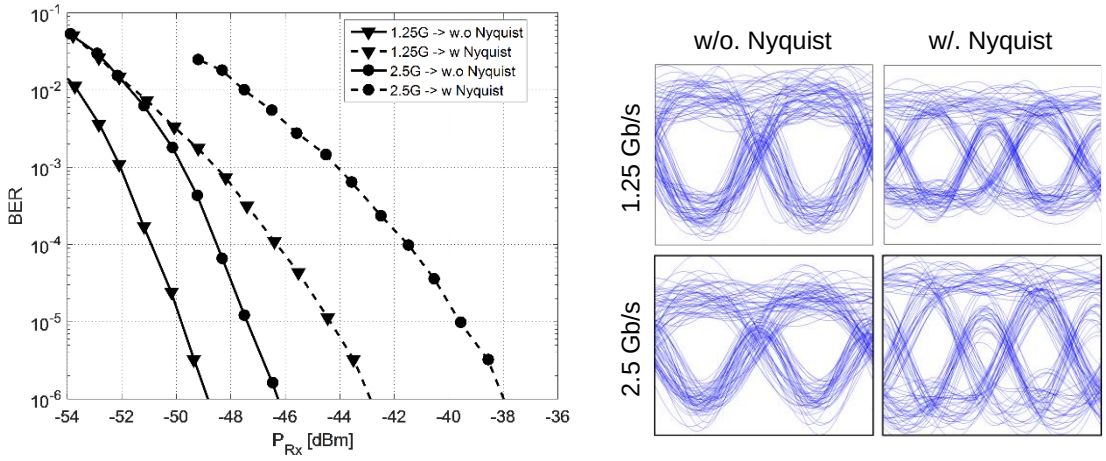

(a) (b)

Figure 3.28. (a) BER against Rx optical power for Tx1 and eye diagrams at BER = 3 · 10–6 without and with Nyquist shaping at 1.25 Gb/s (b,c) and 2.5 Gb/s (d,e) respectively.

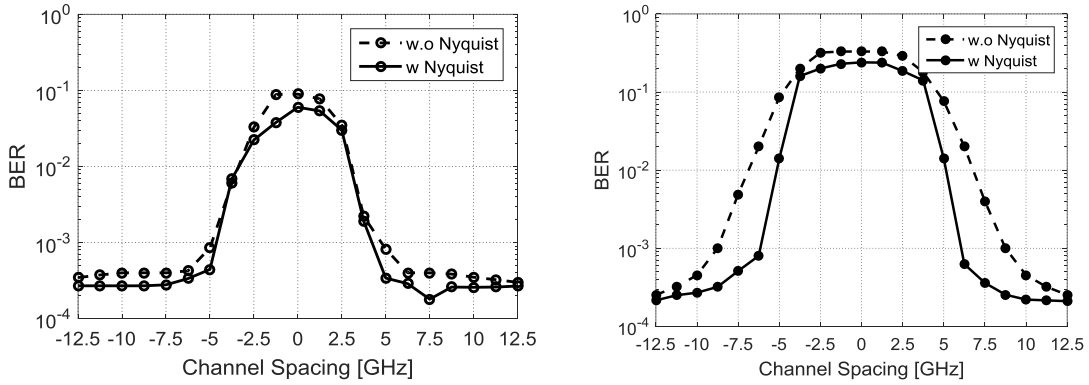

(a) (b)

Figure 3.29. BER against channel spacing for 2.5 Gb/s DPSK with and without Nyquist shaping: (a) both users at the same optical power; (b) the interfering TX2 emitting 15 dB higher in power than TX1.

was swept ±12.5 GHz with respect to TX1. The results plotted in Fig. 3.29(a) show no meaningful channel spacing reduction after applying Nyquist filtering ($\beta = 1$), mostly due to (I) the unchanged main PM modulation-lobe width, and (II) the significant suppression of the other harmonics of the spectrum w/o. Nyquist filtering in Fig. 3.27, due to band limited electronics. Nevertheless, the benefit of the Nyquist shaping becomes more apparent when maximum 15 dB differential optical path losses are allowed in the PON, as specified in [ITU19] for NG-PON2, due to the strong interference of modulation side-lobes on weaker adjacent channels. The BER curves in Fig. 3.29(b) were computed from TX1 emitting 15 dB lower than the interfering TX2. The results indicate that the Nyquist shaping reduces in 25% the required channel spacing for BER = 10^{-3}, allowing that 2.5 Gb/s DPSK users having 15 dB power difference between adjacent channels can be fitted in a 6.25 GHz spaced optical grid.

As a final remark, the benefits of spectral shaping by Nyquist filtering are not exclusive for ONUs with DSP systems. The analog ONUs can also leverage the analog Nyquist shaping by means of sharp electrical brick-wall microstrip filters [Sch15].

3.4.2 Crosstalk by non-ideal isolation and optical reflections

Optical signals travelling through the transmission path in the udWDM-PON can be degraded by a linear crosstalk generated by the non-ideal isolation and the limited return losses of optical devices. A relevant source of reflections at the ODN are the optical connectors due to the glass-air-glass gap created when two fiber ends are connected together, also known as Fresnel reflection. This kind of crosstalk can be classified in two categories: the hetero-wavelength crosstalk (HEC) that appears from the spectral tails of other adjacent channels interfering the transmitted channel, and the homo-wavelength crosstalk (HOC) when the interference comes from spurious components at the same λ than the signal, mainly due to optical reflections. Regarding the HEC, the generated crosstalk is totally out-band and can be reduced by additional filtering. Conversely, crosstalk components from the HOC completely fall into the transmitted channel BW and cannot be filtered out. Hence, system degradation by the HOC is much more severe than that of the HEC when both types of crosstalk are present [Raf99]. This section focuses on the HOC and its effect on the performance of coherent udWDM-PON.

Theoretically, the HOC produced by, e.g., an optical reflection, can be modelled as the linear combination between the transmitted optical signal and a delayed and attenuated version of itself [Dia06]. The highest interference occurs when signal and crosstalk are completely matched in frequency and SOP, then, let us consider hereafter only one SOP and optical frequency matching. From Eq. (2.47) for BPSK, the transmitted signal is expressed as

$$e_S(t) = a(t)E_S e^{j(\omega_S t + \phi_S(t))} \tag{3.16}$$

where $a(t)$ represents the binary phase-modulated data, either differentially encoded or not, and $\phi_S(t)$ stands for the phase noise of the laser. The spurious crosstalk, i.e., the delayed and attenuated version of Eq. (3.16), reads as

$$e_{XTL}(t) = \rho a(t-\tau)E_s e^{j(\omega_S t - \omega_S \tau + \phi_S(t-\tau))} \tag{3.17}$$

Here, ρ is the crosstalk amplitude and τ its optical delay. The optical signal that reaches the RX is the linear combination between signal and crosstalk, as $e_m(t) = e_S(t) + e_{XTL}(t)$. At the RX, with homodyne detection, the signal $e_m(t)$ distorted by HOC is mixed with the LO then photodetected, yielding the following I and Q photocurrents

$$\begin{aligned} i_I(t) &= \mathrm{Re}\{e_m(t) \cdot {e_{LO}}^*(t)\} \\ &= a(t)\sqrt{P_S P_{LO}}\cos\phi_n(t) + \rho a(t-\tau)\sqrt{P_S P_{LO}}\cos(\omega_S \tau + \Delta\phi(t)) \end{aligned} \tag{3.18}$$

$$\begin{aligned} i_Q(t) &= \mathrm{Im}\{e_m(t) \cdot {e_{LO}}^*(t)\} \\ &= a(t)\sqrt{P_S P_{LO}}\sin\phi_n(t) + \rho a(t-\tau)\sqrt{P_S P_{LO}}\sin(\omega_S \tau + \Delta\phi(t)) \end{aligned} \tag{3.19}$$

where $\phi_n(t) = \phi_S(t) - \phi_{LO}(t)$ is the total phase noise contribution (TX + LO lasers), and

$$\Delta\phi(t) = \phi_n(t) - \phi_n(t-\tau) \tag{3.20}$$

represents the evolution of the total phase noise across the crosstalk delay τ. The PDs responsivity was omitted for notation simplicity. Here we introduce the coherence time of the lasers, denoted

by τ_c, and calculated as $\tau_c = 1/(\pi\Delta\nu)$ [Pet88], representing the time interval in which the instantaneous phase $\phi_n(t)$ is deterministic; $\Delta\nu$ is the total laser linewidth (TX + LO). The ratio between the coherence time τ_c and the crosstalk delay τ, as well as the crosstalk level ρ, dictate the degradation of the system. Two different interactions occur in Eqs. (3.18) and (3.19) between signal and crosstalk, corresponding to the first and second term respectively. On the one hand, when τ is lower than τ_c, the phase difference $\Delta\phi(t) = 0$ as $\phi_n(t)$ and $\phi_n(t-\tau)$ in Eq. (3.20) are equal, then the signal and the crosstalk are combined either in-phase or counter-phase depending on the data sequence $a(t)$ and the value of τ. In this case, the HOC does not produce noise but causes fluctuations of the signal power and burst of errors at the data detection [She99]. On the other hand, when τ is larger than τ_c, the phase difference $\Delta\phi(t)$ is completely random, and the crosstalk term in Eqs. (3.18) and (3.19) is totally uncorrelated with the signal, behaving as noise.

To assess the impact of HOC and determine the tolerable crosstalk levels, numerical simulation was carried out using the setup in Fig. 3.30. Two 4MHz linewidth lasers, in the range of commercial DFBs, are used as TX and LO. The DPSK signal generated at the TX is sent through the fiber, then splitted into two paths by an optical 3dB coupler. One of the paths is delayed, attenuated and combined again with the main signal to generate HOC before the coherent homodyne detection. Polarization is matched at the RX input to obtain the maximum crosstalk and BER degradation.

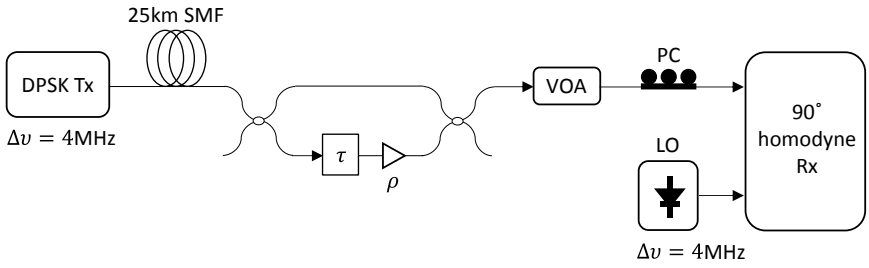

Figure 3.30. Simulation setup to evaluate the HOC effect on 1.25 Gb/s DPSK with homodyne detection.

Depending on the ratio τ/τ_c, the HOC effect can be observed as relative minimums in the RF spectrum at the RX after photodetection. When $\tau < \tau_c$, the value of the crosstalk delay τ can be obtained by the inverse of the distance between the relative minimums in the spectrum. Conversely, if $\tau > \tau_c$ the optical phase of signal and crosstalk are completely uncorrelated and behave as the combination of independent optical sources with Lorentzian shape in the RF spectrum. This holds true when SOP changes are not considered; otherwise, the minimums in the spectrum are continuously changing [Dia06]. This phenomena can be appreciated in the photodetected spectra in Fig. 3.31, for unmodulated optical carrier and fixed SOP. The crosstalk level ρ was set 15 dB lower than the main signal, and the crosstalk delay τ was adjusted to be 2.5 and 300 ns in Figs. 3.31(a) and 3.31(b) respectively. The coherence time was ~40 ns, for a total $\Delta\nu$ = 8 MHz. In Fig. 3.31(a), where $\tau < \tau_c$, the 400 MHz separation between minimums in the spectrum corresponds to the inverse of the crosstalk delay (2.5ns). When $\tau > \tau_c$, as in Fig. 3.31(b), the spectrum is strictly Lorentzian, as expected.

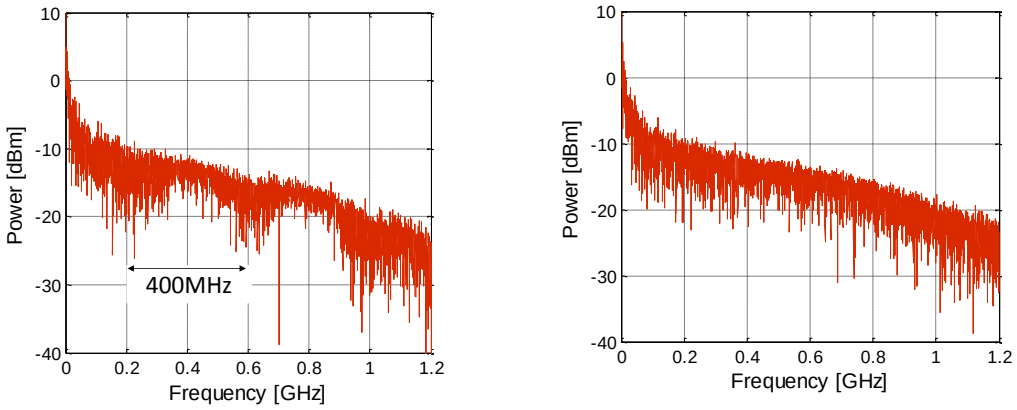

Figure 3.31. Effect of HOC in the RF spectrum after photodetection for crosstalk delay τ of (a) 2.5 ns and (b) 300 ns. Coherence time $\tau_c = 40$ ns (total $\Delta\nu$ = 8 MHz). Crosstalk level ρ = -15 dB.

Afterwards, the BER dependence on the crosstalk delay was evaluated by sweeping τ from 0 to 250 ns to observe the evolution of the BER before and after the coherence time of the lasers ($\tau_c =$ 40 ns). The crosstalk level was ρ = -15 dB, and the Rx power was adjusted to obtain a reference BER = 10^{-4} when no crosstalk. Fig. 3.32(a) shows the BER within the entire simulated time window, whereas Figs. 3.32(b) and 3.32(c) zoom into the waveform in two different time intervals, before and after the coherence time.

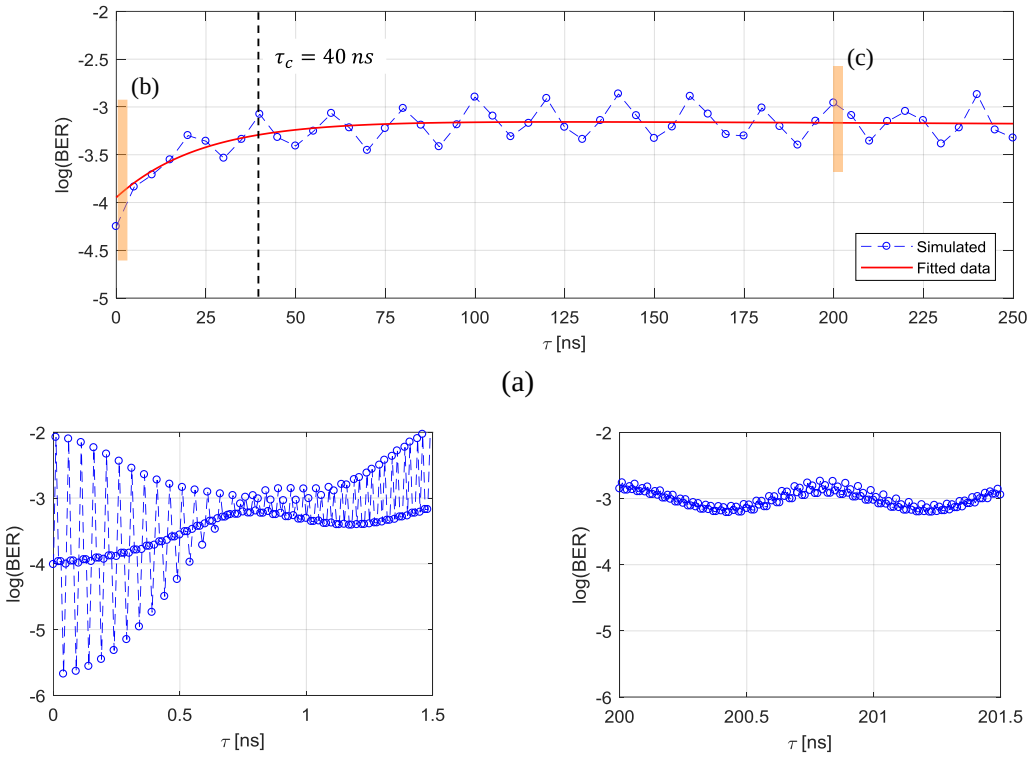

Figure 3.32. (a) Evolution of the BER across 250ns of crosstalk delay τ, and zoom into the waveform for τ ranging: (b) from 0 to 1.5 ns, and (c) from 200 to 201.5 ns, to appreciate the fast BER fluctuations. Coherence time $\tau_c = 40$ ns (total $\Delta\nu$ = 8 MHz). Crosstalk level ρ = -15 dB.

As shown in Fig. 3.32(a), for a given crosstalk level (-15 dB) the mean error probability increases as the crosstalk delay increases, until τ approximately reaches the coherence time (40 ns). After that, the BER is no longer degraded because signal and crosstalk are totally uncorrelated, as stated before, and the latter acts as noise whose power is given by ρ. To analyze the fast BER variations, Fig. 3.32(b) plots the BER evolution for τ ranging from 0 to 1.5 ns, i.e., when $\tau < \tau_c$, and clearly shows the power fluctuations that translate into fast BER oscillations at the rate of the optical frequency ω_S. Note that the amplitude of the oscillation progressively decreases up to 800 ps, where τ_c matches the bit time. In contrast, Fig. 3.32(c) shows the BER evolution after the coherence time, with τ ranging from 200 to 201.5 ns. As expected, the strong BER oscillations have disappeared and only remains a smooth BER fluctuation with period 800 ps, corresponding to the bit time.

Finally, the tolerance to the crosstalk power level was evaluated. Fig. 3.33 computes the sensitivity penalty at BER = 10^{-4} when varying the crosstalk level ρ, for different values of τ and τ_c. The results indicate that the crosstalk power should remain 30 dB lower than signal power in order not to affect the BER, and lower than 14 dB and 18 dB for total $\Delta\upsilon = 200$ KHz and 8 MHz respectively, for maximum 1dB penalty. Another conclusion is that the larger is the total laser linewidth the higher is the BER degradation by the HOC, when using differential demodulation for optical phase detection. In practice, for instance, the amplitude of the optical reflections in connectors depends on the cleaving angle and on the end-to-end physical distance. Usually, angled physical contact (APC) connectors, with 8° angle-polish applied to the end faces, are deployed to minimize reflections.

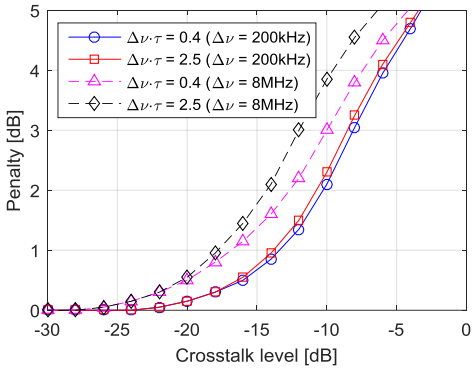

Figure 3.33. Sensitivity penalty at BER = 10^{-4} as a function of the crosstalk level, for several values of total linewidth and crosstalk delay.

3.5 Non-Flat Electro-Optical Frequency Response

The electro-optic devices used in the coherent TRX might exhibit non-flat frequency response within the data BW, that causes signal distortion and BER degradation if not correctly addressed. At the TX side, for instance, direct current modulation of DFB lasers, leveraging the frequency chirp, is pointed out in this thesis as a cost-effective optical modulation strategy for access networks, with remarkable simplicity and power efficiency. Yet, a major challenge arises from the non-ideal FM response of DFBs under injection current modulation [For95]. Moreover,

electronic components of the TX and the RX such as amplifiers, electrical filters, RF mixers, ADCs/DACs, etc., might also exhibit non-flat frequency response in the pass-band. Cascading all those non-flat frequency responses together yield strong signal distortion.

To evaluate the impact of non-flat frequency responses on the coherent RX sensitivity, numerical simulation was carried out with DPSK at 1.25 Gb/s, and detected by a 90º homodyne RX, as illustrated in Fig. 3.34. Note that the same mechanism employed in Fig. 3.30 to generate HOC, thus inducing fluctuations in the frequency response (see Fig 3.31(a)), can be implemented here in the electrical domain to emulate non-flat frequency response and RF spectrum distortion. Accordingly, the I and Q photocurrents after balanced photodetection were impaired each by combining the photocurrent with a delayed and scaled version of itself, as depicted in Fig. 3.34(inset).

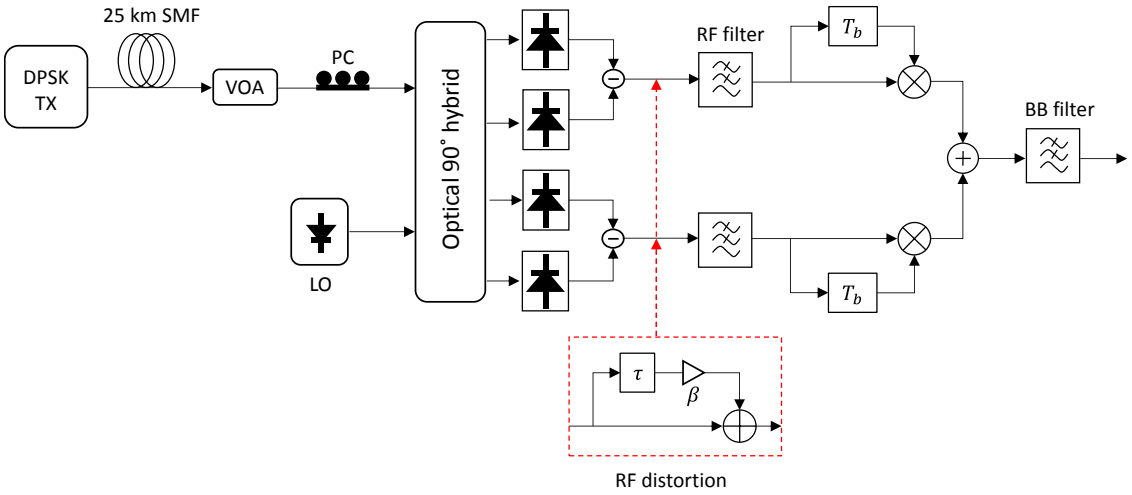

Figure 3.34. Simulation setup to evaluate the impact of non-flat RF frequency response. The inset shows the feedforward modelling of the RF signal distortion.

By adjusting the interference amplitude β, the signal distortion becomes evident as ripple in the magnitude of the RF spectrum, denoted by γ, and expressed in dB as

$$\gamma_{dB} = 20log\left(\frac{1+\beta}{1-\beta}\right) \tag{3.21}$$

Table 3.7 depicts the RF spectrum at the RX after photodetection and signal distortion, as well as the eye diagram after differential demodulation and prior data decision, when varying the amplitude (β) and delay (τ) of the RF distortion. As observed, smaller τ produce a smooth ripple in the RF spectra, whereas larger τ produce fast magnitude oscillations, for the same β. The distance between two minimums or two maximums in the RF spectrum equals to the inverse of the distortion delay τ. From the eye diagrams, the conclusion is that larger τ distorts more at the symbol transitions, while has no meaningful impact on the eye aperture that is mainly governed by β.

To determine the RX sensitivity penalty, the BER was computed as a function of the received optical power by interfering during symbol transitions ($\tau = nT_b$), but also in middle of symbols

Table 3.7. Electrical spectra after photodetection and eye diagram after differential demodulation, for DPSK at 1.25 Gb/s with RF signal distortion.

	RF spectrum	**RX eye diagram**
Non-distorted	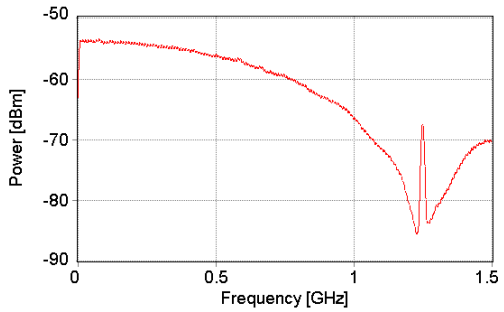	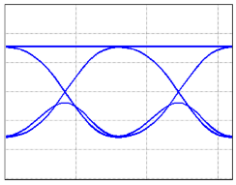
$\beta = 20\%$ $\tau = 2T_b$	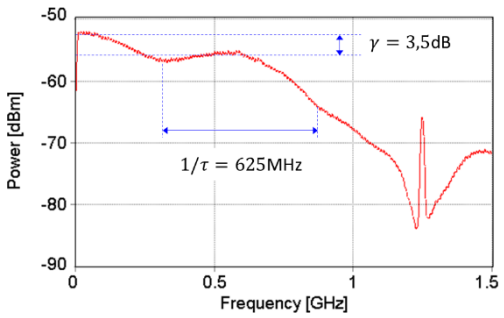	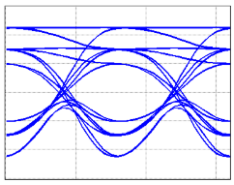
$\beta = 20\%$ $\tau = 10T_b$	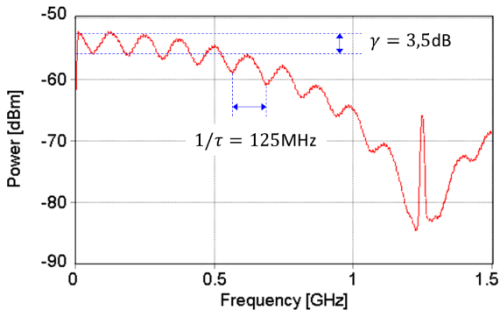	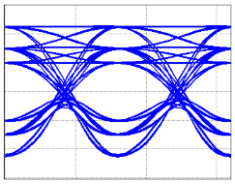

($\tau = nT_b + T_b/2$). Results are presented in Fig. 3.35(a) for $\beta = 10\%$, equivalent to $\gamma = 1.75$ dB, and in Fig. 3.35(b) for $\beta = 20\%$, equivalent to $\gamma = 3.5$ dB. For FEC limit of BER = 10^{-3}, the maximum measured penalty when $\gamma = 1.75$ dB was <1dB, whereas for $\gamma = 3.5$ dB the penalty raises to about 5 dB for the case of maximum distortion. It is worth noting in both graphics that the distortion is more severe when impairing during symbol transitions than in the middle of symbols. Finally, the main outcome is that, in practice, the frequency response ripple must retain lower than 2 dB for less than 1 dB sensitivity penalty at FEC limit, regardless of how fast the frequency response fluctuates, as derived from Fig. 3.35(a). Otherwise, larger ripple yields eye closure and higher power penalty, as indicated by Table 3.7 and Fig. 3.35(b) respectively, and eventually require equalization strategies to flatten the frequency response and mitigate the RF signal distortion. Indeed, the same structure employed for modelling the RF distortion in Fig. 3.34(inset), can be properly adjusted in τ and β to compensate for the non-flat frequency response. It becomes a simple 1-tap feedforward equalizer. Chapter 7 addresses the design and implementation of digital pre-equalization at the TX to compensate for the non-flat FM response

of directly phase-modulated DFBs, and non-ideal and band-limited frequency response of RF amplifiers and DACs.

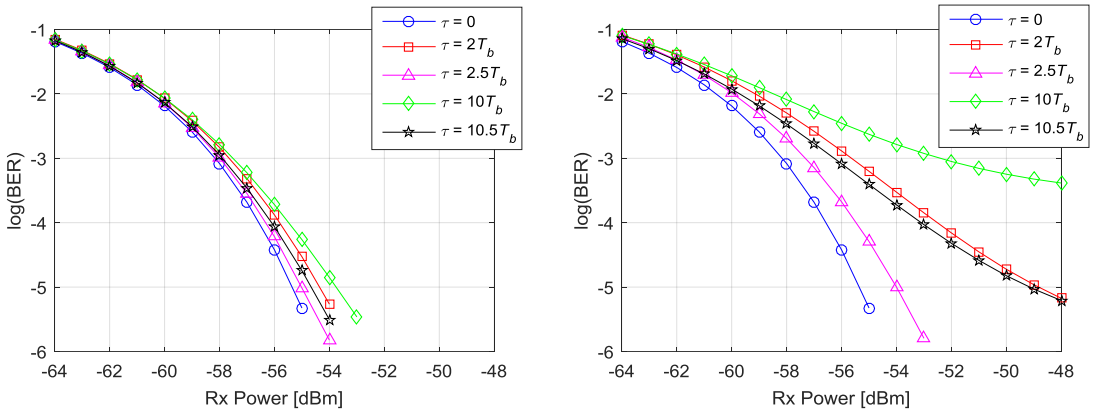

Figure 3.35. BER dependence on the distortion delay (τ), for a magnitude ripple of (a) 1.75 dB and (b) 3.5 dB.

3.5.1 Frequency dip in laser FM response

Besides the ripple in the magnitude, the non-flat FM response of semiconductor lasers also include a frequency dip at low modulation frequencies. This obeys the changes in both the temperature and the carrier density under injection current modulation, which in turn causes variations in the refractive index of the semiconductor active layer, as explained in Section 2.4. As a result, the overall FM response of the laser is the combined effect of thermal modulation and carrier density modulation, which may either produce a dip or an enhancement in the FM response at the frequencies where both effects converge [Vod90]. The thermal modulation, with large time constants, is only effective at low frequencies below few MHz (usually < 10 MHz), whereas the carrier density modulation produces a nearly flat response extending from MHz up to about several GHz, with a resonance peak at higher frequencies. This behavior is illustrated in Fig. 3.36.

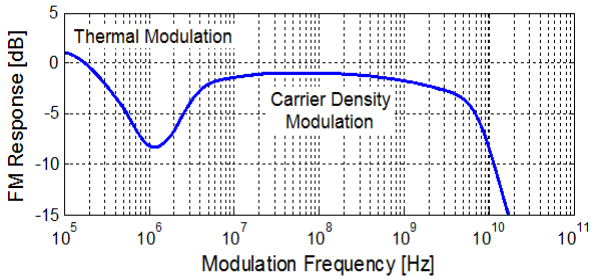

Figure 3.36. General FM response of semiconductor lasers.

Experimental characterization of the laser FM response at lower frequencies is shown in Fig 3.37, using a commercial DFB with sinusoidal current modulation. The laser emitted at λ = 1550.6 nm when biased at I_{bias} = 82 mA. The result is a wideband FM modulation that prevails over the AM modulation, as appreciated in the photodetected spectrum after heterodyning in Fig. 3.37(inset). The laser FM response was measured in terms of the FM efficiency for a modulation current

swing of 3 mA_{pp}, revealing a frequency dip clearly visible whose minimum is located about 400 kHz.

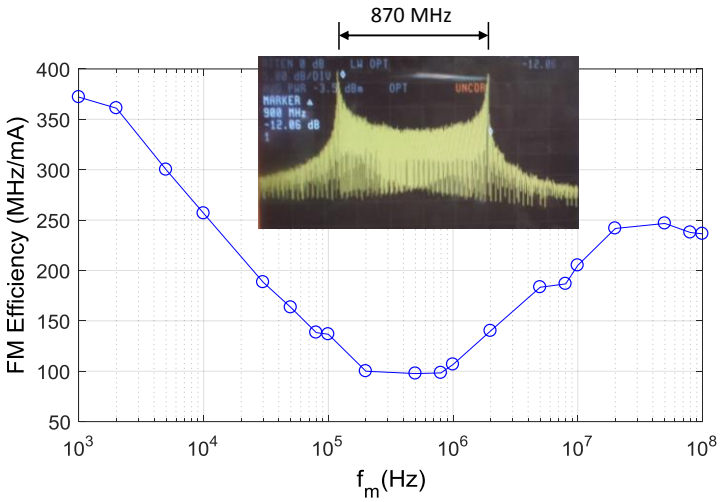

Figure 3.37. Experimental FM response at lower frequencies for a DFB with 3 mA_{pp} sinusoidal current modulation. The inset shows the electrical spectrum for f_m = 10 KHz.

The frequency dip may induce system degradation and pattern-dependent performance, because of the pass-band characteristic of the effective laser BW. The tolerable cut-off frequency imposed by the dip, and its impact on the low frequencies of the data pattern, were evaluated by numerical simulation. The simulation setup was simply implemented by high-pass filtering the NRZ-PRBS data at the TX in Fig. 3.5, to suppress the frequency components falling into the dip of the laser. The high-pass filter (HPF) consisted of a 4th order Bessel whose 3dB cut-off frequency f_c was adjusted for the different values of the laser dip. The optical signal was detected by a 90º homodyne RX. The received optical power was swept and the BER computed for several cut-off frequencies of the HPF, and for two different data sequences: PRBS-7 and PRBS-15, to evaluate the pattern dependence. Higher order PRBS were not considered due to the computational limit of 2^{18} total bits for Monte-Carlo simulation. Results are plotted in Fig. 3.38.

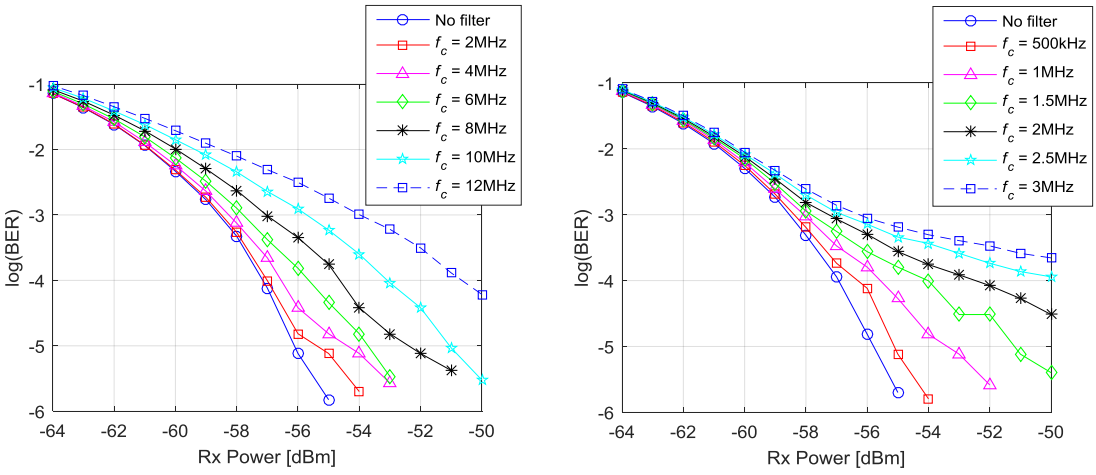

(a) (b)

Figure 3.38. BER as a function of Rx power for several HPF cut-off frequencies, and two different data sequences: (a) PRBS-7 and (b) PRBS-15.

As expected, the frequency dip leads to pattern-dependent performance. For PRBS-7 in Fig. 3.38(a), the maximum cut-off frequency for 1 dB maximum penalty at BER = 10^{-3} is 6 MHz, whereas for PRBS-15 in Fig. 3.38(b) the maximum tolerance is 1.5 MHz, and the performance degradation is much more severe with apparent error-floor. This is ascribed to the repetition rate of the PRBS, that is 9.8 MHz and 38 kHz for PRBS-7 and PRBS-15 respectively, at 1.25 Gb/s. The repetition rate represents the minimum frequency component of data, and dictates the sensitivity penalty at the detection because of the high-pass characteristics of the frequency dip. Several methods have been reported to counteract the low-frequency dip of semiconductor lasers, including pre-equalization at the TX [Ale89] or post-equalization at the RX [Enn90] of the laser FM response, or the use of line coding like the 8B10B code, used to transport Gigabit Ethernet traffic, that removes the low frequency part of the baseband data by adding a codified redundancy [Bar08].

Although the direct-phase modulation of broadband data only leverages the carrier density modulation region of the laser FM response, there is not necessarily a waste of BW in direct laser modulation. Indeed, for an efficient use of the available BW, the thermal modulation region below the laser dip can be exploited for low-frequency FSK signaling [Hon15], [Nak14], [Tan12] useful for implementation of the auxiliary management and control channel (AMCC), mandatory in WDM-PON deployments for network control and optical grid management [ITU19].

3.6 Coherent ONU Specifications for udWDM-PON

The previous sections carried out a comprehensive analysis, through numerical simulation and preliminary experiments, on the techno-economic factors and the transmission impairments that have the highest relevance for the design and operation of the coherent ONUs for PON. The main conclusions drawn and the maximum tolerance found for each of the impairments serve as reference for ONU specifications and PON dimensioning, in terms of number of users and maximum fiber reach –given in this scenario by the final RX sensitivity–, channel spacing, data rate, among others.

In what follows, the identified transmission impairments in udWDM-PON are summarized, highlighting their impact on both the coherent TRX design and the final system performance.

3.6.1 Summary of transmission impairments and mitigation strategies

The list of the main impairments identified here, which affect the performance of the udWDM-PON is presented in Table 3.8. As stated before, this chapter primarily aims at the residential users segment, with dedicated λ at 1.25 – 2.5 Gb/s. For each of the impairments, it is provided: the physical origin, the effect relevance, the key parameters defining the phenomena, the typical expected value, the possible mitigation strategies, and the maximum tolerance for a given RX sensitivity penalty.

Table 3.8. Summary of the most relevant transmission impairments in udWDM-PON.

Laser phase and frequency error	Phase noise	• *Origin:* Internal laser-cavity phase fluctuations. • *Typical expected value:* 1 – 10 MHz, for commercial DFBs. • *Mitigation:* Phase-diversity coherent detection, differential demodulation, DSP phase estimation.
		• *Maximum tolerance at BER = 10^{-3}:* 1dB power penalty for $\Delta\upsilon T_b = 1.6\%$
	Frequency drift	• *Origin:* Thermal fluctuations, noisy current sources. • *Typical expected value:* ± 100 MHz, for thermally-controlled DFBs • *Mitigation:* LO automatic frequency control, DSP frequency estimation.
		• *Maximum tolerance at BER = 10^{-3}:* 1dB power penalty for $\Delta f_{IF} T_b = 6\%$
Additive noise at the RX	Shot and thermal noise	• *Origin:* Thermal noise originates from the electronic part of the RX, mostly from TIAs. Shot noise originates from the photodetection due to the quantum-nature of light. • *Typical expected value:* Thermal noise spectral density $S_f = 10 - 18$ pA/$\sqrt{\text{Hz}}$, for commercial TIAs. • *Mitigation:* LO power increase. Shot noise establishes the quantum-limit RX sensitivity.
		• *Maximum tolerance at BER = 10^{-3}:* LO power higher than 10dBm for maximum 1 dB power penalty, with respect to the quantum-limit sensitivity

Additive noise at the RX	RIN	• *Origin:* Intensity noise contribution from the strong LO • *Typical expected value:* -150 dB/Hz. • *Mitigation:* Balanced photodetection, CMRR improvement.
		• *Maximum tolerance:* CMRR > 25 dB for no meaningful RIN impact. Optimum 8 – 12 dBm LO power for CMRR < 25 dB
Inter- and intra-channel crosstalk	Crosstalk by adjacent udWDM channels	• *Origin:* Modulated spectrum side-lobes interfering adjacent channels in the ultra-narrow optical udWDM grid. • *Typical expected value:* >10dB modulated side-lobes suppression. • *Mitigation:* Electrical pulse-shaping, accurate λ-control of lasers.
		• *Maximum tolerance at BER = 10^{-3}:* $<$1 dB power penalty for channel spacing larger than 4 GHz, 3.1 GHz, and 2.6 GHz for NRZ, Gaussian, and raised cosine pulse-shape respectively. Up to 15 dB power difference tolerance with adjacent channels, for 6.25 GHz spaced udWDM optical grid with raise-cosine pulse shaping.
	Laser side-modes interference	• *Origin:* Laser cavities coupling, mode-partitioning noise. • *Typical expected value:* SMSR $>$ 30 dB. • *Mitigation:* Spectral management, improvement of laser quality.
		• *Maximum tolerance at BER = 10^{-3}:* 1dB power penalty for SMSR = 21 dB, when all the udWDM channels emit at the same power.

Inter- and intra-channel crosstalk	Laser side-modes interference	1dB power penalty for SMSR = 36 dB, when 15 dB power difference between udWDM channels are considered.
	Crosstalk by optical reflections	• *Origin:* Limited return loss of connectors and optical devices, non-ideal isolation. Relevant when the crosstalk has the same λ than the signal (HOC). • *Typical expected value:* Return loss $>$50 dB • *Mitigation:* Optical isolators, APC connectors.
		• *Maximum tolerance at BER = 10^{-3}:* Optical reflections lower than -30 dB have no impact. Optical reflections lower than -18 dB for 1dB power penalty, with total laser $\Delta v =$ 8 MHz (TX+LO), the typical for DFBs.
Non-flat electro-optical frequency response	Non-flat RF frequency response	• *Origin:* Limited RF BW, electrical distortions, impedance mismatching. • *Typical expected value:* magnitude spectrum ripple $<$ 2 dB • *Mitigation:* RF design improvement, electronic and digital equalization.
		• *Maximum tolerance at BER = 10^{-3}:* < 2 dB magnitude spectrum ripple for 1dB power penalty.
	Laser frequency dip	• *Origin:* Thermal and carrier density effects frontier in the laser FM response. • *Typical expected value:* frequency dip nearby 1 MHz • *Mitigation:* pre- and post-equalization, data encoding (e.g., 8B10B).
		• *Maximum tolerance at BER = 10^{-3}:* Pattern dependent performance. 1dB power penalty for 1.5 MHz frequency dip, with PRBS-15, as the worst simulated case.

3.6.2 Performance estimate of coherent receivers for PON

With all these impairments present, if all those sensitivity penalties for each are allowed, one may end up with the total sensitivity penalty summarized in Table 3.9 over the benchmark RX sensitivity▲, for homodyne and heterodyne detection. Yet, the accumulation of impairment effects may not be linear. The values reported in Table 3.9 are first purely orientative, may vary depending on the implemented devices, and will be experimentally assessed in subsequent chapters. Thus, a conservative estimate of the final RX sensitivity for 1.25 Gb/s DPSK users, is of -52 and -49 dBm for homodyne and heterodyne RXs respectively. These coherent RX sensitivities are substantially better than the IM-DD counterpart, that offer -32 dBm sensitivity at the same 1.25 Gb/s bit rate [ITU19].

Table 3.9. Expected performance of coherent RXs in udWDM-PON .

	Power penalty [dB] @ 10^{-3} BER	**Remarks**
Residual IM	1	Direct phase modulation
Thermal noise	1	LO power limited by RIN
Linewidth	1	Commercial DFBs
Frequency drifts	1	Thermally-tuned DFBs
Differential detection	0.5	-
Optical front-end	1 + 0.5	Excess loss + connectors
IF to baseband	3	Heterodyne detection only

	RX sensitivity [dBm] @ 10^{-3} BER	**Remarks**
Benchmark▲	-58.5	Homodyne, simulation
Expected in real scenario	~ -52	Homodyne
	~ -49	Heterodyne

▲Sensitivity curves in Fig. 3.8 from numerical simulation with the best parameter configuration.

Moreover, the theoretical analysis and numerical simulations carried out in this chapter do provide sufficient evidence to support the main claims of the proposed udWDM-PON scenario. More concretely, cost-effective λ-to-the-user enabled by a novel class of coherent TRXs for PON, with superior RX sensitivity. The optical spectrum is efficiently utilized by allocating the λs in ultra-narrow channel spacing, as low as 6.25 GHz in between 1.25 – 2.5 Gb/s users. The coherent ONUs can leverage commercial DFBs, low-cost optics, and simple electrical signal processing – either analog or digital–, but still retaining high the performance.

Among the three options evaluated for coherent RX, the 90º homodyne RX with 8 PDs (for full polarization) and two optical 90º hybrids, is not a feasible candidate for PON, and only served as benchmark. The other two architectures, 3x3 homodyne and 2x2 heterodyne, are the most promising solutions as they exhibit the best trade-off in terms of performance, power consumption, and cost per user. Accordingly, they were selected for implementation in the COCONUT network to demonstrate the complete functionalities of the coherent udWDM-PON. The following Chapter 4 covers this topic.

3.7 Chapter summary

This chapter provided an evaluation of the main transmission impairments that were identified as the main limitations in the udWDM-PON, enabled by simplified coherent systems. The impairments assessments was realized through numerical simulations and preliminary experiments. At the fiber channel, both linear and non-linear propagation effects can degrade the PON performance, thus limiting on the maximum symbol rate and launch power. Yet, impairments from the optical fiber are not considered here as the main limitation for the PON scenario, and the dominant transmission impairment mostly originate from the TX and RX subsystems of the coherent ONU, as the phase noise, frequency drifts, LO-RIN, crosstalk by adjacent channels, non-flat electro-optical frequency response, among others. Possible solutions were discussed to mitigate the impact of such impairments, drawing design rules to implement the PON and optimizing network parameters.

The results indicate the feasibility of using commercial DFBs and simpler optics to implement the coherent ONU, but still achieving high RX sensitivity and transmission robustness. At the TX, bulk IQ modulators are replaced by direct amplitude-and-phase modulation of semiconductor lasers. At the coherent RX, optical 90º hybrids are replaced by much simpler 2x2 and 3x3 fused-fiber couplers, also reducing the number of PD thus lowering the power consumption of the ONU. With this novel class of simplified coherent systems, two application scenarios within the PON, , were proposed: for enterprises and mobile services at 10 – 20 Gb/s, m-(A)PSK optical TXs with 3x3 homodyne RXs; and for residential users at 1.25 – 2.5 Gb/s, DPSK TXs with 2x2 heterodyne RXs. This allows for convergence of services within the same deployed optical fiber.

Chapter 4

The COCONUT PON: Next Generation Wavelength-to-the-User Access

The overview of the PON technologies evolution provided in Section 1.1, emphasized the fundamental idea underpinning the next generation access networks deployment: enhancing the PON performance and capabilities, but retaining the cost down, as it lies on the final PON subscribers. This translates into reducing the complexity, cost and energy consumption of the ONU equipment at most without excessively sacrificing the performance. To fulfill these strict requirements of next generation access, efforts in research are being taken to develop the Gigabit-to-the-user concept, towards user BWs in excess of 1 Gb/s, but enhancing the spectral efficiency by allocating hundreds of λs in ultra-dense grid configuration [Pra16], [Agr16], [Kaz17]. Concerning this, the research involved in the COCONUT –Cost-effective Coherent Ultra-dense WDM-PON for Lambda-to-the-user Access– project (*http://www.ict-coconut.eu*) aimed at the development of cost-effective solutions covering both photonic technologies and system design, that will enable the significant capacity increase in the throughput of an OLT, from several Gb/s offered today by TWDM-PON systems like XG/NG-PON systems, to hundreds of Gb/s supported by the use of coherent technologies and novel signal processing techniques, yet simple and HW-efficient.

Precisely, the main novelty of the COCONUT PON is the use of coherent detection in an optical access network, to realize cost-effective WDM in ultra-dense optical spectrum configuration. The coherent udWDM-PON solution enables, as analyzed in Chapter 3, a large number of λ-channels to be densely allocated in the optical spectrum, while the RX sensitivity is significantly improved, nearby 15 – 20 dB, with respect to conventional DD. This results in connectivity to a larger number of end users (up to 256) compared to standardized PON solutions.

The primary application aimed in COCONUT-PON is next generation FTTH networks, since they constitute a major driving force worldwide. Nevertheless, the different capabilities of the two types of coherent TRXs for PON reported in Section 3.1, potentially suggest the convergence of heterogeneous applications/services within the PON, such as residential, business connectivity and mobile antenna. Hence, the COCONUT-PON uses dedicated λ-channel per user, with channel spacing from ultra-dense 6.25 GHz to conventional 100 GHz ITU-grid, for bit rates ranging from 1.25 to 10 Gb/s respectively, depending on the coherent TRX type and the application scenario.

This chapter reports on the main research outcomes of the European project COCONUT, whose complete functionalities were demonstrated in a field trial open to public visitors, using coherent TRXs prototypes operating in real-time with multimedia traffic, and transmitting trough dark fiber installed across the city center of Pisa, Italy.

4.1 Network Architecture

Fig. 4.1 illustrates the architecture of the COCONUT udWDM-PON, consisting of a standard tree-based PON with pure power splitting, where the drop fiber to every coherent ONU branches from the feeder fiber or from a previous drop. Each user connected to the PON is served by a dedicated λ, efficiently subdividing the optical spectrum into many ultra-densely spaced channels, as low as 6.25 GHz separation between adjacent users, and individually detected by high-selective coherent ONUs without optical filters. The bit rates per λ span from 1.25 or 2.5 Gb/s for the case of residential subscribers, up to 10 or 20 Gb/s for enterprises and mobile services. The bidirectional streams are symmetric, with the upstream (US) and the downstream allocated in different λs and flexibly spaced, according to the coherent detection type as will be explained in upcoming sections.

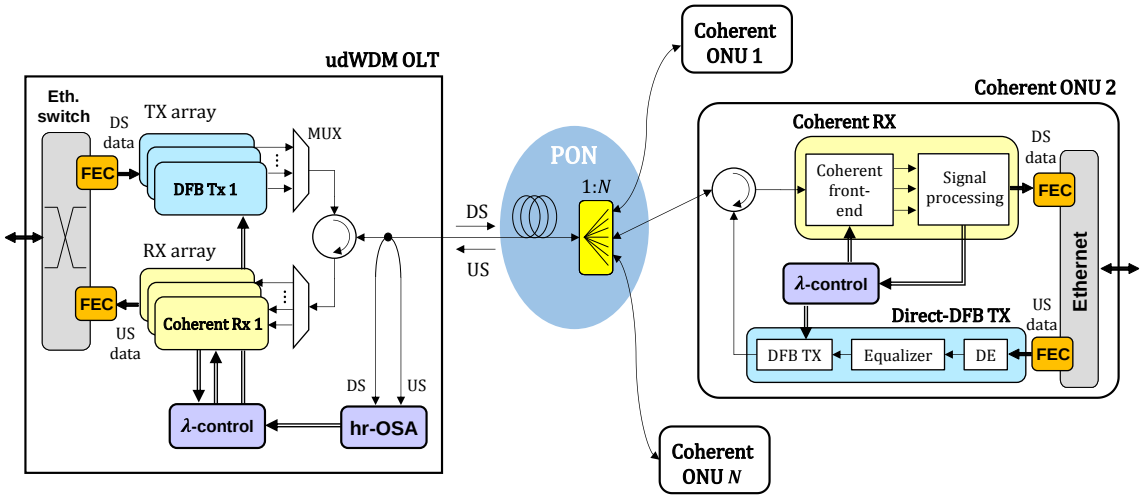

Figure 4.1. Network architecture of the COCONUT udWDM-PON; OLT: optical line terminal, ONU: optical network unit, DS: downstream, US: upstream, FEC: forward error correction, DE: differential encoding, OSA: optical spectrum analyzer.

The splitting ratio of the udWDM-PON has flexibility depending on the balance between fiber distance reach, number of users served and its geographical distribution. The high sensitivity of the coherent RXs enables large power splitting without the need of optical amplification, maintaining the ODN totally passive and compatible with legacy optical access systems. This allows to the PON serving up to 256 users, in contrast with the 32/64 users of typical TWDM-PON [ITU17], [ITU19].

At the customer premises, the ONUs are based on the maximally simplified coherent TRXs architectures described in Section 3.1, replacing the optical 90° hybrids by low-cost fused-fiber couplers (2x2 for heterodyne and 3x3 for homodyne) at the coherent RX front-end, also with less number of photodiodes. The use of directly modulated DFBs at the TX instead of external modulators contributes to reduce the form factor and power consumption of the coherent TRX. Next Section 4.2 outlines the technical details of the coherent ONUs, for both homodyne and heterodyne detection.

The udWDM OLT comprises the coherent TRX array for the virtual point-to-point (P2P) connectivity with the PON users, referring to the fact that each users owns a dedicated λ-channel. The OLT also concentrates the more complex elements, which can be shared, like the high-

resolution optical spectrum analyzer (hr-OSA), and the connection and activation protocol controller. The hr-OSA measures the distribution of power inside the COCONUT network, and detects the optical signals within the channel band in both the US and the DS direction. The OSA designed for the COCONUT PON is said to be high-resolution because of using coherent detection with sharp electrical filtering instead of using an optical resolution filter, which enables thousand times higher resolution BW, as low as 100MHz [Pre17]. Such a high resolution gives to the hr-OSA the ability for differentiating whether if the individual optical channels are modulated or not, useful for the activation and channel allocation process of new ONUs connecting to the PON.

A crucial aspect to be addressed in udWDM-PON is the precise control of hundreds of λs closely allocated in an ultra-dense optical spectrum. To this aim, the COCONUT PON features spectrum monitoring and λ-control systems, as detailed in Fig. 4.1, consisting of three main functionalities: (I) the hr-OSA at the OLT for continuous monitoring of the active λ-channels, in both directions, in the full optical band; (II) the λ-control system at both the OLT and the ONUs for thermal tuning of the TX and LO DFB lasers, driven by the frequency estimation subsystem of the coherent RXs and by the hr-OSA monitoring at the OLT; (III) the low-frequency signaling among the OLT and the ONUs for AMCC, implemented by direct FSK pilot-tones modulation at low frequencies, below the laser FM dip (see Section 3.5.1).

4.2 Coherent Transceivers Technology

Targeting to a simplified and low-cost coherent TRX, intended for mass production and easy provisioning, it is highly relevant to identify the application scenario, differentiating among the PON subscriber type, class of service, fiber distance and bit rate. This allows offering ad hoc solutions that optimize the trade-off between cost and performance, and makes the coherent ONUs accessible by the final PON users with heterogeneous services. Indeed, the two main paradigms in udWDM-PON were already identified in Section 3.1, as follows: premium subscribers such as enterprises and mobile antenna, that demand the highest bit rates, are served by homodyne ONUs with DSP; whereas residential FTTH services that comprise the majority of the PON subscribers, install (not limited to) fully-analog heterodyne ONUs. The digital RX offers superior performance owing to efficient HW implementation of DSP by using e.g., FPGAs, that has demonstrated big potential in terms of performance and flexibility for the future optical access networks [Fer16a], [Smo11]. Yet, its low-cost implementation is partially limited by state-of-the-art available components, especially data converters (DACs and ADCs). Here, the analog RX emerges as a complementary solution in pursuing the highest cost-effectiveness of the udWDM-PON.

To further reduce the complexity and cost, the coherent TRX should resort on the use of commercial and low-cost lasers –such as DFBs– with statistical (i.e., non-preselected) λ, required for mass ONU provisioning and fully transparent network operation. This in turn, imposes extra challenges as the DFBs exhibit λ-instabilities, wide spectral linewidth, and limited tunability. The first two impairments (λ-drifts, linewidth) make strong impact on the coherently detected optical carrier and directly affect the data detection. These two impairments are addressed by the

electrical signal processing part of the coherent RX, as it will be treated in Chapter 5. On the other hand, the limited thermal tunability of the DFBs is critical for the control of the TX and LO λs in the udWDM-PON. Typical DFBs have a tunability ratio of ~0.1 nm / ˚C [Gro14], covering ~3 nm (375 GHz) by ±15 ˚C temperature swing, large enough to spread over many, though not all, udWDM channels. To properly manage the λ activation process and operation, a set of heuristic channel assignment algorithms with dynamic wavelength allocation (DWA) have been proposed to avoid collisions and efficiently organize the udWDM spectrum, lowering the blocking probability of new users connecting to the PON and satisfying network changes in environmental temperature [Sal16].

To demonstrate the functioning of this novel class of low-cost coherent TRXs for PON, prototypes of the coherent ONUs were built for the COCONUT field trial, to operate in real-time over deployed dark-fiber network. A set of coherent TRXs were implemented, based on different modulation formats (ASK or PSK), modulation types (direct or external), detection schemes (homodyne, intradyne or heterodyne), prototyping (analog or digital) and bit rate (1.25 or 10 Gb/s). This emulates a multiservice scenario, and provides worthy comparative of performances and compatibility assessment. This section focuses on the ONU prototypes with PSK modulation at 1.25 Gb/s. The description and technical details of the ASK systems, and the others with higher bit rates, are reported in [Pre17], [Art15], including a novel architecture for polarization-independent intradyne RX using 3x3 coupler, for intensity modulated optical signals [Cia14].

4.2.1 Digital FPGA homodyne ONU

This section presents the design and implementation of the 1.25 Gb/s DPSK homodyne ONU for the COCONUT PON derived from the proposed homodyne TRX architecture in Section 3.1.1, implemented with direct phase-modulated DFBs at the TX, simple and low-cost optical components, and FPGA platform for real time DSP at the coherent RX. The functional block diagram of the homodyne ONU is depicted in Fig 4.2.

The direct-DPSK TX consisted of a directly-modulated DFB laser with 4MHz linewidth, emitting at 1550.92 nm. The launch power was 0 dBm for the US transmission through the COCONUT ODN. The laser modulation was driven either by a Pulse Pattern Generator (PPG) with PRBS-31 binary NRZ sequences for BER measurements, or by a Gigabit Ethernet (GbE) interface emulating real Ethernet traffic. In both cases the data rate was 1.25 Gb/s. The binary data were differentially encoded, then properly equalized for direct phase modulation of the DFB. The equalizer consisted of the high-pass RC filter introduced in section 2.4.2, and implemented with the circuit depicted in Fig. 4.3(b). The cut-off frequency of the HPF is given by $f_c = 1/(2\pi \mathrm{RC})$, and was experimentally optimized by varying the capacitance C with respect to the total R = 100 Ω. Results are plotted in Fig. 4.3(a) in terms of the sensitivity penalty at BER = 10^{-4} after DPSK detection, as a function of the HPF cut-off frequency. Accordingly, 1.5 GHz HPF was selected, corresponding to about 1 pF capacitor.

At the coherent homodyne RX, the implemented RX was polarization dependent because of the limited number of available components, and was realized by a 3x3 optical coupler, a DFB as LO with 4 MHz linewidth, and 3 PIN PDs. The LO power was 3dBm, and its SOP was manually

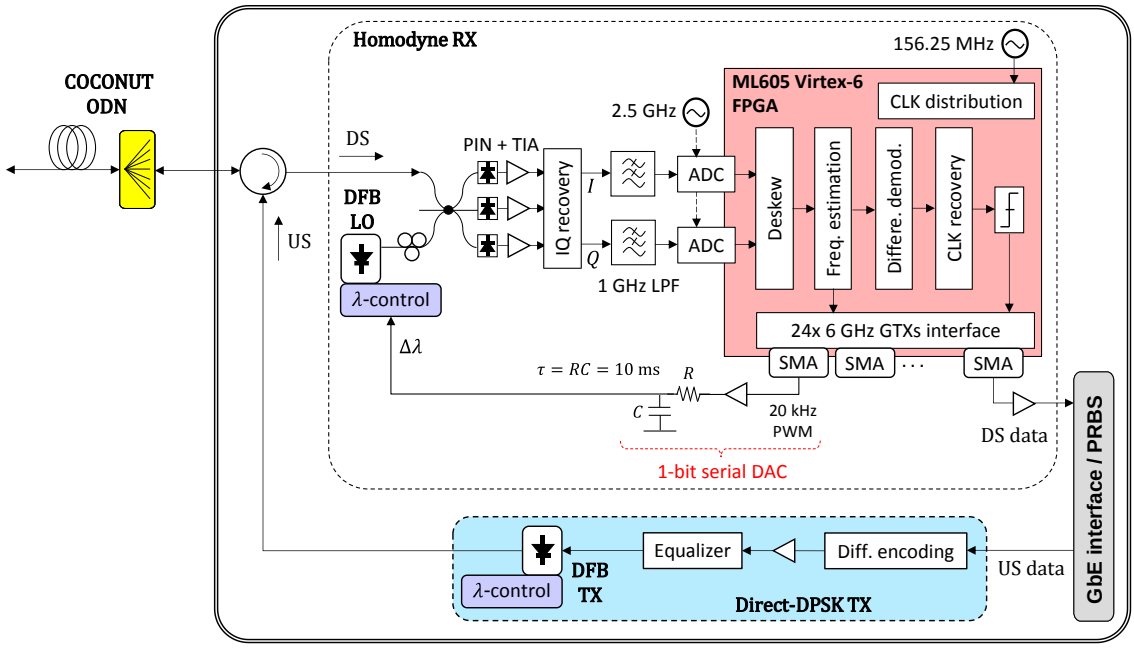

Figure 4.2. 1.25 Gb/s DPSK coherent homodyne ONU architecture, with real-time DSP at the RX implemented in FPGA.

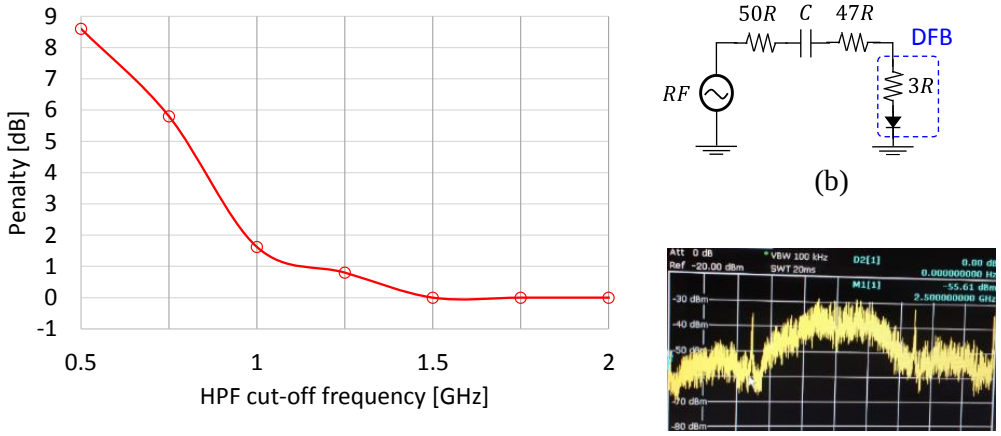

Figure 4.3. (a) Experimental sensitivity penalty at BER = 10^{-4} vs. cut-off frequency of the high-pass equalizer for direct 1.25 Gb/s DPSK; (b) circuit diagram of the first-order HPF equalizer; (c) photodetected spectrum of the obtained DPSK modulation with 1.5 GHz HPF equalizer.

adjusted at the RX input to match that of the received optical signal. The three photocurrents were linearly combined in passive hardware to recover the I and Q components. These front-end functionalities –photodetection, IQ recovery– were integrated in a printed circuit board (PCB) with FR-4 substrate, using commercial TO-CAN packaged PIN + TIA photodetectors with ~2 GHz BW.

Afterwards, the I and Q signals were low-pass filtered by two standard 4th order Bessel filters with 1GHz BW for antialiasing and out-band noise rejection. The filtered IQ signals were individually mapped into the digital domain by two time-interleaved ADCs with 8 bit resolution, sampling at 2.5 GSa/s. All the subsequent DSP was carried out with two samples per bit. The ADCs were connected through the FMC port to a Xilinx ML605 board, which hosted a Xilinx Virtex-6 FPGA

model XC6VL240T. The ML605 board also incorporates DSP slices, RAM blocks, mixed-mode clock manager, Ethernet MAC modules, and 24× 6 GHz Gigabit TXs (GTX) with SMA ports for high-speed input/output digital data transfer. The FPGA is based on 8-parallel bits architecture, thus its process CLK was set to 156.25 MHz for real-time parallel processing of the 1.25 Gb/s data streaming. After the DSP, the recovered data were amplified by a 1 GHz low-noise amplifier, and delivered either to a GbE Ethernet interface or to a BER tester.

The thermally tunable DFB lasers used as TX and LO implemented an electronic fast λ-control system, by simultaneous tuning of the laser bias current and the thermoelectric cooler (TEC) available in the DFB packaging. The implemented λ-control system exhibits a time constant of 700ns for frequency shifts of 12.5 GHz [Pol14], much faster than tuning the λ only by temperature with the TEC, with time constants in the order of tens of seconds. This allows for tuning the coherent ONU to the assigned λ-channel, but also for the fast λ-tracking of the LO for accurate homodyne matching with the received λ. For fast LO tracking, the λ-control is driven by the estimated $\Delta\lambda$ at the DSP, later used to control the duty-cycle of a 20 kHz square wave to generate a pulse-width modulation (PWM), that was low-pass filtered in the analogue domain by a RC filter with a time constant $\tau = 10$ ms, as detailed in Fig. 4.2. It becomes a simple 1-bit serial DAC for low-cost implementation of the feedback loop for AFC.

A picture of the assembled prototype of the coherent homodyne RX is shown in Fig. 4.4, with detail of the Xilinx ML605 FPGA board and the other RX subsystems.

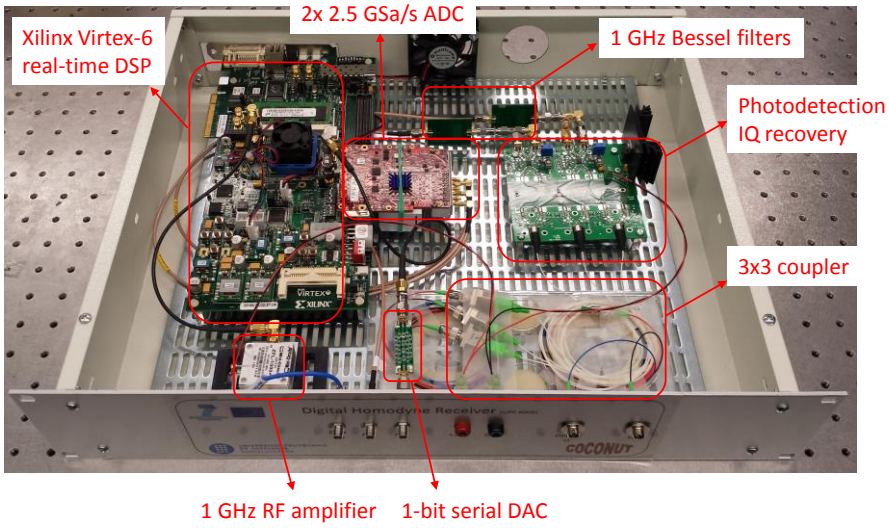

Figure 4.4. Assembled prototype of the 1.25 Gb/s DPSK digital homodyne RX.

For udWDM operation, the homodyne ONU employs separated λ-bands for the US and the DS. The separation between adjacent channels is as low as 6.25 GHz, for 1.25 Gb/s λ-to-the-user, as found in Section 3.4.1.3. The optical spectrum at the homodyne ONU is illustrated in Fig. 4.5.

4.2.1.1 DSP subsystems

The DSP implemented for the coherent RX consisted of simple yet effective techniques, avoiding

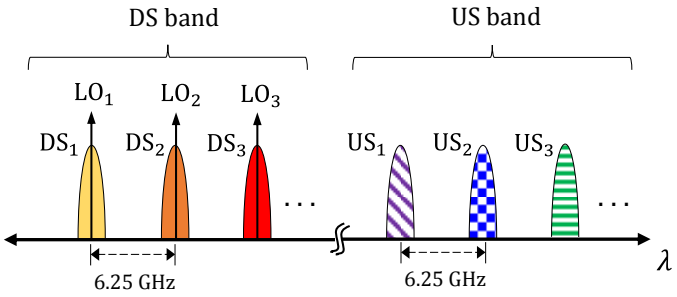

Figure 4.5. Optical spectrum at the homodyne ONU for bidirectional transmission.

sophisticated algorithms that certainly increase the system performance, but also the implementation complexity and total cost. In pursuing this idea, the RX DSP comprised four main subsystems based on well-known DSP algorithms for digital coherent RXs [Sav10], [Bor14].

First, the deskew algorithm calculates the temporal delay between the I and Q signals due to non-symmetrical paths in the RX front-end. The IQ skew is estimated from the cross-correlation between I and Q. A block length of 64 samples was selected for the cross-correlation. Note that it only compensates for integer delays that are multiple of the sampling time T_s (the inverse of the sampling rate R_s). Otherwise, to compensate for fractional delays the deskew must be performed from interpolated signals. The deskew algorithm does not need to be running real-time for each CLK cycle; indeed, the IQ skew is estimated only once, when the receiver lights up, then the estimated delay holds over time for the real-time data streaming.

Next, the frequency estimation block implements the IQ correlation algorithm examined in Section 5.1.2. It estimates the phase increment $\Delta\varphi$ between consecutive samples due to the TX-LO frequency detuning, that was later used to drive both the feedforward data correction and the continuous tuning of the LO. The calculated $\Delta\varphi$ exhibited a linear region across $\pm$500 MHz TX-LO frequency detuning (see Fig. 5.6). After closing the feedback loop with the DFB-LO for continuous λ-tracking, the frequency detuning was kept below $\pm$50MHz, enabling the homodyne detection of the 1.25 Gb/s DPSK data. Right after correcting for the frequency detuning, the differential demodulation deals with the phase noise from the lasers, and extracts the data encoded in the phase of the optical carrier. After demodulating I and Q separately, both signals are added to counteract the phase noise effect.

Last, the CLK recovery algorithm corrects for the timing mismatch between the OLT TX and the ONU RX, as they do not operate with synchronous CLK. The CLK recovery algorithm usually has two components: a timing error detector (TED) and an interpolator. The TED implemented in the FPGA was derived from the Gardner synchronizer [Gar86], leveraging an interpolator to find the optimal sampling point by looking at the maximum eye diagram aperture after demodulation. The interpolation was carried out by a Farrow structure with two 3-tap FIR filters performing piecewise parabolic interpolation. [Väl95]. Often in digital RXs, CLK recovery is carried out before frequency estimation and optical phase recovery. Nevertheless, the simple algorithms implemented here can operate with unrecovered clock, and the timing recovery is achieved at the end of the DSP chain over a frequency-and-phase-noise-free signal, thus relaxing the requirements and complexity of the CLK recovery algorithm. The CLK recovery downsamples the baseband signal from two to one sample per bit, that is finally thresholded for

data decision and bit recovery.

4.2.2 Analog DPSK heterodyne ONU

The 1.25 Gb/s DPSK heterodyne ONU implemented for the COCONUT PON is derived from the proposed heterodyne TRX in Section 3.1.2, with the following TX and RX simplifications: (I) the RX front-end only employs two PDs, one per each polarization; (II) the optical TX reuses the LO λ for the US channel, allowing the coherent ONU to operate with single laser. The architecture of the heterodyne ONU, fully analog, is depicted in Fig. 4.6.

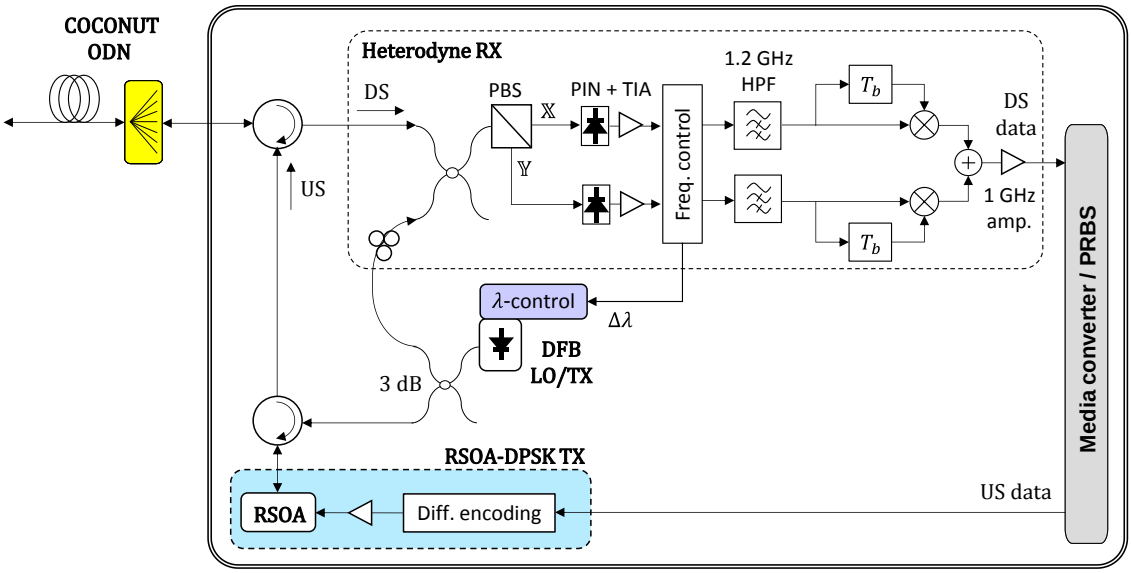

Figure 4.6. 1.25 Gb/s DPSK coherent heterodyne ONU architecture, with fully-analog implementation.

The coherent RX consists of a polarization-diversity heterodyne front-end with single-ended photodetection, reported in [Gla87], [Can14b]. A 3 dB optical coupler mixes the incoming DS signal with the LO, a DFB with 4 MHz linewidth. The output of the coupler passes through a PBS, dividing the optical beating signal into its two orthogonal SOP components. Each polarization was later photodetected by a TO-CAN packaged PIN + TIA photodetector with 7 GHz BW. The LO λ was shifted by 2.5 GHz from the DS λ for heterodyne detection, and its power was 5 dBm.

The electrical processing of the detected DPSK signal is realized with fully analog components, without ADCs nor digital processors. First, the analog AFC system analyzed in Section 5.2 was implemented to accurately control the IF = 2.5 GHz of the heterodyne detection. The linear estimation region of the detuning $\Delta\lambda$ ranges from about 1.25 to 3.75 GHz, i.e., $\pm$1.25 GHz with respect to the target 2.5 GHz separation (see Fig. 5.18). The estimated detuning drives the fast electronic λ-control system described in the previous section, installed to the single DFB of the ONU. Next, the two photocurrents –one per each SOP– were independently filtered by two HPFs having a cut-off frequency of 1.2 GHz. The HPF in combination with the limited BW of the electronic HW, intrinsically performs the optimal pass-band filtering required for heterodyne detection, as reported in Section 3.2. Then, an analog delay-and-multiply circuit differentially

decoded the signal real-time, and subsequently both demodulated data streams were added to overcome SOP mismatching. The baseband electrical data at 1.25 Gb/s were finally low-pass filtered and amplified by a 1 GHz low-noise amplifier, then delivered to a media converter (MC) module connected to multimedia streaming servers through a RJ-45 connector, or to a BER tester for sensitivity measurements.

The direct DPSK TX is based on reflective semiconductor optical amplifier (RSOA) to reuse the same emission λ of the LO for the US link, i.e., shifted by 2.5 GHz from the DS. The RSOA operated in the saturation gain region that, along with the high input power from the DFB (~1 dBm), optimized the PM modulation of the RSOA and lowered the residual IM [Chu15]. The 1.25 Gb/s NRZ data for the US were differentially encoded, then phase-modulated the RSOA. The generated DPSK signal passed through a circulator to be coupled into the COCONUT ODN with 0 dBm optical power. Note that the optical front-end of the heterodyne ONU implements two optical circulators: one for US/DS separation, and other for feeding the RSOA with the LO lightwave.

The optical spectrum at the heterodyne ONU is illustrated in Fig. 4.7. In contrast with the homodyne ONU in previous section, the heterodyne ONU features the closest separation between the US and DS links, set to 2.5 GHz by reusing the DFB LO as TX for the US. Nevertheless, the adjacent udWDM users are separated by 12.5 GHz, twice the homodyne channel spacing, to allocate for the image frequency characteristic of the heterodyne detection, as studied in Section 3.4.1.3.

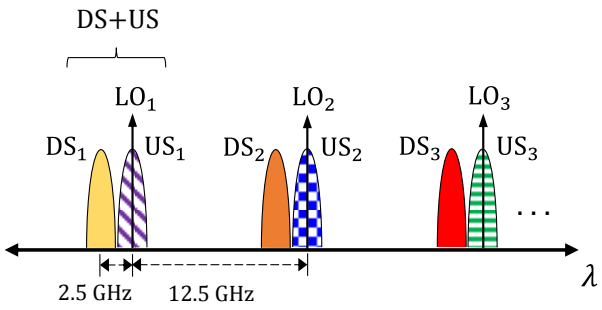

Figure 4.7. Optical spectrum at the heterodyne ONU for bidirectional transmission.

4.3 COCONUT Field-Trial

The udWDM-PON field-trial carried out for the public demonstration of the COCONUT project, was implemented in the access network laboratories of the Scuola Superiore Sant'Anna in Pisa, Italy. The overall scheme of the network is illustrated in Fig. 4.8. The udWDM COCONUT PON consisted of a set of coherent TRXs operating in real-time at 1.25 Gb/s (the 10 Gb/s TRX implemented off-line processing), using various modulation formats (ASK or DPSK) and coherent detection schemes (homodyne, intradyne or heterodyne). The coherent TRX prototypes were implemented by either analog processing with electronic hardware or DSP with FPGA.

At the OLT side, 14 WDM signals performing as DS were multiplexed by an arrayed waveguide

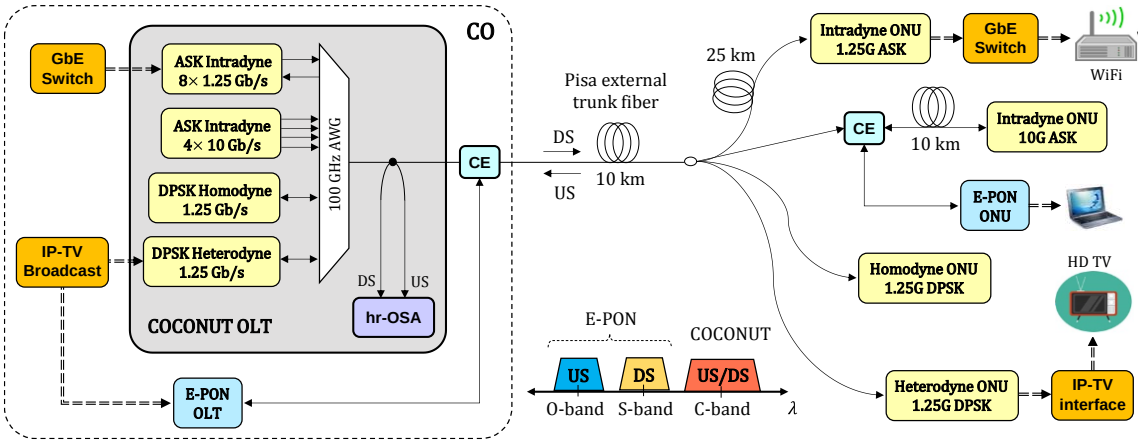

Figure 4.8. COCONUT udWDM-PON field-trial, using real-time coherent ONU prototypes with multimedia services. The inset shows the optical bands used for bidirectional transmission in the trial. CO: central office; CE: coexistence element.

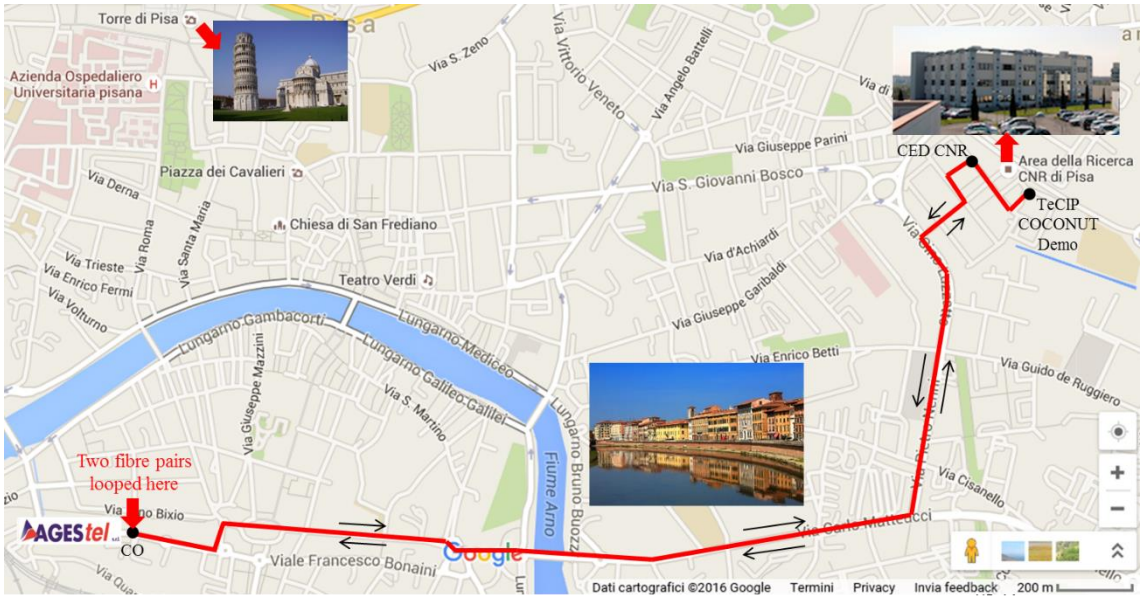

Figure 4.9. Optical distribution network: 10 km external trunk fiber.

grating (AWG) with 100 GHz channel spacing and 100 GHz full-width at half maximum (FWHM) on each channel. The DS signals were connected to seven input ports of the 100 GHz AWG in the following configuration: 1.25 Gb/s DPSK for the homodyne ONU; 1.25 Gb/s DPSK for the heterodyne ONU; 8× 1.25 Gb/s ASK, on a 6.25 GHz grid, for the intradyne ONU; and 4× 10 Gb/s ASK, using four individual 100 GHz AWG channels, also for intradyne ONU. The channel selection at the ONUs was done by tuning the LO to the assigned transmitted λ. In addition, a coexistence element (CE) inserted an E-PON signal into the COCONUT PON to assess the coexistence and seamless integration of the udWDM network with legacy PON systems. The CE consisted of a commercially available optical filter originally designed for NG-PON2 applications, that guaranteed error-free operation of the E-PON system. The COCONUT OLT also implemented the hr-OSA for monitoring the DS and US channels.

The ODN exploited a 10 km G.652 SMF dark-fiber installed across the city center of Pisa, Italy,

as shown in Fig. 4.9, and made available by the local company AGESTEL. It was followed by a cascade of optical power splitters and extra SMF spools, connecting a total of 5 ONUs. With this configuration, the fiber reach ranged from 10 to 35 km. At the OLT, the launched power per udWDM channel was 0 and 3 dBm for the DPSK and ASK systems respectively.

At the ONU side, 3 different options for US allocation were considered: the ASK intradyne systems used two different 100 GHz ITU bands for US and DS, the DPSK homodyne system employed ultra-dense 6.25 GHz spacing between US and DS, and the DPSK heterodyne system featured ultra-narrow 2.5 GHz spacing between US and DS by reusing the LO laser as TX for the US (see Fig. 4.7). Both at the OLT and the ONU sides, some of the coherent TRXs were connected to Ethernet switches or multimedia streaming servers to demonstrate network operations in a heterogeneous distribution of real-time traffic. The COCONUT TRXs have been operated at the C-band, with λs ranging from 1546.12 to 1551.72 nm, as depicted in Fig. 4.10(a), that also shows the λ allocation for the E-PON system hosted in the testbed. Figs. 4.10(b) and 4.10(c) report on the optical spectrum at the OLT, showing the 14 udWDM channels for DS plus the E-PON signal.

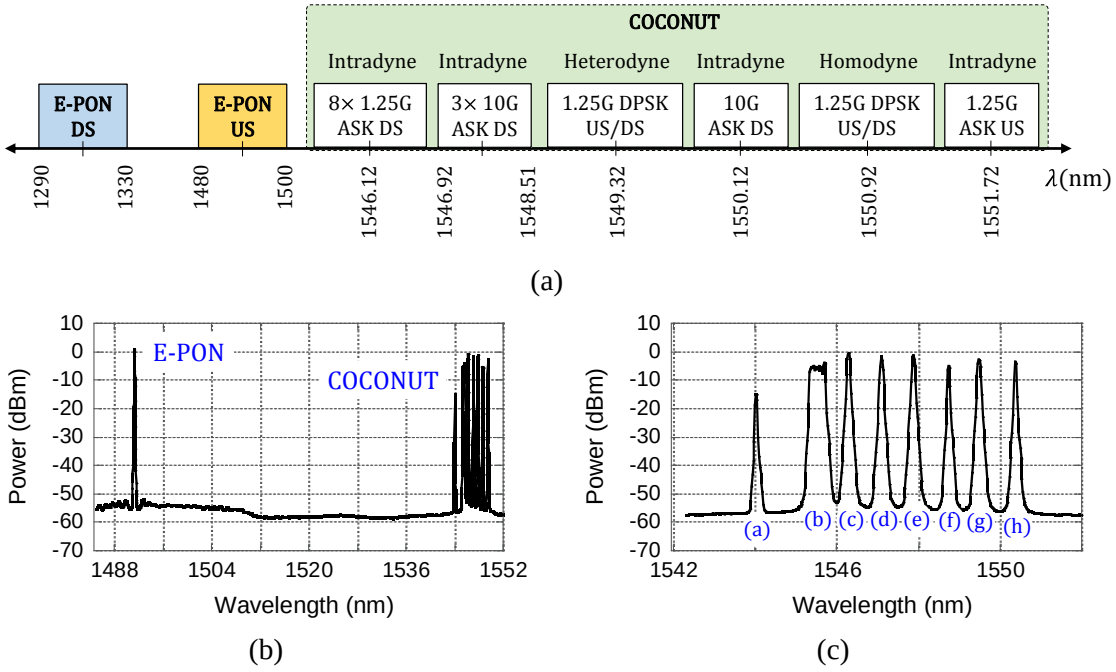

Figure 4.10. (a) Wavelength allocation plan used for the COCONUT field-trial; (b) optical spectrum at the OLT; (c) zoom into the 14 COCONUT DS channels at the C-band: (a) pilot tone, (b) 8× 1.25G ASK, (c)-(e) 10G ASK, (f) 1.25G DPSK, (g) 10G ASK, (h) 1.25G DPSK.

4.4 Results and Discussion

The coherent ONU prototypes were evaluated in the COCONUT testbed in terms of RX sensitivity, ultra-dense WDM multiplexing with narrow channel spacing, and coexistence with heterogeneous real-time traffic and legacy PON systems. Due to the fact that each COCONUT user owns a dedicated λ, the udWDM-PON behaves as a virtual point-to-point network with both DS and US operating full-duplex at different λs; therefore, the results and analysis provided in this section are reasonably valid for both streams. For BER measurements, PRBS-31 digital

sequences at 1.25 or 10 Gb/s were used as data, then detected and processed real-time by the analog/digital coherent TRXs, and the recovered data were finally delivered to BER testers for error computing.

Let us first consider the homodyne ONU with DPSK at 1.25 Gb/s. This system was initially tested in optical back-to-back (btb) as benchmark, and the results are reported in Fig. 4.11(a) in terms of the BER against the received optical power. As observed, the homodyne RX achieved a high sensitivity of -53 and -46 dBm for BER = 10^{-3} and 10^{-9} respectively, that matches well with the performance estimate in Table 3.9. The recovered eye diagrams after differential demodulation and CLK recovery (i.e., data are already at one sample per bit) are depicted in Fig. 4.11(b), for the two BER values in the btb test.

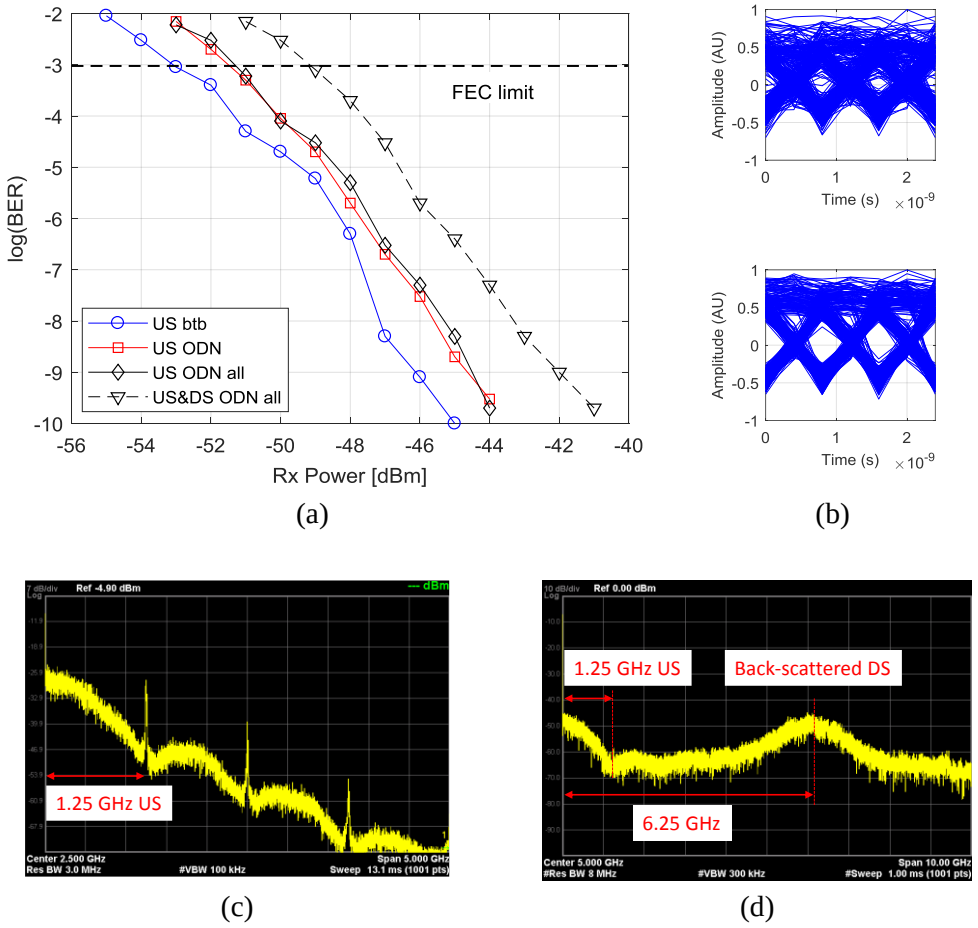

Figure 4.11. (a) Real-time BER vs received power for 1.25 Gb/s DPSK detected with homodyne ONU in the COCONUT PON; (b) normalized eye diagram at the RX after demodulation for btb test, with BER = 10^{-3} (upper) and BER = 10^{-9} (lower). Electrical spectrum at the RX after photodetection for (c) only US direction in btb, and (d) bidirectional transmission through the ODN.

Next, the system was connected to the COCONUT testbed with all the other systems disabled, and the US was detected. As observed in Figure 4.11(a), the RX sensitivity penalty at FEC threshold of BER = 10^{-3} is found to be 1.5 dB compared with btb transmission due to impairments that arise from the ODN, mostly optical reflections. The US direction was detected again with all the systems connected to the PON for the coexistence test, with no apparent penalty as observed

in the curves, thus confirming the filterless operation of the PON driven by the superior selectivity of coherent detection, which uses λ-tuning of the LO in combination with sharp electrical filtering to reject the out-band interference from the other systems in the PON.

Last, the DS was activated to assess the bidirectional udWDM operation. The DFB TX of the OLT modulated PRBS data uncorrelated with the US, to generate the 1.25 Gb/s DPSK signal for DS. The US and DS were separated in λ by 6.25 GHz. The BER curve in Fig. 4.11(a) for the US detection indicates 2.5 dB penalty at FEC threshold for bidirectional operation when compared with only US transmission through the ODN, and 4 dB penalty with respect to the btb test. The sensitivity penalty originates from the back-reflections in the external trunk section of ODN, which included several connections (SC/PC connectors) in outside cabinets. This phenomena can be clearly appreciated when comparing the electrical spectrum at the OLT Rx after photodetection for the btb test, in Fig. 4.11(c), with that of the bidirectional transmission through the ODN, in Fig. 4.11(d). Note that the strong back-reflection of the counter propagating DS channel is comparable in power to the weak detected US channel; although US and DS are separated by 6.25 GHz, the back-scattered spectral tails DS fall into the US BW, producing penalty at the detection.

The BER performance of the heterodyne ONU with 1.25 Gb/s DPSK data is reported in Fig. 4.12(a). The first test, optical btb, differed from the homodyne btb test in that bidirectional US and DS were active, because the single DFB laser in the heterodyne ONU lighted up both the TX and the RX. The BER corresponds to DS detection by the ONU RX, and the achieved sensitivities were nearby -38 and -32 dBm for 10^{-3} and 10^{-9} BER respectively. In this case, the RX sensitivity is lower than the estimated in Table 3.9 due to several reasons: (I) the single-ended detection added 3 dB penalty because one branch of the 2x2 coupler is unused (see Fig. 4.6); (II) the LO power was divided with a 3 dB optical coupler to also feed the RSOA, thus the RX sensitivity was accordingly reduced by 3.5 dB approximately including the coupler excess loss; (III) the common-mode noise and the LO RIN that are not cancelled due to the single-ended detection. The eye diagram in btb after differential demodulation is reported in Fig. 4.12(b) for two BER.

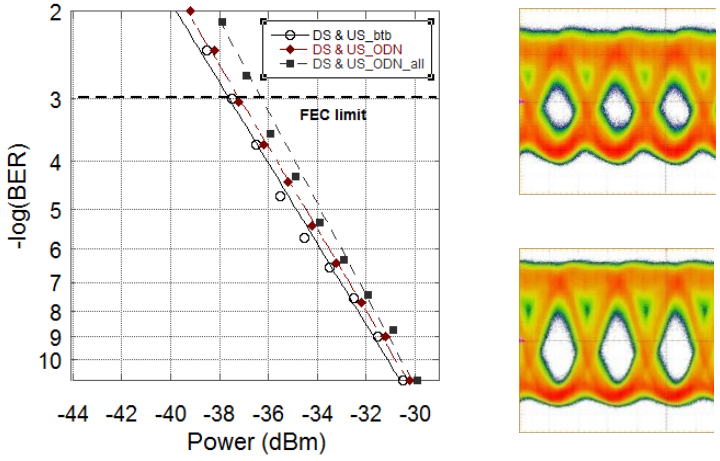

(a) (b)

Figure 4.12. (a) Real-time BER vs received power for 1.25 Gb/s DPSK detected with heterodyne ONU in the COCONUT PON; (b) eye diagram at the RX after demodulation for btb test, with BER = 10^{-5} (upper) and BER = 10^{-9} (lower).

The heterodyne system was later connected to the COCONUT ODN, with and without the other systems. The results in Fig. 4.12(a) indicate that, at FEC threshold, the power penalty after transmitting through the ODN is negligible, but arises up to 1.5 dB when coexisting with all the other COCONUT systems. It is worth noting that, for bidirectional transmission, the heterodyne ONU suffers less sensitivity penalty (1.5 dB) than the homodyne ONU (4 dB), with respect to the b2b test. This can be ascribed to the better sensitivity of the homodyne RX at FEC level: the received signal is very weak (-53 dBm), thus more affected by the strong back-reflections from the ODN that are aliased into the signal BW (see Fig. 4.11(d)).

The functioning of the real-time coherent ONU prototypes was also demonstrated in the trial with multimedia services. For the DPSK prototypes, GbE frames were used to simultaneously transport four data streams, consisting of three multi-service video and one high-definition (HD) video broadcasted by a PROMAX HD video player module. In the case of the ASK systems, several 4K video were transmitted from a multimedia server, as well as WiFi internet connectivity through an ERICSSON access point. In all cases for multimedia real traffic demonstration, the COCONUT ONUs were set to operate error-free (i.e., the received power was adjusted to BER = 10^{-9}), since none of the prototypes incorporated FEC encoders/decoders.

Table 4.1 summarizes the main features and performances of the coherent ONUs for bidirectional transmission in the COCONUT testbed. The results include the ASK systems at 1.25 and 10 Gb/s. For the 10G system, BER values smaller than 10^{-6} were not measured due to the off-line processing. In general, all the systems show excellent RX sensitivities both at BER of 10^{-3} (where 2nd generation FEC can be implemented) and 10^{-9} (used for real-time GbE and video streaming tests). The homodyne ONU achieved the best sensitivity in its polarization-dependent configuration and digital processing with FPGA. Conversely, the heterodyne ONU shows the lowest RX sensitivity but features the simplest architecture and the highest power efficiency by owing single-laser at the ONU.

Table 4.1. Summary of performance and main characteristics of the coherent ONU prototypes operating bidirectional real-time in the COCONUT testbed.

System	**Receiver type**	**Intermediate frequency**	**Channel spacing [GHz]**	**Signal processing**	**Testbed sensitivity [dBm]**	
					BER = 10^{-3} 2nd generation FEC	**BER = 10^{-9} Real-time GbE**
1.25 Gb/s DPSK	2x2 heterodyne	2.5 GHz	12.5	Real-time analog	-36.5	-31
	3x3 Homodyne	< 50 MHz	6.25	Real-time digital with FPGA	-49	-42
1.25 Gb/s ASK	3x3 Intradyne	900 MHz	6.25	Real-time analog	-47	-39
10 Gb/s ASK	3x3 Intradyne	3 GHz	100	Off-line with RTO	-35	–

Overall, the coherent ONUs outperform conventional IM-DD ONUs by improving the RX sensitivity, reported to be -36 (the lowest, for E2 class ODN) and -28 dBm for 1.25 and 10 Gb/s respectively [ITU19]. Furthermore, the trial successfully confirmed that the TRXs preserve their performance also when operated in the testbed, where the systems are affected by reflections in the ODN, and a significant number of channels are lighted up: 17 WDM channels in total, 14 channels as DS and 3 channels as US.

Based on the results from the field-trial in Table 4.1, the COCONUT udWDM-PON can be dimensioned and compared with XG-PON / NG-PON2 standards. Depending on the ODN class, optical power budget (PB) from 30 up to 35 dB are targeted in next-generation PON [ITU19], to coexist with legacy PON systems. The PB is a crucial parameter dictating the choice of technology to deploy next-generation optical access. In udWDM-PON, for instance, larger PB directly translates into larger splitting ratio serving more users, and/or extended fiber reach. Owing to the superior sensitivity of the coherent RXs, even larger PB > 40 dB can be achieved in the COCONUT PON. Table 4.2 details the PON dimensioning when taking as reference a target PB of 40 dB.

Table 4.2. COCONUT udWDM-PON dimensioning and comparison with standards for PON.

	TX power per channel for 40 dB PB[1] [dBm]	**Maximum number of channels[2]**	**Bit rate per λ [Gb/s]**	**Aggregated PON capacity [Gb/s]**	**Channel spacing [GHz]**
XG-PON [ITU17]	12	–	10	10	–
NG-PON2 [ITU19]	12	8	10	80	50/100
COCONUT udWDM-PON	-3	256	1.25	320	6.25

[1]Referred to -28 dBm RX sensitivity at 10G for XG-PON and NG-PON2.
[2]Below the eye safety threshold of 21 dBm.

By considering 21 dBm emitted optical power as the eye safety frontier, and having in mind 256 udWDM users, the emitted power per channel in COCONUT PON must be reduced to -3 dBm, which represents not any limitation by virtue of the high sensitivity of the coherent RXs (regardless the heterodyne DPSK RX sensitivity in the trial, that obeys a particular implementation and can be improved). Hence, the total number of ONUs that can be served by dedicated λs at 1.25 Gb/s is 256, and the aggregated PON capacity reaches 320 Gb/s, four times larger than NG-PON2. The spectral efficiency is further improved by reducing the channel spacing from 50/100 GHz down to ultra-dense 6.25 GHz, and the power consumption of the ONU is lowered as the TRXs operate at lower data rate and lower emitted optical power.

Note that the TWDM-PON (NG-PON2) improves the optical efficiency with respect to TDM-PON (XG-PON) by multiplexing several TDM λs. Alternative techniques for optical access like

radio-over-fiber (RoF) or orthogonal frequency division multiplexing (OFDM) aim at improving the electrical efficiency of the ONU [Cvi12], [Can15a]. Notably, the great improvement in both spectral efficiency domains is achieved with the COCONUT udWDM-PON, which can translate into relevant energy consumption and cost savings. This is particularly relevant in access networks and other optical networks with high terminals density, because any increase in efficiency scales rapidly to significant quantities.

4.5 Chapter summary

This chapter reported on the results and main outcomes of the European COCONUT project, aimed at the development of cost-effective optical access by implementing the λ-to-the-user concept, where hundreds of dedicated λs for each user are efficiently allocated in the optical spectrum in ultra-dense WDM grid. The main enabling technology is the use coherent detection with simplified TRX architecture, thus filling the gap between the high-performance yet costly commercial coherent TRXs, and the simple IM-DD TRXs that dominate the PON market segment.

Prototypes of the novel class of low-cost coherent TRXs developed in COCONUT, were built and tested in real-time in a complete udWDM-PON field-trial. The system testbed has been implemented to demonstrate the most relevant COCONUT-PON concepts: network capacity upgrade by reusing legacy infrastructure, coexistence with legacy PON systems, ultra-dense WDM multiplexing with statistical λ allocation, and support for long reach and/or large splitting ratio thanks to enhanced optical PB. The trial achieved the successful transmission of multiple PON signals and real-time service distribution over a real optical fiber network deployed in the city center of Pisa, Italy.

The results of the COCONUT field-trial indicate that the udWDM-PON can effectively implement dedicated λ-to-the-user at 1.25 Gb/s (or higher, when required) in a filterless PON with channel spacing as low as 6.25 GHz, serving up to 256 users. Optical PBs in excess of 40 dB are obtained by virtue of the high sensitivity of the coherent RXs, implemented with low-cost optics and simple electrical signal processing, either analog or digital. In this regard, the trial demonstrated that the coherent TRX can be assisted by simple DSP optimized for use in PONs, exploiting simpler and cheaper FPGAs at the ONUs rather than custom expensive ASICs, thus revealing their potential for the future coherent optical access networks.

More generally, the proposed COCONUT PON is flexible in λ allocation, and can conveniently be adapted to operate within the C-band, where low-cost DFBs are available. In terms of overall PON consumption, the optimality of the COCONUT udWDM approach with respect to current TWDM-PON systems, is to reduce the electrical BW to match that the demanded user traffic BW, supported by efficient exploitation of the optical domain, therefore reducing the power consumption of the ONUs.

Chapter 5

Optical Carrier Recovery Strategies

Up until now, this thesis focused on investigating the enabling technologies, key design parameters and challenges to implement the next generation λ-to-the-user access networks with low complexity and cost coherent TRXs. The main transmission impairments were identified and addressed in Chapter 3, pointing out their impact and the maximum tolerance against each of them to operate the coherent TRXs reliably below the BER threshold for FEC. The foregoing investigation contributed to the implementation of the COCONUT testbed to demonstrate the performance and functionalities of the coherent udWDM-PON in a field-trial, whose results were reported in Chapter 4. Hereafter, the remainder of the thesis takes a step forward towards the improvement of the udWDM-PON in terms of performance, complexity, cost, and power consumption, by introducing novel and/or enhanced mitigation strategies for the main transmission impairments employing either low-complexity DSP or analog HW design.

To begin with, one of the major challenges in coherent systems is the synchronization of the received optical carrier with the LO. To avoid the use of PLL systems in homodyne RXs, the phase-diversity architectures can operate with free-running LO and overcome phase synchronization problems by further processing the I and Q signals, as it was derived in Section 2.1.2. In such phase-diversity schemes, the optical frequency of TX and LO lasers must remain as close as possible to each other, with an error less than 6% of the bit rate for DPSK (see Section 3.3.2), to avoid penalty at the detection. This contrast with typical low-cost DFB lasers that exhibit severe λ variability due to thermal environment changes and current supply fluctuations. Laser aging is another factor contributing to λ instability. For instance, tunable lasers integrated with external modulator for use in telecommunications equipment operating in the C or L band, exhibit frequency accuracy of ±2.5 GHz over lifetime [OIF08]. This also becomes a major issue in udWDM-PON as the ODN is filterless, and the channel selection is done at the coherent RX by tuning the λ of the LO. Hence, accurate LO λ-control is mandatory for correct data detection and channel stability in such a closely-spaced udWDM grid.

The LO λ-control system is driven by the CR subsystem of the RX, in which this chapter focuses on. The block diagram of a conventional digital coherent RX implementing the complete CR subsystem is illustrated in Fig. 5.1. After coherent beating at the RX front-end, the ADCs gather digital samples of the received I+jQ signal to be processed by the DSP stage, which performs frequency estimation (FE), LO tuning, and optical phase recovery (PR). Usually FE takes place prior PR, although they can be swapped depending on the implemented algorithms. The estimated detuning $\Delta\lambda$ drives both the feedforward correction of the I+jQ signal, and the LO feedback for λ-tuning. Afterwards, the signal I'+jQ' already in baseband is further processed to extract the data encoded in the optical phase, getting rid of the harmful phase noise.

This chapter presents the design and implementation of AFC systems, also known as automatic wavelength control (AWC), for coherent RXs either digital or analog. In the case of digital RXs,

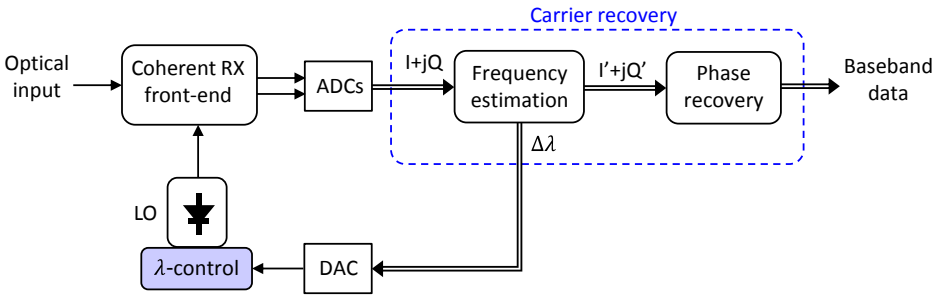

Figure 5.1. Conventional carrier recovery for digital coherent RXs.

simultaneous frequency detuning compensation is achieved by correcting data and tuning the λ of the DFB LO, using the same estimation block, thus lowering the HW complexity. The reported results include frequency noise characterization and DPSK transmission tests. The chapter also present an optimized CR architecture based on differential field detection for digital homodyne RXs, that substantially reduces the required DSP HW resources by reusing the 1-symbol complex correlation required for frequency estimation and differential phase detection. The results indicate improvement in the energy consumption of the digital processor and enhanced tolerance against fast λ-drifts of lasers.

5.1 Algorithms For Frequency Detuning Estimation In Homodyne Receivers

There exist several algorithms reported in literature to estimate the frequency error in digital homodyne RXs. Some of them are based on time domain estimation, while others rely on spectral analysis using fast Fourier transform (FFT) [Sav10]. Alternative strategies have also been proposed like remote λ-control from the OLT by a centralized λ-locker [Rop13].

The goal of the time-domain FE algorithm is to estimate the phase drift $\Delta\varphi = 2\pi\Delta f T_s$ between consecutive samples of the detected signal, produced by the frequency mismatch $\Delta f = f_S - f_{LO}$ between TX (f_S) and LO (f_{LO}) optical frequencies. Here, T_s represents the sampling time. Note that if the m-PSK modulation is removed from the detected $\mathrm{I} + j\mathrm{Q}$ signal, there is no phase drift caused by the laser phase noise over a certain number of consecutive samples, whereas the phase drift caused by frequency mismatch increases a fixed value every T_s. This section considers two algorithms from the variety of available algorithms for time-domain FE in coherent RXs. One approach is the differential mth-power estimator, and the other is based on the cross-correlation between I and Q signals. These algorithms were selected due to their convenient implementation in DSP units, achieving good performance with relatively simple design [Nat84].

5.1.1 Differential mth-power estimator

The first approach consists of a phase-increment estimation algorithm based on the feedforward Viterbi&Viterbi estimation model for m-PSK [Lev07]. The FE architecture is shown in Fig. 5.2.

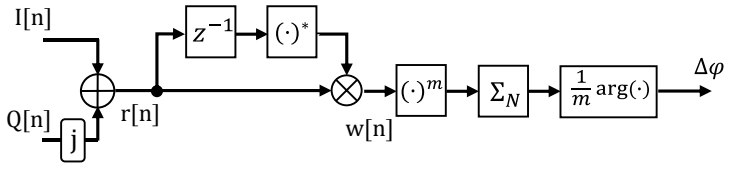

Figure 5.2. Differential mth-power algorithm for FE with m-PSK signals.

The estimate of the phase drift $\Delta\varphi$ is made from digital samples of the received complex signal $r[n] = I[n] + jQ[n]$, which in the general form for m-PSK reads as

$$\begin{aligned} r[nT_s] &= I[nT_s] + jQ[nT_s] \\ &= A[nT_s]e^{j(2\pi\Delta f nT_s + \Delta\phi[nT_s])} \end{aligned} \tag{5.1}$$

with Δf and $\Delta\phi$ the optical frequency and phase difference between signal and LO, respectively. Each sample of $r[n]$ is multiplied by the complex conjugate of the previous sample for differential phase detection, yielding

$$\begin{aligned} w[nT_s] &= r[nT_s] \cdot r^*[(n-1)T_s] \\ &= A^2[nT_s]e^{j(2\pi\Delta f T_s + \Delta\phi[nT_s] - \Delta\phi[(n-1)T_s])} \end{aligned} \tag{5.2}$$

Note that the presence of Δf induces the incremental phase rotation $\Delta\varphi = 2\pi\Delta f T_s$. The other phase term $\Delta\phi[nT_s] - \Delta\phi[(n-1)T_s]$ only varies according to the m-PSK modulation –provided that the total phase-noise is much lower than the sampling rate $R_s = 1/T_s$– and can be cancelled by raising to the power of m. Finally $\Delta\varphi$ is extracted and averaged over the number of block samples N, being expressed as

$$\begin{aligned} \overline{\Delta\varphi} &= \frac{1}{m}\arg\left[\frac{1}{N}\sum_{k=1}^{N}(w[k])^m\right] \\ &= \frac{1}{m}\arg\left[\frac{1}{N}\sum_{k=1}^{N}A^{2m}[k]e^{j(m2\pi\Delta f T_s)}\right] \\ &= \frac{1}{m}\langle m2\pi\Delta f T_s\rangle \end{aligned} \tag{5.3}$$

Here, $\langle\cdot\rangle$ stands for the averaging over a block length of N samples, that counteracts the additive noise and must be optimized at the coherent RX for every specific implementation.

5.1.2 IQ cross-correlation estimator

The second scheme aims at estimate the phase drift $\Delta\varphi$ from the cross-correlation between the detected I and Q signals [Noe05], [Tao07]. Fig. 5.3 shows the block diagram of the correlation based FE algorithm. Indeed, the pair of cross-correlation operations between I and Q in Fig. 5.3 are equivalent to the imaginary part of the complex correlation of $\mathrm{I} + j\mathrm{Q}$ in Fig 5.2, and expressed by $w[nT_s]$ in Eq. (5.2). Hence, the estimate of $\Delta\varphi$ relates to

$$\overline{\Delta\varphi} = \langle I[(n-1)T_s]Q[nT_s] - I[nT_s]Q(n-1)T_s\rangle = \langle \mathrm{Im}\{w[nT_s]\}\rangle \tag{5.4}$$

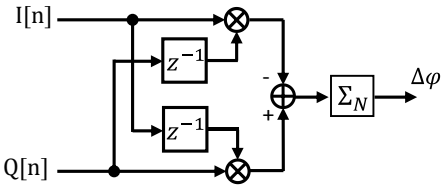

Figure 5.3. IQ cross-correlation FE algorithm for m-PSK signals.

By replacing Eq. (5.2) into Eq. (5.4), one obtains

$$\overline{\Delta\varphi} = \frac{1}{N}\sum_{k=1}^{N} A^2[k]\sin(2\pi\Delta f T_s + \Delta\phi[kT_s] - \Delta\phi[(k-1)T_s]) \tag{5.5}$$

Since the m-PSK modulation is not cancelled as in the previous mth-power FE algorithm, the Eq. (5.5) serves to estimate Δf only if the cross-correlation delay (T_s) is shorter than the symbol time (T_b), i.e., the I and Q signals must be oversampled ($T_s < T_b$). Otherwise, if $T_s = T_b$ the term $\Delta\phi[kT_s] - \Delta\phi[(k-1)T_s]$ varies every T_s due to the m-PSK modulation. Moreover, Eq. (5.5) can be also normalized with respect to the square modulus of $\mathrm{I} + j\mathrm{Q}$ to cancel the dependency of $\overline{\Delta\varphi}$ on $A^2[k]$. Finally, the frequency error estimate becomes

$$\overline{\Delta\varphi} = \langle\sin(2\pi\Delta f T_s)\rangle \tag{5.6}$$

which for smaller values of $\Delta\varphi$ holds the linear relation: $\sin\Delta\varphi \approx \Delta\varphi$. The block length N for averaging must be also experimentally optimized.

5.1.3 Experimental validation

For laboratory assessment of both FE algorithms, the setup depicted in Fig. 5.4 was implemented using a NRZ-PRBS-7 differentially-encoded sequence of 2^{18} bits, stored in an arbitrary waveform generator (AWG) running at 1.25 Gb/s. The PRBS data were used to directly phase-modulate a DFB with 4 MHz linewidth to obtain a DPSK modulation. A VOA was placed at the RX input to adjust the received optical power. At the RX side, the 3x3 coupler mixes the incoming DPSK signal with the LO, that is another 4 MHz linewidth DFB with integrated electronic circuit for λ control, and emitting at 0 dBm. Polarization state of TX and LO was manually adjusted to be matched at the RX input. After photodetection, the three baseband electrical signals were A/D converted by a 50 GSa/s real-time oscilloscope (RTO) operating as a DSP unit. First, low-pass digital filtering at $0.65R_b$ cut-off frequency was applied for noise suppression and subsequently the three signals were adequately combined to obtain the IQ components. Next, a block length of 50 symbols was chosen for frequency detuning estimation using the two algorithms mentioned above. For DPSK data recovery, differential detection of each I and Q signals was performed, then combined to counteract the laser phase noise effect. Finally, the BER was calculated by direct error counting on the received data.

The estimated $\Delta\varphi$ by the DSP is able to drive the feedforward tracking of the frequency error, but also can be used as a feedback metric for LO λ-control [Lav13]. This dual strategy supported by the same FE algorithm in the RX DSP improves the coherent RX performance without the need

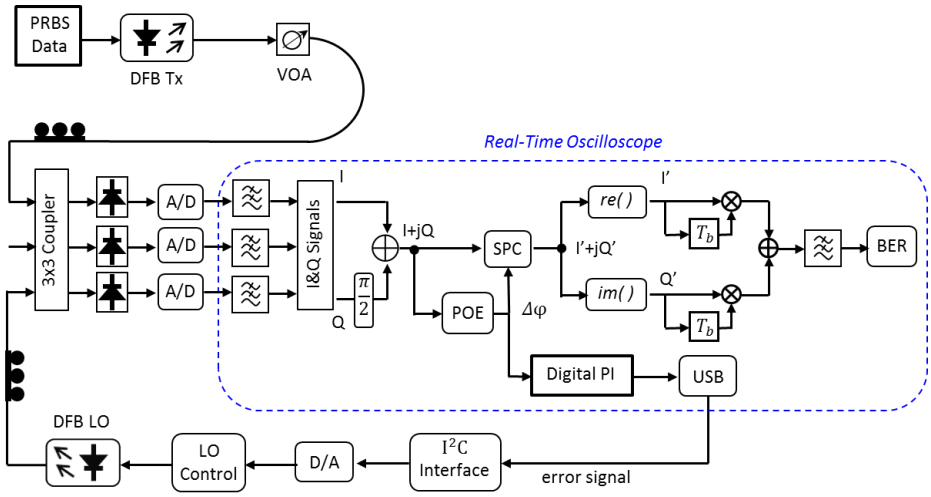

Figure 5.4. Experimental setup. Symbol phase correction (SPC) and phase offset estimation (POE) are performed within the DSP of the coherent RX.

of extra HW for the feedback stabilization of the LO. On the one hand, for fast feedforward tracking of the frequency detuning the accumulated phase offset $k\Delta\varphi$, where k is the symbol index within the estimation block, must be corrected from each sample of the $\mathrm{I} + j\mathrm{Q}$, as illustrated in Fig. 5.5. This cancels the phase rotation of the PSK constellation in the complex plane, as plotted in Fig. 3.15 (Section 3.3.2).

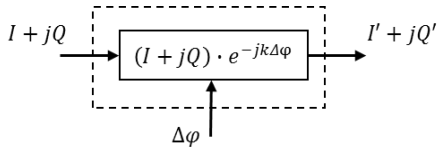

Figure 5.5. Symbol phase correction (SPC) for feedforward frequency error compensation.

On the other hand, for the feedback LO tuning the estimated $\Delta\varphi$ was delivered to a digital proportional-integral (PI) controller whose constants K_P, K_I were adjusted using the Ziegler-Nichols method in order to adequate the control signal to the dynamic response of the tunable DFB LO. The output of the PI controller $u[n\Delta t]$ as a function of $\Delta\varphi[n\Delta t]$, with $\Delta t = 600$ ms the update time of the FE algorithm, reads as

$$u[n\Delta t] = K_P\Delta\varphi[n\Delta t] + \frac{K_I}{1 - z^{-1}}\Delta\varphi[n\Delta t] \tag{5.7}$$

The signal $u[n\Delta t]$ passed on to a 400 kHz inter-integrated circuit ($\mathrm{I^2C}$) interface via USB port, to drive the digital-to-analog (D/A) conversion towards the LO λ-control. The thermally tunable DFB laser used as LO implemented the electronic fast tuning system described in Section 4.2.1, with a time constant of 700 ns for frequency shifts of 12.5 GHz.

Initially, the feedforward frequency error compensation was evaluated in open loop, without LO feedback tuning. The received optical power was set to -47.5 dBm to obtain a reference BER of 10^{-4}. The temperature of the TX DFB was adjusted with an external controller to sweep the optical frequency. After homodyne detection, the $\mathrm{I} + j\mathrm{Q}$ signal was processed to estimate $\Delta\varphi$ for different frequency deviations. Numerical simulation was also performed with the same design parameters

for comparison. As observed in Fig. 5.6, both FE algorithms exhibit a good approximation to a linear $\Delta\varphi$ estimation for $\Delta f = \pm 500$ MHz, with zero-crossing when TX and LO are matched in λ. In addition, frequency errors in between ± 1.25 GHz can be progressively corrected by continuous LO tuning, as the polarity of the estimated $\Delta\varphi$ remains constant for both FE algorithms.

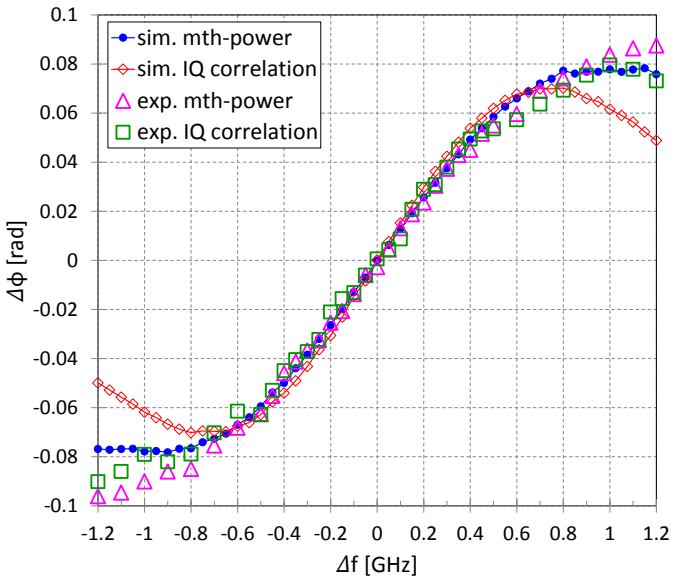

Figure 5.6. Simulated (sim.) and experimental (exp.) estimated $\Delta\varphi$ vs. LO detuning Δf.

Next, the estimated $\Delta\varphi$ was used for feedforward compensation of the detected data. The BER dependence on Δf was measured and plotted in Fig. 5.7(a). The RX performance without $\Delta\varphi$ compensation is highly degraded by the frequency error. On the other hand, compensation of the $\mathrm{I} + j\mathrm{Q}$ signal before data recovery exhibits much more tolerance to Δf, achieving eye opening at $\Delta f = 300$ MHz, as the inset shows. As expected, for Δf larger than ± 500 MHz the compensation performs worse due to the non-linear characteristic of the $\Delta\varphi$ estimation. In Fig. 5.7(b) the BER degradation was translated into sensitivity penalty at BER = 10^{-4}, indicating that in the absence of FE the tolerance to Δf is of ± 100 MHz for 1 dB penalty, whereas data detection with Δf compensation can tolerate up to ± 300 MHz for 1dB penalty, achieving an improvement of 4 dB compared to uncorrected data. It is noticed from the test that there is no meaningful difference in the performance between both FE algorithms.

Afterwards, the dual correction AWC system –feedforward tracking and feedback stabilization– was tested in closed-loop. Fig. 5.8 reports on a long-term measurement of the frequency error over 30 minutes for two scenarios: (I) free-running TX and LO lasers with no AWC system, and physically separated for uncorrelated temperatures, and (II) continuous LO tuning in real-time from the DSP feedback. The results indicate that without AWC the measured Δf shows a random excursion, larger than ± 100 MHz, due to non-stability of DFBs under environment thermal changes. The fastest frequency drift spreads 200 MHz in about 55 seconds, leading to a frequency drift rate of 3.6 MHz/s. In the udWDM grid, as the channel spacing gets narrower, the tolerable frequency drift becomes more severe, yielding strong BER degradation and interference to

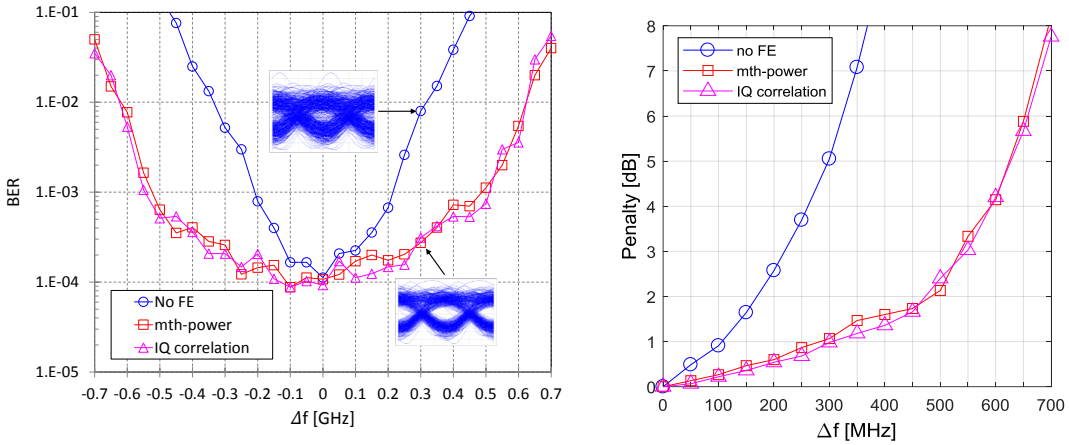

(a) (b)

Figure 5.7. (a) BER dependence on the frequency error for homodyne detection w/ and w/o FE, the insets show the eye diagram for 300 MHz detuning; (b) sensitivity penalty at BER = 10^{-4} vs. frequency error w/ and w/o FE.

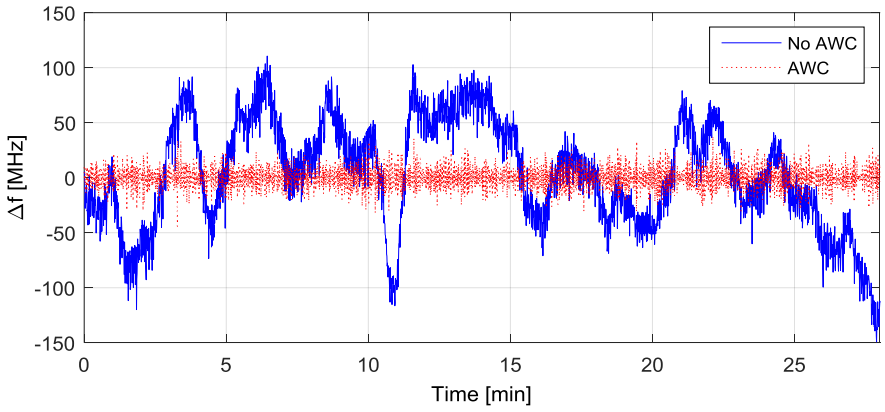

Figure 5.8. Long-term frequency detuning measurement over 30 minutes for homodyne detection w/ and w/o dual AWC system.

adjacent channels. After lighting up the AWC system in closed loop, the Δf was effectively canceled by tuning the LO every 600 ms, fast enough to correct the drifts. Despite the continuous LO tuning, faster oscillations can be observed (also in the case of free-running lasers) due to the faster phase noise, being later removed from data by the differential detection. In addition, sequences of 2048 bits were launched in burst-mode on the 30 minutes test, to record the number of errors for each frame. Results, in terms of the percentage of processed frames with a certain number of errors, are plotted in Fig. 5.9(a). As observed, the AWC at the coherent RX maintains the target BER = 10^{-4} unchanged over time, obtaining about 83% of error-free frames for both FE algorithms.

As a final test, the system was started with arbitrary 500 MHz frequency detuning to analyze the dynamics of the real-time LO tuning process, as well as the benefit of the digital PI. The results in Fig. 5.9(b) show that by using the PI controller to drive the λ-control system of the DFB LO, the 500 MHz error is corrected in a single update time of the AWC loop (600ms) with a further reduction of the Δf oscillations, unlike the AWC loop without PI controller which takes slightly more time for λ stabilization and oscillates more.

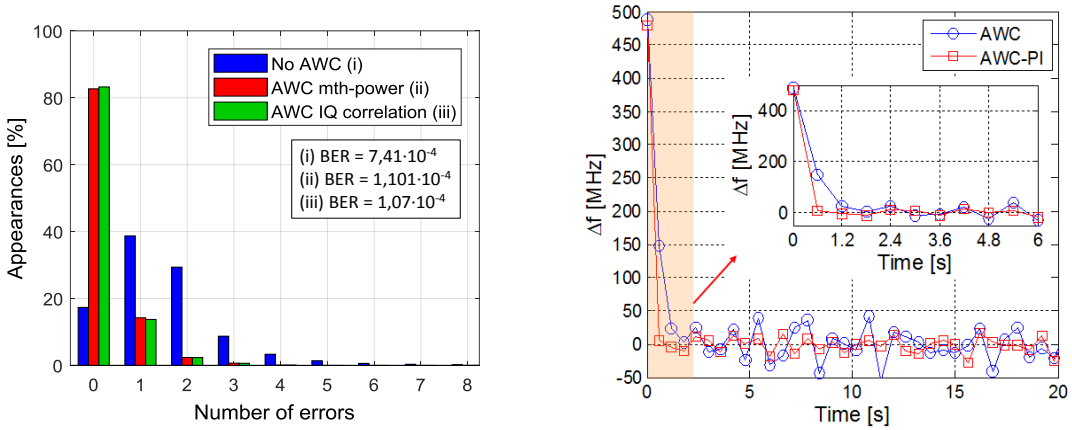

(a) (b)

Figure 5.9. (a) Number of errors recorded in frames of 2048 bits at burst-mode over 30 minutes test for homodyne RX w/ and w/o AWC, the inset shows the measured BER for the three different scenarios; (b) real-time LO tuning evolution for 500 MHz detuning when the AWC lights up.

In summary, the AWC system for digital homodyne RXs with two simultaneous strategies for frequency detuning compensation, can effectively deal with environment temperature changes and high laser frequency noise. The fast feed-forward tracking compensates for any residual detuning after feedback LO tuning, both driven by the same FE algorithm in the RX DSP. Accurate closed-loop performance at a sensitivity of −47.5 dBm, for BER = 10^{-4}, was achieved, as wide as ±500 MHz detuning correction in 600 ms within 2 dB maximum sensitivity penalty. This AWC system is simple enough to be implemented in cost-effective coherent ONUs for udWDM-PON.

5.2 Analog Frequency Detuning Estimation In Heterodyne Receivers

The continuous tracking of the frequency detuning between TX and LO lasers require estimation of the said detuning at the electrical processing part of the coherent RX. In previous Section 5.1 the estimation was carried out digitally by DSP, thus requiring ADCs, DACs, and FPGAs or ASICs. However, for those PON users served by analog ONUs an alternative to FE by DSP consists of a completely analog AWC system where the estimation of the Δf is done electrically by processing the detected photocurrents, with analog HW. This section reports on the design of an AWC (or similarly, AFC) system to control the LO λ in a fully-analog heterodyne RX for PSK or ASK signals.

The system consist of a frequency discriminator placed after the photodetection, at the IF stage, to calculate the detuning with respect to the selected IF of the heterodyne RX. The calculated IF error drives the LO λ-control system. The schematic of the analog frequency discriminator is depicted in Fig. 5.10. To estimate the IF detuning, the detected RF photocurrent $i_{RF}(t)$ is split into two branches that are later low-pass and high-pass filtered respectively by 1st-order RC filters. The 3 dB cut-off frequency of both filters is set to that the IF of the heterodyne RX. Then, a pair

of RF detectors convert the power of the filtered RF signals into a DC level, followed by AC-blocking –i.e., low-pass filtering with narrow BW, in the order of kHz– to reject the residual high frequency components after DC conversion. Finally, the two branches are either subtracted to generate the frequency error signal, and added to obtain the received optical power thus eliminate the dependency of the frequency discriminator on it by means of an automatic gain control (AGC) circuit.

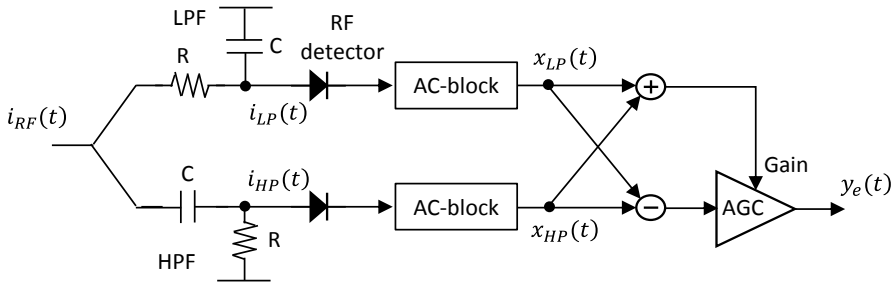

Figure 5.10. Frequency discriminator for AWC system in analog heterodyne RXs.

The output signal $y_e(t)$ is a low frequency signal proportional to the frequency variations of the $i_{RF}(t)$ spectrum with respect to IF. Note that the BW of the signal $y_e(t)$ to make the λ-tracking does not need to be very high because the characterization of the frequency drift rate for free-running TX−LO lasers, as calculated from Fig. 5.8, was about 3.6 MHz/s. It is worth also mentioning that the frequency discriminator in Fig. 5.10 implements 1st-order RC filters because they are the simplest solution; however, the AWC system design can be also extended to higher order filters.

5.2.1 Analytical model

The frequency discriminator implements two complementary filters (LPF and HPF) with cut-off frequency $f_c = f_{IF}$ each. Without loss of generality, these RF filters are linear time-invariant (LTI) whose outputs are the convolution between the input signal and the filter impulse response $h(t)$, as shown in Fig. 5.11. The result at the filter output is the same photocurrent $i_{RF}(t)$ at the input but modified in amplitude and phase by the transfer function of the filters $H(f) = \mathcal{F}\{h(t)\}$, with $\mathcal{F}\{\cdot\}$ the Fourier transform.

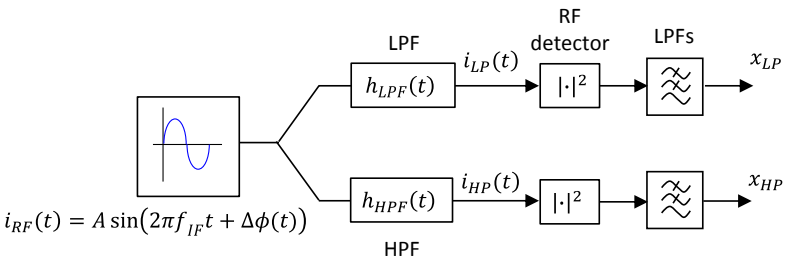

Figure 5.11. Analytical model of the analog frequency discriminator, with sinusoidal carrier at the input.

The filter response $H(f)$ is a complex number that can be expressed in magnitude and phase as

$$H(f) = |H(f)|e^{j\arg\{H(f)\}} \tag{5.8}$$

From Eq. (2.29), the balanced photodetected current in the heterodyne RX writes as

$$i_{RF}(t) = A\sin(2\pi f_{IF}t + \Delta\phi(t)) \tag{5.9}$$

with $A = 2\Re\sqrt{P_S(t)P_{LO}}$. Let us first consider the case where Eq. (5.9) is unmodulated, therefore it corresponds to a sinusoidal carrier oscillating at f_{IF} with Lorentzian-shape spectrum due to the phase noise $\Delta\phi(t)$. By using Eq. (5.8), it can be easily proven that both the low-pass and the high-pass filter outputs assume the form

$$i_{LP/HP}(t) = |H(f_{IF})|A\sin(2\pi f_{IF}t + \Delta\phi(t) + \arg\{H(f_{IF})\}) \tag{5.10}$$

This notation is assumed for clarity, instead of the time convolution with the filter impulse response $h(t)$. Let us define $h_{LPF}(t)$ and $h_{HPF}(t)$ for the 1st-order LPF and HPF respectively, as

$$h_{LPF}(t) = \frac{1}{RC}e^{-\frac{t}{RC}}u(t) \tag{5.11}$$

$$h_{HPF}(t) = \delta(t) - \frac{1}{RC}e^{-\frac{t}{RC}}u(t) \tag{5.12}$$

with $\delta(t)$ the Dirac delta function and $u(t)$ the Heaviside function. By applying Fourier transform, the frequency response of the filters are respectively

$$H_{LPF}(f) = \mathcal{F}\{h_{LPF}(t)\} = \frac{1}{1 + j2\pi RCf} \tag{5.13}$$

$$H_{HPF}(f) = \mathcal{F}\{h_{HPF}(t)\} = \frac{j2\pi RCf}{1 + j2\pi RCf} \tag{5.14}$$

Since the LPF and HPF are followed by RF detectors to calculate the mean power of the filtered RF signals, in this analysis only the magnitude response of the filters $|H(f)|$ is considered, and the phase response $\arg\{H(f)\}$ is of no interest. The magnitude responses read as

$$|H_{LPF}(f)| = \frac{1}{\sqrt{1 + (2\pi RCf)^2}} \tag{5.15}$$

$$|H_{HPF}(f)| = \frac{2\pi RCf}{\sqrt{1 + (2\pi RCf)^2}} \tag{5.16}$$

whose behavior is depicted in Fig. 5.12 with respect to the normalized frequency f/f_c, with $f_c = 1/2\pi RC$ the 3 dB cut-off frequency of both LPF and HPF filters.

By replacing Eqs. (5.15), (5.16) into Eq. (5.10), and normalizing with respect to f_c, the filtered photocurrents are expressed as

$$i_{LP}(t) = \frac{A}{\sqrt{1 + (f_{IF}/f_c)^2}}\sin(2\pi f_{IF}t + \Delta\phi(t) + \arg\{H_{LPF}(f_{IF})\}) \tag{5.17}$$

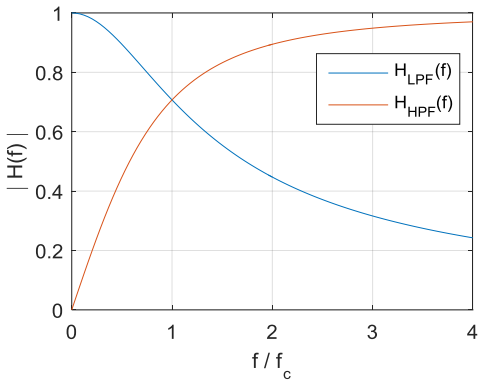

Figure 5.12. Magnitude response vs. normalized frequency for the 1st-order RC filters.

$$i_{HP}(t) = \frac{A(f_{IF}/f_c)}{\sqrt{1+(f_{IF}/f_c)^2}}\sin(2\pi f_{IF}t + \Delta\phi(t) + \arg\{H_{HPF}(f_{IF})\}) \tag{5.18}$$

Next, the RF detectors square the signals to calculate the mean power, and the narrow LPFs reject the frequency-doubled sinusoidal term after RF to DC conversion, yielding

$$x_{LP} = \frac{A^2}{2(1+(f_{IF}/f_c)^2)} \tag{5.19}$$

$$x_{HP} = \frac{A^2(f_{IF}/f_c)^2}{2(1+(f_{IF}/f_c)^2)} \tag{5.20}$$

Finally, these two expressions are added and subtracted to get the received optical power and the frequency error signal respectively. First, by adding Eqs. (5.19) and (5.20), one obtains

$$x_{HP} + x_{LP} = \frac{A^2}{2} \tag{5.21}$$

corresponding to the received optical power. Conversely, subtraction of Eqs. (5.19) and (5.20) produces

$$x_{HP} - x_{LP} = \frac{A^2((f_{IF}/f_c)^2 - 1)}{2((f_{IF}/f_c)^2 + 1)} \tag{5.22}$$

which is a frequency dependent signal that serves as frequency error monitor. The dependency on the carrier amplitude A^2 can be cancelled by using Eq. 5.21 to drive the AGC circuit, as in Fig. 5.10. The behavior of Eq. (5.22) by varying the carrier frequency is plotted in Fig. 5.13(a). As observed, the frequency discriminator output is a bipolar signal with zero-crossing at the cut-off frequency of the filters. The error estimation is not linear as expected, because of the frequency response characteristics of the RC filters (see Fig. 5.12); however, Fig. 5.13(b) indicates that there exists a good approximation to a linear estimation across $\pm 0.3 f_c$ with respect to the zero-crossing point. Replacing the 1st-order RC filters by higher order filters, or different RF filter technology, can modify the output characteristics of the frequency error estimator, and even increase the liner region. Nevertheless, by considering the typical $f_{IF} = 2R_b$ in optical heterodyne RXs, the $\pm 0.3 f_c$

linear region in Fig. 5.13(b) translates into ±60% of the bit rate, enough for practical applications with low HW complexity. Furthermore, frequency errors beyond $\pm 0.3 f_c$ can effectively be corrected under LO feedback tuning as the polarity of the frequency error does not change.

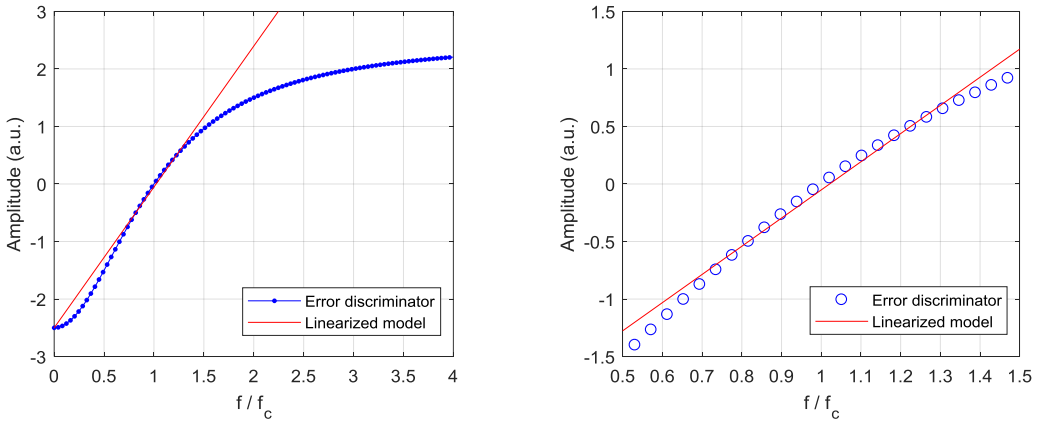

Figure 5.13. (a) Characteristics of the frequency error estimated by the analog frequency discriminator, and (b) zoom into the linear region around the filter's cut-off frequency f_c.

5.2.2 Simulation and implementation in hardware

In order to validate the operation of the frequency discriminator within the analog heterodyne RX, including the phase-modulated data, numerical simulation was carried out with VPI using the setup shown in Fig. 5.14. The data consisted of PRBS-7 sequences running at 1.25 Gb/s, that directly phase-modulated the TX laser. The f_{IF} was set to 2.5 GHz. After photodetection the RF signal was filtered by a Bessel BPF with 1.5 GHz BW at 3 dB, and centered at f_{IF}, and then passed on to the differential demodulator for data recovery. At the same time, the RF photocurrent for the frequency discriminator input was tapped from two different points, before and after the BPF; this helps to figure out what might be, in practice, the effect of the BW limitations of the implemented HW. In the frequency discriminator, the values of R and C were adjusted for f_c = 2.5 GHz, matched with that the IF of the receiver.

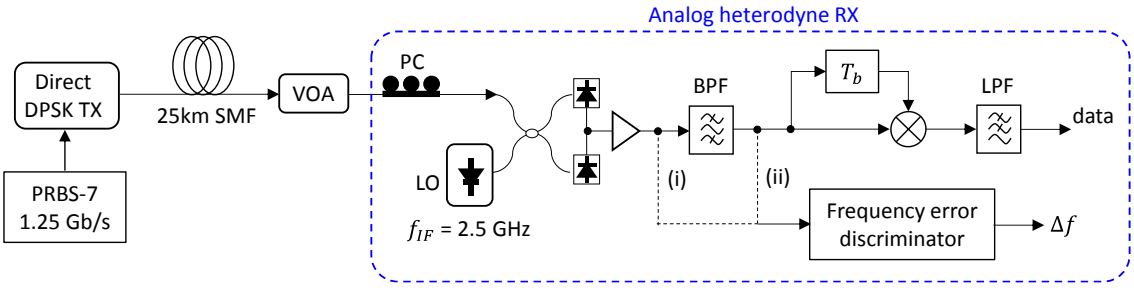

Figure 5.14. Simulation setup for heterodyne RX with analog frequency discriminator.

In Fig. 5.15(a), the LO was swept ±7.5 GHz with respect to the TX, to visualize the characteristics of the frequency error estimation. The results are plotted with and without the Bessel BPF. First, for the case of no BPF the obtained curve is symmetrical against f_{IF} = 0, with the zero-crossing

at IF = ±2.5 GHz. This matches well with the theoretical result in Fig. 5.13 without modulation. On the other hand, the Bessel BPF folds to zero the frequency error estimation beyond the linear region. As stated before, this represents the maximum BW limitation that the system imposes on the range of the frequency discriminator. Nevertheless, Fig. 5.15(b) zooms into the linear region around f_{IF} = 2.5 GHz and shows that ±500 MHz of linear error estimation are still available, even if the system is BW limited.

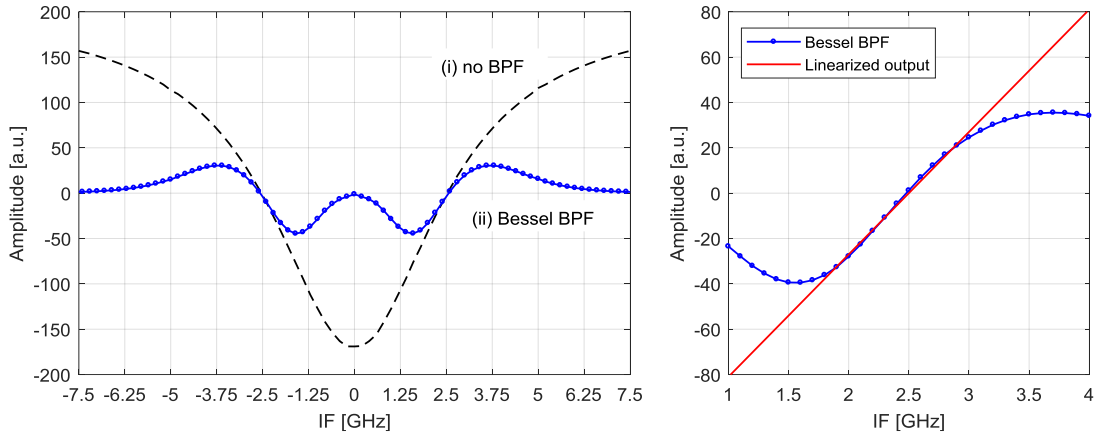

(a) (b)

Figure 5.15. (a) Simulation results for the analog frequency estimation in 1.25 Gb/s heterodyne RX with f_{IF} = 2.5 GHz; (b) zoom into the linear region of the error estimation.

Last, the frequency discriminator was assessed in terms of the tolerance to the phase noise from lasers. The RF photocurrent was tapped after the Bessel BPF, and the results are plotted in Fig. 5.16 in terms of the linear range of the frequency discriminator output against the total linewidth (TX + LO). As expected, the system is practically immune to the laser linewidth because the frequency discrimination is based on the power difference between the two filtered RF spectra, being the phase contribution negligible. Moreover, the detrimental effect of the phase noise becomes apparent at linewidths nearby 1 GHz, close to the bit rate, far from realistic values for typical DFBs.

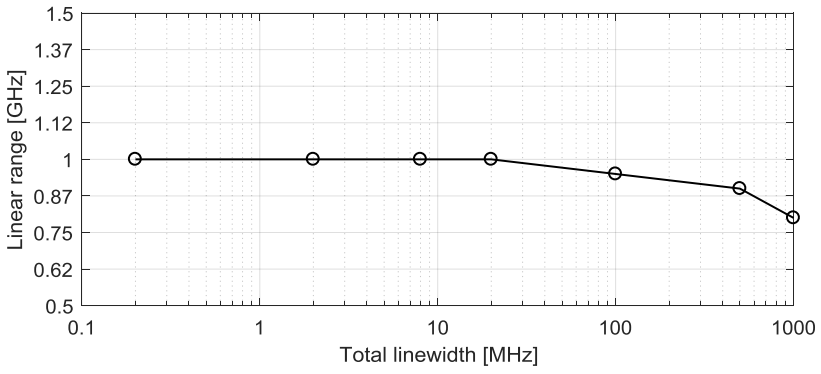

Figure 5.16. Linewidth tolerance of the analog frequency discriminator.

After performance assessment by numerical simulation, a prototype of the frequency discriminator was implemented in a PCB with standard FR-4 substrate and commercial electronic components. Fig. 5.17(a) shows the circuitry of the implemented prototype. The frequency

responses of the two complementary HPF and LPF are depicted in Fig. 5.17(b), showing the crossing-frequency at ~2.5 GHz at -6 dB (calculated as 20log(·)). A low-barrier Schottky diode can be used as RF power detector. In this particular implementation, a HSMS-286Y microwave Schottky diode was configured as zero-bias detector. It operates at RF frequencies from 900 MHz up to 5.8 GHz. To operate the diode with zero-bias, the RF power at the diode input must be higher than -30 dBm to guarantee that the root mean square (RMS) voltage of the RF signal is high enough to polarize the Schottky barrier, without external DC bias, as plotted in Fig. 5.17(c). The negative or positive half-wave rectification can be selected by simply inverting the polarization of the Schottky diode. The rectified signals are then low-pass filtered at 10 kHz to obtain x_{LP} and x_{HP}, that are later delivered to the electronic λ-control system of the DFB LO. The addition and subtraction of x_{LP} and x_{HP} are done in the LO laser board with operational amplifiers.

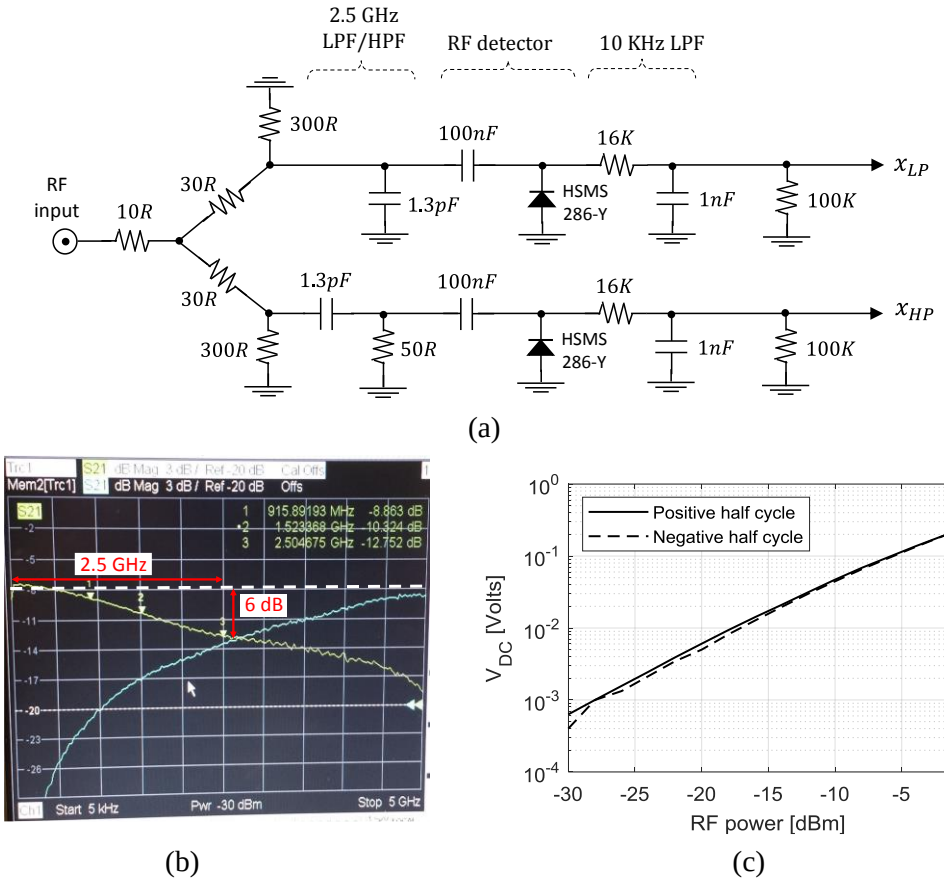

Figure 5.17. Analog circuitry of the frequency error discriminator prototype; (b) frequency responses of both 2.5 GHz low-pass and high-pass 1st-order RC filters; (c) output voltage vs. RF input power for the zero-bias Schottky detector diode.

The frequency discriminator prototype was implemented and tested real-time within the analog DPSK heterodyne ONU for the COCONUT PON, discussed in Section 4.2.2. Note that in such polarization diversity RX architecture, there are not one but two photodetected currents, one per each SOP. Hence, two parallel frequency discriminators are needed, and one will end up with four outputs from the frequency discriminator system: $x_{LP_{\mathbb{X}}}$, $x_{LP_{\mathbb{Y}}}$ and $x_{HP_{\mathbb{X}}}$, $x_{HP_{\mathbb{Y}}}$. On the one hand, the addition of the four signals yields the total received power independent from the received

SOP; this signal drives the AGC circuit for power normalization. On the other hand, the frequency error signal $y_e(t)$ is given by

$$y_e(t) = \left(x_{LP_{\mathbb{X}}} + x_{LP_{\mathbb{Y}}}\right) - \left(x_{HP_{\mathbb{X}}} + x_{HP_{\mathbb{Y}}}\right) \tag{5.23}$$

In Fig. 5.18 the DFB LO of the heterodyne RX was swept in λ to produce a frequency drift of $\pm$1.25 GHz with respect to f_{IF} = 2.5 GHz. The TX laser modulated PRBS-7 at 1.25 Gb/s for direct DPSK. The resulting error signal from the frequency discriminator prototype was evaluated with and without the broadband modulated data. As observed, the analog frequency discriminator correctly tracked the f_{IF} mismatch across the entire LO sweep, exhibiting a good approximation to a linear error signal in the range $\pm$1.25 GHz from f_{IF}, for the case of PRBS data. Interestingly, the frequency discriminator can also operate with unmodulated optical signals, even though the quality of the frequency error estimation is worse because the power of the photodetected RF signal is now concentrated within a narrow frequency band of some MHz –the Lorentzian-shaped spectrum of the phase noise– and the frequency response non idealities of the LPF and HPF filters become more apparent.

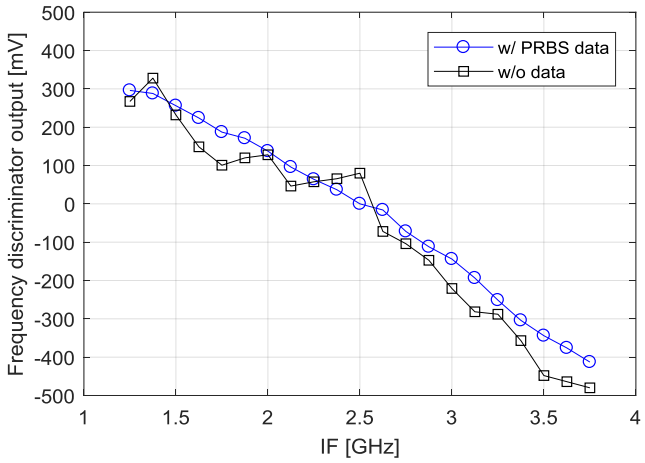

Figure 5.18. Output signal of the analog frequency discriminator prototype, for heterodyne RX with f_{IF} = 2.5 GHz and 1.25 Gb/s DPSK data.

5.3 Differential Carrier Recovery For Homodyne Receivers

One of the key aspects of the DSP implemented in the homodyne RX for the COCONUT-PON was the use of differential field detection to recover the phase-encoded data (see Chapter 4). Its implementation is easy, and shows high robustness against the phase noise from low-cost lasers as studied in Section 3.3.1. Indeed, if the phase noise is dominant at the decision part of the RX, e.g., at lower data rates and/or employing common DFBs or VCSELs with large linewidth, the performance of differential phase detection is comparable to that of the synchronous detection using carrier phase estimation algorithms [Fat13], but with a remarkable lower implementation complexity. To visualize the latter, let us consider the well-known Viterbi & Viterbi feedforward phase estimator [Vit83] illustrated in Fig. 5.19(a), compared with the differential field detector for m-PSK in Fig. 5.19(b).

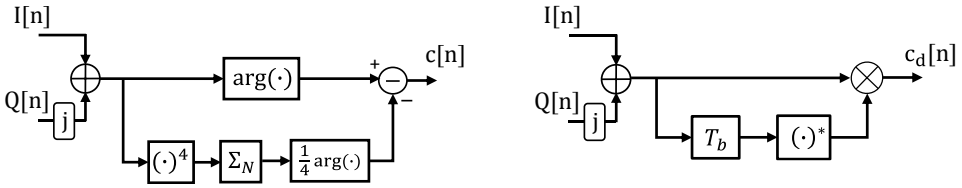

Figure 5.19. (a) Viterbi & Viterbi feedforward phase estimation and (b) differential field detection for optical PR.

In order to calculate the complexity and the required HW resources of both PR algorithms, let us examine the case of QPSK modulation. The HW resources estimate was done by decomposing the mathematical operations with complex numbers into the required number of real multipliers and adders. As an example, raising the complex number $I + jQ$ to the power of two yields: $(I + jQ)^2 = (I^2 - Q^2) + j(2IQ)$; therefore, four real multipliers and two adders are needed. Other operations like the trigonometrical functions to calculate $\arg(\cdot)$ are more efficiently implemented by look-up tables (LUTs). The HW resources estimate for QPSK, as summarized in Table 5.1, indicates that the differential demodulation requires 50% less multipliers, 56% less adders, and no LUTs. Here, M represents the number of parallel bits processed by the digital processor. This directly translates into less complexity for HW prototyping, improved performances, and lower energy consumption of the digital RX. For a fair comparison, it should be mentioned that the differential detection also requires symbol encoding at the TX (see Section 2.3.5.1); however, such differential encoding is widely applied and recommended, even for synchronous detection with phase estimation algorithms, to overcome the phase-noise induced cycle-slips that produce phase ambiguity and error propagation [Kik06], and therefore, represents no significant extra complexity. An alternative to deal with the cycle slips is the use of data-aided DSP by transmitting pilot symbols for carrier synchronization and further channel equalization [Zha10], at the expenses of lowering the net data rate.

Table 5.1. Hardware resources for QPSK phase recovery.

PR algorithm	Multipliers	Adders	LUTs
Viterbi & Viterbi	$8 \times M$	$7 \times M - 2$	$M + 1$
Differential demodulation	$4 \times M$	$3 \times M$	0
Reduction	50%	56%	100%

Owing to the advantages mentioned above, namely simplicity and robustness, this thesis promotes the use of differential phase detection for optical CR in coherent TRXs for access networks, where the cost-effectiveness takes the primary attention. Hence, by selecting the differential mth-power estimator (Section 5.1.1) for FE, and the differential demodulator for PR, the complete CR architecture is as represented in Fig. 5.20. Here, m is the number of constellation points of the m-PSK (e.g., $m = 2$ for DPSK), N is the block length for averaging, k is the symbol index within the estimation block, and D is the process delay of the FE algorithm. In this CR algorithm, the phase shift $\Delta\varphi$ induced by the frequency detuning between Tx and LO lasers is estimated from each sample of the received signal $r[n] = I[n] + jQ[n]$, then cancelled by the phase rotator

$e^{-jk(\cdot)}$ before PR. Afterwards, the corrected signal $r'[n]$ is differentially demodulated by a 1-symbol complex correlation (i.e., 1-symbol delay-and-multiply) to recover the phase-encoded data $d[n]$. Note that both FE and PR stages implement a complex correlation with different signal delay to extract the phase difference between samples (z^{-1}) in FE, or between symbols (z^{-P}) in PR, where $P = R_s/R_B$ represents the oversampling factor and is defined as the ratio between the sample rate (R_s) and the symbol rate (R_b). Usually, $R_s \geq 2R_B$ at the ADCs for mapping into the digital domain, to satisfy the Nyquist sampling criterion.

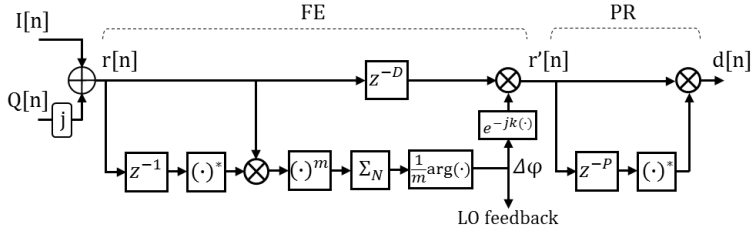

Figure 5.20. CR algorithm based on differential mth-power for FE and differential demodulation for PR.

5.3.1 Hardware optimization

The CR architecture in Fig. 5.20 can be further optimized for HW prototyping based on the fact that the differential mth-power algorithm for FE cancels the m-PSK modulation by rising to the power of m, then the frequency detuning can be correctly estimated either between consecutive samples or symbols. This contrasts with the IQ cross-correlation algorithm in Section 5.1.2 that was specifically conceived to estimate the frequency detuning between samples, and requires a signal delay for the cross-correlation shorter than the symbol duration to avoid the influence of the phase-modulated data. In consequence, by going back to Fig. 5.20, if the CLK recovery at the RX DSP is carried out prior the CR (i.e., the I and Q signals for CR were already downsampled to one sample per symbol), then $P = 1$ and both FE and PR algorithms need the same 1-symbol complex correlation for differential phase detection; otherwise, for unrecovered CLK ($P \geq 2$) the signal delays for correlation are different.

Therefore, for the case of $P = 1$ (recovered CLK) the architecture in Fig. 5.20 can be rearranged to now calculate the 1-symbol correlation for PR only once per symbol, then reuse it for the next feedforward FE algorithm, as illustrated in Fig. 5.21(a), thus optimizing the implementation and saving the HW resources. A related idea was proposed and tested in [Fer16b], working with differential mth-power estimator for FE and Viterbi & Viterbi phase estimator for PR, both requiring the calculation of the mth-power. In such architecture, the HW optimization was achieved by calculating the mth-power only once, then sharing it to the FE and the PR algorithms.

Fig. 5.21(b) shows the evolution of the signal constellation within the simplified CR algorithm, for the case of DPSK. First, the complex received signal $r[n]$ ((i), left handed) completely rotates over the complex plane due to the phase noise and the frequency error. Next, the information-bearing optical phase is recovered by differential demodulation, getting rid of the phase noise effect. However, each symbol of $w[n]$ ((ii), center) has a phase shift $\Delta\varphi = 2\pi\Delta f/R_b$ due to the

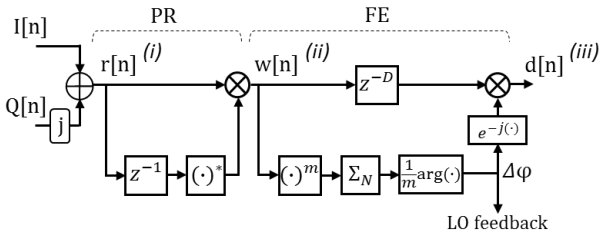

(a)

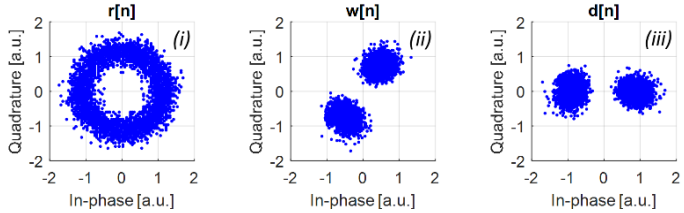

(b)

Figure 5.21. (a) Simplified CR architecture that reuses the 1-symbol complex correlation required for both the FE and the PR algorithms; (b) evolution of the DPSK constellation within the simplified CR.

frequency detuning, denoted by Δf, as analyzed in Section 3.3.2. This produces a fixed incremental rotation of the constellation in the complex plane. Finally, the residual phase shift $\Delta\varphi$ is estimated and corrected from the phase of each symbol, yielding a phase/frequency-noise-free signal $d[n]$ ((iii), right handed) that goes on to the decision part of the RX. The estimated $\Delta\varphi$ simultaneously drives the feedforward symbol phase correction $w[n] \times \exp[-j\Delta\varphi]$, and the LO feedback for automatic λ-tuning, as demonstrated in Section 5.1. Note that the phase rotator $\exp[-j\Delta\varphi]$ in the simplified CR in Fig. 5.21(a) does not include the symbol index k, as in Fig. 5.20 for the conventional CR, because the frequency error of the signal $w[n]$ after differential demodulation translates into a constant phase shift for all the symbols within the estimation window of length N, with time-dependency already suppressed.

The proposed CR algorithm in Fig. 5.21(a) with optimized architecture requires less operations than the conventional CR in Fig. 5.20, thus relaxing the HW resources and the energy consumption per processed symbol when the coherent RX is prototyped in a FPGA for real-time operation. Table 5.2 summarizes the required HW resources for DPSK, indicating 23% and 25% of savings in the number of real adders and multipliers respectively with the simplified architecture.

Table 5.2. Hardware resources for DPSK carrier recovery.

CR architecture	Multipliers	Adders	Process delay [symbols]
Conventional	$16 \times M$	$13 \times M - 2$	$4 \times M$
Proposed	$12 \times M$	$10 \times M - 2$	$3 \times M$
Reduction	25%	23%	25%

More interestingly, 25% reduction in the overall process delay of the CR algorithm is achieved, expressed in number of symbols. The arg(·) to extract $\Delta\varphi$ is realized by LUTs, with similar size for both CR architectures. It is also worth mentioning that both differential CR architectures are completely feedforward, thus are expected to be more robust against the phase noise, and less challenging for parallel HW implementation in FPGA or ASIC, compared with feedback CR algorithms [Lev10].

A second optimization to the differential CR in Fig. 5.21(a) arises from the fact that the LUT to store the trigonometrical functions to calculate arg(·), can be replaced by a set of decision rules over the complex plane $I+jQ$ to estimate $\Delta\varphi$, as demonstrated in [Gha19] for DPSK, thus lowering the memory resources in the FPGA.

5.3.2 Experimental validation real-time

To evaluate the proposed CR with simplified HW, a real-time experiment was conducted with DPSK data at 1.25 Gb/s, using the FPGA homodyne RX for COCONUT presented in Section 4.2.1. The experimental setup is depicted in Fig. 5.22. The TX implemented a DFB laser ($\lambda = 1550$ nm) with linewidth $\Delta\nu = 4$ MHz, emitting at 0 dBm, that was properly equalized for direct-DPSK modulation. The data consisted of NRZ-PRBS sequences from a PPG running at 1.25 Gb/s. Since PRBS data were used, differential encoding can be assumed at the TX. After optical DPSK modulation, the signal was transmitted through a SMF spools with variable length. The VOA emulated the ODN losses in the PON. This experiment only considers one SOP, manually adjusted at the input of the RX.

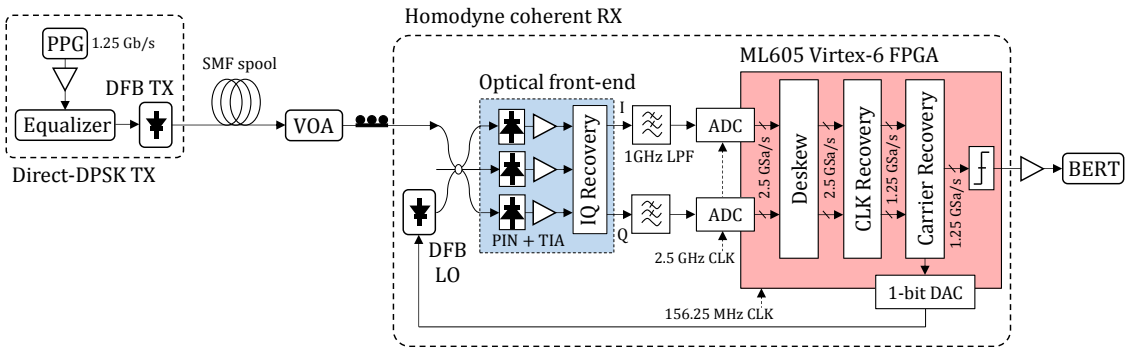

Figure 5.22. Experimental setup for real-time evaluation in FPGA of the proposed CR, transmitting DPSK at 1.25 Gb/s.

The homodyne RX included a DFB-LO with electronic λ-control system for automatic tuning from the DSP feedback. The LO emitted at 3 dBm, and had $\Delta\nu = 4$ MHz. After coherent beating in the 3x3 coupler, the three photocurrents were linearly combined to recover I and Q, then low-pass filtered by two standard 4^{th}-order Bessel filters with 1 GHz cut-off frequency, for antialiasing and noise suppression. Last, the I and Q signals were mapped into the digital domain by two ADCs sampling at 2.5 GSa/s each. All the subsequent DSP was carried out by an ML605 Xilinx Virtex-6 FPGA with 8-bit architecture. Its process clock was set to 156.25 MHz for parallel processing of the real-time 1.25 Gb/s data streaming. In the CR subsystem of the RX DSP, the two architectures for differential CR were prototyped: the conventional in Fig.5.20 and the

simplified in Fig. 5.21(a). As stated before and along this chapter, the estimated $\Delta\varphi$ due to the frequency detuning is also fed-back towards the LO for automatic λ-control. The D/A conversion to generate the analog error signal was performed by the serial 1-bit PWM DAC shown in Fig. 4.2. Finally, the binary data were extracted by comparing with a decision threshold, and the real-time error rate was measured by a BER tester (BERT).

5.3.3 Results and discussion

Initially, the optical transmission system comprising the DPSK TX based on direct-DFB modulation and the digital homodyne RX prototyped in the FPGA with both CR algorithms, was lighted up, achieving error-free transmission of DPSK at 1.25 Gb/s in real-time. Next, the CR algorithm was optimized by evaluating the optimal block length N for averaging. The received optical power was adjusted to -53 dBm for BER = 10^{-4}. The LO detuning was set to an arbitrary value of 300 MHz, and the estimation of the frequency error Δf was evaluated 100 times for each value of N. Results are plotted in Fig. 5.23, in terms of the RMS of the estimated Δf as a function of the block length N in symbols, for two different PRBS data. As observed, the FE accurately converges to the applied LO detuning (300 MHz) for N larger than 200 symbols. In this work, N was set to 2^8 symbols in agreement with the test. The same optimal N was observed for the two PRBS data, as well as for both CR architectures.

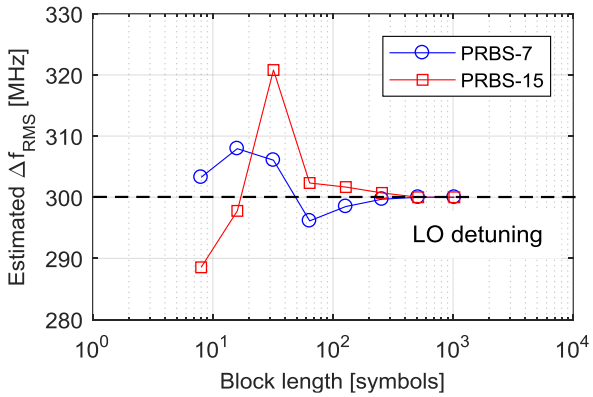

Figure 5.23. RMS of the estimated Δf against the block length N for averaging. The RMS value is calculated over 100 estimations for each value of N.

Afterwards, the system was evaluated in terms of sensitivity and tolerance to the phase noise, related with the total $\Delta\nu$. For the test, three different lasers were used as LO: an ECL with narrow linewidth of 100 kHz, and two commercial DFBs with 4 MHz and 15 MHz linewidth respectively. Hence, the total linewidth $\Delta\nu$ ranged from 4 MHz to 19 MHz, including the 4 MHz linewidth of the DFB TX. The results in Fig. 5.24(a) show that, for FEC threshold of BER = 10^{-3}, a high sensitivity of -55 dBm was achieved, with no apparent penalty for $\Delta\nu = 4$ MHz and $\Delta\nu = 8$ MHz. In the case of $\Delta\nu = 19$ MHz, the sensitivity penalty at FEC level was about 4 dB, and exhibiting error-floor close to BER = 10^{-5}. Both CR architectures perform almost the same.

In Fig. 5.24(b), the sensitivity penalty at BER = 10^{-3} is recorded and compared with numerical simulation carried out with VPI-MATLAB under similar conditions and using the same DSP. As

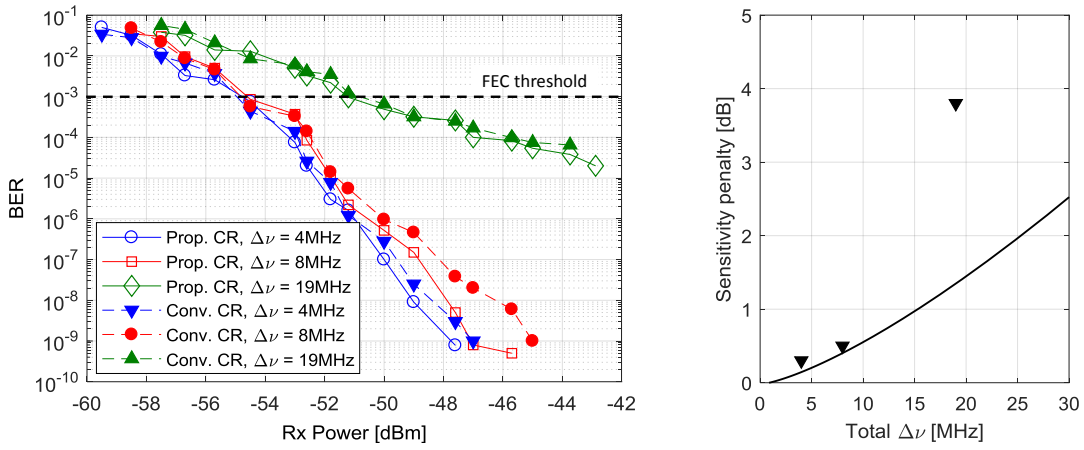

(a) (b)

Figure 5.24. (a) BER vs. received power for DPSK at 1.25 Gb/s with the proposed (prop.) and conventional (conv.) CR, for different total $\Delta\nu$; (b) sensitivity penalty at BER = 10^{-3} vs. total $\Delta\nu$: simulation (solid line) and real-time experiment (marker).

observed, the experimental results are in good agreement with simulation for $\Delta\nu = 4$ and 8 MHz, but differ by about 2 dB for $\Delta\nu = 19$ MHz. This behavior can be ascribed to the lower emission power of the 15 MHz DFB acting as LO, of about 2 dBm, which directly impacts on the RX sensitivity. Note that 1.25 Gb/s, proposed for residential users in the udWDM-PON, is the most challenging scenario for the CR system because R_B is the closest to the total $\Delta\nu$, and therefore, the phase noise has the strongest impact on the PSK data. Notably, in this experiment the differential CR achieved a high sensitivity of -55 dBm at a ratio $\Delta\nu/R_B = 6.4{\cdot}10^{-3}$, with total $\Delta\nu = 8$MHz, outperforming the real-time experiments reported in literature with synchronous detection, to the best of the author knowledge. The obtained results are in the range of commercial low-cost DFBs, and confirm the high performance and robustness of the differential detection despite its simplicity, and its feasibility for PON. For higher order modulation formats at the same R_B, the tolerance to $\Delta\nu$ is correspondingly lower, as stated in Section 3.3.1. In Chapter 7, the simplified CR is demonstrated with complex modulations up to 8-APSK.

Next, the DPSK transmission was assessed for several fiber link distances, spanning from btb up to 100 km of standard SMF. The results reported in Fig. 5.25(a) clearly confirm that neither the CD nor the nonlinear impairments from the fiber take relevance in this udWDM scenario, because of the lower data BWs and launched power per λ. Additionally, the system was also tested with PRBS-7 and PRBS-15 to discard any performance dependency on the data pattern. Fig. 5.25(b) reports on the normalized DPSK eye diagram after CR and before data decision, for BER of 10^{-3} (upper) and 10^{-9} (lower) respectively.

The frequency error estimation and correction was experimentally assessed by first sweeping the LO λ in open loop, i.e., without feedback to the LO for automatic tuning. Fig. 5.26 depicts the phase shift $\Delta\varphi$ induced by the LO detuning and estimated by the FPGA within ± 1 GHz. Larger LO detuning values led to failure of the CLK recovery algorithm and synchronization loss. As expected, cycle-slip in the estimated $\Delta\varphi$ occurs for values beyond $\pm\pi/m$ ($\pm\pi/2$ for DPSK), the theoretical limit due to the mth-power in the FE algorithm. In this case, for 1.25 Gb/s the first cycle slip occurs exactly at $\Delta f = \pm 312.5$ MHz. This problem was solved by implementing phase

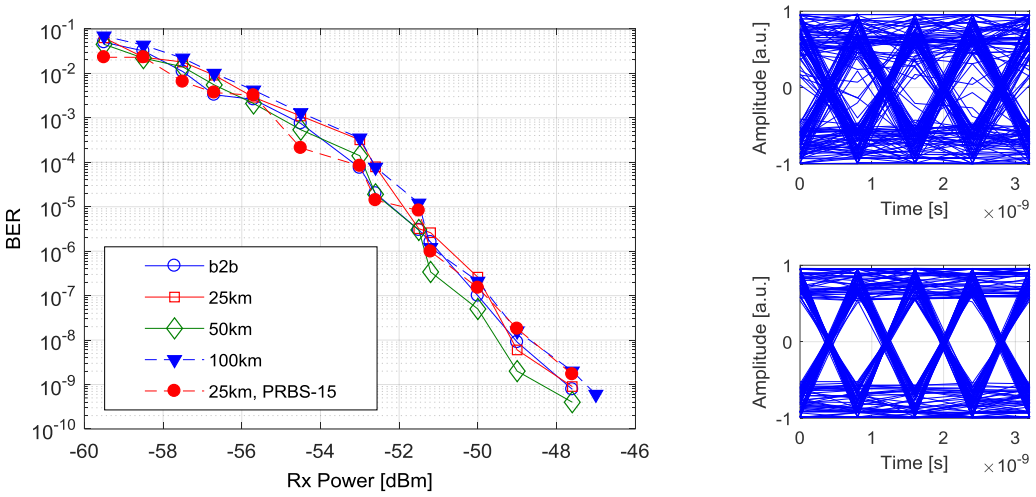

Figure 5.25. (a) BER vs. received power for DPSK at 1.25 Gb/s, with several fiber link distances; (b) normalized DPSK eye diagram after CR for 10^{-3} (upper) and 10^{-9} (lower) BER.

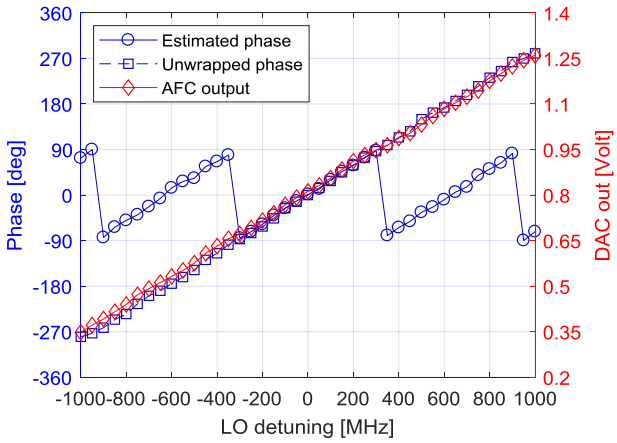

Figure 5.26. Estimated $\Delta\varphi$ for frequency error correction, and output of the 1-bit DAC for LO λ-control, as a function of the LO detuning.

unwrapping [Tay09], resulting in a completely linear $\Delta\varphi$ for all across the LO detuning. It is worth mentioning that the estimated $\Delta\varphi$ in Fig. 5.6, applying the same mth-power FE algorithm, does not show any cycle-slip because the FE algorithm operated upon the samples, before the CLK recovery; the sampling rate was $>10R_B$, then the cycle-slip occurs at much higher LO detuning. Fig. 5.26 (right axis) also plots the analog signal measured at the output of the 1-bit DAC, and going towards the LO for automatic λ-control.

The BER curves in Fig. 5.27(a) show the system performance without FE (i.e., only the differential demodulation), compared with the complete CR with the conventional and simplified algorithms, for two different values of total $\Delta\nu$. The received power was adjusted to obtain a reference BER = 10^{-4}. As observed, without FE the BER is highly degraded by the frequency detuning, with about $\pm$60 MHz tolerance for 1 dB sensitivity penalty. On the other hand, the FE can effectively correct the frequency error up to $\sim \pm$400 MHz for 1 dB penalty even in presence of strong phase noise, as there is no difference in the test for 4 MHz and 19 MHz total linewidth.

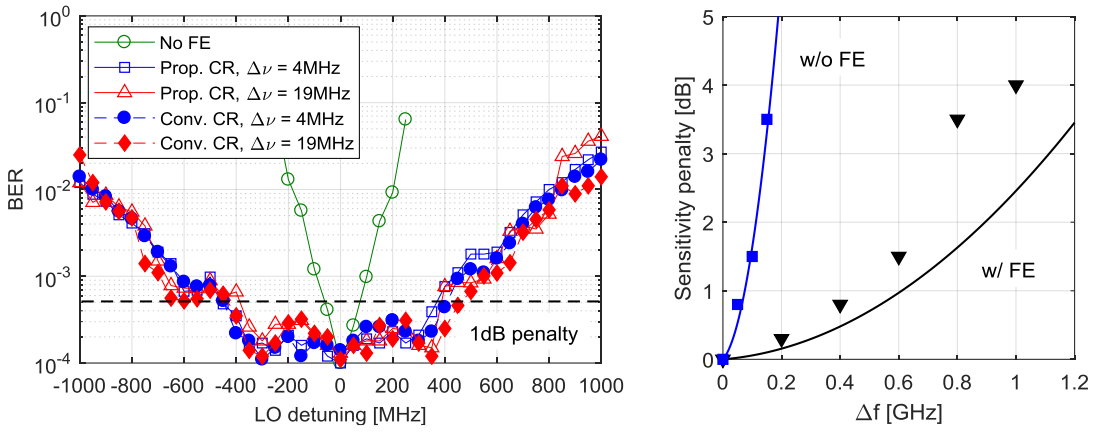

(a) (b)

Figure 5.27. (a) BER versus LO detuning for DPSK at 1.25 Gb/s, processed by the proposed (prop.) and conventional (conv.) CR with/out FE; (b) sensitivity penalty at BER = 10^{-4} vs. LO detuning with/out FE: simulation (solid line) and real-time experiment (marker).

Both CR architectures perform the same. The BER degradation in Fig. 5.27(a) was translated to a sensitivity penalty at BER = 10^{-4} in Fig. 5.27(b), also comparing with the numerical simulation. In all cases, the experimental results are in reasonable agreement with simulation. From Fig. 5.27(b), note that the FE algorithm does not completely cancel the power penalty when the LO detuning increases, even in simulation. This phenomenon is not related to incorrect estimation of the frequency detuning, which is linear all across the LO sweep (see Fig. 5.26), but due to the BW of the RX that was adjusted to be 1 GHz to optimize the detection of the 1.25 Gb/s DPSK. Then, as the LO detuning increases the received spectrum falls beyond the RX BW, producing penalty at the detection. This key conclusion serves to emphasize the benefit of the two simultaneous strategies to correct the LO detuning: the feedforward DSP corrects the remaining frequency error from each symbol in real-time, whereas the feedback to the LO continuously adjusts its λ to maintain the photodetected spectrum in baseband and matched with the electrical filtering of the RX, which rejects out-band noise and optimizes the detection.

The following test aimed at evaluating the udWDM operation and the minimum required channel spacing. The high sensitivity achieved by the homodyne RX (-55 dBm) easily comply with the foreseen PB in coherent PON and enables the large power splitting to serve many users, as large as 256, equivalent to $10 \cdot \log_{10}(1/256) = -24$ dB splitting losses. For the test, a second user (hereafter User 2) with another direct-DPSK modulated DFB at 1.25 Gb/s was lighted up, as illustrated in Fig. 5.28. A 5 km fiber spool was installed at the output of User 2 to decorrelate the data, as well as a VOA to vary the transmitted power, with respect to User 1. At the RX, the received power was first adjusted to obtain BER = 10^{-4} for the case of single user (only User 1), then the λ of User 2 was swept $\pm$10 GHz with respect to User 1 to compute the power penalty at the reference BER. The electrical spectra after photodetection are reported in Fig. 5.29 for two considered scenarios: both users emitting at the same optical power (a), and User 1 emitting 15 dB lower than the interferer User 2 (b). The latter emulated the maximum allowed differential optical path loss, as specified in the ITU-T standard for NG-PON2 [ITU14]. The signal-to-interference ratio –SIR– denotes the optical power ratio between User 1 and the interferer User 2.

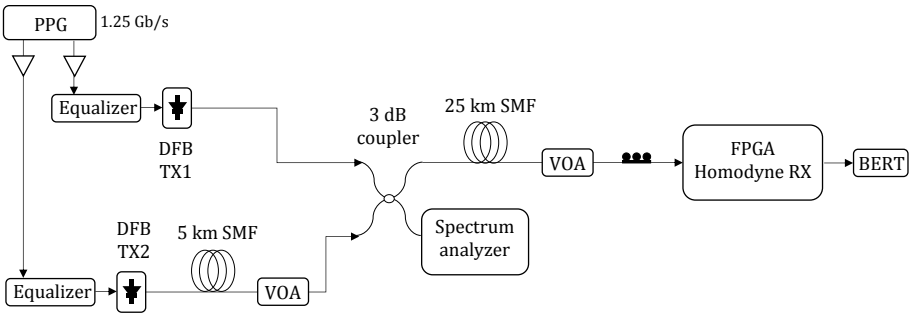

Figure 5.28. Experimental setup to evaluate the udWDM operation and the required channel spacing.

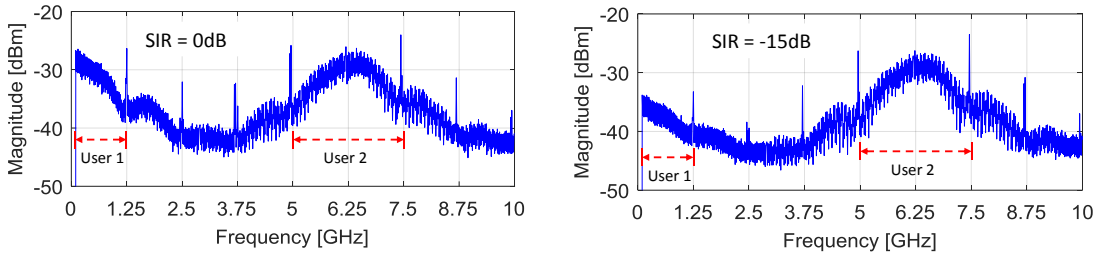

(a) (b)

Figure 5.29. Photodetected spectra of two 1.25 Gb/s DPSK users spaced by 6.25 GHz, in two scenarios: (a) both users emitting at the same optical power, and (b) with 15 dB optical power difference.

The results in Fig. 5.30, in terms of the sensitivity penalty at BER = 10^{-4} as a function of the spectral separation between users, indicate that for a maximum sensitivity penalty of 0.5 dB, the proposed 6.25 GHz channel spacing for 1.25 Gb/s users with homodyne ONUs can be implemented in the udWDM-PON, even for 15 dB differential link loss with adjacent channels. It should be stressed out that the results in Fig. 5.30 show the impact of a single adjacent channel interfering the measured channel; however, the conclusions for the minimum channel separation at 0.5 dB penalty can be extended to the real udWDM scenario, where the individual users are interfered by two adjacent channels –one at each side–, by adding extra 0.5 dB penalty as derived from Eq. (3.15), yielding 1 dB total power penalty at BER = 10^{-4}.

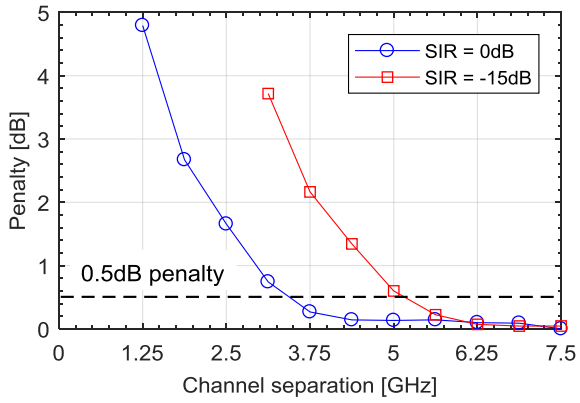

Figure 5.30. Sensitivity penalty at BER = 10^{-4} versus channel separation between DPSK users at 1.25 Gb/s, for the two differential link loss scenarios depicted in Fig. 5.28.

These results were obtained from direct laser modulation and band limited electronics that influenced the spectral width of the DPSK modulation. Further DSP at the transmitter for spectral shaping may lower the required channel spacing, as examined in Section 3.4.1.

5.3.3.1 Tolerance to optical frequency dithering

Motivated by the reduction in the process delay of the proposed CR algorithm, by 25% (see Table 5.2), a further experiment was designed to evaluate how fast the CR, prototyped in the FPGA, can effectively estimate and correct the frequency detuning. The test consisted of applying a low-frequency triangle current waveform to the bias of the DFB TX, as illustrated in Fig. 5.31(a), to produce an optical frequency dithering in the frequency band where the thermal chirp is dominant, and below the laser dip, up to few MHz (see Sections 2.4 and 3.5.1). The amplitude of the dithering (i.e., the maximum deviation with respect to its central frequency) is controlled by the amplitude of the bias current swing, and was set to $\pm$250 MHz to operate in the region of Fig. 5.27(b) where the sensitivity penalty is almost negligible after detuning compensation. The frequency of the dithering varied from 1 Hz up to 1 MHz to determine the impact on the RX sensitivity and the maximum tolerance. Fig. 5.31(b) reports on the electrical spectra at the RX after photodetection, for DPSK at 1.25 Gb/s without dithering (upper) and with $\pm$250 MHz dithering amplitude (lower).

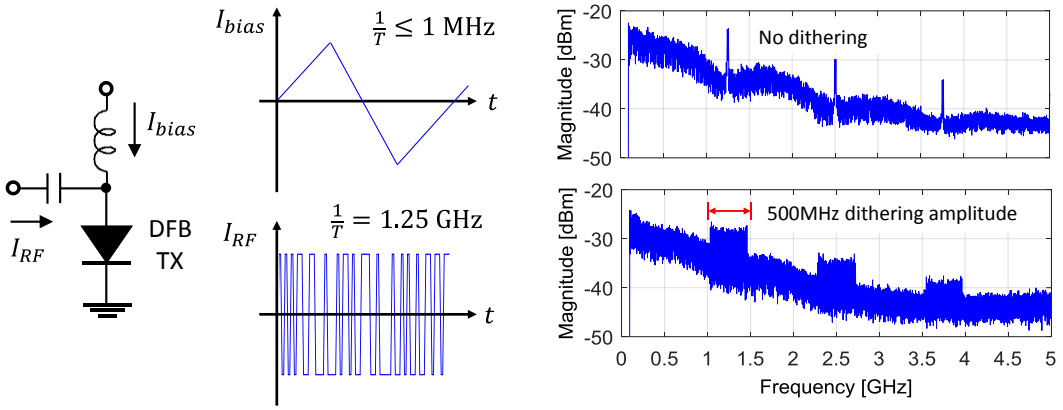

(a) (b)

Figure 5.31. (a) Implementation of the optical frequency dithering in the DFB TX; (b) DPSK photodetected spectra at 1.25 Gb/s without dithering (upper), and with $\pm$250 MHz dithering amplitude (lower).

The results plotted in Fig. 5.32, in terms of the BER as a function of the frequency of the optical dithering, show that the conventional CR can tolerate up to 70 kHz dithering frequency for 1 dB sensitivity penalty, whereas the proposed CR tolerance extends up to 350 kHz thanks to the substantial reduction in the number of operations and process delay of the CR algorithm, which translates into faster tracking of the frequency error. This confirms the feasibility of inserting the low frequency FSK signaling among the OLT and the ONUs for network control and management, as discussed in Chapter 4, without interfering the broadband data modulation.

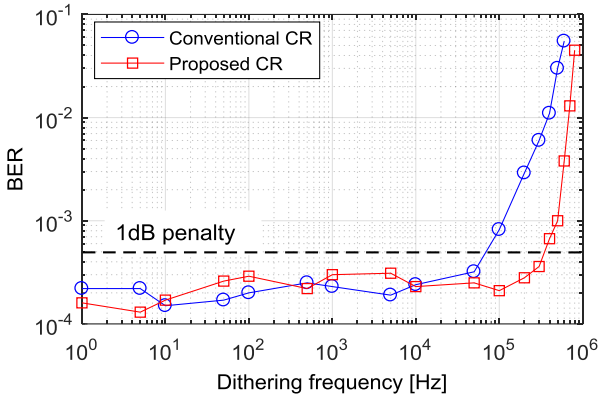

Figure 5.32. BER against frequency of the optical dithering, with ±250 MHz amplitude of the dithering, for conventional and proposed CR algorithms.

5.4 Chapter summary

This chapter explored the strategies for optical carrier synchronization at the coherent RX, dealing with the phase noise and the frequency drifts of lasers, which are more notorious when working with low-cost DFBs or VCSELs. First, for optical frequency matching between TX and LO, a complete DSP-aided AWC system for homodyne RXs was demonstrated with dual correction strategies: feedforward error tracking and feedback stabilization of the LO. The two simultaneous strategies can effectively deal with strong environment temperature changes and laser frequency noise, as the feed-forward DSP corrects any residual frequency error after LO tuning. Accurate performance in closed-loop was achieved, with ±500 MHz detuning correction in 600ms within 2 dB maximum penalty in sensitivity. The proposed AWC system is simple enough to be implemented in a cost-effective ONU for udWDM-PON, using common DFBs.

For the case of fully analog ONUs without DSP, an analog frequency discriminator for AWC was designed and implemented in a 1.25 Gb/s heterodyne RX. The frequency error is calculated from the power of the photodetected current, properly filtered by two complementary LPF/HPF filters. The system is robust and requires simple electronics with few complexity. The experimental tests included characterization of the frequency drift of DFB lasers free-running and under environment temperature conditions. The maximum measured drift rate was about 3.6 MHz/s, and indicates that the thermal tuning of conventional DFBs suffices for the coarse correction of the LO detuning, despite the slow nature of the thermal tuning with time constants in the order of seconds.

On the other hand, to recover the phase-encoded data in presence of optical phase noise, a simplified CR algorithm based on differential field detection for homodyne m-PSK RXs was proposed and tested real-time. The proposed method shares the 1-symbol complex correlation required for the FE and the PR algorithms, thus lowers the required HW resources, the power consumption, and the process delay of the RX DSP. The CR was prototyped in FPGA and tested with DPSK at 1.25 Gb/s, achieving a high sensitivity of -55 dBm for BER = 10^{-3}, with robustness against the frequency drifts of lasers. Notably, the proposed CR with simplified architecture increases by a factor of five the tolerance against fast frequency drifts of lasers, compared with

the conventional CR architecture. The good results obtained with direct laser modulation, phase noise tolerance of $\Delta\upsilon T_b$ = $6.4 \cdot 10^{-3}$ with common DFBs, and 6.25 GHz spaced udWDM grid, demonstrates that a cost-effective PON can be implemented with user terminals based on low-cost components and simple techniques, but still maintaining high the performance.

Chapter 6

Novel Architectures for Polarization-Independent Coherent Receivers

Polarization handling has been a major concern in coherent optical communications because in the optical link the transmitted signal reaches the coherent RX at the destination with random SOP, that evolves unpredictably along the birefringent fiber channel. This fact is particularly critical in coherent detection because incorrect SOP matching with the LO can even completely prevent the coherent mixing in the PDs, as analyzed in Section 2.2. The conventional methods to cope with the signal SOP variations are: (I) the use of polarization-maintaining fibers, not feasible for coherent PON that is planned to reuse the fiber infrastructure already deployed for legacy optical access systems; (II) polarization-diversity RX architectures that duplicate the optical front-end to process separately each SOP, widely used in commercial coherent RXs for transport networks; or (III) fast polarization tracking systems [Koc13], [Li19], that add the corresponding extra HW complexity.

Since the adoption of coherent systems for PON and other short reach applications with high terminal density, like DCI, is mainly limited by the complexity of the coherent RX, efforts in research have been conducted in pursuing novel polarization-independent coherent detection techniques. One of them is polarization switching in time [Can14c], [Erk16], in which the RX front-end reduces to an optical 3dB coupler and one or two PDs, for single-ended or balanced photodetection respectively. This solution, however, requires polarization modulation at the TX with external modulators. Another attractive alternative –outcome of the research in the COCONUT project– is a novel front-end configuration based on simple 3x3 coupler and PBS [Cia14], [Bot15], intended for ASK signals with envelope demodulation.

This chapter presents two different approaches for low complexity polarization-independent coherent detection: one for analog heterodyne RXs with DPSK signals, exploiting the simple front-end composed by 3x3 coupler + PBS; and the other for digital homodyne RXs leveraging low-complexity DSP that uses only 1 sample per symbol, thus lowering the ADCs requirements for implementation of the polarization-diversity front-end.

6.1 Polarization-Independent 3x3 Heterodyne Receiver

In previous chapters, the optical front-end for polarization-diversity heterodyne RXs was implemented with 2x2 couplers, in two different configurations. The first option is the conventional 2x2 heterodyne RX presented in Fig. 3.3(b) and hereafter named “4-PD balanced”, that implements a pair of PBSs and 2x2 couplers to separate the orthogonal SOP components of the received signal and the LO, later photodetected and processed separately. The four PDs are connected in pairs for balanced photodetection, as illustrated in Fig. 6.1(a). The analytical model can be found in Section 2.2.2.2.

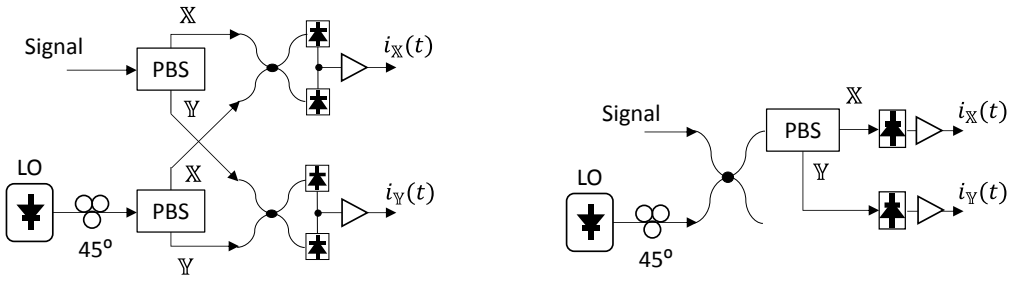

(a) (b)

Figure 6.1. Optical front-end for (a) 4-PD balanced and (b) 2-PD single-ended heterodyne RX.

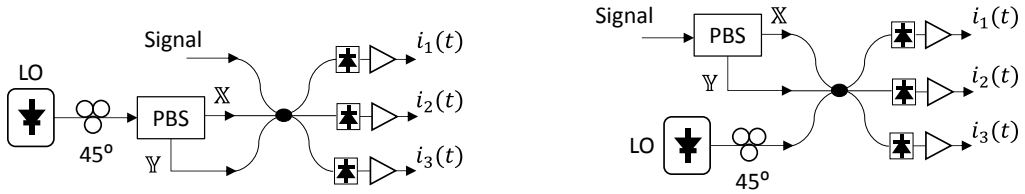

(a) (b)

Figure 6.2. Novel 3x3 optical front-end with the PBS attached (a) to the LO, and (b) to the input signal path.

The second option is the simplification of the previous front-end, which was implemented in the heterodyne ONU for the COCONUT-PON (Fig. 4.6). It consists of a 2x2 coupler that mixes signal and LO, followed by a PBS that separates the SOP components of the coherent mixing to be photodetected by a single PD each, as shown in Fig. 6.1(b). This scheme is hereafter named "2-PD single-ended". It pretty simplifies the complexity of the RX front-end, but suffers from the influence of the DD terms and the common-mode noise due to the single-ended detection; it also has an inherent 3 dB sensitivity penalty as only one arm of the coherent beating is processed. The 2x2 coupler with 50:50 coupling ratio could be replaced by, e.g., a 90:10 coupler such that the TX input loss is 0.5 dB only, much lower than 3 dB, but at the expenses of increasing the LO input loss to 10dB.

Now, let us consider the 3x3 homodyne RX introduced in Fig. 3.6(b). If the LO is first attached to a PBS, and the second PBS output is connected to the unused input port of the 3x3 coupler, the result is the novel and simple front-end depicted in Fig. 6.2(a) for polarization-independent coherent detection. Note that the PBS can also be attached to the signal path, as seen in Fig. 6.2(b), but the first connection to the LO is preferred in order not to add extra insertion loss from the PBS to the already weak received signal. With this novel front-end, Ciaramella analytically demonstrated in [Cia14] that by applying a large frequency detuning between signal and LO (larger than $0.75R_b$), the random SOP components affecting data fall beyond the RX BW and can be suppressed by electrical filtering. This holds for ASK modulation that is quite insensitive to the frequency detuning. Nevertheless, it does not suit for PSK because the phase modulated signals are highly affected by the frequency detuning, as reported in Chapter 5. This motivated to investigate the heterodyne detection of DPSK signals using this new 3x3 optical front-end.

6.1.1 Receiver architecture

The proposed RX is depicted in Fig. 6.3, and implements the 3x3 optical front-end of Fig. 6.2(a) to beat the incoming signal with the 𝕏 and 𝕐 components of the LO SOP, previously separated by the PBS. For optimality of the coherent mixing, the LO is polarized linearly at 45° so that the 𝕏 and 𝕐 components are the same. Three PDs perform single-ended detection, but the photocurrents are later balanced when they are linearly combined for IQ recovery, similar than the 3x3 homodyne RX in Section 2.1.2.2. This cancels the DD terms, which is of particular interest in udWMD-PON with hundreds of users, as outlined below. The IQ recovery can be realized by passive hardware for fully analog RXs, or inside the DSP unit if the preferred RX implementation is digital.

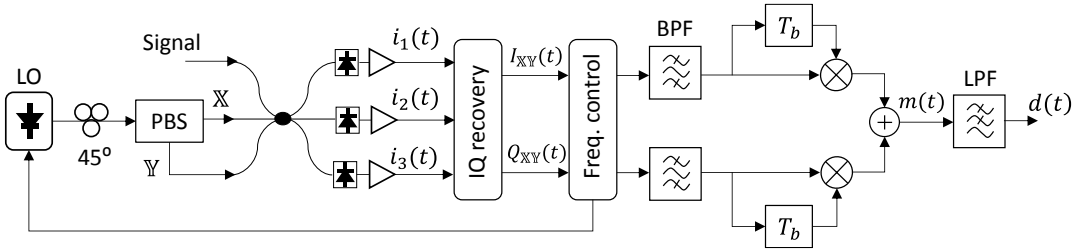

Figure 6.3. Polarization-independent 3x3 balanced heterodyne RX for DPSK.

At the electrical processing part of the RX, the recovered $I_{\mathbb{XY}}(t)$ and $Q_{\mathbb{XY}}(t)$ signals enter the frequency control systems that, for analog heterodyne RX, consists of the frequency discriminator analyzed in Section 5.2. Later on the two signals are band-pass filtered and differentially demodulated to recover the DPSK data, then combined and low-pass filtered to overcome the polarization effects before the decision part of the RX. Indeed, the complete RX in Fig. 6.3 is quite similar than that of Fig. 3.6(b) for phase-diversity homodyne, but replacing the LPFs by BPFs and adding the PBS at the input. Here, though, the detection is heterodyne with the f_{IF} properly selected as an integer multiple of the bit rate to maximize the amplitude of the decision variable (see Section 2.3.2). It is worth mentioning that the proposed RX achieves the polarization-independent detection of DPSK signals with a remarkably simple front-end, and without adding extra complexity to the electrical differential detection process nor the optical TX, compared with the schemes based on 2x2 coupler.

6.1.2 Analytical model

For the system model, let us consider the Jones notation in Eq. (2.31) for the arbitrary-polarized received signal, and given by

$$\mathcal{J}_S(t) = \begin{bmatrix} e_{S,\mathbb{X}}(t) \\ e_{S,\mathbb{Y}}(t) \end{bmatrix} = \begin{bmatrix} \cos\varphi\, \mathbb{X} \\ \sin\varphi\, e^{j\psi}\, \mathbb{Y} \end{bmatrix} \left[E_S(t) e^{j(\omega_S t + \phi_S(t))} \right] \tag{6.1}$$

where φ, ψ are the azimuth and ellipticity of the signal SOP respectively. The LO is linearly polarized at 45° ($\varphi = 45°$, $\psi = 0$) at the input of the PBS to ensure optical beating with LO components at the same power; then, its Jones vector reads as

$$\mathcal{J}_{LO}(t) = \begin{bmatrix} e_{LO,\mathbb{X}}(t) \\ e_{LO,\mathbb{Y}}(t) \end{bmatrix} = \frac{1}{\sqrt{2}} \begin{bmatrix} \mathbb{X} \\ \mathbb{Y} \end{bmatrix} \left[E_{LO}(t) e^{j(\omega_{LO} t + \phi_{LO}(t))} \right] \tag{6.2}$$

The optical mixing between signal and LO in the 3x3 coupler is described by the following scatter matrix

$$\begin{bmatrix} e_1(t) \\ e_2(t) \\ e_3(t) \end{bmatrix} = \frac{1}{3}\begin{bmatrix} a & b & b \\ b & a & b \\ b & b & a \end{bmatrix}\begin{bmatrix} \mathcal{J}_S(t) \\ e_{LO\mathbb{X}}(t) \\ e_{LO\mathbb{Y}}(t) \end{bmatrix} \tag{6.3}$$

with a, b the 3x3 scatter matrix coefficients given by Eqs. (2.20) and (2.21). If ideal photodetection is assumed, the three photocurrents are derived by $i_k(t) = \Re\left(\left|e_{k,\mathbb{X}}(t)\right|^2 + \left|e_{k,\mathbb{Y}}(t)\right|^2\right)$, with $k = \{1, 2, 3\}$ and $\Re$ the responsivity of the PD. The result is the following set of photocurrents

$$i_1(t) = \frac{\Re}{3}\left[P_S(t) + 2P_{LO} + 2\sqrt{P_S(t)P_{LO}}\left(cos\varphi\ cos\left(\omega_{IF}t + \Delta\phi(t) + \frac{2\pi}{3}\right) + sin\varphi\ cos\left(\omega_{IF}t + \Delta\phi(t) + \psi + \frac{2\pi}{3}\right)\right)\right] \tag{6.4}$$

$$i_2(t) = \frac{\Re}{3}\left[P_S(t) + 2P_{LO} + 2\sqrt{P_S(t)P_{LO}}\left(cos\varphi\ cos\left(\omega_{IF}t + \Delta\phi(t) - \frac{2\pi}{3}\right) + sin\varphi\ cos(\omega_{IF}t + \Delta\phi(t) + \psi)\right)\right] \tag{6.5}$$

$$i_3(t) = \frac{\Re}{3}\left[P_S(t) + 2P_{LO} + 2\sqrt{P_S(t)P_{LO}}\left(cos\varphi\ cos\left(\omega_{IF}t + \Delta\phi(t)\right) + sin\varphi\ cos\left(\omega_{IF}t + \Delta\phi(t) + \psi - \frac{2\pi}{3}\right)\right)\right] \tag{6.6}$$

Here, $P_S(t)$ and P_{LO} are the signal and LO power respectively, $\omega_{IF} = 2\pi f_{IF}$ is the intermediate frequency, and $\Delta\phi(t) = \phi_d(t) + \phi_n(t)$ is the phase difference between signal and LO that carries the phase modulated data $\phi_d(t)$, along with the random phase term $\phi_n(t)$. Each photocurrent is composed by the DD terms in baseband and the coherent terms oscillating at ω_{IF}. Afterwards, the three signals are linearly combined according to Eqs. (2.23) and (2.24), to obtain two orthogonal I and Q signals and also cancel the DD terms, yielding

$$I_{\mathbb{XY}}(t) = \Re\sqrt{P_S(t)P_{LO}}\left[cos\varphi\ cos\left(\omega_{IF}t + \Delta\phi(t) - \frac{2\pi}{3}\right) + sin\varphi\ cos(\omega_{IF}t + \Delta\phi(t) + \psi)\right] \tag{6.7}$$

$$Q_{\mathbb{XY}}(t) = \Re\sqrt{P_S(t)P_{LO}}\left[-cos\varphi\ sin\left(\omega_{IF}t + \Delta\phi(t) - \frac{2\pi}{3}\right) + sin\varphi\ sin(\omega_{IF}t + \Delta\phi(t) + \psi)\right] \tag{6.8}$$

Note that the first term of each of the equations above is the $\mathbb{X}$- polarization contribution, whereas the second term is the $\mathbb{Y}$- polarization, and that is precisely the reason why the notation $\mathbb{XY}$ appears in the subindexes. In practice this means that there is spectral overlap between the SOP components, thus potential destructive interference depending on the values of φ, ψ. This contrasts with the 2x2 heterodyne RXs in Fig 6.1 that produce one photocurrent for each SOP. However, a key point worth noting here is the inverted sign in the two terms of $Q_{\mathbb{XY}}(t)$ originated at the optical mixing in the 3x3 coupler because the $\mathbb{X}$- and $\mathbb{Y}$- polarizations of the LO are shifted in phase by relative $2\pi/3$, and the quadrature signal is sensitive to that change of quadrant.

Next, both signals are filtered by two BPFs centered at f_{IF} and properly adjusted in BW to be matched with the data BW. Differential demodulation is carried out to extract the DPSK data $\Delta\phi_d(t) = \phi_d(t) - \phi_d(t - T_b)$, then the signals are added into $m(t)$ to obtain

$$m(t) = \Re^2 P_S(t) P_{LO} \Big[cos\big(\omega_{IF} T_b + \Delta\phi_d(t)\big) + sin(2\varphi) cos\left(2\omega_{IF} t - \omega_{IF} T_b + \Delta\phi(t) + \Delta\phi(t - T_b) + \psi - \tfrac{2\pi}{3}\right)\Big] \quad (6.9)$$

This key equation shows a very clean term in baseband that contains the demodulated data $\Delta\phi_d(t)$, and a polarization-dependent term at high frequency –oscillating at $2\omega_{IF}$– that contains the random SOP coordinates $\varphi,\ \psi$. Since in heterodyne detection the f_{IF} is usually two or three times the data rate R_B, low-pass filtering of $m(t)$ completely filters out the polarization-dependent term at $2f_{IF}$ in Eq. (6.9), thus canceling the SOP overlap. This is illustrated in Fig. 6.4 that shows frequency domain representation of $m(t)$.

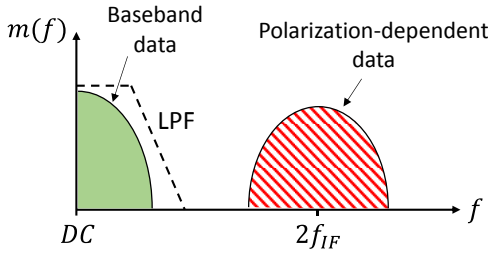

Figure 6.4. Frequency domain representation of $m(t)$ after adding the differentially demodulated signals.

At the baseband data (first term of Eq. (6.9)), in order to maximize the variable for data decision, the f_{IF} is set to be nR_B, with $n = \{2, 3, \ldots\}$; then $\omega_{IF} T_b = 2n\pi$ and has no impact on the recovered data $\Delta\phi_d(t)$. Finally, the recovered DPSK signal after the LPF is found to be

$$d(t) = \Re^2 P_S(t) P_{LO} \cos \Delta\phi_d(t) \quad (6.10)$$

demonstrating the polarization-independent detection of DPSK signal. Therefore, the main outcome is that in the coherent RX with 3x3 optical front-end, the polarization independent detection is achieved by the joint effect of the intermediate frequency that eliminates the spectral overlap, and the subsequent sharp electrical filtering that suppress the random SOP components.

If the 3x3 front-end is configured with the PBS in the signal path, as in Fig. 6.2(b), the three photodetected currents are correspondingly written as

$$i_1(t) = \frac{\Re}{3}\Big[P_S(t) + 2P_{LO} + 2\sqrt{P_S(t)P_{LO}}\Big(cos\varphi\ cos\left(\omega_{IF} t + \Delta\phi(t) + \tfrac{2\pi}{3}\right) + sin\varphi\ cos(\omega_{IF} t + \Delta\phi(t) + \psi)\Big)\Big] \quad (6.11)$$

$$i_2(t) = \frac{\Re}{3}\Big[P_S(t) + 2P_{LO} + 2\sqrt{P_S(t)P_{LO}}\Big(cos\varphi\ cos\big(\omega_{IF} t + \Delta\phi(t)\big) + sin\varphi\ cos\left(\omega_{IF} t + \Delta\phi(t) + \psi + \tfrac{2\pi}{3}\right)\Big)\Big] \quad (6.12)$$

$$i_3(t) = \frac{\Re}{3}\Big[P_S(t) + 2P_{LO} + 2\sqrt{P_S(t)P_{LO}}\left(cos\varphi\ cos\left(\omega_{IF}t + \Delta\phi(t) - \frac{2\pi}{3}\right) + sin\varphi\ cos\left(\omega_{IF}t + \Delta\phi(t) + \psi - \frac{2\pi}{3}\right)\right)\Big] \quad (6.13)$$

which only differ from Eqs. (6.4)–(6.6) in the distribution of the phase shift $\pm 2\pi/3$ and the SOP ellipticity ψ among the three photocurrents. The recovered $I_{\mathbb{XY}}(t)$ and $Q_{\mathbb{XY}}(t)$ after cancelling the DD terms are now

$$I_{\mathbb{XY}}(t) = \Re\sqrt{P_S(t)P_{LO}}\big[cos\varphi\ cos\big(\omega_{IF}t + \Delta\phi(t)\big) + sin\varphi\ cos\big(\omega_{IF}t + \Delta\phi(t) + \psi + \tfrac{2\pi}{3}\big)\big] \quad (6.14)$$

$$Q_{\mathbb{XY}}(t) = \Re\sqrt{P_S(t)P_{LO}}\left[cos\varphi\ sin\big(\omega_{IF}t + \Delta\phi(t)\big) - sin\varphi\ sin\left(\omega_{IF}t + \Delta\phi(t) + \psi + \tfrac{2\pi}{3}\right)\right] \quad (6.15)$$

This time, the sign inversion in $Q_{\mathbb{XY}}(t)$ occurs for the $\mathbb{Y}$- polarization term. The signal $m(t)$ after differential demodulation and signals addition becomes

$$m(t) = \Re^2 P_S(t)P_{LO}\left[cos\big(\omega_{IF}T_b + \Delta\phi_d(t)\big) + sin(2\varphi)cos\left(2\omega_{IF}t - \omega_{IF}T_b + \Delta\phi(t) + \Delta\phi(t - T_b) + \psi + \tfrac{2\pi}{3}\right)\right] \quad (6.16)$$

that produces identical result after the LPF than the configuration with the PBS attached to the LO, preferred in this thesis to minimize the power loss of the received signal.

Another important characteristic of the 3x3 heterodyne RX is the cancellation of the DD terms. By looking at the three photocurrents in Eqs. (6.4)–(6.6) –or equivalently (6.11)–(6.13)– after the single-ended detection, the DD terms are composed by the strong DC component from the LO due to the high LO power P_{LO}, and by the received signal power $P_S(t) = |E_S(t)|^2$ that normally is much smaller than the coherent term. However, in the udWDM-PON scenario with hundreds of users, the DD term $P_S(t)$ accumulates the power of all the individual udWDM channels, being expressed as

$$P_S(t) = \sum_{k=1}^{N} |E_k(t)|^2 \quad (6.17)$$

with N the number of users. Taking the example of the COCONUT PON in Chapter 4, with equal 256 users spaced by 12.5 GHz for heterodyne ONUs, the total optical power is $10 \times log_{10}(256)$ = +24 dB at the PDs input, thus the DD term might become comparable in power to the coherent term. This scenario is illustrated in Fig. 6.5, and makes us to conclude that for a large number of users the DD terms can cause interference and negative impact on the detection if they are not cancelled correctly.

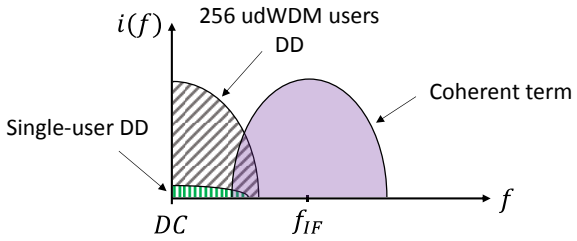

Figure 6.5. Frequency domain representation of the single-ended heterodyne detection.

6.1.3 Experimental validation

To validate correct DPSK detection with the 3x3 heterodyne RX, independent from the received signal SOP, the experimental setup depicted in Fig. 6.6 was implemented. At the TX, PRBS data from a PPG running at 1.25 Gb/s were properly amplified and equalized to drive the direct modulation of a 4 MHz linewidth DFB (λ = 1549 nm) and emitting at -10 dBm. The signal was transmitted through 50 km of SMF, and the VOA emulated for the ODN losses. At the RX, the received signal was mixed with LO using the three optical front-ends mentioned above, namely 4-PD balanced, 2-PD single-ended and 3x3 balanced. The LO was an ECL with 100 kHz linewidth and emitting at 3dBm, that entered linearly polarized at 45º to the RX front-end. The f_{IF} was set to 2.5 GHz. After photodetection, the two photocurrents from the 2x2 coupler-based front-ends were digitalized by a 50 GSa/s RTO for differential demodulation and BER computing. In the case of 3x3 coupler front-end, the balancing of the photocurrents was carried out by DSP, thus a third ADC channel sampled the output of the third photodiode, as shown in Fig. 6.6 (dotted line). Within the DSP, the BPF was achieved by combination of two 4th order 1.5 GHz high-pass and 3.5 GHz low-pass Bessel filters. After the differential demodulation both signals were added, then low-pass filtered at 1 GHz and thresholded for data decision. The BER was calculated by direct error counting over 2^{18} bits.

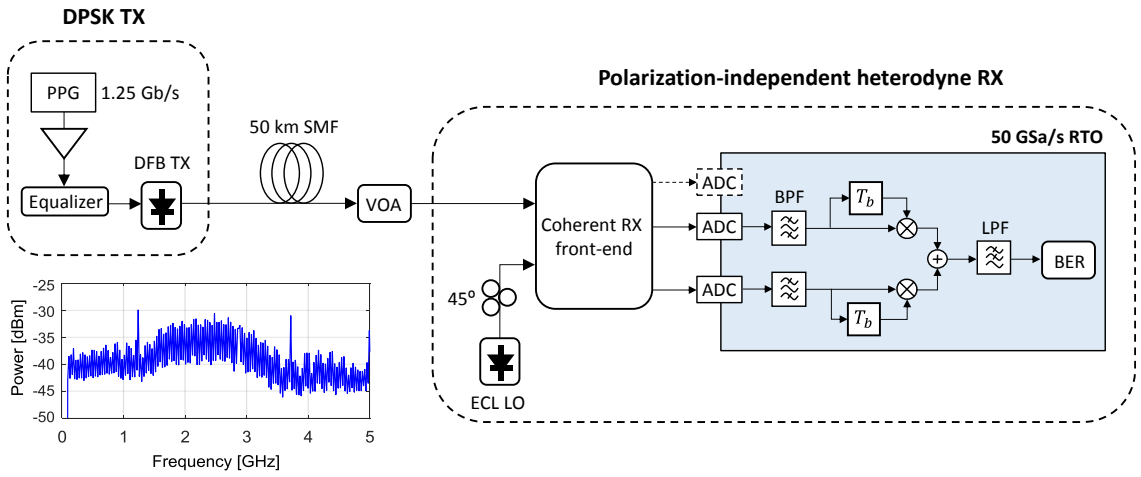

Figure 6.6. Experimental setup with 1.25 Gb/s DPSK transmission. The inset shows the DPSK spectrum after heterodyne detection at $f_{IF} = 2.5$ GHz.

First, the BER was evaluated in terms of the received optical power for 0 (b2b) and 50km SMF. The results in Fig. 6.7(a) reveal that, at BER = 10^{-3} FEC threshold, the 3x3 balanced RX achieved a sensitivity of -49 dBm, 0.7 dB worse than the 4-PD balanced RX mostly due to the excess losses from the 3x3 coupler, that ranged from 0.11 to 0.59 dB between ports. For the 2-PD single-ended RX, the power penalty rises to 2.6 dB, close to the 3 dB expected from theory. No meaningful difference was observed between b2b and 50km tests. Fig. 6.7(b) reports the eye diagram after differential demodulation for the 3x3 balanced RX.

Next, the RX tolerance to the frequency detuning was measured by sweeping the LO λ. The results are plotted in Fig. 6.8 in terms of the power penalty at BER = 10^{-4} against the LO detuning. As observed, the detuning must be kept lower than 60 MHz in the three RXs to avoid penalties larger

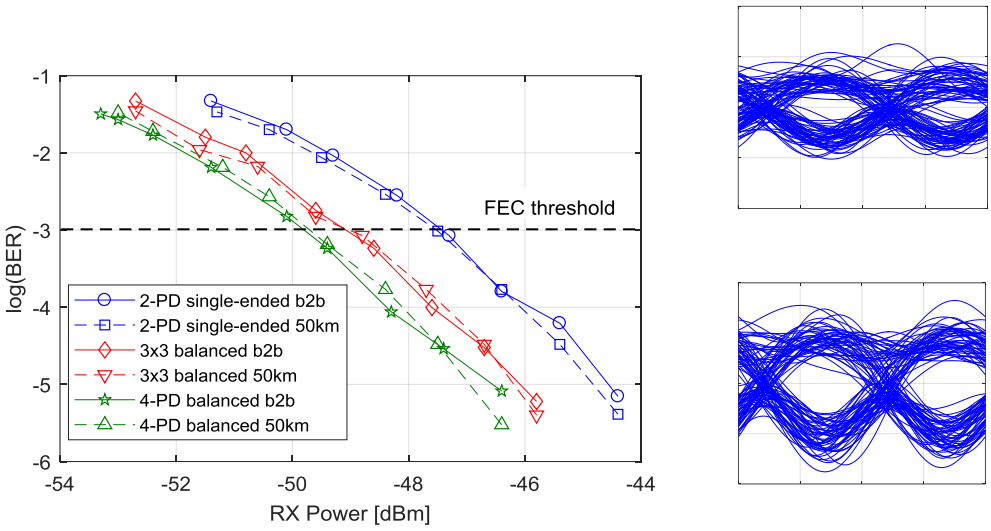

(a) (b)

Figure 6.7. (a) BER vs. received power for 1.25 Gb/s DPSK; (b) eye diagram at BER of 10^{-3} (upper) and 10^{-5} (lower) for the 3x3 balanced RX.

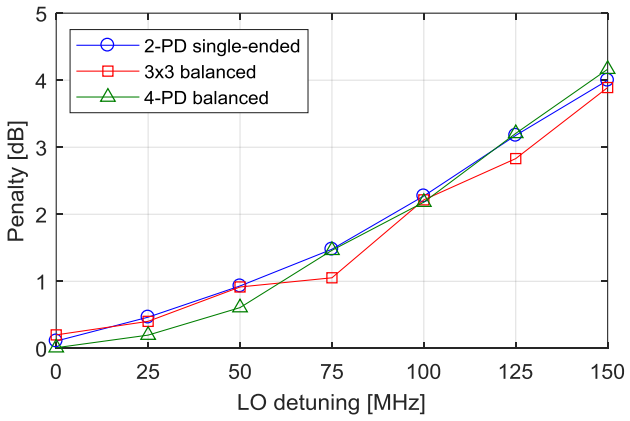

Figure 6.8. Sensitivity penalty at BER = 10^{-4} as a function of LO detuning.

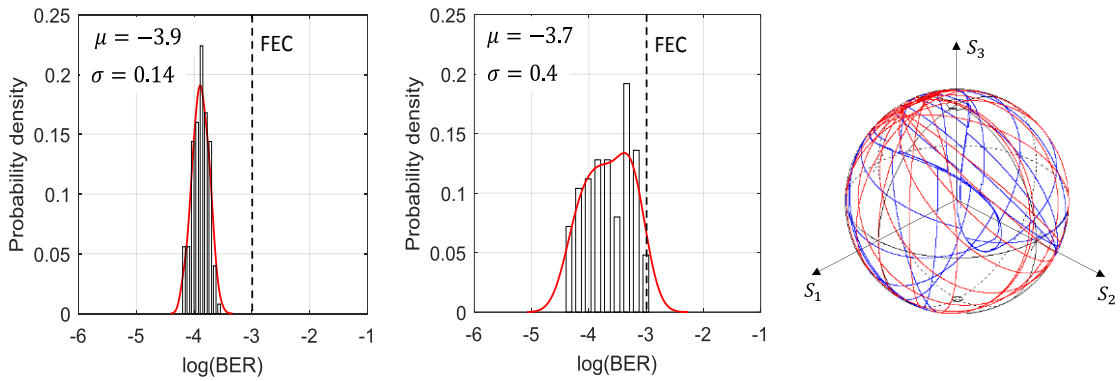

(a) (b) (c)

Figure 6.9. Probability density vs. BER over 125 measurements on the 3x3 balanced RX with (a) fixed SOP and (b) different random SOP each point; (c) trajectories of the signal SOP over the Poincaré sphere for the 125 BER mesurements.

than 1dB. This makes evident the large impact of frequency error on the detection of PSK signals, and confirms that the 3x3 intradyne solution for ASK, with $0.75R_B$ LO detuning, does not fit for DPSK.

In order to assess the polarization-independent operation of the proposed 3x3 balanced RX, an experiment was conducted to measure the BER 125 times with different random SOP of the received signal each, to compute the statistics of the BER. The received power was fixed to -47 dBm to obtain a reference BER = 10^{-4}, and the BER measurement was first repeated 125 times without changing the signal SOP to determine the inherent variance of the measurement; the results are reported in Fig. 6.9(a). Then, the signal SOP was randomly varied 125 times in Fig. 6.9(b), spreading over all the Poincaré sphere surface by following the trajectories shown in Fig. 6.9(c). The results indicate that the average BER increased from 1.26×10^{-4} to 2×10^{-4} and the standard deviation from 0.14 to 0.4, for the BER measured 125 times with fixed and random SOP each point respectively. In terms of sensitivity, these values correspond to a mean power penalty of about 0.8 dB when detecting any random SOP of the signal, in agreement with the unbalanced excess losses of the 3x3 coupler, and maximum of 1.6 dB penalty in the worst 5% of the measurements.

The last tests aimed at comparing the three RXs in terms of common-mode rejection and thus their tolerance to the presence of other channels in the PON with higher power. For the tolerance test, a second user with another direct phase-modulated DFB, with uncorrelated data, was placed at 12.5 GHz from the TX λ. Its power was increased with respect to User 1 to evaluate the impact of the DD power increase in the baseband on the coherent detection of User 1. The electrical spectra after photodetection in Fig. 6.10 reports on the two users separated by 12.5 GHz and detected by heterodyne RX with $f_{IF} = 2.5$ GHz, for two different SIR, defined as the power ratio between User 1 and User 2. When both users transmit at the same power (SIR = 0 dB), as in Fig. 6.10(a), the DD terms in the baseband are much smaller than the coherent term, thus are negligible; in contrast, when the power difference is as large as 25 dB emulating the total power of ~256 users, as in Fig. 6.10(b), the DD terms become relevant and are comparable in power to the coherent spectrum of User 1, producing penalty at the detection if not cancelled. The results of the test are plotted in Fig. 6.11 in terms of the power penalty at BER = 10^{-4} as a function of the SIR, when the power difference ranges from 10 to 30 dB over the TX power.

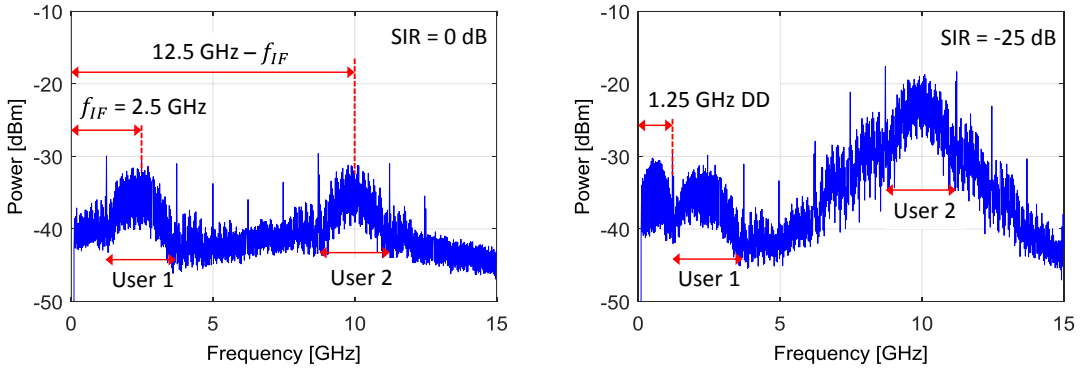

(a) (b)

Figure 6.10. Electrical spectra at the RX for two 1.25 Gb/s DPSK users, spaced by 12.5 GHz, and transmitting (a) at the same power and (b) with 25 dB power difference.

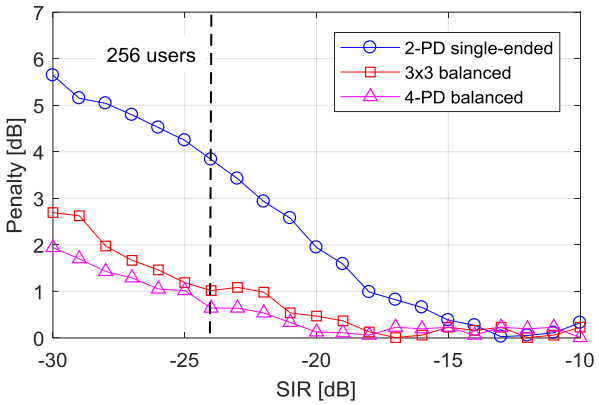

Figure 6.11. Sensitivity penalty at BER = 10^{-4} vs. power difference between two DPSK users spaced by 12.5 GHz.

As observed in Fig. 6.11, the 2-PD single-ended RX can tolerate up to -18 dB with respect to the interfering power for 1 dB maximum sensitivity penalty. Conversely, in the 4-PD balanced and the 3x3 balanced RXs the tolerance extends up to -25 dB power difference, due to the benefit of canceling the DD. Moreover, if the results are considered with respect to the interfering power from a fixed number of users, e.g. 256 (vertical dotted line), the balanced detection outperforms by about 3 dB the single-ended detection, thus revealing its importance in a closely spaced udWDM-PON with a large number of users. In this particular coherent PON scenario with direct DFB modulation, the DD term in the baseband is given by the residual IM of the direct-phase modulation, in which the laser driving current is equalized with a high-pass response to modulate the laser chirp. Fig. 6.12 reports on the residual IM of the DFB TX used in the experiment, with analog equalizer for direct DPSK, and biased at 75 mA. The residual IM can be appreciated in any of the photocurrents at the RX by turning off the LO, and shows ER lower than 1 dB.

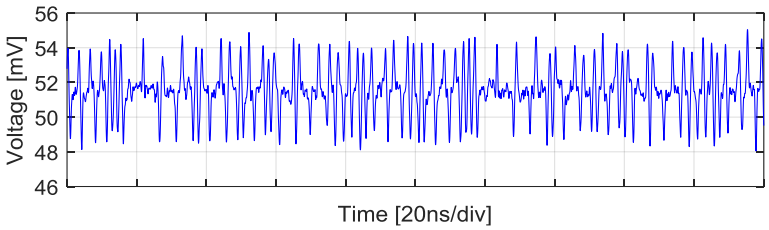

Figure 6.12. Direct detection of the residual IM from direct-phase modulation of a DFB, using analog high-pass equalizer.

6.2 Polarization-Diversity 3x3 Homodyne Receiver

The other paradigm of coherent RX considered in this thesis, the homodyne RX aided by DSP, faces a more complex challenge when attempting to simplify its architecture for polarization independent detection. In recent research all the solutions explored require extra BW at the RX; this translates into larger BW and sampling rate of the ADCs, which unfavorably scales with the symbol rate. For instance, the novel 3x3 optical front-end studied in previous sections –mainly intended for analog implementation– requires intradyne or heterodyne detection with large

enough f_{IF} to eliminate the spectral overlap between data and random SOP components. Alternatively, in polarization time-switching (also referred to as polarization scrambling) [Can15b], [Erk16] the detection can be homodyne, but at the cost of introducing 50% redundancy of the symbols for the two orthogonal SOP, thus doubling the required RX BW compared with polarization diversity homodyne RXs operating at the same bit rate.

In consequence, as state-of-the-art optics lacks alternatives to polarization-diversity RX front-end for homodyne detection with baseband processing, the opportunities for system simplification here focus on the DSP and the electrical subsystems of the homodyne RX. By going back to Section 3.1, the key conditions to facilitate the adoption of digital coherent RXs for PONs were listed as follows: (I) reduce the footprint of the coherent TRX photonic elements; (II) lower the requirements for ADCs and DACs in terms of BW, resolution, and sample rate; (III) simplify the DSP complexity, thus reducing the energy consumption and overall cost of the digital processor. Regarding (I), along this thesis the use of external modulators at the TX has been replaced by direct amplitude-and-phase modulation of low-cost DFBs, and complex 90° hybrids at the RX have been replaced by common 3x3 fused-fiber couplers, also employing less number of PDs. The (II) and (III) are now addressed in this section that presents the development and real-time implementation of a complete RX DSP for polarization-diversity homodyne RXs, in which the ADCs and all the DSP for m-PSK operates at only one sample per symbol.

6.2.1 Receiver architecture

The polarization-diversity homodyne RX is illustrated in Fig 6.13. Its architecture is essentially the same low-complexity 3x3 homodyne RX proposed in Fig. 3.2, but differs in that the ADCs now acquire data at one sample per symbol (sps), and the equalization is not performed by the RX due to the lower sampling rate of the photocurrents, below the Nyquist sampling limit –twice as high as the maximum frequency of the signal– in order to avoid aliasing. This concept will be elaborated later. The schematic in Fig. 6.13 also shows the two feedback paths from the DSP. One is the timing error ε_k estimated by the CLK recovery that feeds a numerically controlled oscillator (NCO), which in turn drives the sampling instants of the ADCs.

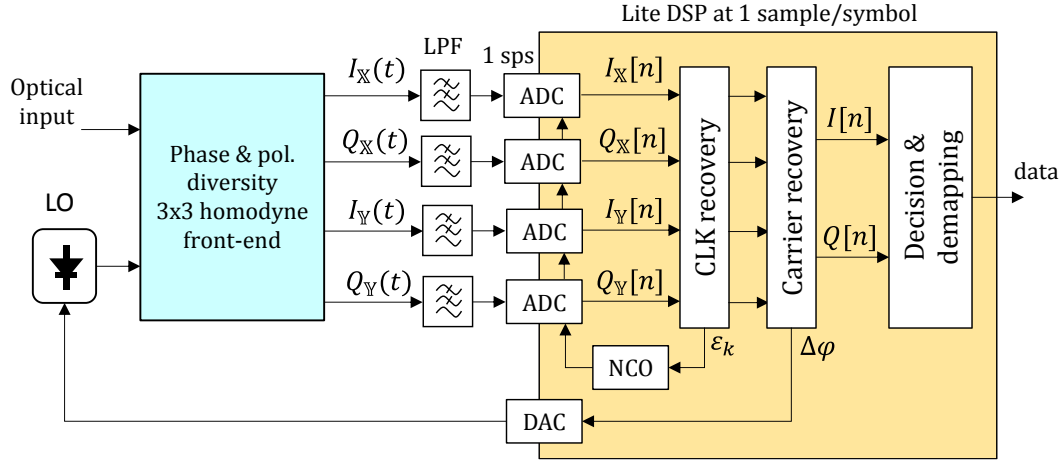

Figure 6.13. Polarization-diversity 3x3 homodyne receiver with ADCs and DSP operating at the symbol rate.

The other is the frequency error $\Delta\varphi$ estimated by the carrier recovery, that is sent towards the LO for λ-tuning; the latter requires extra digital-to-analog conversion that, given the low BW of $\Delta\varphi$, can be carried out by a simple serial 1-bit DAC, as demonstrated in Section 4.2.1.

The CLK recovery is crucial in any digital RX to synchronize the received data with the DSP, as the ADCs might not operate at the same speed as the received data. Within the CLK recovery algorithm, the TED estimates the optimal sampling phase ϕ_τ that minimizes the timing error ε_k. The Gardner algorithm [Gar86] is a widespread non-data aided TED that requires ×2 oversampling (i.e., two samples per symbol) to determine early, ideal and late sampling instants. This fulfills the Nyquist sampling theorem as $R_S = 2B$, where $B = 1/T_b$ is the BW of the photodetected signals. Other systems also perform fractional sampling $R_S = \gamma B$, with $1 < \gamma < 2$, to digitalize data, that are later resampled to $R_S = 2B$ by digital interpolators at the DSP [Kik16]. In contrast, the novelty here is that the CLK recovery algorithm works with only 1 sps and without resampling nor interpolation by DSP; the key enabling technique is a TED based on the power of the detected electrical field, together with a simple maximum finding algorithm for continuous tracking of the optimal sampling phase.

In this scenario, as the sampling rate is $R_S = 1/T_b$, linear equalization at the RX must be performed by T-spaced FIR filter, which depends heavily on the correct sampling phase and impose strict requirements to the CLK recovery subsystem. Conversely, when the analog signals are oversampled the linear FIR equalizer is fractionally spaced, i.e., the tap spacing is a fraction of the symbol time T_b. Typical sampling rate $R_S = 2/T_b$ yields $T_b/2$-spaced FIR equalizer that can compensate for any time delay and much less depends on the sampling phase. Therefore, for systems with symbol-rate ADCs the linear equalization must be performed at the TX side, thus ensuring that signals reach the RX without any distortion for optimality of the CLK recovery and all the DSP at one sample per symbol.

6.2.2 Symbol-rate digital signal processing

Let us first focus on the CLK recovery algorithm. Normally, the TED estimates the timing error from the detected signal amplitude, as in Gardner, early-late synchronizer, Mueller & Müller, etc. An alternative was presented in [Tan08], [Yan13], in which the estimation of the timing error is purely based on the power of the received signal. This power-based TED is particularly attractive in the udWDM-PON scenario because of the robustness against the phase noise and frequency drift from low-cost DFBs, as the phase content of the detected field does not influence on the CLK recovery process. Fig. 6.14 presents the block diagram of the CLK recovery algorithm implementing the power-based TED. First, digital sampling of the four outputs from the polarization-diversity homodyne front-end, consisting of the *I* and *Q* signals for each SOP, takes place. The analog to digital conversion comprises the conventional low pass-filters with impulse response $h(t)$ for out-band noise suppression, followed by the ADCs that gather samples of each filtered photocurrent at the rate of $nT_b + \phi_\tau$, with T_b the symbol duration and ϕ_τ the sampling phase. This allows to reconstruct the sampled complex field for each SOP in the digital domain, according to

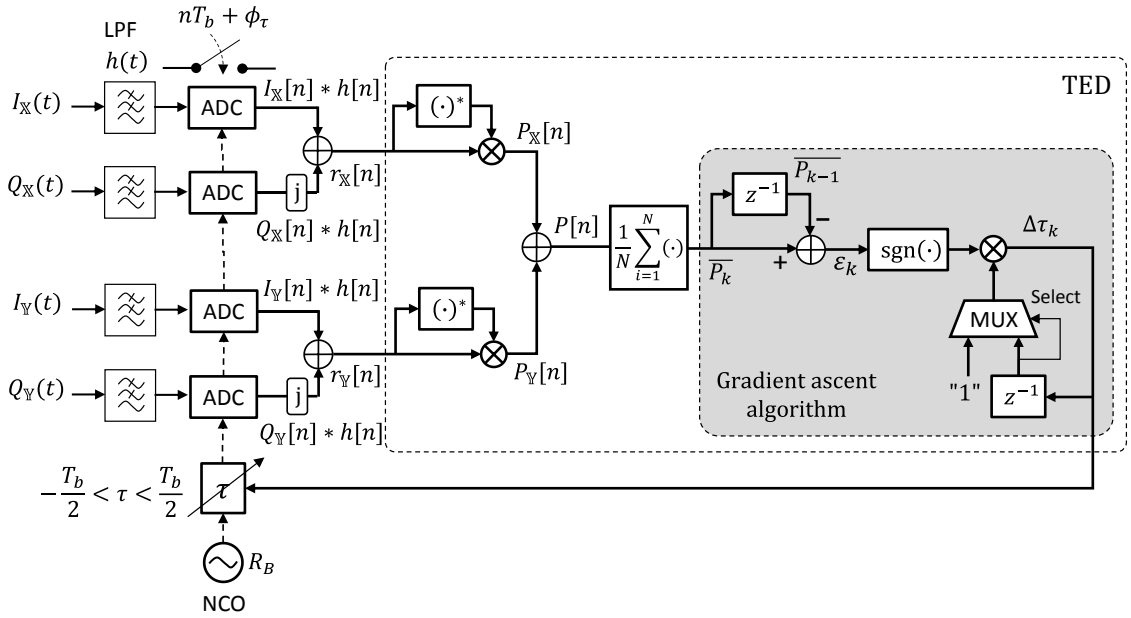

Figure 6.14. Power-based CLK recovery to operate with ADCs sampling at the symbol rate, i.e., one sample per symbol.

$$r_{\mathbb{X}}[n] = (I_{\mathbb{X}}[n] + jQ_{\mathbb{X}}[n]) * h[n] \tag{6.18}$$

$$r_{\mathbb{Y}}[n] = (I_{\mathbb{Y}}[n] + jQ_{\mathbb{Y}}[n]) * h[n] \tag{6.19}$$

After A/D conversion, the power of the received signal for each SOP $P_{\mathbb{X}}[n]$ and $P_{\mathbb{Y}}[n]$ is calculated by $|r_{\mathbb{X}}[n]|^2$ and $|r_{\mathbb{Y}}[n]|^2$ respectively, then added to eliminate polarization effects. Next, the total power $P[n] = P_{\mathbb{X}}[n] + P_{\mathbb{Y}}[n]$ is averaged over a block of N symbols for noise suppression, as the SNR of the received signal is typically low. In conventional CLK recovery with $R_S \geq 2B$, the magnitude and sign of the timing error ε_k is computed from the balance among the set of available samples within a symbol time T_b. Here, though, due to the fact that only one sample per symbol is acquired, there is no any information about the sign of ε_k when the sampling phase varies. This problem is solved by implementing a gradient ascent algorithm that continuously searches for the maximum of the averaged power $\overline{P_k}$. In it, the sign of ε_k is extracted from the difference between $\overline{P_k}$ and $\overline{P_{k-1}}$, where k updates every N symbols after averaging; here, sgn(·) stands for the sign function. The output of the gradient ascent algorithm is the sampling phase delay $\Delta\tau_k$ taking the values 0 or ±1 depending on the required timing adjustment, as follows

$$\Delta\tau_k = \begin{cases} -1, & \text{a timing advance is required} \\ 0, & \text{no timing adjustment is required} \\ +1, & \text{a timing delay is required} \end{cases} \tag{6.20}$$

Calculation of $\Delta\tau_k$ requires the sign of ε_k and knowledge of the previous timing $\Delta\tau_{k-1}$. The multiplexer (MUX) is to prevent passing the value 0 through the feedback that would result in persistent $\Delta\tau_k = 0$ at the output of the TED. If the value at the select port is either -1 or 1, the MUX passes the $\Delta\tau_{k-1}$ value; otherwise, the MUX output will be 1. The computed $\Delta\tau_k$ then passes on to the NCO that drives the ADC sampling instants, to dynamically adjust the sampling

phase ϕ_τ progressively in steps of $\Delta\tau$, and within $-T_b/2 < \tau < T_b/2$, until converge to the optimal sampling point. This timing adjustment process is graphically illustrated in Fig. 6.15. Let us assume that there is a positive timing delay $+\Delta\tau$ between $\overline{P_{k-1}}$ and $\overline{P_k}$, which means that the last calculated $\Delta\tau_{k-1} > 0$. If the sampling is early (Fig. 6.15 left hand), $\varepsilon_k = \overline{P_k} - \overline{P_{k-1}}$ is positive, $\Delta\tau_{k-1}$ is also positive, then the TED output $\Delta\tau_k$ indicates that a timing delay by $+\Delta\tau$ is required for the next symbols. On the other hand, if the sampling is late (Fig. 6.15 right hand), and assuming the same $+\Delta\tau$ between $\overline{P_{k-1}}$ and $\overline{P_k}$, then $\varepsilon_k < 0$, $\Delta\tau_{k-1} > 0$, and $\Delta\tau_k$ indicates that a timing advance by $-\Delta\tau$ is required for the next symbols. Within the loop, the sampling phase ϕ_τ is updated every N symbols.

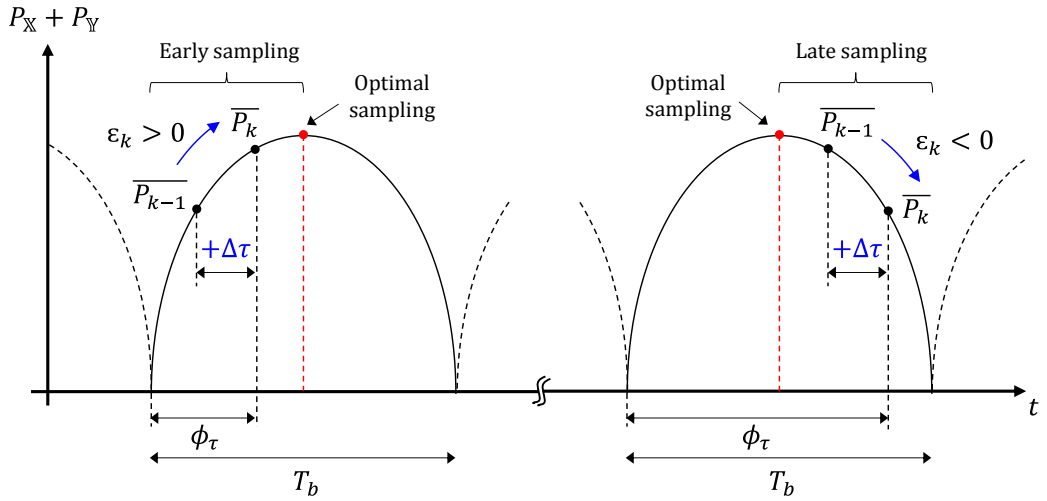

Figure 6.15. Graphic representation of the ADC sampling phase tuning by maximum finding algorithm over the total received signal power $P_{\mathbb{X}} + P_{\mathbb{Y}}$.

An immediate conclusion from Fig. 6.15 is that the performance of the proposed CLK recovery and the ADC sampling tuning process highly depends on the shape of the received signal power, which is mainly determined by the LPF filter response $h(t)$ if other BW limitations and signal distortions are not considered, in the ideal case. Accordingly, the influence of $h(t)$ on the power-based TED was assessed by numerical simulation using standard low-pass Bessel filters of the 4th order, with variable BW. The results are plotted in terms of the timing error ε_k in open loop, as a function of the sampling phase deviation with respect to the optimal sampling point, in Fig. 6.16(a) for DPSK at 1 Gb/s, and in Fig. 6.17(a) for QPSK at 2 Gb/s. Without filtering, $\varepsilon_k = 0$ as expected because of the constant envelope of the m-PSK modulation. Conversely, after low-pass filtering ε_k draws the typical S-curve of the TED, which is smoother and steeper for filter BWs between $0.75R_b$ and R_b. This matches well with the BWs used in homodyne detection.

Additionally, Figs. 6.16(b) and 6.17(b) show the impact of the frequency detuning Δf on the TED for DPSK and QPSK respectively. As Δf increases, most of the received signal power falls beyond the BW of the LPFs at the RX input, and is filtered out, then the slope of the S-curve reduces accordingly. The results indicate that for $\Delta f = 400$ MHz (40% of the baud rate) the S-curve slope reduces about 55% with respect to $\Delta f = 0$. Despite the slope reduction, the tolerance against the frequency detuning is much higher than conventional TED based on signal amplitude; for instance, Fig. 2(a) of [Tan08] shows that the Gardner TED fails for Δf larger than 50% of the

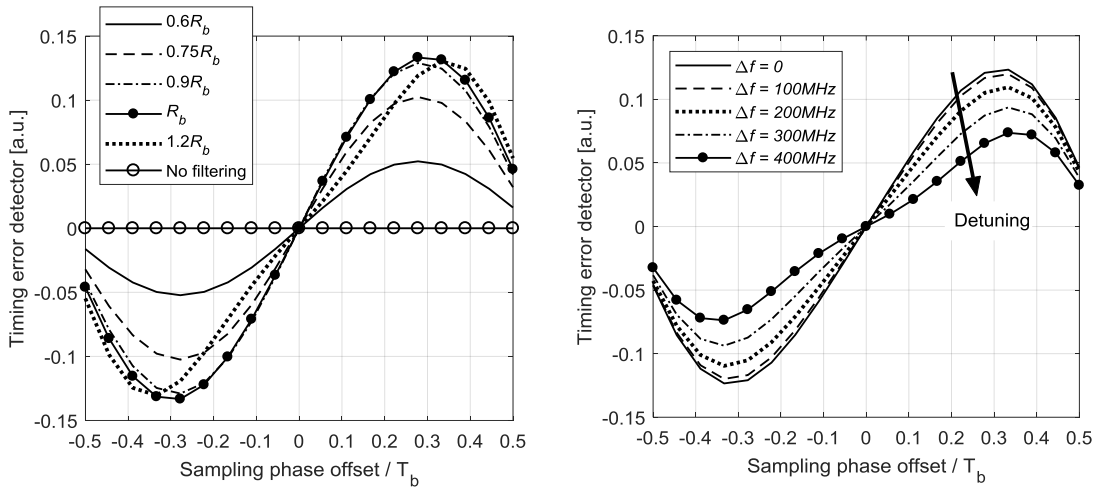

(a) (b)

Figure 6.16. S-curves of the power-based TED for DPSK at 1 Gb/s, for various (a) LPF filter BWs and (b) frequency detuning of the homodyne detection.

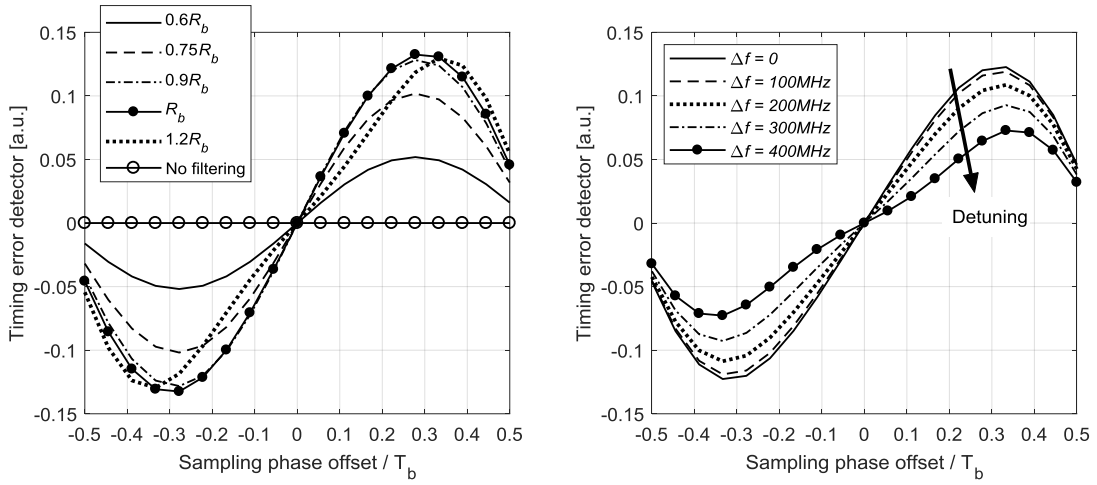

(a) (b)

Figure 6.17. S-curves of the power-based TED for QPSK at 2 Gb/s, for various (a) LPF filter BWs and (b) frequency detuning of the homodyne detection.

baud rate, because the slope of the S-curve is almost cero. Without loss of generality, the S-curves in Figs. 6.16 and 6.17 were computed by assuming positive sampling phase delay $+\Delta\tau$ between $\overline{P_{k-1}}$ and $\overline{P_k}$, similar to Fig. 6.15, with sampling phase tuning resolution of $\Delta\tau \times 0.05T_b$. It is also worth noting that DPSK and QPSK perform the same, thus confirming the independency of the power-based TED on the optical phase content.

The other subsystem of the symbol-rate DSP in Fig. 6.13 is the CR algorithm. It implements the simplified differential CR studied in Section 5.3, that was specifically conceived to operate at one sample per symbol. The differential CR algorithm in its polarization-diversity configuration is depicted in Fig. 6.18. The digital samples of the received complex signal $I[n] + jQ[n]$ are differentially demodulated individually for each SOP to recover the *m*-PSK information from the phase difference between consecutive symbols; here *m* is the order of the PSK modulation (e.g., *m* = 4 for QPSK). This operation cancels the phase noise effect, as long as the symbol rate is several orders of magnitude larger than the total laser linewidth (TX + LO), and depending on the

modulation format (see Section 3.3.1). Since the direct laser modulation at the TX proposed in this thesis is single-polarization, the demodulated signals for each received SOP $d_{\mathbb{X}}[n]$ and $d_{\mathbb{Y}}[n]$ are added to counteract variations of the transmitted SOP after propagating through the fiber channel. Last, the FE compensates for the frequency detuning of the non-ideal homodyne detection, and the recovered PSK symbols $s[n]$ are finally delivered to the decision and demapping subsystem of the DSP for symbol-to-bit recovery.

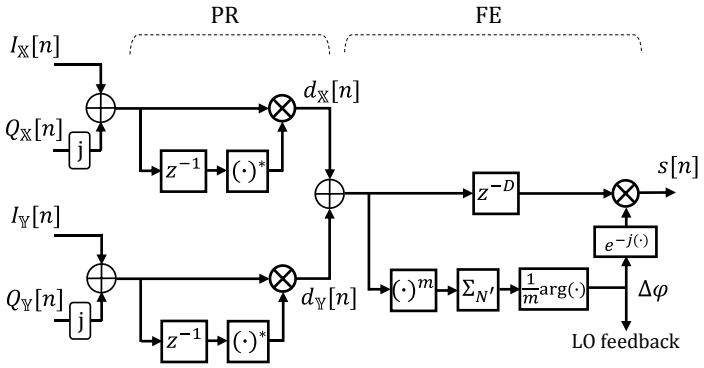

Figure 6.18. Differential CR architecture for symbol-rate polarization-diversity *m*-PSK receivers.

6.2.3 Experimental validation real-time

The symbol-rate DSP described in previous section was prototyped in a commercial FPGA for real-time assessment, using the FPGA homodyne RX for COCONUT presented in Section 4.2.1. This time, however, the optical front-end was polarization-diversity 3x3 homodyne, as depicted in Fig. 6.19. The experiment featured direct-DPSK modulation at the TX, generated from a PPG running at 1.25 Gb/s.

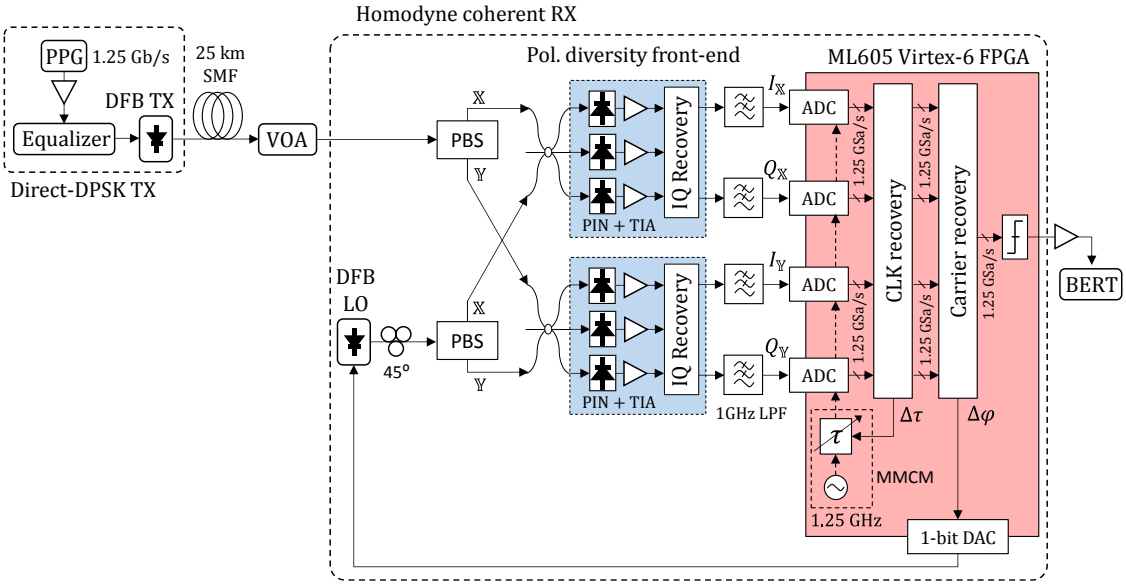

Figure 6.19. Real-time prototype of the polarization-diversity homodyne RX for 1.25 Gb/s DPSK, with the ADCs and the DSP operating at 1 sample per symbol.

Two DFBs with linewidth $\Delta\nu$ = 4 MHz each were used as TX and LO. The DPSK signal was transmitted through 25 km of SMF, then coherently detected by the polarization-diversity homodyne RX. The LO SOP was adjusted to 45° for optimality of the detection. The four photodetected signals $I_{\mathbb{X}}$, $Q_{\mathbb{X}}$, $I_{\mathbb{Y}}$ and $Q_{\mathbb{Y}}$ were low-pass filtered by standard 4th-order Bessel filters with 1 GHz cut-off frequency, then mapped into the digital domain. The ADC was the FMC125 from 4DSP vendor that has four high-speed channels at 1.25 GSa/s each. In the COCONUT test-bed in Section 4.2.1, the four ADC channels were interleaved in pairs to configure 2× 2.5 GSa/s ADC channels to sample the I and Q signals at 2 samples per symbol. This work instead, uses all four ADC channels independently at 1.25 GSa/s to sample the four polarization-diversity photocurrents at 1 sample per symbol.

At the DSP of the RX, the CLK recovery and the carrier recovery subsystems implemented the algorithms reported in Figs. 6.14 and 6.18 respectively. In this FPGA prototyping, the computed timing delay $\Delta\tau$ from the CLK recovery drives a mixed-mode CLK manager (MMCM) that dynamically shifts the phase of a 1.25 GHz reference CLK embedded in the FPGA board. This in turn drives the ADC sampling instants with a sampling phase tuning resolution of $\Delta\tau \times$ 23 ps, representing 2.8% of T_b. The other RX functionalities are similar to that of the Section 4.2.1.

To experimentally validate the functioning of the proposed DSP, the sensitivity of the coherent RX operating at 1 sps was evaluated in two different configurations: single polarization and polarization diversity. First, the single polarization test used only the upper branch of the optical front-end in Fig. 6.19, without PBS. Then, only I and Q were detected and processed by the FPGA at 1 sps; the received signal SOP was manually adjusted at the RX input. Besides the DFB LO with $\Delta\nu$ = 4 MHz, other ECL with $\Delta\nu$ = 100 kHz also performed as LO to evaluate the impact of the phase noise. The results in Fig. 6.20 show RX sensitivity of -54 dBm for BER = 10^{-3} FEC threshold, with no meaningful difference in the performance between 4 MHz and 8 MHz total

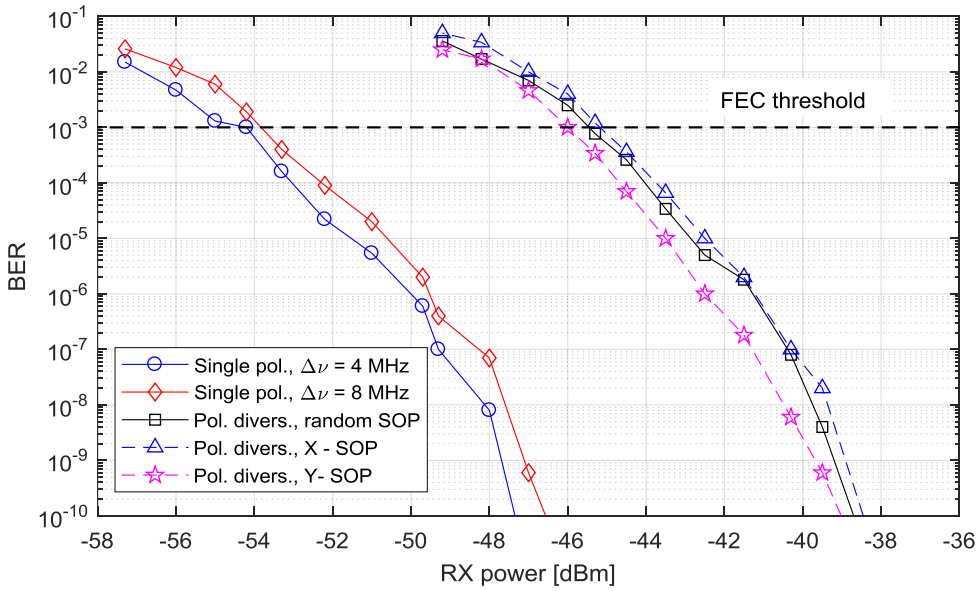

Figure 6.20. BER vs. received power for 1.25 Gb/s DPSK, detected by 3x3 homodyne RX operating at 1 sample per symbol in single polarization (Single pol.) and polarization diversity (Pol. divers.) configuration.

linewidth. The extra phase noise had no impact on the CLK recovery performance, as expected, due to the timing error estimation based on the received signal power thus immune to the carrier phase, as stated before. Notably, the measured BER curves are roughly similar to Figs. 4.11(a) and 5.25(a) that utilized conventional ADC sampling and CLK recovery at 2 sps.

After successfully validating the symbol-rate DSP in single polarization, the system was evaluated in polarization-diversity configuration with the two DFBs as TX and LO (total $\Delta\nu$ = 8 MHz). The BER curves in Fig 6.20 were computed for three cases of interest: adjusting the received signal SOP to (I) 𝕏-polarization, (II) 𝕐-polarization, and (III) random. At FEC threshold, less than 1 dB penalty in sensitivity was observed among the different received signal SOP, and 8 dB penalty compared with the single polarization test due to the extra excess losses from the more complex optical front-end with the PBSs.

The tolerance of the CLK recovery algorithm against CLK detuning between TX and RX was also evaluated in real time. The CLK frequency of the PPG was swept $\pm$4 kHz with respect to R_B (1.25 Gb/s), and the BER was measured for three different received optical powers. The block length for averaging in the CLK recovery was N = 2048 bits. The results are reported in Fig. 6.21 and reveal that the CLK recovery has non-symmetric tolerance to the CLK mismatch as the received power decreases, with the lowest BER at ~1 kHz CLK detuning for the lowest received power (-43 dBm). This behavior is ascribed in part to accuracy errors in the implemented system for tuning the sampling phase of the ADCs with the FPGA, and in part to non-flat frequency response of the electronic HW that causes non-ideal pulse shape of the received signal at the ADCs input; this might produce different slopes for the rising edge and the falling edge of the calculated power $P_{\mathbb{X}} + P_{\mathbb{Y}}$ in Fig. 6.15. The test also shows that, when the optical power is as high as -34 dBm, the CLK recovery at 1 sps tolerates up to ±2.5 kHz CLK detuning in a constant BER regime. For -41 dBm and -43 dBm received power the tolerance lowers to ±1.5 kHz and ±1 kHz respectively (with respect to the optimal), which represents 40% and 60% reduction compared with high received power.

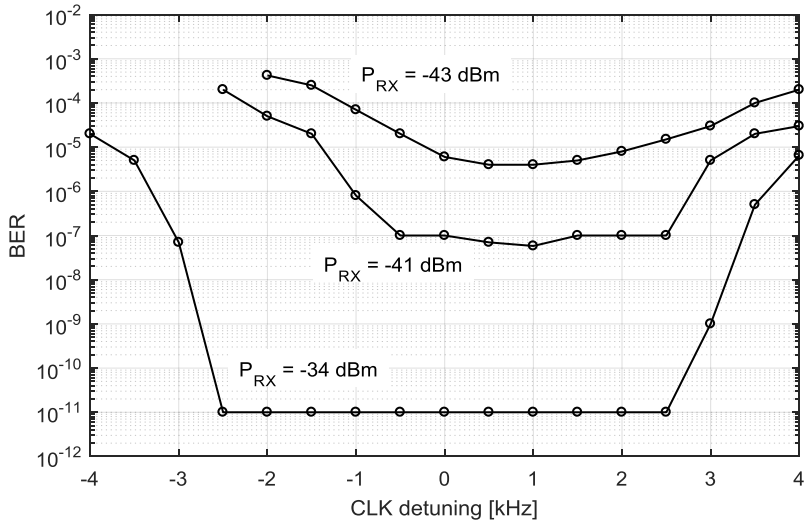

Figure 6.21. BER vs. CLK detuning between TX and RX, for real-time DPSK at 1.25 Gb/s sampled by 1.25 GSa/s ADCs (1 sample per symbol).

The good performance achieved in real-time demonstrates the feasibility of the proposed lite DSP at 1 sample per symbol, leveraging low-speed ADCs and cheap FPGAs. However, the main challenge of this technique is that the accuracy of the CLK recovery highly depends on the quality of the detected pulses, as the maximum finding algorithm establishes the optimal sampling point at the maximum of the detected signal power, determined by the pulse shape. Therefore, pre-equalization at the TX of the linear channel response seems to be necessary for optimal RX performance. This topic is addressed in the next chapter.

6.3 Chapter Summary

This chapter reported on a novel architecture for polarization-independent heterodyne detection, based on 3x3 optical coupler and differential field detection. The proposed RX exploits a simple front-end consisted of 3x3 coupler, PBS and three single-ended PDs. The electrical signal processing requires no extra complexity compared with standard heterodyne RXs with differential demodulation, and makes the proposed RX simple enough to be implemented with analog HW. The concept was successfully demonstrated with DPSK at 1.25 Gb/s, achieving -49 dBm sensitivity at BER = 10^{-3}, after 50 km SMF transmission. Notably, the RX exhibits less than 1dB power penalty for a reference BER of 10^{-4} when the SOP of the received signal is randomly varied. The RX can also tolerate up to 25 dB power difference with adjacent channels by featuring cancellation of the direct-detection terms, thus outperforming by 7 dB the single-ended detection in the multiuser udWDM-PON scenario. The high performance along with the low-complexity of the RX, with common components and simple electronics, constitutes an attractive technology for cost-effective next generation udWDM-PON.

Besides the heterodyne RX with analog HW, this chapter also explored solutions for the digital homodyne RX counterpart, aiming at simplifying the complexity of the polarization-diversity detection. In this regard, a complete DSP for polarization-diversity m-PSK RXs that operates at the symbol rate has been successfully implemented in FPGA and evaluated in real-time for short-reach coherent applications. The CLK recovery algorithm estimates the timing error from the detected signal power, and takes profit from a maximum finding algorithm for continuous tuning of the sampling phase of the ADCs, which operate at 1 sample per symbol. The proposed DSP is simple and robust. It can withstand to ±2.5 kHz detuning between TX and RX CLK for 1.25 Gb/s DPSK data, if the received optical power is high, and to ±1 kHz CLK detuning if the received power is near to the BER threshold for FEC. The homodyne RX achieved a high sensitivity of -46 dBm at BER = 10^{-3} using low-complexity DSP at 1 sps, commercial DFB lasers, and direct-DPSK modulation.

Chapter 7

Digital Pre-Emphasis for Optical Transmitters

As it has been stressed throughout the different chapters of this thesis, the next generation PONs and other optical networks with high terminal density like DCI, present strict requirements in terms of power budget, cost, and footprint of the photonic devices [Agr16], [Nes17]. Therefore, the adoption of coherent technologies for those systems will depend heavily on the overall cost, complexity and footprint reduction that can be achieved on the coherent TRX. To this aim, the previous chapters explored and proposed effective solutions to lower the complexity of the coherent RX. This chapter, now, focuses on the optical TX and particularly in direct laser modulation as an alternative to the IQ modulators employed in commercial coherent TXs for core networks, which encompass optical losses and substantial footprint.

In order to keep on using the very low-cost direct laser modulation technology of actual commercial TDM-PON systems –that is limited to binary intensity modulation–, optical m-PSK TXs based on direct modulation of DFB lasers have been proposed and successfully demonstrated in [Hu15], [Can16b] using the laser chirp to achieve the optical phase modulation, as studied in Section 2.4.2. This technique is particularly attractive in the udWDM-PON scenario, and has been adopted in this thesis, because it employs commercial low-cost lasers and reduces the form factor and power consumption of the coherent TX. This TX simplification though, does not imply sacrificing the capacity and spectral efficiency of the coherent PON because complex modulation formats can still be generated, thus fully exploiting the quadrature detection capabilities of the coherent RX. Nonetheless, commercial DFBs present different challenges for an effective implementation, as they exhibit non-flat frequency response and suffer from severe BW limitation. Moreover, to scale from binary to higher modulation formats, a DAC is required to drive the injection current modulation of the laser. To keep the cost of the coherent TX down, a low-cost DAC might present narrow BW and/or low resolution, quantified through the effective number of bits (ENOB).

The last chapter of this thesis explores digital pre-emphasis (DPE) linear filtering at the TX to jointly mitigate the BW limitations and flatten the frequency responses of the laser and DAC. The design of the DPE filter also takes into account the quantization noise introduced by a DAC with low-resolution. The chapter also presents a novel and simple 8-ary coherent TX by simultaneous amplitude-and-phase modulation of an integrated DEML. Bit rates up to 10 Gb/s are experimentally achieved by applying DPE at the TX to mitigate the non-ideal DEML response.

7.1 Directly Modulated Lasers For Coherent Transmitters

The high level block diagram of the considered optical transmission system with directly modulated lasers (DMLs) is illustrated in Fig. 7.1. The optical TX does not employ external IQ modulators to generate complex modulation formats; instead, they are replaced by simpler and cheaper direct laser chirp modulation for m-PSK, or alternatively, by integrated DEML for m-

APSK constellations, as examined in Sections 2.3.4 and 3.1.1. Referring to Fig. 7.1, let us initially consider the case of DML at the TX. First, the binary NRZ data are mapped into the constellation symbols $s[nT_s]$, which consist of a m-level signal needed for direct m-PSK; here, T_s is the sampling time. The m-PSK symbols can be differentially-encoded or not, depending on the detection scheme. Next, the signal $s[nT_s]$ passes through a linear DPE filter designed to mitigate the non-ideal frequency responses of the TX HW, including the DAC and the DML. After the DPE the signal $r[nT_s]$ enters a differentiator to perform the time-derivative of the modulating signal, as required to modulate the optical phase of the DML by its inherent frequency chirp.

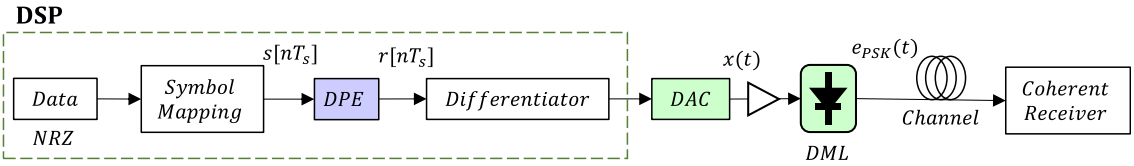

Figure 7.1. Considered optical transmission system for m-PSK, with DPE, DAC and DML at the TX, and coherent detection at the RX.

For the ideal case, i.e., ideal frequency responses and no DPE, the differentiator output is $\Delta_{T_s} r[nT_s]$, where Δ_{T_s} is the discrete time difference operator with respect to the sampling time, as given by Eq. (2.70). Afterwards, the DAC performs two operations. First, the digital quantization of $\Delta_{T_s} r[nT_s]$ as a function of the ENOB. Then, the sample-and-track circuit of the DAC reconstructs in the analog domain the output signal $x(t)$ that drives the direct laser chirp modulation, according to

$$e_{PSK}(t) = E_c(t) e^{j\left[2\pi f_c t + 2\pi k_f \int_0^t x(\tau) d\tau + \varphi_c(t)\right]} \tag{7.1}$$

This corresponds to the small-signal approach to the laser rate equations examined in Section 2.4, in which the DML behaves as an optical FM modulator with residual IM. Here, $E_c(t)$ identifies the residual IM, f_c and $\varphi_c(t)$ are the frequency and the random phase of the optical carrier respectively, while k_f denotes the frequency modulation depth, derived from Eq. (2.67) and expressed as

$$k_f = \frac{\alpha_H \kappa \eta}{4\pi} \tag{7.2}$$

with α_H the Henry coefficient, κ the adiabatic chirp parameter, and η the current-to-power efficiency of the laser. This holds for modulation frequencies from few MHz up to several GHz, the region where the adiabatic chirp is dominant.

After propagating through the optical fiber channel, the transmitted m-PSK signal finally reaches the coherent RX that first recovers the information-bearing optical phase thanks to the linear field detection properties of the coherent RX, and afterwards recovers the transmitted m-PSK symbols $s[nT_s]$ free from phase noise by utilizing either synchronous detection with phase estimation algorithms or differential field detection.

7.1.1 Linear pre-emphasis filter design

The linear DPE filter with transfer function $P(f)$ is designed in the frequency domain with respect to the equivalent system model of the optical TX with DML illustrated in Fig. 7.2. The m-PSK symbols $s(f)$ in frequency domain first pass through the DPE filter $P(f)$; then, to convert from digital to analog domain, the DPE output $r(f)$ is converted by a DAC with transfer function $D(f)$, that also introduces the quantization noise $n_q(f)$ as a function of the ENOB. Note that the transfer function of the differentiator depicted in Fig. 7.1 is cancelled by the integral term of the optical phase modulation in the DML (compare with Eq. (2.69)), and therefore, does not impair the signal neither is considered in Fig. 7.2. The resulting signal $x(f)$ after the DAC drives the modulation of the DML that behaves as an optical FM modulator, and whose transfer function $L(f)$ is derived from Eq. (2.67) in the adiabatic regime, as

$$L(f) = \frac{\Delta\nu(f)}{\Delta x(f)} = \frac{\alpha_H \kappa \eta}{4\pi} \tag{7.3}$$

where $\nu(f)$ is the optical frequency, and the rest of terms follow the definition of k_f in Eq. (7.2). Theoretically, $L(f)$ draws a totally flat frequency response if the DML operates in the adiabatic chirp regime only (from MHZ up to several GHz). In practice, however, commercial low-cost DMLs suffer from BW limitation and ripple in the passband of $L(f)$ that can be ascribed to constraints in the RF circuitry and package parasitic effects. This, in turn, limits the maximum bit rates that can be achieved with the DMLs. The optical channel is modeled with transfer function $H(f)$, while $n_{ch}(f)$ stands for the additive channel noise. Last, the transmitted m-PSK symbols are recovered at the coherent RX output, denoted by $y(f)$.

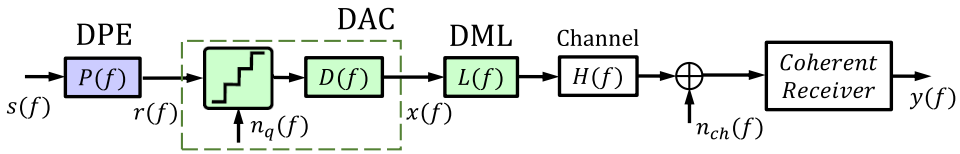

Figure 7.2. Frequency-domain equivalent system model of the optical TX with DML depicted in Fig. 7.1.

The objective of the DPE filter $P(f)$ is to jointly mitigate the BW limitation and flatten the frequency response $L(f)$ of the DML (that might include the diver amplifier response), and $D(f)$ of the DAC. To this aim, the most conventional method consists of assigning to $P(f)$ the inverse frequency responses of the DML and DAC, as

$$P(f) = \frac{1}{D(f)L(f)} \tag{7.4}$$

known in literature as zero-forcing (ZF) equalization, which can cancel all linear distortion and ISI if extra sources of noise are not considered [Don12], [Zho11]. This technique, however, presents some disadvantages since it might over-amplify the noise greatly in the spectral region where $D(f)L(f)$ is more attenuated. It might also produce large peaks in the time domain signal that could lead to quantization noise enhancement if the DAC has low resolution, as well as driver amplifier saturation and clipping.

A more advanced solution, yet simple, for pre-equalization at the TX consist of calculating the linear filter $P(f)$ through the minimum mean squared error (MMSE) between the desired and the real system output. This does not eliminate the distortion and ISI completely, but minimizes the total power of the noise and the interference components [Che12], [Zha14]. Precisely, it is optimal in presence of significant quantization noise due to ADCs/DACs with low ENOB [Nap16], as one could expect from the low-cost converters intended for deployment in PONs. For the analytical derivation of $P(f)$, this work aims at optimizing the TX only, then the channel and the coherent RX are assumed ideal and noiseless (i.e., $H(f) = 1$ and $n_{ch}(f) = 0$). This assumption is correct for the transmission rates and fiber link lengths considered in this thesis for the access scenario, of <10 GBd and <60 km respectively, where the impairments from the fiber are not dominant, as analyzed in Chapter 3.

Let $y_{id}(f) = s(f)$ be the ideal output signal from the coherent RX, i.e., the transmitted m-PSK symbols are ideally recovered. On the other hand, the real system output in Fig. 7.2 is given by

$$y(f) = s(f)P(f)D(f)L(f) + n_q(f)D(f)L(f) \tag{7.5}$$

Here, $s(f)$ and $n_q(f)$ are stochastic processes, whereas $P(f)$, $D(f)$ and $L(f)$ are linear transfer functions. The DPE filter $P(f)$ is obtained through the mean squared error (MSE) between $y(f)$ and $y_{id}(f)$, calculated as

$$MSE\big(P(f)\big) = \int_{-R_b}^{R_b} \mathrm{E}[|y(f) - y_{id}(f)|^2]df \tag{7.6}$$

where E[·] is the expectation operator with respect to the stochastic processes $s(f)$ and $n_q(f)$, and R_b is the symbol rate. By replacing Eq. (7.5) into Eq. (7.6) one obtains

$$MSE\big(P(f)\big) = \int_{-R_b}^{R_b} \mathrm{E}\left[\left|s(f)[P(f)D(f)L(f) - 1] + n_q(f)D(f)L(f)\right|^2\right] df \tag{7.7}$$

that can be solved using the triangle inequality for complex numbers: $|z_1 + z_2|^2 \leq (|z_1| + |z_2|)^2$. Accordingly, the upper bound (considering the equality) of the MSE in Eq. (7.7) is found to be:

$$\begin{aligned} MSE\big(P(f)\big) = \int_{-R_b}^{R_b} \mathrm{E}\Big[&|s(f)[P(f)D(f)L(f) - 1]|^2 + \left|n_q(f)D(f)L(f)\right|^2 \\ &+ 2\left|s(f)n_q(f)D(f)L(f)[P(f)D(f)L(f) - 1]\right|\Big] df \end{aligned} \tag{7.8}$$

which can be rewritten as

$$\begin{aligned} MSE\big(P(f)\big) = &\int_{-R_b}^{R_b} |P(f)D(f)L(f) - 1|^2 \mathrm{E}[|s(f)|^2]df \\ &+ \int_{-R_b}^{R_b} |D(f)L(f)|^2 \mathrm{E}\left[\left|n_q(f)\right|^2\right] df \\ &+ 2\int_{-R_b}^{R_b} |D(f)L(f)[P(f)D(f)L(f) - 1]|\mathrm{E}\big[\left|s(f)n_q(f)\right|\big]df \end{aligned} \tag{7.9}$$

Now, the three integrals in Eq. (7.9) depend on the statistics of the signal and the quantization noise, denoted by $\mathrm{E}[|s(f)|^2]$, $\mathrm{E}\left[\left|n_q(f)\right|^2\right]$ and $\mathrm{E}\left[\left|s(f)n_q(f)\right|\right]$. In Fig. 7.2 and in Eq. (7.5), the quantization process was straightforwardly modeled as an additive perturbation $n_q(f)$ to the DAC input $r(f)$. This approach is known as the *additive quantization noise model* [Ben02], [Riz08], and follows the assumption that the quantization noise $n_q(f)$ is: (I) approximately white; (II) uncorrelated with the DAC input $r(f)$; and (III) uniformly distributed over the quantization step size Δ_q, such that

$$\mathrm{PDF}\left[n_q\right] = U\left[-\frac{\Delta_q}{2}, \frac{\Delta_q}{2}\right] = \begin{cases} \dfrac{1}{\Delta_q}, & n_q \in \left[-\dfrac{\Delta_q}{2}, \dfrac{\Delta_q}{2}\right] \\ 0, & \text{elsewhere} \end{cases} \tag{7.10}$$

Here, the notations $\mathrm{PDF}[\cdot]$ and $U[\cdot]$ stand for the probability density function and the uniform distribution respectively. This quantization noise model is more plausible when the ENOB is large enough, nearby ENOB ≥ 5; otherwise, for lower ENOB the DAC input $r(f)$ and the noise $n_q(f)$ are becoming correlated, and the noise spectrum is not white.

Since $n_q(f)$ has a uniform distribution over Δ_q, the noise variance σ_q^2 –equivalent to the noise power– is given by [Ben02]

$$\begin{aligned} \sigma_q^2 &= \int_{-R_b}^{R_b} \mathrm{E}\left[\left|n_q(f)\right|^2\right] df \\ &= 2R_b \mathrm{E}\left[\left|n_q(f)\right|^2\right] = \frac{{\Delta_q}^2}{12} \end{aligned} \tag{7.11}$$

Moreover, for the case of a uniform quantizer with mid-tread output (zero crossing), and assuming that the maximum of $r(f)$ is adjusted to match the full scale of the DAC so that there is no signal clipping, the quantization step Δ_q can be expressed as

$$\Delta_q = \frac{r_{max}}{2^{ENOB-1} - 1} \tag{7.12}$$

with r_{max} the maximum of $r(f)$, that relates to the peak-to-average power ratio (PAPR) of $r(f)$ at the DAC input by

$$PAPR_{dB} = 10\log_{10}\left(\frac{{r_{max}}^2}{{\sigma_r}^2}\right) \tag{7.13}$$

where σ_r^2 is the power of $r(f)$, given by

$$\begin{aligned} \sigma_r^2 &= \int_{-R_b}^{R_b} \mathrm{E}[|r(f)|^2] df \\ &= \int_{-R_b}^{R_b} |P(f)|^2 \mathrm{E}[|s(f)|^2] df \end{aligned} \tag{7.14}$$

Therefore, by using the definition in Eq. (7.13), and assuming that $2^{ENOB-1} - 1 \approx 2^{ENOB-1}$ because in the considered model ENOB ≥ 5, the Eq. (7.12) becomes

$$\Delta_q = \frac{\sqrt{{\sigma_r}^2 \cdot 10^{\frac{PAPR_{dB}}{10}}}}{2^{ENOB-1}} \tag{7.15}$$

Finally, using Eqs. (7.11), (7.14) and (7.15) the analytical expression for $\mathrm{E}\left[\left|n_q(f)\right|^2\right]$ can be derived as

$$\begin{aligned}\mathrm{E}\left[\left|n_q(f)\right|^2\right] &= \frac{{\Delta_q}^2}{24R_b} \\ &= \frac{1}{24R_b}\left(\frac{10^{\frac{PAPR_{dB}}{10}}}{2^{2ENOB-2}} \cdot {\sigma_r}^2\right) \\ &= \frac{10^{\frac{PAPR_{dB}}{10}}}{6R_b \cdot 2^{2ENOB}} \int_{-R_b}^{R_b} |P(f)|^2 \mathrm{E}[|s(f)|^2]\, df\end{aligned} \tag{7.16}$$

which represents the power spectral density (PSD) of the quantization noise $n_q(f)$. By going back to the MSE expression in Eq. (7.9), note that $\mathrm{E}\left[\left|s(f)n_q(f)\right|\right] = 0$ because signal and noise are said to be uncorrelated in the additive quantization noise model; therefore, the third integral equals 0. By substituting for $\mathrm{E}\left[\left|n_q(f)\right|^2\right]$ from Eq. (7.16) in the remainder of Eq. (7.9), one obtains

$$\begin{aligned}MSE\big(P(f)\big) = &\int_{-R_b}^{R_b} |P(f)D(f)L(f) - 1|^2 \mathrm{E}[|s(f)|^2] df \\ &+ \int_{-R_b}^{R_b} |D(f)L(f)|^2 \left[\frac{10^{\frac{PAPR_{dB}}{10}}}{6R_b \cdot 2^{2ENOB}} \int_{-R_b}^{R_b} |P(f)|^2 \mathrm{E}[|s(f)|^2]\, df\right] df\end{aligned} \tag{7.17}$$

that turns out to be

$$\begin{aligned}MSE\big(P(f)\big) = &\int_{-R_b}^{R_b} |P(f)D(f)L(f) - 1|^2 \mathrm{E}[|s(f)|^2] df \\ &+ \xi_0 \int_{-R_b}^{R_b} |P(f)|^2 \mathrm{E}[|s(f)|^2] df\end{aligned} \tag{7.18}$$

where ξ_0 is

$$\xi_0 = \frac{10^{\frac{PAPR_{dB}}{10}}}{6R_B \cdot 2^{2ENOB}} \int_{-R_b}^{R_b} |D(f)L(f)|^2\, df \tag{7.19}$$

Now, Eq. (7.18) is the cost function to be minimized with respect to $P(f)$ to calculate the MMSE

$$MMSE\big(P(f)\big) = \min_{P(f)} \{MSE(P(f))\} \tag{7.20}$$

Mathematically, this is realized by the partial derivative with respect to $P(f)$, as follows

$$\frac{\partial MSE(P(f))}{\partial P(f)} \stackrel{\text{def}}{=} 0, \quad \forall f \in [-R_b, R_b] \tag{7.21}$$

that applied on Eq. (7.18), and using the Leibniz integral rule, yields the following expression

$$\int_{-R_b}^{R_b} D(f)L(f)[P^*(f)D^*(f)L^*(f) - 1]\mathrm{E}[|s(f)|^2]df + \xi_0 \int_{-R_b}^{R_b} P^*(f)\mathrm{E}[|s(f)|^2]df = 0 \tag{7.22}$$

A particular solution of Eq. (7.22) is

$$D^*(f)L^*(f)[P(f)D(f)L(f) - 1] = -\xi_0 P(f) \tag{7.23}$$

which finally gives the DPE solution

$$P(f) = \frac{D^*(f)L^*(f)}{|D(f)L(f)|^2 + \xi_0} \tag{7.24}$$

where $(\cdot)^*$ is the complex conjugate. The parameter ξ_0 as defined in Eq. (7.19), balances the trade-off between the BW compensation and the amount of quantization noise introduced within the effective BW. The ξ_0 accounts for the DAC resolution through the ENOB, and also for the PAPR at the DAC input, in both cases aiming at lowering the impact of the quantization noise. In practice, the PAPR can be either optimized by numerical simulation for a given ENOB, or left as a design parameter according to the HW specifications (e.g., linear dynamic range of the driver amplifier).

7.1.2 Impact of quantization noise from DACs

The impact of the DAC resolution and its influence on the DPE filter in Eq. (7.24) calculated through the MMSE criterion, is discussed in this section. To visualize the DAC quantization effect, let us consider the case of direct 8-PSK that requires uniform 8-level modulating signal representing the eight phase symbols. In Fig. 7.3(a) the PSD of the modulating symbols $s(f)$ is reported for different ENOB. For clarity, raised-cosine pulse-shape filtering with roll-off = 1 was applied to correctly appreciate the noise floor; otherwise, the significant power of the NRZ side-lobes totally overlap and mask the quantization noise floor. As observed, lowering the ENOB introduces strong quantization noise and lowers the signal-to-quantization-noise ratio (SQNR), such that SQNR ≅ 66 dB for ENOB = 10, and reduces down to SQNR ≅ 23 dB for ENOB = 3.

Analytically, the SQNR can be derived using Eqs. (7.11) and (7.12) as

$$\begin{aligned} SQNR_{dB} &= 10\log_{10}\left(\frac{{\sigma_r}^2}{{\sigma_q}^2}\right) \\ &= 10\log_{10}\left(\frac{{\sigma_r}^2}{{\Delta_q}^2/12}\right) \\ &= 10\log_{10}\left(3 \cdot 2^{2ENOB} \cdot \frac{{\sigma_r}^2}{{r_{max}}^2}\right) \end{aligned}$$

$$SQNR_{dB} = 4.77 + 6.02ENOB + 10\log_{10}\left(\frac{{\sigma_r}^2}{{r_{max}}^2}\right) \tag{7.25}$$

and clearly shows that increasing by one the ENOB leads to increase the SQNR by 6 dB. This is in agreement with the ~43 dB SQNR difference observed in Fig. 7.3(a) when varying the ENOB from 3 to 10. Moreover, the PSD and the PDF of the quantization noise plotted in Figs. 7.3(b) and 7.4 respectively for various ENOB, confirm that the noise is white and has uniform probability distribution for ENOB ≥ 5.

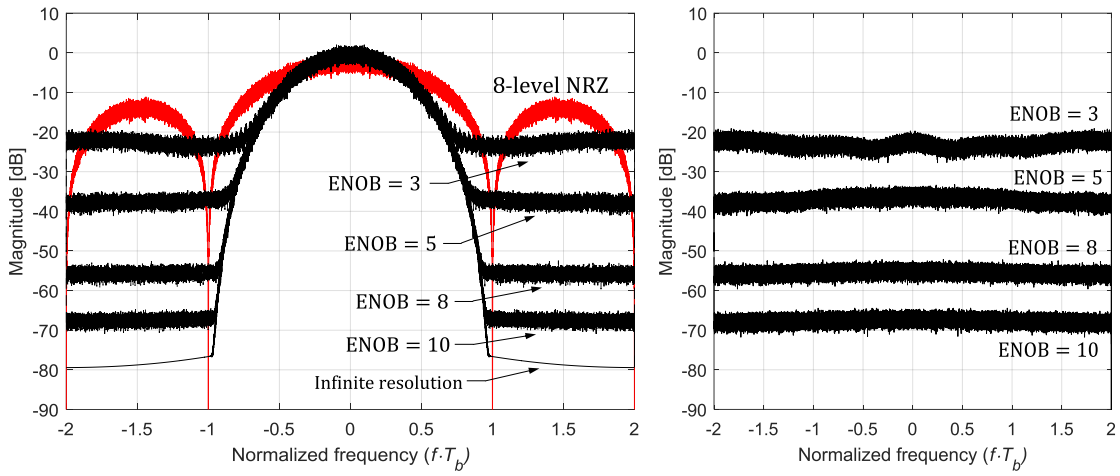

Figure 7.3. (a) Power spectral density of the 8-level signal for direct 8-PSK, with raised-cosine pulse shape (roll-off = 1), and different ENOB; (b) quantization noise floor as a function of the ENOB.

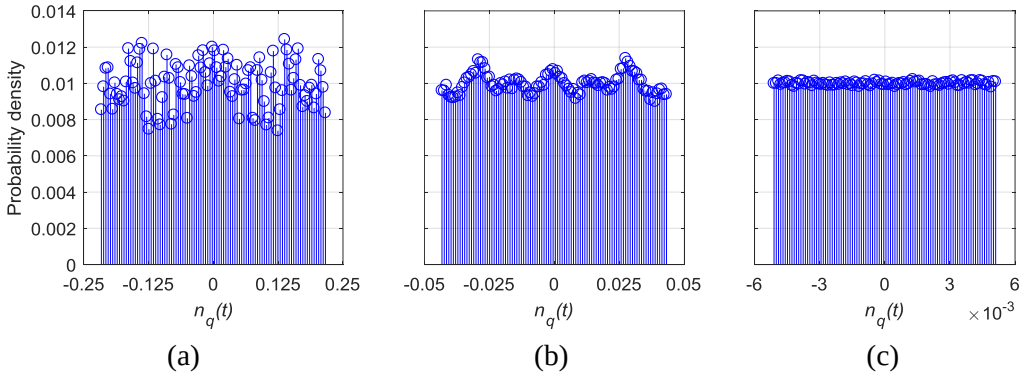

Figure 7.4. Probability density function of the quantization noise for (a) ENOB = 3, (b) ENOB = 5, and (c) ENOB = 8.

The foregoing analyses make evident the disadvantage of conventional ZF equalization over the proposed MMSE equalization if the implemented DAC has low resolution: the quantization noise enhancement. To better understand the role of the DAC ENOB in the DPE filter response, Fig. 7.5 reports on the experimental characterization of the DML response $L(f)$ of a common DFB, showing non-flat response with ~2.5 dB ripple in the pass-band, and ~6 GHz BW_{3dB}. The frequency response of the DAC is assumed ideal. The DPE response $P(f)$ from Eq. (7.24) is also plotted for various ENOB, and shows that the ENOB –required for calculating ξ_0– determines the optimal roll-off of $P(f)$ minimizing over-amplification of the quantization noise. Note that

for large ENOB the ξ_0 reduces, and the DPE filter in Eq. (7.24) calculated through the MMSE converges to the ZF equalizer in Eq. (7.4), which is sub-optimal if the quantization noise dominates at the TX.

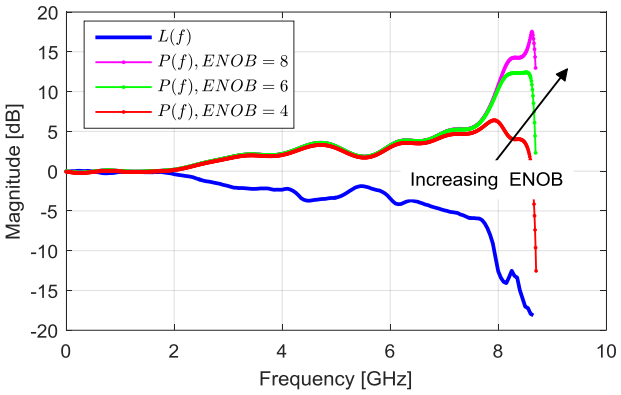

Figure 7.5. DPE frequency response when varying the ENOB of the DAC.

7.1.3 Simulation results

To evaluate the performance of the proposed DPE, numerical simulation was carried out employing the experimental characterization of the FM modulation response of two low-cost DFBs, reported in Fig. 7.6(a) as $L_1(f)$ and $L_2(f)$. They show ~6 and ~8 GHz modulation BW_{3dB} respectively, and ~2.5 dB ripple in the pass-band; depending on the package parasitic effects and the transition between adiabatic and transient chirp, the ripple in the passband can be larger. A third high-performance laser $L_3(f)$ was also measured as benchmark. The codes in the legend indicate their part numbers. The considered optical transmission system for simulation is similar to Fig 7.1, with the DAC transfer function $D(f)$ modeled here as a Bessel 4th-order filter with BW_{3dB} = 8 GHz; the ENOB was modeled as variable. The data consisted of NRZ-PRBS-23 binary sequences that were mapped into the m-PSK symbols $s(f)$ and differentially encoded.

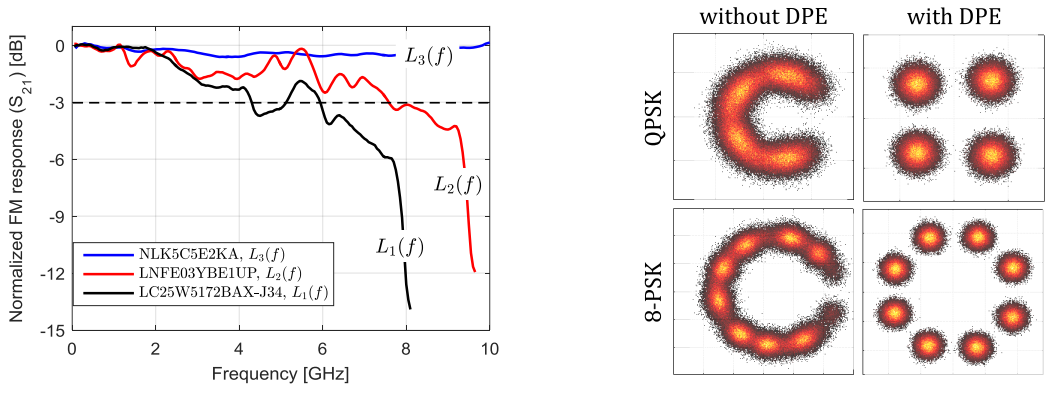

(a) (b)

Figure 7.6. (a) Experimental DML modulation responses considered for simulation; (b) using $L_1(f)$: constellation diagrams without and with DPE for QPSK and 8-PSK at 9.5 and 7.5 GBd respectively, ENOB = 8 and 32 DPE taps.

The first test assessed the limitation imposed by the DML responses in Fig. 7.6(a) to the maximum bit rates that can be achieved with direct phase modulation, with and without DPE, for different modulation formats. Visually, the benefit of the DPE is clearly observed in the constellations in Fig. 7.6(b) for QPSK at 9.5 GBd and 8-PSK at 7.5 GBd respectively, using $L_1(f)$. In both cases, the constellations without DPE are significantly distorted, while after 32-tap DPE are completely recovered. In this tests, the ENOB was set to 8 and the PAPR to 9 dB.

The simulation results were obtained for DPSK, QPSK and 8-PSK, and employing $L_{1,2}(f)$ of Fig. 7.6(a). For the sake of brevity, Fig. 7.7 presents only plots with $L_1(f)$, the worst $L(f)$ among the measured DML responses, yet the main conclusions are valid for the two considered DMLs. The results are computed in terms of the SNR penalty, defined as RSNR – RSNR$_{L_3(f)}$, where RSNR is the required SNR at BER = 10^{-4} and $L_3(f)$ is the benchmark DML response. In all cases, a DAC BW_{3dB} = 8 GHz was assumed, the ENOB was first set to 8, and all the conclusions refer to a maximum SNR penalty of 1 dB. Fig. 7.7 depicts the SNR penalty curves when varying the number of DPE filter taps: no DPE, 16, 32, and 1024 (e.g., the upper bound for performance improvement), and the results indicate that DPE significantly extends the effective modulation BW of the DML in all cases. More precisely, for target 10 Gb/s per user in the udWDM-PON (denoted by dotted vertical lines), 32 DPE taps enable bit rates *well* beyond 10 Gb/s for all the modulation formats. In detail, 11, 9.5 and 7.5 GBd were achieved for DPSK, QPSK and 8-PSK respectively, with 32 taps, which translate into 11, 19 and 22 Gb/s respectively. Note that DPSK requires the highest R_b to transmit at 10 Gb/s, and thus the highest number of DPE taps. However, DPSK has the advantage that can be detected by an analog coherent RX without ADC nor DSP. Last, the performance utilizing $L_2(f)$ was better without DPE, while with DPE all curves behave similarly to the ones shown in Fig. 7.7 for $L_1(f)$, i.e., the DPE enables equivalent performances with different laser types.

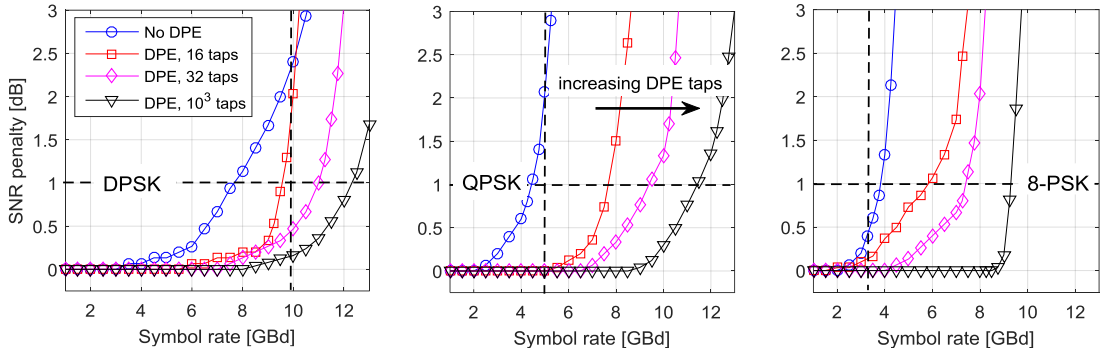

(a) (b) (c)

Figure 7.7. SNR penalty at BER = 10^{-4} vs. symbol rate for (a) DPSK, (b) QPSK, and (c) 8-PSK, when varying the number of DPE taps for $L_1(f)$.

With these results in mind, the impact of the quantization noise from the DAC was investigated on the DPE filter calculated through the MMSE in Eq. (7.24), and the ZF in Eq. (7.4). This test considered the achieved R_b = 11, 9.5 and 7.5 GBd in Fig. 7.7, for DPSK, QPSK and 8-PSK respectively, with ENOB = 8 and 32 DPE taps for all cases. Now, the ENOB was varied to compute the SNR penalty at BER = 10^{-4}, and the results are summarized in Fig. 7.8. Overall, the MMSE-DPE better tolerates the quantization noise introduced by low ENOB than the ZF-DPE, for all the modulation formats and with similar number of DPE filter taps. For the case of MMSE-

DPE (solid lines), not surprisingly the higher is the modulation format order the larger is the required ENOB. The results show that at 1 dB SNR penalty, 3.5, 4.5 and 5.5 ENOB are required for DPSK, QPSK and 8-PSK respectively, with a DAC BW_{3dB} = 8 GHz. On the other hand, the ZF-DPE (dotted lines) offers interesting results because, in this case, the larger SNR penalty for a given ENOB occurs to the lowest modulation order, contrary to what one would intuitively expect. The insight behind this behavior is that in the simulations in Fig. 7.7, DPSK reached the highest R_B (11 GBd) for 1 dB SNR penalty, thus lowering the ENOB affects more the ZF-DPE than the MMSE-DPE because the ZF further emphasizes the quantization noise at the higher frequencies beyond 6 GHz, the BW of $L_1(f)$. Accordingly, 8-PSK achieved the lowest R_B (7.5 GBd) then the quantization noise enhancement, and therefore the SNR penalty when reducing the ENOB, is substantially lower for ZF-DPE with respect to MMSE-DPE.

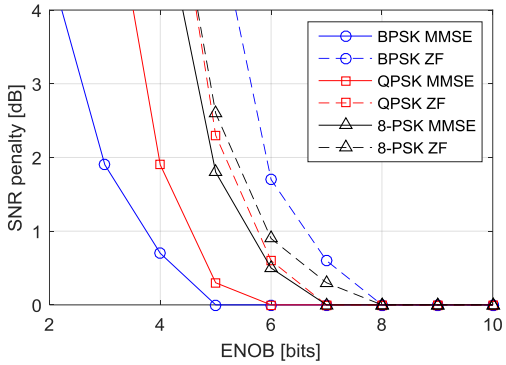

Figure 7.8. SNR penalty at BER = 10^{-4} vs. ENOB, for ZF-DPE and MMSE-DPE comparison with different modulation formats.

The obtained results suggest that the MMSE-DPE can enable the targeted bit rates for the udWDM-PON, >10 Gb/s per user, employing direct modulation of commercial DFBs and low-cost DACs with limited resolution, as low as 4-bit.

7.2 Dual-EML Coherent Transmitter

The counterpart of commercial DMLs for intensity modulation is the photonic integration of DFB laser with EAM in an electro-absorption modulated laser –EML– module. This is advantageous for increasing the modulation BW as the EAMs usually exhibit BWs >20 GHz, much faster than the DMLs that are more band-limited (<10 GHz). Also, the DFB operates in CW, then its wavelength stabilization is easier. The typical application of EMLs is generation of IM signals (e.g. PAM-*m*) by modulating the fast EAM section only. Nevertheless, the chirp of the DFB can be handled to transmit information in the phase of the optical carrier, as it has been treated intensively along this thesis. Hence, an interesting strategy consists of dual drive configuration of the EML –i.e. DEML– that allows controlling amplitude with the EAM and frequency/phase with the DFB in a cascade manner. This enables lightwave vector modulation by a very compact and cost-effective TX compared with external IQ modulator based on MZM.

Thanks to the versatility of this dual-drive scheme, a variety of applications have been reported in literature for the DEML. In [Era14] and [Cha18], single side-band (SSB) NRZ/OFDM signals

were generated with the DEML by properly adjusting the IM (with the EAM) and FM (with the DFB) modulation indexes, to increase the tolerance to CD in dispersion uncompensated optical links. Similarly, in [Kim06] a 10G CPFSK+ASK optical TX with DEML was demonstrated over 175 km SMF, more tolerant to CD than transmitting ASK only. Other application aims at increasing the ER and output power of the TX by modulating both DEML sections with the same data, as tested in [Can20] with 25G NRZ and DD. Conversely, in [Chu16] the DFB and the EAM were modulated by data and inverted data respectively to cancel the residual IM of the direct DPSK modulation of the DFB at 5 Gb/s. Last, [Man18] proposes the DEML as a complex ligthwave modulator controlling amplitude with the EAM and phase with the DFB; for direct phase modulation of the DFB, data are pre-coded with 8B10B code that naturally exhibits a high-pass response, but at the cost of lowering the net data rate due to the coding redundancy compared with the high-pass pulse shaping adopted in this thesis.

So far, all the experiments reported in literature with DEML use binary modulations, except [Man18] that demonstrates up to QPSK and [Vel18a] that demonstrates 4-APSK. In this section, the capabilities of the DEML are extended by modulating QPSK at the DFB plus two-level ASK at the EAM, thus achieving a differential 8-APSK coherent TX at 10 Gb/s with this low footprint photonic device.

7.2.1 Characterization of the photonic integrated DEML chip

The DEML is a monolithically integrated photonic device in which the same active layer is composed by two sections, a DFB laser and an EAM, in our case with lengths of 470 µm and 75 µm respectively, as indicated in Fig. 7.9(a). The term "dual" denotes the dual-drive configuration of the EML chip, which incorporates two independent RF electrodes to simultaneously modulate the DFB and the EAM sections using different data. The DEML chip was fixed on a ceramic sub-mount, as shown in Fig. 7.9(b), with a temperature sensor, TEC, and a lensed fiber faced and properly aligned to the EAM output. An optical isolator also was fused to the lensed fiber for minimizing optical back-reflections.

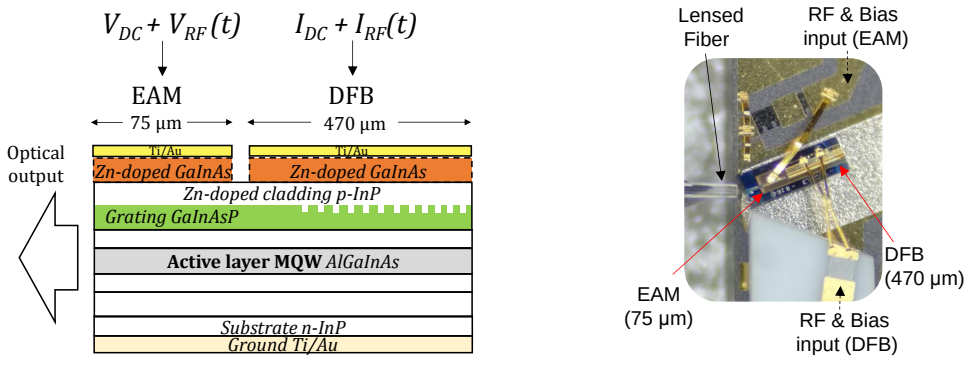

(a) (b)

Figure 7.9. (a) Sectional view of the DEML showing all relevant layers; (b) photo of the DEML assembly.

After assembling the chip on the sub-mount, the static and dynamic characteristics of the DEML were measured, including the FM and AM responses of the DFB and the EAM respectively, and the frequency chirp. The first static characterization was the electro-optical conversion efficiency of both DEML sections, and the results are plotted in Fig. 7.10. To measure the DFB, the EAM was first deactivated (V_{EAM} = 0). The DFB threshold current was found to be as low as 7 mA. For direct-PSK modulation the DFB was operated at a high bias current I_{DFB} = 60 mA to minimize the ER of the residual IM. Next, the optical output power of the DEML chip was measured to determine the effective insertion loss of the EAM that, in turn, depends on the reverse bias voltage. For the measurement, the DFB was set to I_{DFB} = 60 mA. The overall EAM response is non-linear, with a linear region from about V_{EAM} = -2.3 V to -1.1 V. When static bias V_{EAM} = -2 V was applied to the EAM, the DEML output power was 0 dBm. Moreover, the DFB wavelength was 1556.16 nm for I_{DFB} = 60 mA and V_{EAM} = 0, and the measured DFB linewidth was 300 KHz.

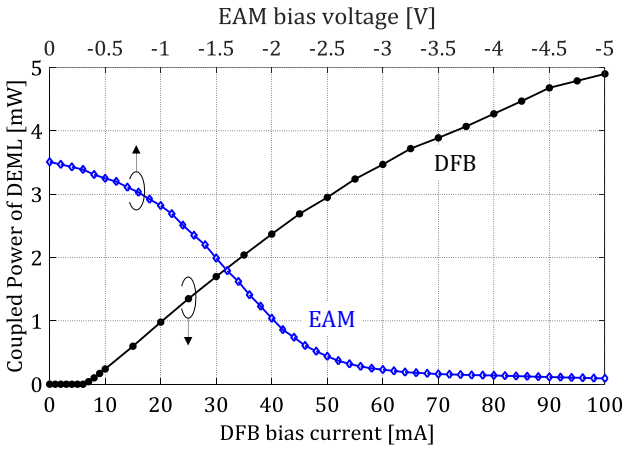

Figure 7.10. Electro-optical conversion efficiency of the DFB (V_{EAM} = 0 V) and the EAM (I_{DFB} = 60 mA) sections of the DEML.

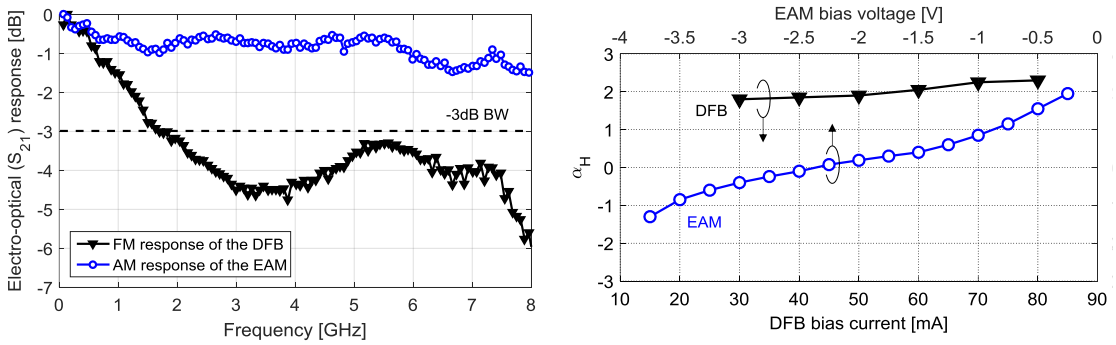

(a) (b)

Figure 7.11. (a) AM, FM modulation responses and (b) linewidth enhancement factor α_H of the EAM and DFB sections of the DEML.

Next, the dynamic modulation characteristics of the DEML were measured. Fig. 7.11(a) reports on the FM and AM modulation responses for the DFB and the EAM respectively. While the EAM has minor BW limitation up to 8 GHz (with less than 1.5 dB attenuation), the DFB exhibits non-flat frequency response and severe BW limitation, with ~1.7 GHz BW at 3 dB, mostly due to constraints in the RF circuitry (wire bonding, package parasitic, RF cables). Ideally, one would like to consider both sections of the DEML completely independent for the lightwave vector

modulation: the DFB as a pure frequency modulator through the laser chirp effect, and the EAM as a pure amplitude modulator. In practice, though, this is not the case and strict evaluation of the DEML chirp is required. To this aim, the DFB and EAM chirp characteristics were measured using an optical filter as frequency discriminator [Sat05]. According to Eq. (7.3) assuming adiabatic chirp regime, the ratio between the variations of the optical frequency and the modulating signal is proportional to α_H, that was measured in Fig. 7.11(b) for different DFB and EAM bias. The results show that the α_H for the DFB is roughly constant regardless the applied bias current, whereas the α_H for the EAM is strongly dependent on the bias voltage, ranging approximately from -1.2 to 2. This inherent chirp of the EAM makes impact on the phase modulation produced by the DFB. Accordingly, the EAM was properly biased at V_{EAM} = -2.2 V, around the zero-chirp point, to generate the phase modulation with the DFB only. Additionally, the DFB characterization at bias I_{DFB} = 60 mA, f_m = 1.25 GHz, and modulation current swing of 11 mA_{pp} resulted in κ = 10.8 GHz/mW with residual IM of about 1 dB.

7.2.2 Experimental validation

The experimental setup to demonstrate the complex amplitude-and-phase modulation of the DEML is illustrated in Fig. 7.12. The two DEML sections were modulated simultaneously with independent data. For the DFB, the data to generate QPSK consisted of two uncorrelated PRBS sequences (in Fig. 7.12, Data 1 and 2 respectively) that were mapped into the phase symbols $\{0, \pm\pi/2, \pi\}$, then differentially encoded. The QPSK symbols then passed through the DPE according to Eq. (7.24), to compensate for the following non-ideal FM response of the DFB. The DAC response had no significant impact compared with the DFB response at the tested bit rates, and therefore, was assumed ideal ($D(f)$ = 1).

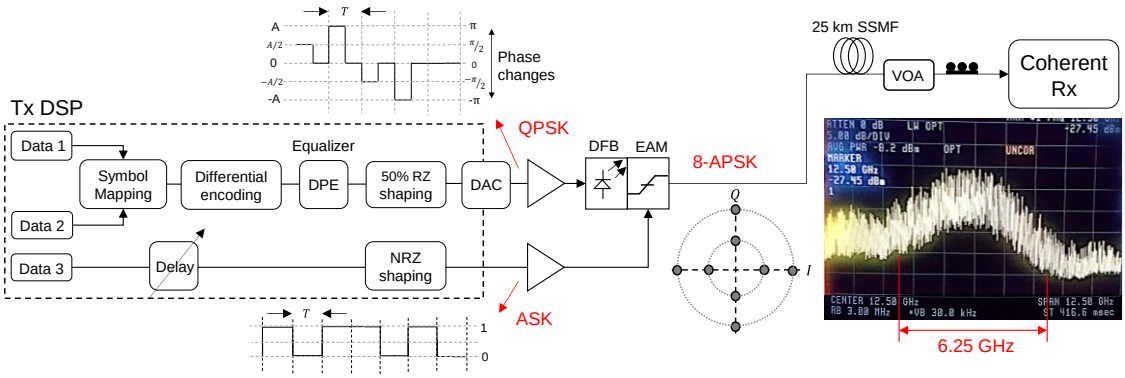

Figure 7.12. Experimental setup. The inset show the photodetected RF spectrum for 8-APSK at 3.125 GBd, centered at 12.5 GHz.

The DPE was implemented as a linear FIR filter with real-valued taps spaced by T_b/2, being T_b the symbol time. Next, a RZ pulse-shaping filter with 50% duty-cycle properly adapted the signal for direct phase modulation through the chirp of the DFB. The digital symbols sequence was generated at 2 samples per symbol, and converted to analogue domain by a 6.25 GSa/s DAC with 8-bit resolution; this limited the modulated symbol rate to R_b = 3.125 GBd. The resulting five-level electrical signal at the DAC output (Fig. 7.12 inset) for the case of ideal laser response $L(f)$

(as in Eq. (7.3)), represents the current needed to directly phase-modulate the DFB in four orthogonal phases; otherwise, for non-ideal $L(f)$ the signal is pre-emphasized by the DPE and no longer has five levels. Simultaneously, a third PRBS sequence (Data 3) coded as NRZ and uncorrelated with the DFB data was injected to the EAM, producing the two-level ASK modulation. The electrical path of the EAM did not require neither DPE nor DAC. The cascade of the two simultaneous modulations, QPSK and ASK, generates complex 8-APSK modulated optical signals at the DEML output without the need of external IQ modulator. The extinction ratio of the ASK was set to 3.8 dB with the purpose that all 8-APSK symbols had the same Euclidean distance among them. It is worth mentioning that the chirp of the EAM could potentially be utilized to rotate 45° the two PSK rings, as in Fig. 2.16(b), thus enhancing the constellation SNR, e.g., by about 1.2 dB for coherent synchronous detection as reported in Fig. 2.15. For differential detection, however, the differential encoding at the TX of the 8-APSK constellation rotated 45° produces a 16-APSK constellation with ambiguous symbols (compare with Fig. 3 of [Fis00]). To avoid this problem and to use differential detection at the coherent RX, here only the star-like 8-APSK constellation is considered, with the EAM biased at the zero-chirp point.

In the experiment, the optical signal was transmitted through 25 km of standard SMF, then detected by a coherent homodyne RX. The VOA adjusted the received optical power, and the received signal SOP was manually controlled at the RX input. The coherent RX consisted of the 3x3 phase-diversity homodyne with three single-ended PDs, similar to Fig. 2.5. The local oscillator was a 100 kHz linewidth ECL emitting at 3 dBm. The DSP was performed by a 50 GSa/s RTO. At the DSP, the received complex signal $I[n] + jQ[n]$ was splitted into two parallel branches to recover simultaneously the amplitude information by envelope detector and the phase information by differential demodulation. For the latter, the complex signal was normalized by its modulus in order to cancel the multiple radii of the 8-APSK constellation and demodulate the phase information only. Finally, the BER was computed by direct error counting over 2^{20} bits. Fig. 7.13 shows a photo of the implemented setup in the laboratory, with detail of the optical components and the recovered QPSK and 8-APSK constellations after the DSP by the RTO.

The first tests evaluated separately the BER of the three modulation formats generated by the DEML: ASK, QPSK and 8-APSK, at 3.125 GBd. The results plotted in Fig. 7.14(a) for FEC threshold of BER = 10^{-3}, show that 8-APSK at the highest bit rate of 9.375 Gb/s achieved a sensitivity of -36 dBm, improving by 8 dB the required sensitivity of that the standardized 10 Gb/s NG-PON2 IM-DD TRXs [ITU19]. The sensitivities of the individual QPSK and ASK separately were 3 and 6 dB better, respectively, at expenses of lower bit rates. The eye diagram at BER < 10^{-5} of the ASK generated at the EAM is shown in Fig. 7.14(b), as well as the constellations for QPSK at the DFB and 8-APSK at the DEML in Figs. 7.14(c) and (d) respectively, for the same BER. It is worth noting the phase widening of the constellation symbols for 8-APSK in Fig. 7.14(d) (more visible in the outer ring) compared to that of QPSK in Fig. 7.14(c) where the EAM is off. This behaviour can be ascribed in part to the residual chirp of the EAM, and in part to an apparent increment of the spectral linewidth caused by small portion of light that is coupled back to the DFB when the EAM is active, and depends on the EAM bias [Era14].

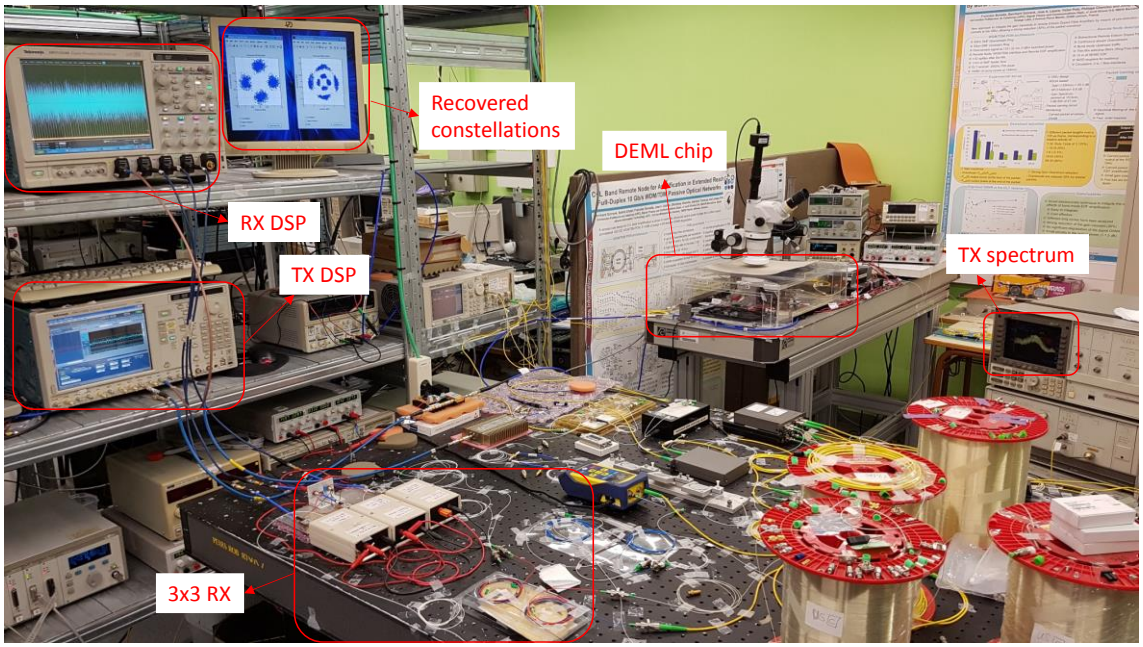

Figure 7.13. Experimental setup implemented in the laboratory in the UPC facilities.

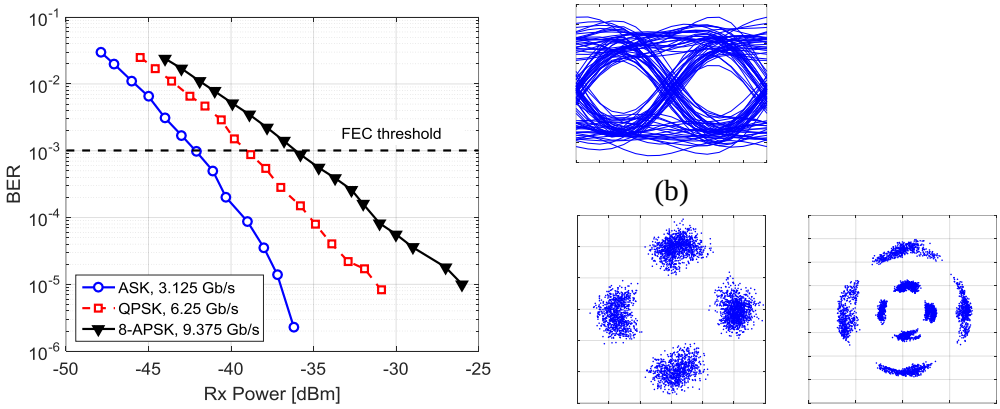

Figure 7.14. (a) BER vs. received power for different modulation formats with the same DEML at R_b = 3.125 GBd. Eye diagram and constellations at BER < 10^{-5} for (b) ASK, (c) QPSK and (d) 8-APSK.

Another important result can be derived from the photodetected spectrum in Fig 7.12 (inset) for 8-APSK at 3.125 GBd, and centered at 12.5 GHz, that shows modulated spectral width below 6.25 GHz, and suggests a feasible optical grid of 12.5 GHz spacing between dedicated wavelength channels at 10 Gb/s.

To mitigate the non-ideal response $L(f)$ of the DFB, depicted in Fig. 7.11(a), DPE linear filtering at the TX was applied preceding the DFB modulation. The constellations in Fig. 7.15(a) illustrate the benefit of DPE at 3.125 GBd, when the received power was set to -35 and -31 dBm for QPSK and 8-APSK respectively. In both cases, the constellations without DPE are highly distorted and the BER is > 10^{-2}, whereas after 16-tap DPE they are recovered with BER = 10^{-4}. In Fig. 7.15(b) the performance of the DPE is assessed when the number of filter taps varies. The results in terms of the power penalty at BER = 10^{-4} as a function of the number of taps, indicate that at 1 dB

maximum penalty, a DPE with only 12 taps is needed to transmit 10 Gb/s using the DEML. As expected, QPSK and 8-APSK require the same number of DPE taps since the AM response of the EAM does not have any BW limitation at the tested R_b and makes no substantial impact on the QPSK at the selected EAM bias.

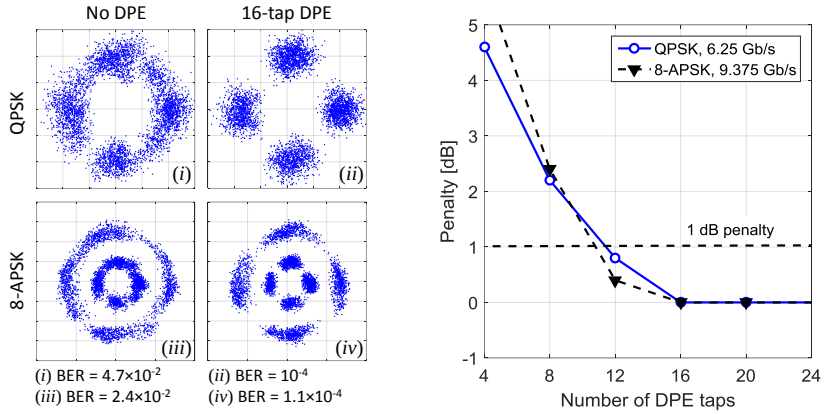

(a) (b)

Figure 7.15. With R_b = 3.125 GBd: (a) constellation diagrams with/without DPE for QPSK and 8-APSK; (b) power penalty at BER = 10^{-4} vs. number of DPE filter taps.

With these results in mind, the 10G coherent udWDM-PON with DEML at the optical TX can be dimensioned and compared with the WDM solution for NG-PON2 [ITU19], as summarized in Table 7.1. The NG-PON2 allocates up to 8 channels separated by a minimum of 50 GHz, achieving aggregated PON capacity of 80 Gb/s in an optical band of 400 GHz. In contrast, the proposed 8-APSK coherent udWDM-PON can allocate up to 32 channels separated by 12.5 GHz within the same optical spectrum. This implies an aggregated PON capacity of 320 Gb/s, i.e., four-times the capacity of NG-PON2 without increasing the optical and the electrical BW requirements. Besides, the 8 dB enhanced RX sensitivity also improves the available power budget, allowing for either additional power splitting serving more users or extended fibre reach. The proposed solution can be directly used at higher bit rates and at different applications where simple coherent TRXs are required.

Table 7.1. 10G PON dimensioning and comparison.

	Sensitivity [dBm]	**Channel spacing [GHz]**	**Number of channels**	**Aggregated PON capacity [Gb/s]**
8-APSK (Coherent)	-36	12.5	32	320
NG-PON2 (IM-DD)	-28	50	8	80

7.3 Chapter Summary

This chapter studied DPE linear filtering at the TX as an enabling technology for high-speed coherent optical access, employing direct-phase modulation of commercial DMLs and low-cost DACs with limited resolution. The analytical derivation of the linear DPE through the MMSE criterion, accounts for the resolution bits of the DAC in order to minimize the impact of the quantization noise. The proposed technique was first validated by numerical simulation, utilizing experimental measurements of the FM response of low-cost DFBs. The numerical results demonstrated that a simple linear DPE filter at the TX, with only 32 taps, can enable transmission well beyond 10 Gb/s with all considered modulation formats, up to 8-PSK, and regardless of the employed DFB laser. In terms of the DAC requirements, the numerical results were obtained by considering a band-limited (8 GHz BW at -3 dB) and low-resolution DAC, as low as 4-bit, lowering by up to 3-bit resolution the DAC requirements for conventional zero-forcing DPE.

The chapter also presented the EML with dual drive configuration –DEML– as a compact and cost-effective alternative to external IQ modulators for complex lightwave modulation. With this low footprint photonic integrated device, a simple 8-APSK coherent TX for udWDM-PON was demonstrated at 10 Gb/s per user, achieving enhanced sensitivity and better spectral efficiency than the standard 10G NG-PON2. To properly operate the DEML as a complex lightwave modulator, careful optimization of the bias current/voltage for each of the DEML sections is necessary to isolate the amplitude modulation at the EAM from the phase modulation at the DFB. The DFB section was biased far from the threshold current to minimize the ER of the residual IM at most, so that the DFB behaves as an optical FM modulator through the laser chirp. Similarly, the FM contribution of the EAM by its inherent chirp can be minimized by biasing the EAM near to the zero-chirp region. Additionally, the band-limited electro-optical modulation response of the DEML was effectively mitigated by the linear DPE, thus extending the BW for high-speed coherent optical access.

The DEML was capable of generating a set of polar-like modulation formats, spanning from BPSK up to at least 8-APSK, without adding extra HW complexity, flexibly adapting to the required type of service and different bit rates. This technique of simultaneous amplitude-and-phase modulation of the DEML can be directly extended to higher order modulation formats, with more amplitude and phase levels, depending on the total laser linewidth and the SNR constraints. Moreover, if m-APSK constellations with only 2-rings are generated, the coherent TX only requires a DAC for the DFB, thus further reducing the complexity, cost and energy consumption of the PON.

Chapter 8

Conclusions and Future Work

The research conducted in this thesis brings a novel perspective on the design rules, main subsystems, and key parameters for implementing the user equipment –namely ONU– of a next generation optical access network that introduces the groundbreaking concept of dedicated λ-to-the-user in a PON, with individual user BWs >1 Gb/s for residential services, and >10 Gb/s for enterprises and mobile antenna. This updates the paradigm of actual standards for PON of sharing the same λ among several users (e.g., 32/64), and distributing the data traffic by TDM. The proposed next-generation udWDM-PON becomes cost-effective by efficiently allocating hundreds of λs (i.e., individual users, up to 256) in ultra-dense optical grid configuration, with bidirectional transmission over a single optical fiber channel, thus achieving a remarkably high aggregate PON capacity, in excess of 300 Gb/s, but still retaining the bit rate per single λ down. The enabling technology to turn the envisioned udWDM-PON into reality is a novel class of low-cost coherent TRX that outperforms the conventional IM-DD TRXs deployed in T(W)DM-PON. It is precisely the feature "low-cost" the main motivation and primary target of the investigation in this thesis, and more generally, in the research worldwide for future PON technologies. Not surprisingly, the high cost and complexity of commercial coherent TRXs for optical core networks have been the main barriers for their direct adoption in PONs. To overcome this techno-economic hurdles, this thesis presented a comprehensive investigation on the key techniques to simplify the coherent transmission systems in the PON scenario, having in mind that lower complexity and cost take more relevance over achieving the highest performance. The result is a coherent TRX conceptually complex, but affordable in cost by exploiting photonic integration, simplified optical modulation, low-cost optics, consumer electronics, and HW efficient DSP. In what follows, the most relevant solutions/contributions presented in this thesis are pointed out.

(I) Commercial low-cost DFBs, thermally-tunable, and with statistical λ (non-preselected), are implemented as optical sources for the TX and the LO of the coherent RX. The λ-stabilization of the DFBs was achieved by an electronic control system with Peltier TEC, integrated in the laser PCB. The tunability range is ~3 nm (375 GHz) by 30° temperature variation, and the time constant for reference 12.5 GHz frequency shift is ~700 ns (by fast injection current tuning). To increase the accuracy of the λ-stabilization system, critical in the udWDM-PON to avoid penalty at the coherent detection and interference to adjacent channels, the mechanisms for further LO feedback stabilization by the frequency estimation subsystem of the coherent RX, were investigated in Chapter 5 either for homodyne RXs with DSP, or fully-analog heterodyne RXs. The results shown optical frequency locking range as wide as $\pm$1 GHz for 1.25 Gb/s bit rate, with residual frequency offset $<\pm$25 MHz.

(II) To fully exploit the linear field detection capability of the coherent RX, directly-modulated DFBs are proposed as low-cost optical m-PSK modulators through the adiabatic laser chirp. The optical frequency variations are converted to phase variations by pre-filtering the modulating current to the DFB with a high-pass filter response. Moreover, photonic

integration of DFB with EAM in dual-drive configuration –DEML– was examined in Chapter 7 for full amplitude-and-phase lightwave vector modulation, more compact and energy-efficient than conventional IQ modulators based on MZM because of the lower insertion loss of the DEML (then no extra optical amplification is needed) and the lower amplitude of the voltage/current swing for modulation. With this small-footprint, simple and cheap optical modulation technique, complex constellations spanning from DPSK up to 8-APSK –for the first time– were achieved, with bit rates from 1.25 to 10 Gb/s.

(III) The complexity of the coherent RX front-end for polarization-independent detection has been lowered by replacing costly optical 90° hybrids by simpler 2x2 or 3x3 fused-fiber couplers, depending on the detection scheme. In the case of homodyne detection, the RX front-end is implemented with 2x 3x3 coupler and 6 PDs, instead of conventional 2x 90° hybrid with 8 PDs. In the case of heterodyne detection, the investigation reported in Chapter 6 yielded a novel architecture for polarization-independent heterodyne front-end, that implements only a PBS, a 3x3 coupler and 3 single-ended PDs, one PD less and simpler optics than the conventional balanced heterodyne RX. The photocurrents are balanced by a linear combination in passive HW, to cancel the direct detection terms and the common-mode noise.

(IV) The different types of services and PON users determine the electrical signal processing scheme to be implemented at both the TX and the RX sides of the coherent ONU. On the one hand, the FTTH or residential users (not limited to) with dedicated λ at 1.25 – 2.5 Gb/s, which require mass ONUs deployment, and therefore, cost impacts the most, can be served by fully analog heterodyne ONUs without DACs/ADCs nor DSP. The binary DPSK information is recovered at the coherent RX by simple and robust differential demodulation, which was demonstrated in this thesis to operate up to total laser linewidth $\Delta\nu$ = 0.64% of the bit rate for DPSK in real-time, with high RX sensitivity. On the other hand, for those PON services that demand higher bit rates, homodyne ONUs with real-time DSP can offer bit rates >10 Gb/s with high spectral-efficiency by transmitting high-order complex modulation formats. Yet, the DSP proposed in this thesis for homodyne ONUs is simple and HW-efficient, intended for short-reach coherent applications. Chapter 7 investigated on a novel digital pre-emphasis algorithm for coherent TXs with direct phase modulation, that is more tolerant to strong quantization noise from a DAC with limited resolution. This permits to extend the modulation BW of commercial DFBs, beyond 10 Gb/s, employing low-resolution DACs, as low as 4-bit. At the RX, Chapter 6 presented a complete DSP for polarization-diversity homodyne RXs that operates at only 1 sample per symbol, and opens the possibility of using low-speed ADCs that are a common technology in mobile handset industry.

Despite the simplification of the coherent TRX, the performance still retains high and the proposed udWDM-PON outperforms the actual PON technologies, and fulfills the requirements for next generation PON, which targets optical power budget >30 dB in 30/40 km fiber link, with >100 Gb/s aggregate PON capacity. Table 8.1 summarizes the most important results achieved in the thesis with different modulation formats, bit rates, and coherent ONU type.

Table 8.1. Performance of low-cost coherent ONUs for PON investigated in this thesis.

RX type	Modulation format	Bit rate [Gb/s]	Sensitivity at BER = 10^{-3} [dBm]	Min. channel spacing [GHz]	Remarks	Chapter
Homodyne	DPSK	1.25	-46	3.5	-DFB TX & LO -Polarization independent -Real-time RX DSP at 1sps with FPGA	6
	QPSK	6.25	-39	< 10	-DFB TX, ECL LO -Single polarization -Off-line RX post-processing with RTO	7
	8-APSK	10	-36	< 10	-DEML TX, ECL LO -Single polarization. -Off-line RX post-processing with RTO	7
Heterodyne	DPSK	1.25	-38	7.3	-DFB TX & LO -Polarization independent -Real-time analog RX -RX front-end: 2x2 coupler, 2-PDs single-ended.	4
	DPSK	1.25	-49	7.3	- DFB TX, ECL LO -Polarization independent - Off-line RX post-processing with RTO -RX front-end: 3x3 coupler, 3-PDs balanced.	6

With this novel class of low-cost coherent ONUs, optical power budgets well beyond 30 dB can be achieved in a filter-less PON with higher splitting ratio, transparent to diverse type of users, bit rates and protocols, for convergence of heterogeneous services over the same installed fiber, and fully compatible with deployed legacy PON systems. The use of coherent technologies in the PON also brings outstanding spectral efficiency, enabling ultra-narrow 6.25 to 12.5 GHz channel spacing in the udWDM optical grid, for 1.25 to 10 Gb/s individual user BW with dedicated λ.

Another conclusion worth mentioning is the reduction in CAPEX and OPEX incurred by the telecommunications operators. The coherent udWDM-PON uses the same optical fiber already deployed for current commercial PON systems, thus the operators are not required to invest in new infrastructure. Also, the channel selection by λ-tuning of the TX and LO lasers at the coherent ONU allows for flexible optical spectrum management with elastic user allocation, and the PON can conveniently be flexibly adapted to operate within the C-band where low-cost DFBs are available.

Last, the main outcomes and conclusions of this thesis, validated through intensive experiments that included a field-trial with real-time ONU prototypes and real multimedia traffic, provide

sufficient evidence that coherent systems will no doubt be the future for broadband fixed-line access networks, and cost-effective λ-to-the-user becomes a reality.

8.1 Future Research

To continue this work, there are a variety of open lines and opportunities for future research derived from the investigation presented here, mostly focused on scaling the udWDM-PON to higher bit rates than the considered in this thesis. Following are two relevant topics worth to be developed, in the opinion of the author of the thesis.

1) Chapter 6 presented a CLK recovery algorithm based on the power of the received symbols, that allows operating the ADCs and the whole DSP of the RX at only 1 sps. In this system, the optimal sampling phase of the ADCs is set to be at the maximum of the detected signal power, and therefore, the accuracy of the CLK recovery will evidently depend on the quality of the received pulse shape. In case that the modulation BWs increase to > 10 GBd, the transmitted signals that propagate through the fiber channel are now more affected by CD, producing pulse spreading and distortion that degrades the CLK recovery performance. Here, the challenge is that conventional CD post-compensation is hard to be applied due to the sub-Nyquist sampling rate of the ADCs (only 1 sps). This offers an interesting opportunity to investigate on simple strategies for CD pre-compensation at the TX with non-linear direct phase modulation of DFBs, exploiting the laser chirp.

2) Chapter 6 also revealed a novel and simplified architecture for polarization-independent coherent detection that does not require duplicating the RX front-end, as usual in polarization-diversity coherent RXs. The detection scheme is heterodyne, which is less complex than the homodyne counterpart, but also imposes critical challenges as the larger electrical BW of the RX, and the larger channel spacing due to the image frequency band. Unfortunately, these two features unfavorably scale with the bit rate. Therefore, the novel and promising 3x3 coherent RX architecture presented in this thesis can be further developed to lower the required IF (ideally down to cero, for homodyne detection) and/or reduce the required channel spacing to increase the spectral efficiency.

References

[Agr10] G. Agraval, *Fiber-optic communications systems,* 4th ed., New Jersey, USA, Wiley, 2010.

[Agr16] E. Agrell, *et al.,* "Roadmap of optical communications," *J. Opt.,* vol. 18, pp. 1–40, 2016.

[Ale89] S. Alexander *et al.*, "Passive Equalization of Semiconductor Diode Laser Frequency Modulation," *J. Lightw. Technol.*, vol. 7, no. 1, pp. 11-23, Jan. 1989.

[Amn84] Y. Amnon and P. Yeh, Optical Waves in Crystals: Propagation and Control of Laser Radiation, New York:Wiley, 1984

[Art15] M. Artiglia *et al.*, "Coherent Systems for Low-Cost 10 Gb/s Optical Access Networks," *J. Lightw. Technol.*, vol. 33, no. 15, pp. 3338-3344, Aug. 1, 2015.

[Bar08] P. Baroni, V. Miot, A. Carena, P. Poggiolini, "8B10B line coding to mitigate the non-uniform FM laser response of direct modulated CPFSK transmitter", *OSA Optics Express* 16, 7279-7284 (2008).

[Ben02] N. Benvenuto and G. Cherubini, *Algorithms for Communications Systems and their Applications*, West Sussex, England, Wiley & Sons, 2002.

[Bje96] L. Bjerkan *et al.*, "Measurement of laser parameters for simulation of high-speed fiberoptic systems," *J. Lightw. Technol.*, vol. 14, no. 5, pp. 839-850, May 1996.

[Bor14] R. Borkowski, D. Zibar, and I. T. Monroy, "Anatomy of a digital coherent receiver," *IEICE Trans. Commun.*, vol. 97, no. 8, pp. 1528-1536, Aug. 2014.

[Bot15] F. Bottoni, et al., "Coherent PON system with high-sensitivity polarization-independent receiver and no ADC/DSP," *ECOC 2015*, Th.1.3.2.

[Can14a] I. N. Cano *et al.*, "Direct phase modulation DFBs for cost-effective ONU transmitter in udWDM PONs," *IEEE Photon. Technol. Lett.*, vol. 26, no. 10, pp. 973-975, May 15, 2014.

[Can14b] I. Cano *et al*, "Simplified polarization diversity heterodyne receiver for 1.25Gb/s cost-effective udWDMPON," In *Proceedings of the Conference on Optical Fiber Communication, 2014 (OFC/NFOEC 2014)*, San Francisco (CA), paper W4G.2.

[Can14c] I. Cano, et al., “Polarization independent single-PD coherent ONU receiver with centralized scrambling in udWDM-PONs,” *ECOC 2014*, P.7.12.

[Can15a] I. Cano *et al*., “Experimental demonstration of a statistical OFDM-PON with multiband ONUs and elastic bandwidth allocation,” *IEEE J. Opt. Commun. Netw*., vol. 7, no. 1, pp. A73–A79, Jan. 2015.

[Can15b] I. Cano *et al.*, “Flexible D(Q)PSK 1.25-5 Gb/s UDWDM-PON with directly modulated DFBs and centralized polarization scrambling,” In *Proceedings of 41st European Conference on Optical Communications, 2015 (ECOC 2015)*, paper Th.1.3.7.

[Can16a] I. Cano *et al*., “DQPSK directly phase modulated DFB for flexible coherent udWDM-PONs,” *IEEE PTL*, vol. 28, no. 1, *2016.*

[Can16b] I. N. Cano, J. C. Velásquez, and J. Prat, “7.5 Gb/s direct DFB phase modulation with 8-DPSK for 6.25 GHz spaced coherent UDWDM-PONs,” in *Proc. Conf. OFC*, 2016, pp. 1-3, paper M3C.4.

[Can20] I. Cano *et al.,* “25-Gb/s laser modulated EML with high output power,” *IEEE Photon. Technol. Lett.*, vol. 32, no. 8, pp. 489–491, Apr. 15, 2020.

[Cha18] M. E. Chaibi, *et al.*, “Dispersion-Uncompensated Transmission of NRZ and PAM-4 Single-Sideband Signals using D-EML,” in *Proc. Opt. Fiber Commun. Conf. Exhib. (OFC)*, 2018, Paper Tu2C.3.

[Che12] X. Chen *et al.*, “Equalization of two-mode fiber based MIMO signals with larger receiver sets,” *Opt. Express*, vol. 20, no. 26, pp. B413-B418, Dec. 10, 2012.

[Che19] J. Cheng *et al*, “Comparison of coherent and IMDD transceivers for intra datacenter optical interconnects,” in *Proc. Conf. OFC*, 2019, paper W1F.2.

[Chu11] Y. C. Chung, “Recent advancement inWDM-PON technology,” In *Proceedings of 37th European Conference on Optical Communications, 2011 (ECOC 2011)*, Geneva (Switzerland), paper Th.11.C.4.

[Chu15] G. Y. Chu, V. Polo, A. Lerín, J. Tabares, I. N. Cano and J. Prat, “1.25–3.125 Gb/s per user PON with RSOA as phase modulator for statistical wavelength ONU”, *Opt. Commun.*, vol. 357, pp. 34-40, 2015.

[Chu16] G.Y. Chu *et al.,* “Application on minimizing residual AM in DPSK UDWDM-PON ONU by integrated dual-EML”, *IEEE Photonics J*., vol. 8, no. 3, Jun. 2016.

[Cia14] E. Ciaramella, "Polarization-independent receivers for low-cost coherent OOK systems," *IEEE PTL*, vol. 26, no. 6, 2014.

[Cvi12] N. Cvijetic, "OFDM for next-generation optical access networks," *J. Lightw. Technol.*, vol. 30, pp. 384–398, Feb. 2012.

[Dia06] O.M. Diaz, J. Prat, I. Tafur-Monroy, and H. de Waardt, "Monitoring of Mixed PMD and Coherent Crosstalk in a 10 Gb/s NRZ System with an Electrical Spectrum Domain Technique", In *Proceedings of 32nd European Conference on Optical Communications, 2006 (ECOC 2006)*, Cannes (France), pp 1–2.

[Don12] Z. Dong *et al.*, "6x144-Gb/s Nyquist-WDM PDM-64QAM generation and transmission on a 12-GHz WDM grid equipped with Nyquist-band pre-equalization," *J. Lightw. Technol.*, vol. 30, no. 23, pp. 3687-3692, Dec. 1, 2012.

[Eff17] F. Effenberger *et al.*, "Industrial Trends and Roadmap of Access," *J. Lightw. Technol.*, 2017, 35, (5), pp. 1142-1146

[Enn90] B. Enning and G. Lange, "Adaptive quantized feedback equalization of laser FM-response for optical FSK transmission," *IEEE Photon. Technol. Lett*., vol. 2, no. 11, pp. 838-839, Nov. 1990.

[Era14] D. Erasme, *et al*., "The Dual-Electroabsorption Modulated Laser, a Flexible Solution for Amplified and Dispersion Uncompensated Networks Over Standard Fiber," *J. Lightw. Technol.*, vol. 32, no. 21, pp. 4068–4078, Nov. 1, 2014.

[Erk16] M. S. Erkilinç *et al*, "Polarization-insensitive single-balanced photodiode coherent receiver for long-reach WDM-PONs," *J. Lightw. Technol.*, vol. 34, no. 8, pp. 2034-2041, Apr. 15, 2016.

[Fat13] I. Fatadin, D. Ives, and Seb Savory, "Differential carrier phase recovery for QPSK optical coherent systems with integrated tunable lasers," *Opt. Exp.*, vol. 21, no. 8, pp. 10166-10171, 2013.

[Fer16a] R. M. Ferreira *et al*, "Coherent nyquist UDWDM-PON with digital signal processing in real time," *J. Lightw. Technol.*, vol. 34, no. 2, pp. 826-833, Jan. 15, 2016.

[Fer16b] R. M. Ferreira *et al*, "Hardware optimization for carrier recovery based on M^{th} power schemes," in *Proc. Conf. OFC*, 2016, pp. 1-3, paper Th2A.43.

[Fer17] R. Ferreira *et al*, "Coherent UDWDM-PON with dual-polarization transceivers in real-time," *J. Lightw. Technol.*, vol. 29, no. 11, pp. 909-912, Jun. 1, 2017.

[Fis00] R. Fischer, L. Lampe, and S. Calabrò, "Differential encoding strategies for transmission over fading channels," *Int. Journ. Electr. Commun.*, vol. 54, no 1, p. 59-67, 2000.

[For95] E. Forestieri in G. Prati, "Analysis of Delay-and-Multiply Optical FSK Receivers with Line Coding and Non-Flat Laser FM Response", *IEEE Journal on Selected Areas in Communications*, 13, 543-556 (1995).

[Gar86] F. Gardner, "A BPSK/QPSK timing-error detector for sampled receivers," *IEEE Trans. Commun.*, vol. COMM-34, no. 5, pp. 423–429, May 1986.

[Gha19] S. Ghasemi *et al*, "LUT-free carrier recovery for intradyne optical DPSK receivers in udWDM-PON," *J. Lightw. Technol.*, vol. 37, no. 6, pp. 1608-1613, Mar. 15, 2019.

[Gin98] F. Gini and G. B. Giannakis, "Generalized differential encoding: A nonlinear signal processing perspective," *IEEE Trans. Signal Process.*, vol. 46, no. 11, pp. 2967-2974, Nov. 1998.

[Gla87] B. Glance, "Polarization independent coherent optical receiver," *J. Lightw. Technol.*, vol. LT-5, no. 2, pp. 274-276, Feb. 1987.

[Gon11] N. G. Gonzalez *et al.*, "Reconfigurable digital coherent receiver for metroaccess networks supporting mixed modulation formats and bit-rates," In *Proceedings of the Conference on Optical Fiber Communication, 2011 (OFC/NFOEC 2011)*, Los Angeles (CA).

[Gro14] K. Grobe *et al.*, "Access networks based on tunable lasers," *J. Lightw. Technol.*, vol. 32, no. 16, pp. 2815-2823, Aug. 15, 2014.

[Häg13] C. Häger *et al*., "Design of APSK constellations for coherent optical channels with nonlinear phase noise", *IEEE Trans. Commun.*, vol. 61, no. 8, pp. 3362-3373, Aug. 2013.

[Hay01] S. Haykin, *Communications Systems*, 4th ed., New York, USA, Wiley, 2001.

[Hen82] C. Henry, "Theory of the linewidth of semiconductor lasers," *IEEE J. Quantum Electron*, vol. QE-18, no. 2, pp. 259-264, Feb. 1982.

[Hon15] K. Honda, T. Kobayashi, T. Shimada, J. Terada, and A. Otaka, "WDM passive optical network managed with embedded pilot tone for mobile fronthaul". In *Proceedings of 41st European Conference on Optical Communications, 2015 (ECOC 2015)*, Valencia (Spain), pp. 1-3.

[Hou19] V. Houtsma and D. van Veen, “Optical strategies for economical next generation 50 and 100G PON,” in *Proc. Conf. OFC*, 2019, paper M2B.1

[Hu15] Q. Hu *et al.*, “Complex modulation and detection with directly modulated lasers,” *OSA Optics Express*, vol. 23, no. 25, pp. 32809-32819 (2015).

[ITU14] ITU-T G.989.2 Recommendation: “40-Gigabit-capable Passive Optical Networks (NG-PON2): Physical media dependent (PMD) layer specification”, Dec. 2014.

[ITU16] ITU-T G.652 Recommendation: “Characteristics of a single-mode optical fibre and cable”, Nov. 2016.

[ITU17] ITU, “10-Gigabit-capable passive optical networks (XG-PON): Physical media dependent (PMD) layer specification,” ITU-T G.987.2 Recommendation, Aug. 2017.

[ITU19] ITU-T G.989.2 Recommendation: “40-Gigabit-capable Passive Optical Networks (NG-PON2): Physical media dependent (PMD) layer specification”, Feb. 2019.

[Kan12] S. Kaneko, *et al.,* “Spectrally efficient WDM-PON employing multiwavelength coherent detection with wavelength-swept local light,” In *Proceedings of the Conference on Optical Fiber Communication, 2012 (OFC/NFOEC 2012)*, Los Angeles (CA), paper OTh1F4.

[Kaz17] L. Kazovsky, A. S. Gowda, and J. Prat, “Small Networks, Large Energy: New Frontiers in Green IT”, in *Proc. Conf. ICTON*, Girona, Spain, 2017, pp. 1-6.

[Kaz96] L. Kazovsky, S. Bennedeto and A.Willner, *Optical Fiber Communications Systems*, Artech House Inc., USA 1996.

[Kha16] G. Khanna *et al.*, “A robust adaptive pre-distortion method for optical communication transmitters,” *IEEE Photon. Technol. Lett.*, vol. 28, no. 7, pp. 752-755, Apr. 1, 2016.

[Kik06] K. Kikuchi, “Phase-diversity homodyne detection of multilevel optical modulation with digital carrier phase estimation,” *IEEE J. Sel. Topics Quantum Electron*, vol. 12, no. 4, pp. 563-570, Jul./Aug. 2006.

[Kik12] K. Kikuchi, “Characterization of semiconductor-laser phase noise and estimation of bit-error rate performance with low-speed offline digital coherent receivers,” *OSA Optics Express*, vol. 20, 5291-5302 (2012).

[Kik16] K. Kikuchi, “Fundamentals of coherent optical fiber communications,” *J. Lightw. Technol.*, vol. 34, no. 1, pp. 157-179, Jan. 1, 2016.

[Kim06] H. Kim *et al.*, "A novel way to improve the dispersion-limited transmission distance of electroabsorption modulated lasers," *IEEE Photon. Technol. Lett.*, vol. 18, no. 8, pp. 947–949, Apr. 15, 2006.

[Koc13] B. Koch *et al.*, "First endless optical polarization and phase tracker," in *Proc. Conf. OFC/NFOEC*, 2013, paper OTh3B.7.

[Lav13] D. Lavery, R. Maher, D. S. Millar, B. C. Thomsen, P. Bayvel, and S. J. Savory, "Digital coherent receivers for long-reach optical access networks," *J. Lightw. Technol.*, vol. 31, no. 4, pp. 609–620, Feb. 15, 2013.

[Lev07] A. Leven, N. Kaneda, U.-V. Koc, and Y.-K. Chen, "Frequency estimation in intradyne reception," *IEEE Photon. Technol. Lett.*, vol. 19, no. 6, pp. 366–368, Mar. 15, 2007.

[Lev10] A. Leven, N. Kaneda, and S. Corteselli, "Real-time implementation of digital signal processing for coherent optical digital communication systems," *IEEE Journal of Selected Topics in Quantum Electronics*, vol. 16, no. 5, pp. 1227–1234, (2010).

[Li19] J. Li *et al.*, "Real-time fast polarization tracking based on polarization phase locking least mean square algorithm", *OSA Optics Express*, vol. 27, no.16, 22116-22126 (2019).

[Luo19] M. Luo *et al*., "Real-time coherent UDWDM-PON with dual-polarization transceivers in a field trial," in *IEEE/OSA Journal of Optical Communications and Networking*, vol. 11, no. 2, pp. A166-A173, Feb. 2019.

[Man18] U. Mankong *et al*., "Vector modulation by laser and electroabsorption modulator with digital pre-coding and pre-compensation," *J. Lightw. Technol.*, vol. 36, no. 19, pp. 4633–4639, Oct. 1, 2018.

[Mat19] K. Matsuda and N. Suzuki, "Hardware-efficient signal processing technologies for coherent PON systems," *J. Lightw. Technol.*, vol. 37, no. 6, pp. 1614-1620, Mar. 15, 2019.

[Mec16] A. Mecozzi, C. Antonelli, and M. Shtaif, "Kramers–Kronig coherent receiver," *Optica*, vol. 3, no. 11, pp. 1220-1227, Nov. 2016.

[Nak14] G. Nakagawa *et al.,* "Crosstalk analysis of FSK light label on 112 Gbps DP-QPSK signal in CNCG ROADM network", In *Proc. Conf. on Optical Fiber Communication, 2014 (OFC/NFOEC 2014),* San Francisco (CA), pp. W3B-1.

[Nap14a] A. Napoli *et al*, "On the next generation bandwidth variable transponders for future flexible optical systems," in *Proc. Conf. EuCNC*, Jun. 2014, pp. 1-5.

[Nap14b] A. Napoli *et al.*, "Reduced complexity digital back-propagation methods for optical communication systems," *J. Lightw. Technol.*, vol. 32, no. 7, pp. 1351-1362, Apr. 1, 2014

[Nap16] A. Napoli *et al.*, "Digital compensation of bandwidth limitations for high-speed DACs and ADCs," *J. Lightw. Technol.*, vol. 34, no. 13, pp. 3053-3064, Jul. 1, 2016.

[Nat84] F. D. Natali, "AFC tracking algorithms," *IEEE Transactions on Communications*, vol. 32, no. 8, pp. 935–947, Aug. 1984.

[Nes17] D. Nesset, "PON Roadmap," *J. Opt. Commun. Netw.*, vol. 9, no. 1, pp. A71–A76, Jan. 1, 2017.

[Nic89] G. Nicholson and T. Stephens, "Performance analysis of coherent optical phase-diversity receivers with DPSK modulation," *J. Lightw. Technol.*, vol. 7, no. 2, pp. 393-399, Feb. 1989.

[Noe05] R. Noé, "Phase noise-tolerant synchronous QPSK/BPSK baseband-type intradyne receiver concept with feedforward carrier recovery," *J. Lightw. Technol.*, vol. 23, no. 2, pp. 802-808, Feb. 2005.

[OIF08] Optical Internetworking Forum (OIF), "Integrable tunable transmitter assembly MSA," OIF-ITTA-MSA-01.0, *Opt. Internetw. Forum*, Fremont, CA, USA, Nov. 2008.

[OIF15] Optical Internetworking Forum (*OIF*), "Technology options for 400G implementation," Jul. 2015.

[Pet88] K. Petermann, *Laser Diode Modulation and Noise*, Dordrecht, the Netherlands, Kluwer Academic, 1988

[Pfa09] T. Pfau, S. Hoffmann, and R. Noé, "Hardware-Efficient Coherent Digital Receiver Concept With Feedforward Carrier Recovery for *M*-QAM Constellations," *Journal of Lightwave Technology*, vol. 27, no. 8, pp. 989 (2009).

[Pie89] J. Pietzsch, "Scattering Matrix Analysis of 3 x 3 Fiber Couplers," *J. Lightw. Technol.*, vol. 7, no. 2, pp. 303-307, Feb. 1989.

[Pol14] V. Polo, P. Borotau, A. Lerín, and J. Prat, "DFB laser reallocation by thermal wavelength control for statistical udWDM in PONs," In *Proceedings of 40th*

European Conference on Optical Communications, 2014 (ECOC 2014), Cannes (France), pp. 1–3, paper P.4.13.

[Pra12] J. Prat, V. Polo, P. Zakynthinos, I. Cano, J. Tabares, J.M. Fàbrega, D. Klonidis, and I. Tomkos, "Simple intradyne PSK system for UDWDM-PON," *OSA Optics Express*, vol. 20, no. 27, pp. 28758–28763, Dec. 2012.

[Pra16] J. Prat *et al*, "Technologies for cost-effective udWDM-PONs," *J. Lightw. Technol.*, vol. 34, no. 2, pp. 783-791, Jan. 15, 2016.

[Pre17] M. Presi *et al.*, "Field-trial of a high budget, filterless, λ-to-the-user, UDWDM-PON enabled by an innovative class of low-cost coherent transceivers," *J. Lightw. Technol.*, vol. 35, no. 23, pp. 5250–5259, Dec. 1, 2017.

[Pro02] J. Proakis and M. Salehi, *Communication Systems Engineering*, 2nd Ed., Prentice Hall, USA, 2002.

[Pro11] J.-G. Provost and F. Grillot, "Measuring the chirp and the linewidth enhancement factor of optoelectronic devices with a mach–zehnder interferometer," *IEEE Photon. Journ.*, vol. 3, no. 3, pp. 476-488, Jun. 2011.

[Raf99] A. Rafel *et al.*, "A novel methodology for measuring coherent homo-wavelength crosstalk in an Optical Signal Supervisory System," In *Proceedings of the Conference on Optical Fiber Communication, 1999 (OFC/NFOEC 1999),* San Diego (CA), paper WM49.

[Rei11] J.D. Reis and A.L. Teixeira, "Architectural optimization of coherent ultra-dense WDM based optical access networks," In *Proceedings of the Conference on Optical Fiber Communication, 2011 (OFC/NFOEC 2011),* Los Angeles (CA).

[Rei12] J.D. Reis, D. Neves, and A. Teixeira, "Analysis of Nonlinearities on Coherent Ultradense
WDM-PONs Using Volterra Series," *Journal of Lightwave Technology*, vol. 30, no. 2, pp. 234 (2012).

[Riz08] U. Rizvi *et al.*, "BER analysis of BPSK and QPSK constellations in the presence of ADC quantization noise," *14th Asia-Pacific Conference on Communications*, Akihabara, Japan, 2008, pp. 1-5.

[Roh11] H. Rohde, S. Smolorz, J.S. Wey, and E. Gottwald, "Coherent optical access networks," In *Proceedings of the Conference on Optical Fiber Communication, 2011 (OFC/NFOEC 2011),* Los Angeles (CA).

[Rop13] M. Roppelt, M. Lawin, and M. Eiselt, “Single-fibre operation of a metro access system with network based wavelength control,” in *Proc. 39th ECOC*, 2013, pp. 309–311, paper Tu.3.F.1.

[Sal16] V. Sales *et al*., “UDWDM-PON using low-cost coherent transceivers with limited tenability and heuristic DWA,” *IEEE J. Opt. Commun. Netw*., vol. 8, no. 8, pp. 582–599, Aug. 2016.

[Sat05] K. Sato, S. Kuwahara, Y. Miyamoto, “Chirp Characteristics of 40-Gb/s Directly Modulated Distributed-Feedback Laser Diodes,” *J. Lightw. Technol.*, vol. 23, no. 11, pp. 3790–3797, Nov. 1, 2005.

[Sav10] S. Savory, “Digital coherent optical receivers: Algorithms and subsystems,” *IEEE J. Sel. Topics Quantum Electron*, vol. 16, no. 5, pp. 1164-1179, Sep./Oct. 2010.

[Sch15] B. Schrenk *et al.*, “Analogue Nyquist-filtering in DSP-less ONU for mitigation of bidirectional channel crosstalk in coherent PON,” In *Proceedings of 41st European Conference on Optical Communications, 2015 (ECOC 2015),* Valencia (Spain), paper Th.1.3.6.

[She99] Y. Shen, K. Lu, and W. Gu, “Coherent and Incoherent Crosstalk in WDM Optical Networks,” *Journal of Lightwave Technology*, vol. 17, no. 5, pp. 759 (1999).

[Shi19] W. Shi *et al*, “Silicon photonic modulators for high-capacity coherent transmissions,” in *Proc. Conf. OFC*, 2019, paper Tu2H.1.

[Smo11] S. Smolorz, E. Gottwald, H. Rohde, D. Smith, and A. Poustie, “Demonstration of a coherent UDWDM-PON with real-time processing,” in *Proc. Conf. OFC/NFOEC*, 2011, pp. 1-3, paper PDPD4.

[Tan08] T. Tanimura *et al*, “Digital clock recovery algorithm for optical coherent receivers operating independent of laser frequency offset,” in *34th European Conference on Optical Communication (ECOC 2008),* paper Mo.3.D.2.

[Tan12] T. Tanimura *et al*, “Superimposition and Detection of Frequency Modulated Tone for Light Path Tracing Employing Digital Signal Processing and Optical Filter”, In *Proceedings of the Conference on Optical Fiber Communication, 2012 (OFC/NFOEC 2012),* Los Angeles (CA), paper OW4G4.

[Tao07] Z. Tao *et al*, “Simple, robust, and wide-range frequency offset monitor for automatic frequency control in digital coherent receivers,” in *Proc. 33rd ECOC*, Sep. 2007, pp. 1–2, paper 3.5.4.

[Tay09] M. G. Taylor, “Phase estimation methods for optical coherent detection using digital signal processing,” *J. Lightw. Technol.*, vol. 27, no. 7, pp. 901-914, Apr. 1, 2009.

[Tei20] A. Teixeira *et al.*, “DSP Enabled Optical Detection Techniques for PON,” *J. Lightw. Technol.* 2020, 38, 684–695.

[Tuc85] R. Tucker, “High-speed modulation of semiconductor lasers,” *J. Lightw. Technol.*, vol. LT-3, no. 6, pp. 1180-1192, Dec. 1985.

[Väl95] V. Välimäki, “A new filter implementation strategy for Lagrange interpolation,” in *Proc. IEEE Int. Symp. Circuits Syst.*, 1995, vol. 1, pp. 361–364.

[Vel18a] J. C. Velásquez *et al.*, “Simultaneous DPSK-ASK modulated dual-EML transmitter for coherent UDWDM-PON,” in *Proc. Opt. Fiber Commun. Conf. Exhib. (OFC)*, 2018, Paper M3B.4.

[Vel18b] J.C. Velásquez *et al*., “15-dB differential link-loss udWDM-PON with direct beat phase modulated DFBs,” *IEEE PTL*, vol. 30, no. 2, *2018.*

[Vit83] A. Viterbi, “Nonlinear estimation of PSK-modulated carrier phase with application to burst digital transmission,” *IEEE Trans. Inf. Theory*, vol. IT-29, no. 4, pp. 543–551, Jul. 1983.

[Vod90] R.Vodhanel, A. Elrefaie, M.Z. Iqbal, R. Wagner, J. Gimlett, and S. Tsuji, “Perfomance of Directly Modulated DFB Lasers in 10-GB/s ASK, FSK, and DPSK Lightwave Systems”, *Journal of Lightwave Technology*, 8, 1379-1386 (1990).

[Xie12] C. Xie, P. Winzer, G. Raybon, A. Gnauck, B. Zhu, T. Geisler, and B. Edvold, “Colorless coherent receiver using 3x3 coupler hybrids and single-ended detection,” *OSA Optics Express*, vol. 20, 1164-1171 (2012).

[Yan13] M. Yan *et al.*, “Digital clock recovery algorithm for Nyquist signal,” in *Proc. Conf. OFC/NFOEC*, 2013, paper OTu2I.7.

[Zha10] S. Zhang, X. Li, P. Y. Kam, C. Yu, and J. Chen, “Pilot-assisted decision-aided maximum-likelihood phase estimation in coherent optical phase-modulated systems with nonlinear phase noise,” *IEEE Photon. Technol. Lett.*, vol. 22, no. 6, pp. 380-382, Mar. 15, 2010.

[Zha12] B. Zhang, C. Malouin and T. Schmidt, “Design of coherent receiver optical front end for unamplified applications”, *OSA Optics Express*, vol. 20, 3225-3234 (2012).

[Zha14] J. Zhang *et al.*, "Time-domain digital pre-equalization for band-limited signals based on receiver-side adaptive equalizers," *OSA Optics Express*, vol. 22, no. 17, pp. 20515-20529, Aug. 25, 2014.

[Zho11] X. Zhou *et al.*, "64-Tb/s, 8 b/s/Hz, PDM-36QAM transmission over 320 km using both pre- and post-transmission digital signal processing," *J. Lightw. Technol.*, vol. 29, no. 4, pp. 571-577, Feb. 15, 2011.

List of Acronyms

A/D	Analog-to-digital
ADC	Analog-to-digital converter
AFC	Automatic frequency control
AGC	Automatic gain control
AM	Amplitude modulation
AMCC	Auxiliary management and control channel
APC	Angled physical contact
APSK	Amplitude-and-phase shift keying
ASIC	Application-specific integrated circuit
ASK	Amplitude shift keying
AWC	Automatic wavelength control
AWG	Arbitrary waveform generator
	Arrayed waveguide grating
AWGN	Additive white Gaussian noise
b2b	Back-to-back
BB	Base-band
BER	Bit error ratio
BPF	Band-pass filtering
BPSK	Binary phase shift keying
BW	Bandwidth
CAPEX	Capital expenditures
CD	Chromatic dispersion
CE	Coexistence element
CLK	Clock
CMOS	Complementary metal-oxide-semiconductor
CMRR	Common-mode rejection ratio
CO	Central office

COCONUT	Cost-effective coherent udWDM-PON for λ-to-the-user access
CR	Carrier recovery
CW	Continuous wave
D/A	Digital-to-analog
DAC	Digital-to-analog converter
DCI	Data center interconnect
DD	Direct detection
DEML	Dual electro-absorption modulated laser
DFB	Distributed feedback
DML	Directly modulated laser
DP	Dual polarization
DPE	Digital pre-emphasis
DPSK	Differential phase shift keying
DS	Downstream
DSP	Digital signal processing
DWA	Dynamic wavelength allocation
EAM	Electro-absorption modulator
ECL	External cavity laser
EDFA	Erbium-doped fiber amplifier
EML	Electro-absorption modulated laser
ENOB	Effective number of bits
ER	Extinction ratio
ESA	Electrical spectrum analyzer
FE	Frequency estimation
FEC	Forward error correction
FFT	Fast Fourier transform
FIR	Finite impulse response
FLIPER	Flexible wavelength distribution for PONs with elastic BW range
FM	Frequency modulation

FPGA	Field-programmable gate array
FSAN	Full service access network
FSK	Frequency shift keying
FTTB	Fiber-to-the-business
FTTH	Fiber-to-the-home
FTTx	Fiber-to-the-x
FWHM	Full-width at half maximum
FWM	Four-wave mixing
GbE	Gigabit Ethernet
GMSK	Gaussian-filtered minimum shift keying
GPIB	General purpose interface bus
GTX	Gigabit transmitter
HD	High definition
HEC	Hetero-wavelength crosstalk
HOC	Homo-wavelength crosstalk
HPF	High-pass filter
hr-OSA	High-resolution optical spectrum analyzer
HW	Hardware
I	In-phase
IF	Intermediate frequency
IM	Intensity modulation
IoT	Internet of things
ISI	Inter-symbol interference
ITU	International telecommunication union
LD	Laser diode
LO	Local oscillator
LPF	Low-pass filter
LTI	Linear time-invariant
LUT	Look-up table

MAC	Media access control
MC	Media converter
MMCM	Mixed-mode clock manager
MMSE	Minimum mean squared error
MSE	Mean squared error
MUX	Multiplexer
MZM	Mach-Zehnder modulator
NCO	Numerically controlled oscillator
NL	Non-linear
NLSE	Non-linear Schrödinger equation
NRZ	Non-return to zero
NTC	Negative temperature coefficient
OA	Optical amplifier
ODN	Optical distribution network
OFDM	Orthogonal frequency division multiplexing
OLT	Optical line terminal
ONU	Optical network unit
OPEX	Operational expenditures
OSA	Optical spectrum analyzer
P2MP	Point-to-multipoint
P2P	Point-to-point
PAM	Pulse-amplitude modulation
PAPR	Peak-to-average power ratio
PB	Power budget
PBC	Polarization beam combiner
PBS	Polarization beam splitter
PCB	Printed circuit board
PD	Photodiode
PDF	Probability density function

PI	Proportional-integral
PLL	Phase-locking loop
PM	Phase modulation
PMD	Polarization mode dispersion
POE	Phase offset estimation
PON	Passive optical network
PPG	Pulse pattern generator
PR	Phase recovery
PRBS	Pseudo-random binary sequence
PSD	Power spectral density
PSK	Phase shift keying
PWM	Pulse-width modulation
Q	Quadrature
QAM	Quadrature amplitude modulation
QPSK	Quadrature phase shift keying
RBS	Rayleigh backscattering
RC	Resistor-capacitor
RIN	Relative intensity noise
RMS	Root mean square
RoF	Radio-over-fiber
RSOA	Reflective semiconductor optical amplifier
RTO	Real-time oscilloscope
RX	Receiver
RZ	Return to zero
SIR	Signal-to-interference ratio
SMF	Single-mode fiber
SMSR	Side-mode suppression ratio
SNR	Signal-to-noise ratio
SOA	Semiconductor optical amplifier

SOP	State of polarization
SPC	Symbol phase correction
SPM	Self-phase modulation
sps	Samples per symbol
SQNR	Signal-to-quantization-noise ratio
SSB	Single side-band
TDM	Time division multiplexing
TEC	Thermoelectric cooler
TED	Timing error detector
TIA	Transimpedance amplifier
TRX	Transceiver
TWDM	Time-and-wavelength division multiplexing
TX	Transmitter
udWDM	Ultra-dense wavelength division multiplexing
US	Upstream
VCSEL	Vertical-cavity surface-emitting laser
VOA	Variable optical attenuator
WDM	Wavelength division multiplexing
XPM	Cross-phase modulation
ZF	Zero-forcing